MEASUREMENTS OF Λ AND Λ_b BARYON PROPERTIES IN THE ATLAS EXPERIMENT

by

Daniel Scheirich

A dissertation submitted in partial fulfillment
of the requirements for the degree of
Doctor of Philosophy
(Physics)
in the University of Michigan
2013

Doctoral Committee:

Professor Homer A. Neal, Chair
Professor Gordon L. Kane
Professor Sara A. Pozzi
Professor Jianming Qian
Professor Bing Zhou

Acknowledgments

This thesis was written by and contains results of physics analyses done by Daniel Scheirich, with extensive support and help of Homer Neal, Junjie Zhu, and Eva Bouhova. The entire effort would not be possible without hundreds of people in the ATLAS collaboration who ensured smooth operation of the ATLAS experiment.

Contents

List of Figures

Figure

List of Tables

Table

List of Appendices

Appendix

Abstract

To study the bound system of 3 valence quarks, Λ and Λ_b baryons represent ideal particles, since they are produced in relatively high quantities at the Large Hadron Collider (LHC) and decay into fully reconstructible final states. This thesis summarizes results of two important measurements with Λ and Λ_b baryons: a measurement of the Λ_b lifetime and mass, and a measurement of the Λ polarization in minimum bias and di-jet events.

The Λ_b lifetime is predictable within a framework of the heavy quark expansion (HQE) calculations, which is widely and successfully used in b-physics. In past decade, the Λ_b lifetime has received some special attention due to a discrepancy between the theoretical prediction and experimental results. The measurement presented here improves on the precision of the previous measurements and helps resolving this discrepancy. The Λ_b lifetime and mass are measured to be $\tau_{\Lambda_b} = 1.449 \pm 0.036(\text{stat}) \pm 0.017(\text{syst})$ ps and $m_{\Lambda_b} = 5619.7 \pm 0.7(\text{stat}) \pm 1.1(\text{syst})$ MeV. A value of the Λ_b and B_d^0 lifetime ratio is measured, too, with the value of $R = \tau_{\Lambda_b}/\tau_{B_d} = 0.960 \pm 0.025(\text{stat}) \pm 0.016(\text{syst})$. The measured value of the ratio is compatible with the theoretical predictions, which range between 0.86 and 0.97.

Large hyperon polarization observed at low-energy fixed target experiments has been puzzling physicists for decades, since their results are incompatible with pQCD calculations. This suggests that some unknown mechanism, which cannot be described by pQCD, is responsible for the hyperon polarization. Measurements at the LHC open up a new avenue for study of the hyperon polarization, since the measurement of polarization of the Λ hyperon produced within a jet becomes possible for the first time. This measurement probes non-perturbative QCD processes, such as fragmentation and hadronization, as possible sources of the hyperon polarization. Λ polarization is measured to be $-0.007 \pm 0.006(\text{stat}) \pm 0.012(\text{syst})$ in the minimum bias and $0.007 \pm 0.011(\text{stat}) \pm 0.007(\text{syst})$ in the di-jet sample. The observed results agree with the extrapolation of the low-energy data.

Chapter 1

Introduction

B-physics and soft-QCD physics are part of a rich physics program in the ATLAS experiment, which also includes study of baryon production and its spin-related properties. This thesis summarizes results of analyses studying production and decay of Λ and Λ_b baryons. They are the lightest baryons containing s and b quarks, respectively, and are therefore produced in copious quantities at the LHC. Their decays $\Lambda \to p\pi^-$ and $\Lambda_b \to J/\psi(\mu^+\mu^-)\Lambda(p\pi^-)$ are fully reconstructible and have clear experimental signature, which makes them ideal final states for study of these baryons. The Λ_b mass is too high to be produced in B-factories, i.e. the e^+e^- colliders with the center-of-mass energy tuned to the mass of $\Upsilon(4S)$ state, which is immediately above the production threshold for a pair of B-mesons. Therefore, Λ_b properties can only be measured at the hadron colliders such as the LHC. As a consequence, the basic properties of Λ_b baryon, such as its lifetime, has not been measured with a great accuracy, yet. The need for a more precise measurement is further strengthen by the fact that two major Tevatron experiments, CDF and DØ, disagree on the value of the Λ_b lifetime. Unlike pseudo-scalar mesons (K and B), the baryons carry spin of 1/2, which makes them ideal experimental tools for study of spin dynamics. Measurements of Λ (and eventually also Λ_b) polarization offer a natural extension of the previous experimental observations of the large hyperon polarization – which has been puzzling physicists for decades – into a completely new energy regime.

This thesis summarizes results of two measurements at the ATLAS experiment: the measurement of the Λ_b lifetime and the measurement of the Λ polarization. The document is structured into 5 chapters. After a brief introduction into the the ATLAS experiment in Chapter 2, there follow a detail description of the two main

analyses in Chapters 3 and 4. An outlook for possible future measurements is given in the final Chapter, 5. Each of the two main sections has its own introduction outlining the physics motivation for the measurement.

The analyses presented in here (and some additional results not included here) were done during the first 3 years of the LHC running. The results are presented in several ATLAS notes and papers, of which Scheirich is the main author. The first observation of the B_d^0 meson in ATLAS 2010 data is reported in Ref [1]. A fully reconstructible cascade decay $B_d^0 \to J/\psi(\mu^+\mu^-)K_S^0(\pi^+\pi^-)$ was used to identify the mesons. Although properties of the B_d^0 meson are well known, this analysis was extremely important for understanding of the ATLAS reconstruction performance and in preparation for the forthcoming Λ_b studies. The first Λ_b study, using the decay $\Lambda_b \to J/\psi(\mu^+\mu^-)\Lambda(p\pi^-)$, was finished in mid of 2011 (using 1.2 fb^{-1} of data) and is reported in Ref [2]. This preliminary measurement was then followed by the measurement of the Λ_b lifetime and mass using the full 2011 statistics (4.9 fb^{-1}), which is published in Ref [3]. The measurement of the Λ polarization is currently in the ATLAS reviewal process, the internal documentation of the analysis can be found in Ref [4].

Apart from the physics analyses, the author of this thesis participated in commissioning and calibration of the Level-2 b-physics trigger in the earlier months of 2010. Without these efforts the ATLAS b-physics program would have not been possible, since the trigger represents a very first selection step in any physics analysis on a hadron collider. Results of the measurement of the b-physics trigger efficiency after the calibration is are reported in paper [5].

Chapter 2

ATLAS Experiment

ATLAS (A Toroidal LHC ApparatuS) [6, 7] is one of the four main experiments at the Large Hadron Collider (LHC) at CERN (European Centre for Nuclear Research). The LHC is proton-proton (or lead ion) collider, currently the largest one in the World in terms of both energy and luminosity of its beams. Four interaction points at the collider circumference are each occupied by one of the main experiments: ATLAS, LHCb, CMS and ALICE. Between November 2009 and December 2012 the LHC operated at reduced center-of-mass energy of 900 GeV (2009), 7 TeV (2010 and 2011) and 8 TeV (2012). After the planned shutdown, which should last till the end of 2014, the machine will restart its operation at the center-of-mass energy close to the design value of 14 TeV. The peak luminosity of the LHC steadily increased throughout the initial period of running until it reached its maximal value of about 8×10^{33} cm^{-1}s^{-1} in 2012, as shown in Figure 2.1. After the shutdown, the LHC is expected to reach the nominal design luminosity of 10^{34} cm^{-1}s^{-1} or higher. The ATLAS experiment has collected integrated luminosities of about 45 pb^{-1}, 5.2 fb^{-1}, and 23 fb^{-1} in years 2010, 2011, and 2012, respectively.

The ATLAS experiment is designed to exploit a full discovery potential of the LHC. The ATLAS physics program focuses mainly on the origin of the mass at electroweak scale based on a spontaneous symmetry breaking, which manifests itself by existence of the standard model (SM) Higgs boson, a family of Higgs particles or a strongly interacting Higgs system. Already the first period of the LHC running provided enough data to allow experiments ATLAS and CMS to discover particle compatible with the standard model Higgs boson with mass around 126 GeV [8]. Searches for heavy W and Z-like objects and final states with the large missing

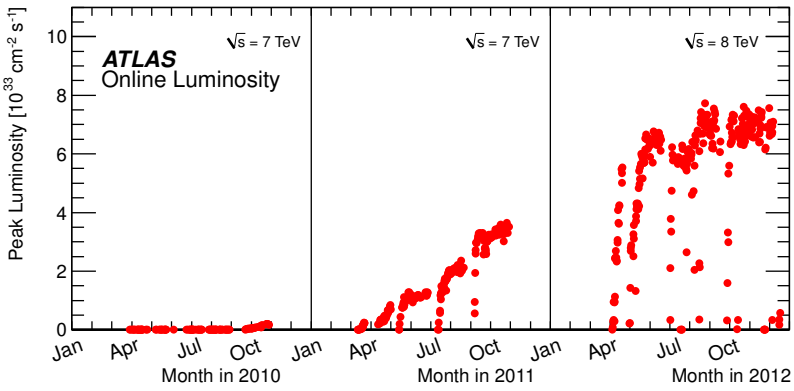

Figure 2.1: Peak luminosity of the LHC vs. time.

energy predicted by super-symmetry (SUSY) and other beyond-standard model theories, as well as searches for exotic physics signatures like black holes, extra dimensions, gravitons and dark matter represent another goal of the experiment. To date, no evidence of physics beyond the standard model has been observed. Figure 2.2, shows measured cross-sections of main SM production processes and their agreement with the theoretical prediction, Figure 2.3, shows the mass reach of ATLAS SUSY searches for a representative selection of the available results. High rate of b and t-quarks allows physicists to study properties of t quark (production cross-section, charge, mass, ...) and properties of B hadrons. The ATLAS B-physics program includes a general spectroscopy of B-states, study of their production mechanisms including measurement of polarization of baryons (Λ, Λ_b) and quarkonia (J/ψ, Υ), precise measurements of CP violation, determination of elements of Cabbibo-Kobaiashi-Maskawa matrix (CKM), and indirect searches for new physics.

The layout of the ATLAS detector is shown in Figure 2.4. It is designed as a general purpose detector for wide variety of physics measurements. It consists of the following sub-detectors serving for reconstruction of main classes of physics objects: the inner detector (ID) for charged particle tracking, the electromagnetic and hadronic calorimeters for electron, photon, τ, and jet reconstruction and the muon spectrometer (MS) for identification and reconstruction of muons. The magnet system, needed for momentum measurement, consists of a thin solenoid placed at the outer radius of the inner detector and three air core toroids in the muon spectrometer outside of the hadronic calorimeter. The ATLAS physics program requires very good electromagnetic calorimetry for a photon and electron

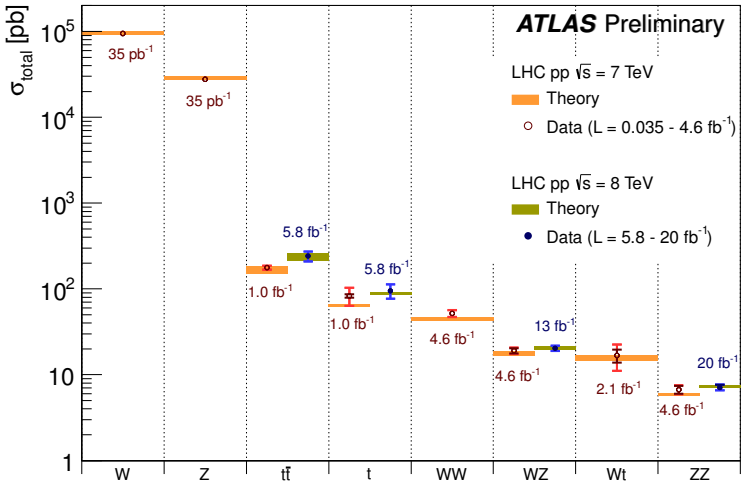

Figure 2.2: Summary of several Standard Model total production cross section measurements, corrected for leptonic branching fractions, compared to the corresponding theoretical expectations. The inclusive b cross section has not been measured by ATLAS, yet.

identification. The hadronic calorimeter must provide accurate measurements of jets and a good η and full ϕ coverage, which is necessary for precise determination of missing transverse energy. The muon spectrometer together with the inner detector tracking system must be able to accurately measure low-p_{T} muons with possibility to measure high-p_{T} muons with the muon spectrometer alone. The tracking is required to be efficient for high-p_{T} lepton momentum measurement, an electron and photon identification and τ-lepton and heavy-flavor tagging.

2.1 Magnet System

The superconducting solenoid is 5.3 m long with a diameter of 2.44 m and provides a magnetic field of 2 T for precise momentum measurements in the ID. It shares its cryostat with the liquid-argon (LAr) electromagnetic calorimeter. The MS magnet system consists of three toroid magnets: barrel toroid and two endcap toroids. Each of them is made of eight independent superconducting coils arranged with an eight-fold symmetry. The outer and inner diameter of the barrel toroid are 20.1 m and 9.4 m, respectively, and it is 25.3 m long. Two endcap toroids enclose the magnet system from sides and they have an outer diameter of 10.7 m. The toroid magnets provide a magnetic field for momentum measurements in

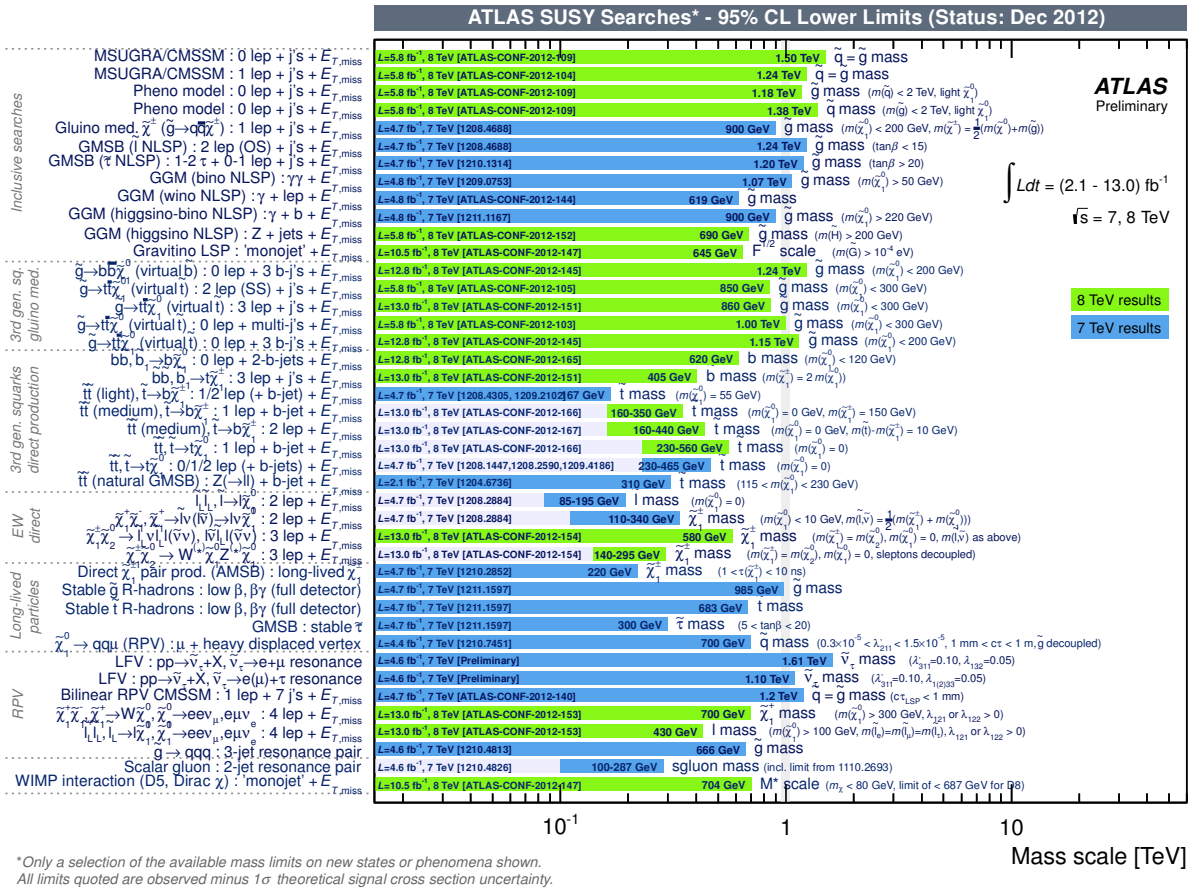

Figure 2.3: Mass reach of ATLAS searches for SUSY. Only a representative selection of the available results is shown. No evidence of physics beyond SM has been observed to date.

the MS that is independent of the ID. The magnetic field of the toroids is not homogeneous and its peak value is 3.9 T and 4.1 T for the barrel and the endcap toroids, respectively.

2.2 Inner Detector

The inner detector [9] is contained in the cavity of the electromagnetic calorimeter. It is 7 m long with a radius of 1.15 m. A pattern recognition, accurate momentum and vertex measurements and electron identification are achieved with a combination of discrete high-resolution silicon pixel and strip detectors in the inner part of the tracking volume, and continuous straw-tube tracking detectors with transition radiation capability in its outer part. The layout of the ID is shown in Figure 2.5.

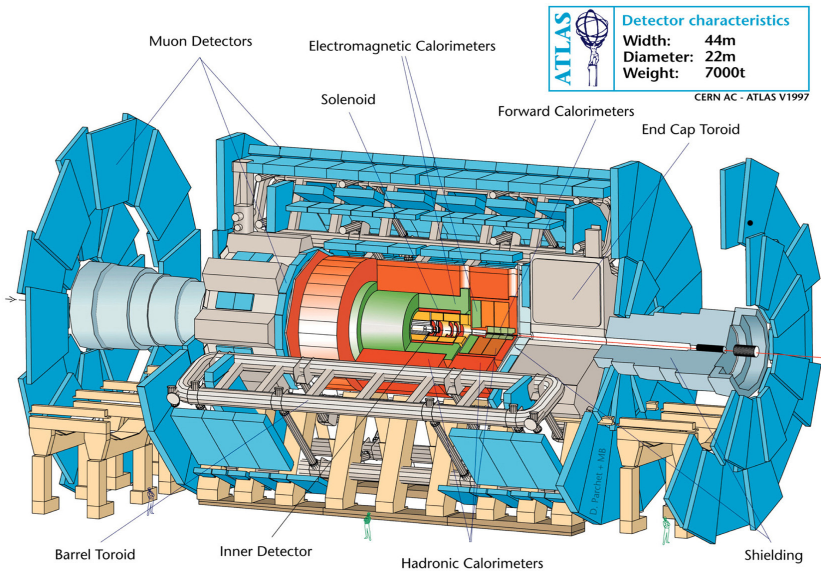

Figure 2.4: ATLAS experiment.

The silicon detectors are arranged in cylindrical layers parallel to the beam axis in the barrel region and perpendicular discs in the endcap regions. Each layer consists of a number of detector modules with an independent read-out electronics. For purpose of vertex reconstruction a high granularity around the interaction point is needed. Therefore, a pixel technology is used for the innermost part of the tracking system. The pixel detectors form three layers in the barrel region and three endcap discs on each side. The pixel detectors have digital readout, allowing for limited measurement of charge (energy) deposited in the pixel by charged particles. The pixel detector have the finest granularity of all the ID

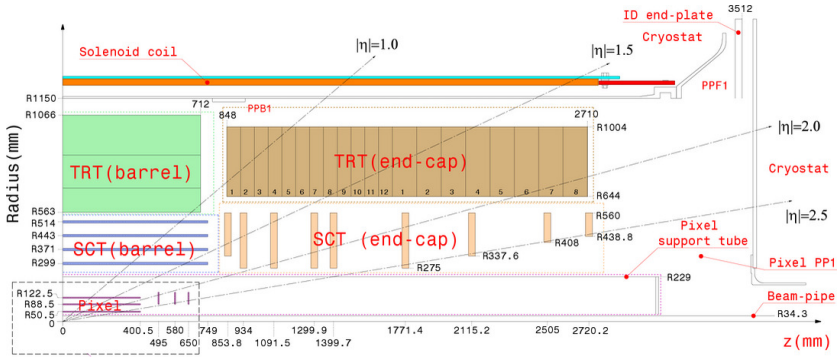

Figure 2.5: Layout of the ATLAS inner detector.

components and over 80 million of the read channels. The spacial resolution is 10 μm in the ϕ direction and 115 μm in the z direction.

The semi-conductor tracker (SCT) is made of four barrel layers and nine end-cap discs on each side provides precise measurement of track space-points. A silicon micro-strip technology is used in order to minimize cost and the number of read-out channels (in total about 6 million) while preserving excellent space-point resolution. The strip detectors allow to measure position only in one dimension (perpendicular to the strips). The two-dimensional position measurement in each module is achieved by using two silicon wafers that are rotated by an angle of 40 mrad. The spacial resolution of the SCT detector module is 17 μm in the ϕ direction and 580 μm along the z direction. The SCT detectors have binary readout, considering only hits with deposited charge above certain threshold.

The transition-radiation tracker (TRT) represents the outermost part of the ID. TRT straws are laid in parallel to the beam in the barrel region and radially in the endcaps. The spacial resolution of the TRT detector is only 2-dimensional, with the resolution along ϕ direction of about 130 μm. TRT straws are surrounded by a radiator (felt-like substrate) packed between the straws. A charged particle passing the radiator produces transition radiation proportional to its Lorentz factor, γ. Two thresholds on the charge deposited in the straws – which is proportional to an intensity of a transition radiation – allow to distinguish between relativistic electrons and low-p_{T} hadrons.

Typically, three pixel layers and eight strip layers (four space points) are crossed by each track. A large number of tracking points (typically 36 per track) is provided by TRT.

2.3 Calorimeters

The calorimeter system [10] provides measurement of energy of hadrons, electrons, and photons. It consists of the two main parts, the electromagnetic (EM) calorimeter and the hadronic calorimeter. Both calorimeters are of sampling type, which means they consist of the inactive medium (absorber) of high density (lead, iron, copper or tungsten) interlaced with the active detectors for measurement of energy. When electromagnetically or strongly-interacting particle enters the calorimeter, secondary particles are created from interactions with the absorber medium and the particle shower propagates through the calorimeters. The calorimeters are

build to fully contain both electromagnetic and hadronic showers. Only a small portion of the energy deposited by the particle is converted to electronic signal and read out by the active detectors, however, this sample of the total together with the information about the longitudinal and transverse profile of the shower is sufficient to determine the original particle's energy, after proper calibration.

The highly granular liquid argon (LAr) EM calorimeter provides an energy measurement and identification of photons, electrons and τ leptons. It is a sampling calorimeter with accordion-shaped layers of lead used as an absorber and liquid argon as active medium. Charge deposited in the liquid argon is collected on segmented copper electrodes immersed in the medium. The EM calorimeter covers pseudorapidity of $|\eta| < 4.9$ and it is hermetic in ϕ. The EM calorimeter has a thickness of $22 - 33$ radiation lengths, X_0, in its central part and $24 - 36$ X_0 in the forward regions. The radiation length is defined as a length that an electron or positron has to travel in the medium to loose all but $1/e$ of its energy due to the radiation loss. The energy resolution of the EM calorimeter is given by the formula [11]:

$$\frac{\sigma_E}{E} = \frac{a}{\sqrt{E/GeV}} \oplus \frac{b}{E} \oplus c, \tag{2.1}$$

where parameter a parametrizes uncertainty due to fluctuations in the deposited energy (stochastic term), b parametrizes the strength of the electronic noise (noise term), and c is the constant term. Values of all the parameters are η-dependent, with the mean values $a \approx 10\%$, $b \approx 0.17$ GeV, and $c \approx 0.7\%$.

The bulk of the hadronic calorimetry is provided by a scintillator-tile sampling calorimeter (TileCal) with iron used for an absorber medium. The tile calorimeter is separated into a large barrel and two smaller extended barrel cylinders, one on each side of the main barrel, covering pseudorapidity up to $|\eta| < 1.7$. Both calorimeters are contained in a cylinder with a radius of 4.25 m and width of 12.2 m. The layout of the calorimeters is shown in Figure 2.6. The thickness of the hadronic calorimeter is 7.4 interaction lengths, λ, defined as the mean free path of a hadronic particle before undergoing an inelastic interaction in the medium. Hadronic calorimetry in the endcap ($1.5 < |\eta| < 3.2$) and forward ($3.1 < |\eta| < 4.9$) regions is provided by the LAr calorimeters, using copper and tungsten as passive material. The resolution of the tile calorimeter and the LAr hadronic endcaps is

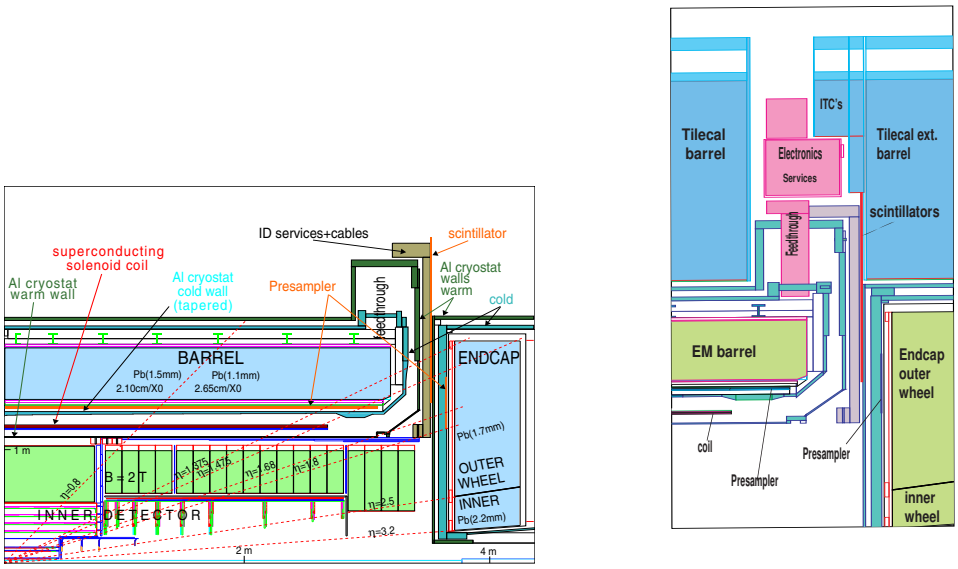

Figure 2.6: Layout of the ATLAS electromagnetic (left) and hadronic (right) calorimeters.

given by the formula [11]:

$$\frac{\sigma_E}{E} = \frac{50\%}{\sqrt{E/GeV}} \oplus 3\%, \tag{2.2}$$

whereas the resolution of the forward calorimeter is

$$\frac{\sigma_E}{E} = \frac{100\%}{\sqrt{E/GeV}} \oplus 10\%. \tag{2.3}$$

2.4 Muon Spectrometer

The layout of the muon system [12] is shown in Figure 2.7. Four types of muon detectors are used. In the barrel, resistive plate chambers (RPC) are used for muon trigger and monitored drift tube chambers (MDT) for accurate tracking, with resolution of about 80 μm. In the endcaps, thin gap chambers (TGC) are used for trigger, MDT and cathode strip chambers (CSC) for tracking (resolution of 80 μm). Momentum measurement is based on deflection of muon trajectories in the magnetic fields of three air-core toroids. In a pseudorapidity region $|\eta| < 1$ the tracks are bent by the field of the barrel toroid. For a pseudorapidity

$1.4 < |\eta| < 2.7$ the deflection is provided by the endcap toroids. In the region of $1.0 < |\eta| < 1.4$, so called transition region, deflection is provided by a combination of the barrel and endcap fields. The magnet configuration provides field that is mostly orthogonal to the muon trajectories.

In the barrel region, the muon chambers are arranged into three super-layers or so called stations. Each station consists of six or eight layers of the monitored drift tubes. The three stations are placed near inner and outer field boundaries and inside the field volume in concentric cylinders with radii of about 5, 7.5 and 10 m, respectively. They cover pseudorapidity of $|\eta| < 1$. A muon momentum is determined from the measurement of a sagitta of the track. In the transition and the endcap regions, the chambers are arranged in four discs orthogonal to the beam axis placed in distances of 7, 10, 14 and 21–23 m from the interaction point. Cryostats of the endcap toroids don't allow to place chambers inside the magnetic field. Therefore, the momentum is determined from a point-angle measurement.

Both in the barrel and the endcaps the chambers are arranged in a sixteen-fold symmetry while the magnetic field have an eight-fold symmetry reflecting the position of the toroid coils. Over the most of the pseudorapidity range the high-precision tracking is provided by MDT chambers. At a large pseudorapidity close to the beam axis, CSC are used to sustain high radiation conditions. In the barrel region two chambers at the bottom side have special shape since they have to make space for the rails supporting the calorimeters. Chambers at the pseudorapidity of $\eta = 0$ are missing to make space for cables and other support lines.

The muon trigger system covers a pseudorapidity range of $|\eta| < 2.4$. In the barrel, RPC are placed in three layers: on both sides of the middle MDT chamber station and directly below the outer one. TGC's are located near the middle station of the endcaps.

2.5 Trigger

A nominal bunch crossing frequency of the LHC is 40 MHz which corresponds to a period of 25 ns [7]. In the initial period of the LHC operation in years 2010 to 2012, the typical bunch separation was larger, ranging from 75 to 50 ns (30 to 20 MHz). The full detector information can be read out at a rate of 75 kHz and stored at a rate of only 200 Hz. Reduction of the event rate is provided by a so

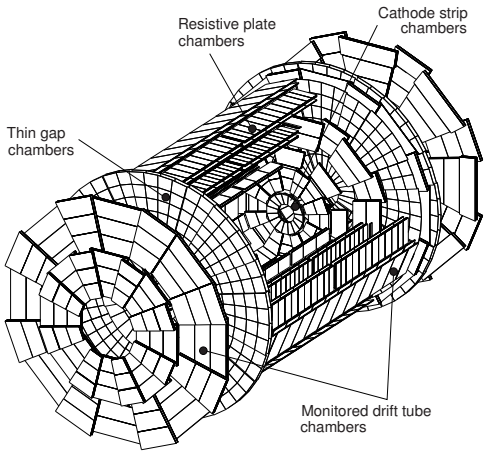

Figure 2.7: Layout of the muon chambers.

called trigger, which is a fast real-time event filtering system being able to reduce the event rate while preserving events with signatures of an interesting physics (e.g. Higgs boson, super-symmetric particles, etc.)

ATLAS employs a three-level trigger system [13, 14], with each level reducing the event rate to the next level and providing seeds for the object reconstruction. The respective levels are called Level-1 (hardware-based), and Level-2 and Event Filter, together called the High Level Trigger (HLT, software-based). An available processing time at each trigger level together with the output rate is shown in Figure 2.8.

The Level-1 trigger is entirely hardware based and it uses only a subset of ATLAS detectors in order to increase the decision speed. High p_{T} muons (with $p_{\mathrm{T}} \geq 4$ GeV at the initial run and $p_{\mathrm{T}} \geq 6$ GeV at nominal luminosity) are reconstructed using only RPC and TGC subdetectors. In both electromagnetic and hadronic calorimeters the reduced granularity is used for an event selection. No information from the inner detector is available at Level-1.

The Level-1 trigger uses simple algorithms to make a decision. The algorithms are executed by custom electronics with adjustable parameters and reduce the initial event rate down to about 75 kHz, with execution times of the order of 2 μs. Before the decision is made, data from all of the $\sim 10^7$ ATLAS detector channels are stored in pipeline memories waiting to be read out in case the event

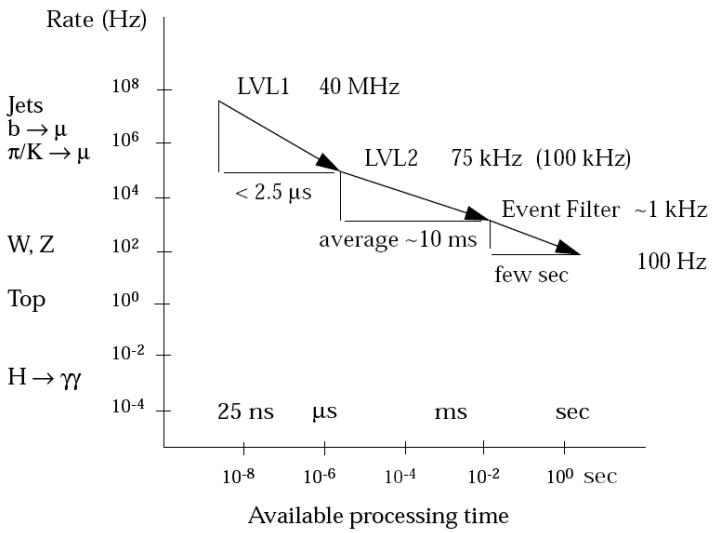

Figure 2.8: Available processing time vs. the output rates of the three trigger levels.

is accepted, which gives the Level-1 trigger necessary time to make the decision.

The Level-one trigger distinguishes the following types of trigger objects:

Muon: muon candidate object reconstructed by the muon spectrometer. The Level-1 muon trigger provides six independently programmable p_{T} thresholds. The selection is based on a requirement of the coincidence of the muon hits in the two or three-station spacial coincidence window. Because of the muon track's bending in the magnetic field, the low-p_{T} muons require a larger coincidence window than the high-p_{T} ones, whose trajectory is more straight.

EM/Tau: electron, photon or τ lepton candidate reconstructed by the EM calorimeter. The EM showers of electrons and photons have the same shape and are therefore indistinguishable at the Level-1. τ leptons decayed into a hadronic final state create a narrow jet of pions which makes a signal in the EM and hadronic calorimeters, that is however distinguishable from the signal of jets. 16 E_{T} thresholds as well as criteria on isolation (both EM and Tau candidates) and hadronic veto (EM candidates) can be applied on the EM/Tau objects.

Jet RoI: hadronic jet candidate reconstructed by hadronic calorimeter. Two different sets of E_{T} thresholds are available for central and forward jets. 8

to central and 4 to forward jets.

Missing ET: signature of neutral weakly interacting particles. E_{T} of all reconstructed jets (or jets with E_{T} above some optional threshold) is converted to E_x and E_y using their ϕ coordinate which are then summed. Set of 8 thresholds can be applied on the global sum.

Total ET: total transverse energy calculated as a sum of E_{T} of all jets (or jets with E_{T} above some optional threshold). 4 thresholds can be applied on total energy sum.

Min. Bias Event: any inelastic-scattering event. The minimum bias trigger uses two segmented minimum bias scintillators located on both faces of the inner detector, which detect any particle with pseudorapidity $2 < |\eta| < 4$, thus selecting any event where the hard p-p collision occurred.

The software-based high level trigger must reduce the rate coming from the Level-1 to about 200 Hz where most of the reduction is done by the Level-2 trigger. Level-2 algorithms are seeded by the Level-1 objects, which means that only a small portion of the event around the Level-1 object, so called Region of Interest (RoI), is transferred to the Level-2 trigger processors. Fast tracking, muon, electron, photon, τ and jet reconstruction is performed in these regions of interest. Since information from the inner detector is now available, more complicated objects such as b-jets or heavy b hadron decays can be reconstructed at Level-2. The employed algorithms usually use simplified versions of algorithms used for the offline reconstruction and have therefore worse resolution. The Level-2 trigger decision is based on requirement of a single object (e.g. single muon trigger), combination of objects (e.g. di-muon trigger), or a more complicated topology of multiple objects (e.g. J/ψ trigger).

The event filter represents the last layer of the trigger selection. It has already access to the whole event and it uses complex algorithms with the performance similar to the one of the offline algorithms. Even though it has already access to the whole event, the event filter algorithms are still guided by the Level-2 objects similarly as Level-2 algorithms are seeded by Level-1. The task of the event filter is to perform the final selection and reduce the output rate from Level-2 to approximately 200 Hz which can be stored on disks and tapes.

Chapter 3

Λ_b Lifetime and Mass

3.1 Introduction

The Λ_b baryon (and its charge conjugate $\bar{\Lambda}_b$) is the lightest baryon containing a b ($\bar{b}$) quark. With the mass of about 5620 MeV [15, 16] it is not produced at B-factories, where the collision center-of-mass energy is tuned to produce pairs of B mesons. Currently, hadron colliders are the only facilities where the properties of b-baryons can be studied. This thesis presents a measurement of the Λ_b mass and lifetime in the ATLAS experiment [11] using the decay channel $\Lambda_b \to J/\psi(\mu^+\mu^-)\Lambda(p\pi^-)$ (the charge conjugate mode is implied throughout the document unless explicitly stated otherwise). The Λ_b lifetime, although measured by many experiments [15, 17, 18, 19], still suffers from a large experimental uncertainty. The decay $B_d^0 \to J/\psi(\mu^+\mu^-)K_S^0(\pi^+\pi^-)$ has the same topology as the studied Λ_b decay. The B_d^0 mass and lifetime are measured with good precision [15], and therefore this decay provides a useful tool to validate the Λ_b results, as both measurements are subject to similar systematic uncertainties. Furthermore, measurement of the Λ_b and B_d^0 lifetime ratio is of great theoretical interest, as explained in the following Section. The lifetime and mass are determined using a simultaneous unbinned maximum likelihood fit to the reconstructed mass and decay time.

3.1.1 Theoretical Considerations

Both Λ_b baryon and B_d^0 meson decay through weak interaction. It means that the b quark inside the hadron decays through exchange of a virtual W boson into

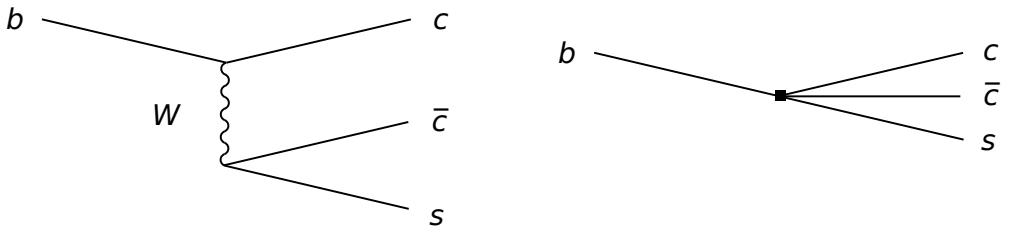

Figure 3.1: Tree-level Feynman diagram of the free b-quark decay $b \to c\,\bar{c}\,s$ in full theory (left) and in the effective Fermi theory (right).

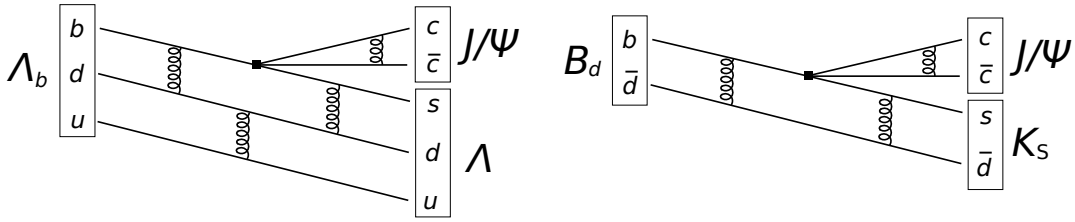

Figure 3.2: Schematic diagram of the decay $\Lambda_b \to J/\psi(\mu^+\mu^-)\Lambda(p\pi^-)$ (left) and $B^0_d \to J/\psi(\mu^+\mu^-)K^0_S(\pi^+\pi^-)$ (right). Curly lines represent color fields binding the constituent quarks into hadrons.

a lighter u or c quark. For example, in the case of the decays studied in this analysis, $\Lambda_b \to J/\psi(\mu^+\mu^-)\Lambda(p\pi^-)$ and $B^0_d \to J/\psi(\mu^+\mu^-)K^0_S(\pi^+\pi^-)$, the relevant quark-level weak decay, $b \to c\,\bar{c}\,s$, is the same in both cases. A tree-level Feynman diagram of such a decay is shown in Figure 3.1, left. Because the mass of the b quark is negligible compared to the mass of the W boson, an effective Fermi theory with a 4-fermion couping (Figure 3.1, right) is sufficient to describe the b quark decay. These simple diagrams, however, correspond to the decay of a free b quark, while in reality the b quark, and also the final state quarks, are enclosed in hadrons, which implies presence of accompanying (spectator) quarks and strong interaction among them, schematically illustrated in Figure 3.2. Similar diagrams can be drawn for other decay channels. Strong interaction with the spectator quarks causes a difference between the inclusive decay rates of Λ_b and B^0_d.

Unlike in the case of light hadrons, lifetimes of heavy b hadrons are predictable by theory with a reasonably good precision. This is possible because the energy release in the decay of heavy b quark is so large that the decay rate is dominated

by the short-distance physics. Large momentum transfer also justifies use of the heavy quark expansion framework (HQE) [20, 21, 22, 23, 24], which leads to a separation (factorization) of the short-distance and long distance effects. Using the HQE, the inclusive decay rate of hadron H_b is expressed as a sum of terms suppressed by powers of the b quark mass, $1/m_b^k$:

$$\Gamma_{H_b} = \sum_k \frac{1}{m_b^k} C_k \langle H_b | \mathcal{O}_k | H_b \rangle. \tag{3.1}$$

In this expansion, the short-distance effects are encoded in the Wilson coefficients, C_k, which are calculated perturbatively, and the long distance physics is confined in the matrix elements of the local $\Delta B = 0$ operators of increasing dimension, $\langle H_b | \mathcal{O}_k | H_b \rangle$, to be obtained from the heavy hadron spectroscopy and the lattice QCD calculations.

It is customary to express the decay rates in terms of ratios, e.g. $\tau_{\Lambda_b}/\tau_{B_d} = \Gamma_{B_d}/\Gamma_{\Lambda_b}$, since this way many theoretical uncertainties cancel out. Up to the second order contribution of HQE (i.e. the term proportional to $1/m_b^2$), the light quark fields do not enter the short-distance weak decay (in such approximation the lifetime ratio would be 1). The spectator quarks contribution appear at order of $1/m_b^3$, and is therefore suppressed by a factor $\sim 1/m_b$ relative to the leading contributions, suggesting that the spectator quark effect is small. This seems to be true in case of lifetime ratios for B mesons, i.e. τ_{B_u}/τ_{B_d} and τ_{B_s}/τ_{B_d}, where excellent agreement between the experimental measurements and the theoretical prediction can be seen [18, 24]:

$$\begin{aligned}
\tau_{B_u}/\tau_{B_d}\big|_{\text{ex}} &= 1.088 \pm 0.009, \\
\tau_{B_u}/\tau_{B_d}\big|_{\text{th}} &= 1.07 \pm 0.03, \\
\tau_{B_s}/\tau_{B_d}\big|_{\text{ex}} &= 0.951 \pm 0.038, \\
\tau_{B_s}/\tau_{B_d}\big|_{\text{th}} &= 1.00 \pm 0.02.
\end{aligned}$$

The situation is more complicated in case of the Λ_b to B_d^0 ratio. The HQE calculations including leading order spectator quark effects [20, 21, 22, 23] (i.e. term proportional to $1/m_b^3$) predict value ranging between 0.93 to 0.95. At the time these predictions were made (i.e. 90's of the 20th century), this value seemed to be quite inconsistent with the experimental results from LEP experiments [15]

that reported value close to 0.8. The controversy persisted even with early CDF [25] and DØ results [26], $\tau_{\Lambda_b}/\tau_{B_d} = 0.797 \pm 0.053$ and 0.81 ± 0.10, respectively, which are still inconsistent with the theoretical prediction.

This lead theorists to investigate next-to-leading order (NLO) spectator effects (the term proportional to $1/m_b^4$ in the HQE) and improving the pQCD calculations of the Wilson coefficients, yielding the new theoretical prediction of the ratio, $R^{\rm NLO} = 0.86 \pm 0.05$, bringing theoretical and experimental values into agreement and seemingly resolving the controversy. However, the situation gets complicated again with the updated CDF and DØ results [18, 19], analyzing the full Tevatron Run II datasets. While the new DØ result, $R^{\rm D\O} = 0.864 \pm 0.052({\rm stat}) \pm 0.033({\rm syst})$, remains consistent with the theoretical prediction, the new CDF value, $R^{\rm CDF} = 1.020 \pm 0.030({\rm stat}) \pm 0.008({\rm syst})$, is now inconsistent with both the theoretical prediction and also the DØ result. It is clear that new experimental measurements at the LHC are needed to resolve this new (this time experimental) controversy. The result reported in this thesis (and also Ref [3]) is the first of such measurements.

Testing of the HQE calculations is of great importance, since the same theoretical calculation methods are also used to predict exclusive b-hadron decay rates which are sensitive to the new physics, such as anomalous CP violation or rare and semi-rare decays. These indirect searches for new physics would not be possible without the excellent understanding of the b hadron decay dynamics.

3.2 Data Samples and Trigger Selection

The ATLAS experiment [11] is a general-purpose detector at the Large Hadron Collider (LHC). It covers nearly the entire solid angle around the interaction point with layers of tracking detectors, calorimeters, and muon chambers. The coordinate system has the z-axis aligned with the beam direction. The transverse momentum, $p_{\rm T}$, and pseudo-rapidity, η, of reconstructed particles are defined with respect to that direction. This analysis uses two ATLAS sub-systems: the inner detector (ID) and the muon spectrometer (MS). Both are situated in a magnetic field and serve as tracking detectors. The ID consists of three types of detector: the silicon pixel detector (Pixel), the silicon micro-strip detector (SCT) and the transition radiation tracker (TRT). The MS consists of monitored drift tube chambers (MDT) and cathode strip chambers (CSC) for precision muon measurements, resistive plate chambers (RPC) and thin gap chambers (TGC) employed by the

muon trigger system. Tracks are reconstructed in the ID and the MS is used to identify muons. Only tracks with p_{T} above 400 MeV and pseudorapidity $|\eta| < 2.5$ are used in this analysis.

The analysis is based on data collected in 2011 using single-muon, di-muon, and J/ψ triggers. The ATLAS trigger system [5] has three levels: the hardware-based Level-1 trigger and the two-stage High Level Trigger (HLT). At Level-1 the muon trigger uses dedicated fast muon-trigger chambers to search for patterns of hits corresponding to muons passing different p_{T} thresholds. Regions of Interest (RoI) around these Level-1 hit patterns then serve as seeds for the HLT muon reconstruction. Since the rate from the low-p_{T} muon triggers was too high for all accepted events to be saved, prescale factors were applied to a subset of the triggers to reduce the output rate. The muon transverse momentum thresholds for single and di-muon triggers range from 4 GeV to 22 GeV. The J/ψ di-muon triggers require that the muons originate from a common vertex, have opposite charge, and the di-muon mass is in the range 2.5 GeV $< m_{\mu\mu} <$ 4.3 GeV. The majority of the sample was collected by the J/ψ trigger with a p_{T} threshold of 4 GeV applied to each muon. This was the lowest-p_{T} unprescaled trigger in the 2011 data taking, however other complementary triggers were used, too. The p_{T} spectrum of the selected muons peaks at 5 GeV, the lowest muon p_{T} is above 2.5 GeV.

The list of triggers used to collect the data sample is shown in Table 3.1. The number of Λ_b events accepted by the individual triggers is shown in Figure 3.3 (top). Only events passing the offline Λ_b selection are counted. One event can be accepted by multiple triggers. Figure 3.3 (bottom) shows the average prescale of each trigger item.

The average prescales extracted from data are used to modify the trigger efficiency in the MC. This means that for a given trigger item only the fraction of events that correspond to the average prescale is considered as accepted by the trigger. For example if the prescale factor is 10 on average only every 10-th event is accepted from events that fired that trigger.

3.3 Monte Carlo Samples

A Monte Carlo (MC) sample of five million anti-baryon $\bar{\Lambda}_b$ events is used to study systematic effects and to correct for the efficiency and acceptance of the detector.

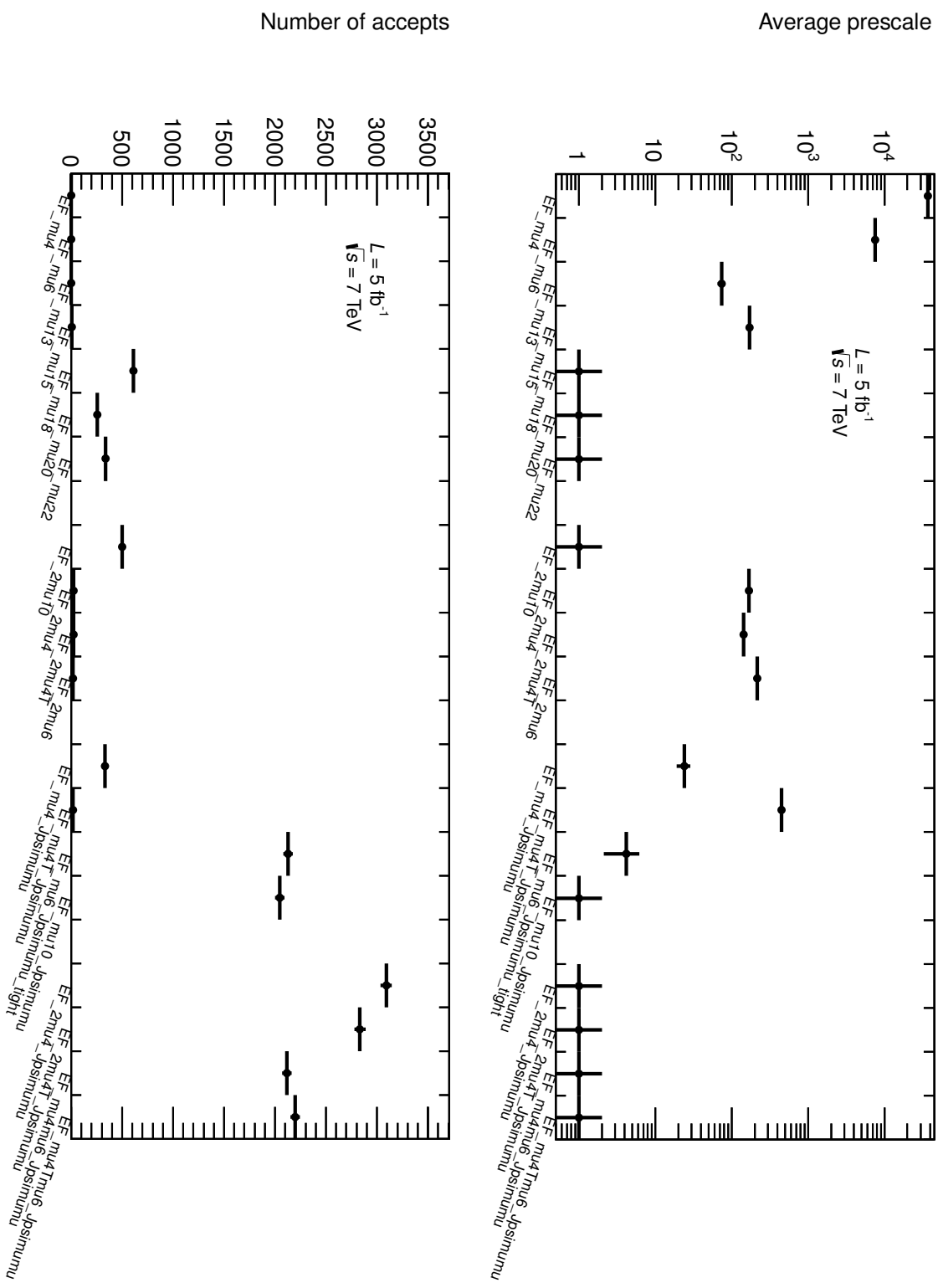

Figure 3.3: Number of events accepted by the triggers (left) and the corresponding average prescales (right)

Table 3.1: List of the used triggers

Single muon triggers	**Di-muon triggers**	***J/ψ* triggers**
EF_mu4	EF_2mu10	EF_mu4_Jpsimumu
EF_mu6	EF_2mu4	EF_mu4T_Jpsimumu
EF_mu13	EF_2mu4T	EF_mu6_Jpsimumu_tight
EF_mu15	EF_2mu6	EF_mu10_Jpsimumu
EF_mu18		EF_2mu4_Jpsimumu
EF_mu20		EF_2mu4T_Jpsimumu
EF_mu22		EF_mu4mu6_Jpsimumu
		EF_mu4Tmu6_Jpsimumu

The sample is generated using the Pythia 6 MC generator [27] with the 2011 ATLAS AUET2B L0** tune [28] and the events are filtered so that each accepted event has a decay $\bar{\Lambda}_b \to J/\psi(\mu^+\mu^-)\bar{\Lambda}(\bar{p}\pi^+)$ with the muons having transverse momenta of at least 2.5 GeV. The MC sample is generated with a Λ_b lifetime of $\tau_{\Lambda_b}^{\mathrm{MC}} = 1.391$ ps.

In addition to the Λ_b and B_d^0 Monte Carlo samples, 4 background samples are used to determine the selection cuts. The Monte Carlo samples are listed in Table 3.2. Since the Monte Carlo samples are not disjoint, events containing a signal decay are removed from the background samples to avoid double counting. Events containing $b \to J/\psi X$ decays are removed from the direct J/ψ sample and events containing J/ψ are removed from $b\bar{b} \to \mu^+\mu^- X$ and $c\bar{c} \to \mu^+\mu^- X$. The individual Monte Carlo samples are weighted by the corresponding cross sections. The $b\bar{b} \to J/\psi(\mu^+\mu^-)X$ sample contains too many decays $\Lambda_b \to J/\psi(\mu^+\mu^-)\Sigma^0(\Lambda^0\gamma)$ as the branching ratio for this decay has the same value as $\Lambda_b \to J/\psi(\mu^+\mu^-)\Lambda(p\pi^-)$ in the Monte Carlo simulation. Though the real branching ratio is unknown, this clearly does not reflect reality. Therefore, the weight of these candidates is scaled down by an arbitrary factor 0.1.

3.3.1 Residual Misalignment and Extra Material Geometries

Before the Inner Detector can be used for a precise momentum measurement, positions of the detector modules have to be determined with a good accuracy. This procedure is called detector alignment. Approximate positions of the modules

Table 3.2: Signal and background Monte Carlo samples. σ denotes the cross section obtained from the MC generator.

Sample	**Stat.**	**Generator cuts**	$\boldsymbol{\sigma}$ **(nb)**
$\Lambda_b \to J/\psi(\mu^+\mu^-)\Lambda(p\pi^-)$	500k	$p_T^{\mu_{1,2}} > 2.5$ GeV	0.062
$B_d^0 \to J/\psi(\mu^+\mu^-)K_S^0(\pi^+\pi^-)$	500k	$p_T^{\mu_{1,2}} > 2.5$ GeV	5.64
Inclusive direct $J/\psi(\mu^+\mu^-)X$	1M	$p_T^{\mu_{1,2}} > 2.5$ GeV	425
Inclusive $b\bar{b} \to J/\psi(\mu^+\mu^-)X$	1M	$p_T^{\mu_{1,2}} > 2.5$ GeV	55.8
Inclusive $b\bar{b} \to \mu^+\mu^-X$	6M	$p_T^{\mu_{1,2}} > 2.5$ GeV	509
Inclusive $c\bar{c} \to \mu^+\mu^-X$	3M	$p_T^{\mu_{1,2}} > 2.5$ GeV	166

are known from the detector blueprints, however, actual position of individual modules may be shifted due to manufacturing imperfections and distortions of the supporting structure. The alignment algorithm [29, 30] uses real data tracks and adjusts positions of individual modules to minimize the residuals, i.e. distance between the hit position measured by the detector and the position interpolated from the track. Although the alignment procedure improves the tracking position and momentum resolution significantly, there will still be some imperfections in the knowledge of the detector module positions, given by the fact the the finite number of tracks is used in the alignment procedure and also that some collective alignment degrees of freedom are not sensitive to the alignment procedure. The detector misalignment after the alignment procedure is performed is called residual misalignment.

To study the effects of the residual misalignment of the Inner Detector, an additional MC sample of 500k events is used. This sample is generated the same way as the default one, however, it is reconstructed using a detector geometry where the position of the individual modules is shifted to model the residual misalignment in the real detector. The detailed description of this distorted geometry can be found in Ref [31]. To get the distorted geometry the following procedure is used:

1. Using real data the distributions of the track transverse impact parameter, d_0, are obtained in 25×25 bins of η and ϕ. In each bin the mean shift of the impact paremeter, δd_0, is determined creating an impact parameter bias map.

Table 3.3: Detector geometry with additional material

Detector subsystem	**Extra material (X_0)**
The whole ID	5%
Pixel services	20%
SCT services	20%
SCT/TRT End-cap	15%
ID endplate	15%

2. The ID alignment algorithm [29, 30] is performed on the Monte Carlo tracks, where the simulated tracks are refitted with a constraint on the impact parameter forcing the bias $d_0 + \delta d_0$, with δd_0 taken from the map. This way the tracking detector modules are misaligned to reflect the impact parameter bias observed in real data.

3. The obtained misaligned geometry is used to re-reconstruct the signal $\bar{\Lambda}_b$ sample.

To study effects of uncertainty in the amount of ID material, the detector simulation is performed assuming some additional material in the detector. The geometry with extra material (see Table 3.3) is used for the simulation, however, the default matrial map is used in the reconstruction of the sample. This creates a discrepancy between real and assumed amount of material in the ID. In Ref [32] the uncertainty on the material amount is measured for the beam pipe, the Pixel detector and the first layer of the SCT. The cited analysis uses secondary vertices to estimate rates of hadronic interactions within ID material and compares results for data and MC. The measured ratio of the hadronic interaction rates in data and MC differs by less than 6% in the Pixel detector and 9% in the first layer of SCT. The used extra material geometry contains 20% extra material in Pixel and SCT sub-systems and one can therefore use this geometry to make a conservative estimate of the material uncertainty systematic uncertainty.

3.4 Reconstruction and Signal Selection

3.4.1 Muon Reconstruction

The muon reconstruction uses two sub-detectors: the Inner Detector (ID) and the Muon Spectrometer (MS). Both are situated in a magnetic field and serve as tracking detectors. ID tracks are reconstructed by 3 types of detector: silicon pixel detector (Pixel), silicon micro-strip detector (SCT) and the transition radiation tracker (TRT). They are reconstructed with pseudorapidity $|\eta| < 2.5$ and transverse momentum $p_{\mathrm{T}} > 400$ MeV. Two types of muons are used in the analysis, known as tagged muons and combined muons. Combined muons are formed from a MS track which is matched to an ID track. The pseudorapidity coverage of combined muons is $|\eta| < 2.5$. Tagged muons consist of ID tracks extrapolated to the Muon Spectrometer and matched to patterns of MS hits and they cover pseudorapidity range $|\eta| < 2.2$. Although both the ID and the MS provide a momentum measurement, in the p_{T} range relevant for this analysis the MS momentum resolution is worse than that of the ID due to energy loss in the calorimeters. Therefore the MS is used only to identify muons, and the momentum measurement is taken from the ID. The standard muon quality requirements must be satisfied by the muon tracks:

- The ID track must have a hit in the first layer of the pixel tracker (b-layer) whenever expected. If the track falls out of the b-layer coverage or if there is a cluster of dead pixels the presence of the hit is not required;
- The number of pixel hits plus the number of crossed dead pixel sensors must be greater than one for the ID track;
- The number of SCT hits plus the number of crossed dead SCT sensors must be greater than five;
- The number of pixel holes plus the number of SCT holes on the track must be less than two;
- Let n_{TRT} stands for the number of TRT hits on the track, $n_{\mathrm{TRT,out}}$ the number of TRT outliers, and $n = n_{\mathrm{TRT}} + n_{\mathrm{TRT,out}}$. Then for tracks with $|\eta| < 1.9$ it is required that $n > 5$ and $n_{\mathrm{TRT,out}} < 0.9n$. For tracks that have $|\eta| > 1.9$ and $n > 5$ the number of outliers must be $n_{\mathrm{TRT,out}} < 0.9n$.

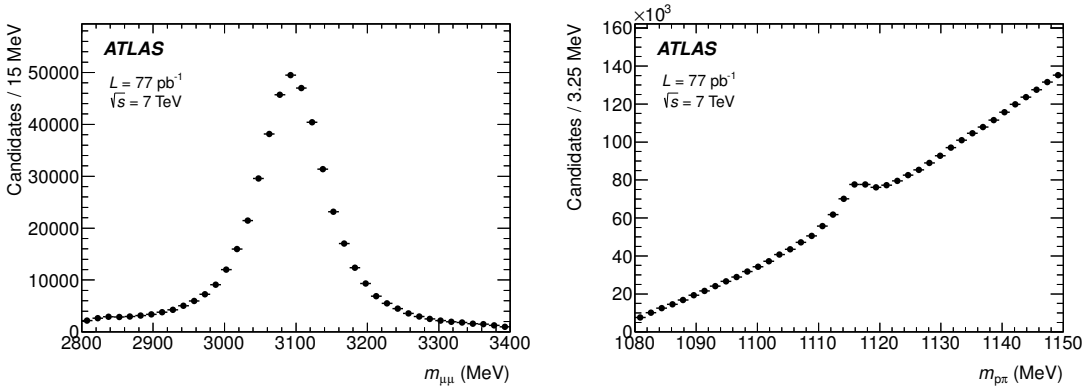

Figure 3.4: Invariant mass distribution of pre-selected J/ψ (left) and Λ (right) candidates. A single run of 77 pb^{-1} is used to make the plots.

3.4.2 J/ψ and Λ Pre-selection

The decay $\Lambda_b \to J/\psi(\mu^+\mu^-)\Lambda(p\pi^-)$ has a cascade topology. The J/ψ decays instantly at the same point as the Λ_b (secondary vertex) while the Λ lives long enough to form a displaced tertiary vertex. There are four final-state particles: two muons from the J/ψ, and a proton and a pion from the Λ decay.

The di-muon and di-hadron (V^0) pairs are pre-selected by requiring that their tracks can be successfully fitted to a common vertex satisfying some basic quality requirements. The J/ψ and V^0 pre-selection is very loose, so that potential candidates are not excluded at this stage. The di-muon candidates are accepted if the J/ψ vertex-refitted invariant mass lies in the range 2.8 GeV $< m_{\mu\mu} <$ 3.4 GeV. The di-hadron candidates are accepted if the invariant mass is in the range 1.08 GeV $< m_{p\pi} <$ 1.15 GeV. The masses of a proton and a pion are assigned to the tracks when the invariant mass is calculated; $p\pi^-$ and $\bar{p}\pi^+$ combinations are tested so that both Λ and $\bar{\Lambda}$ candidates are accepted. J/ψ and V^0 candidates are pre-selected using loose selection criteria so that potential signal candidates are not lost at this stage. Using one large run from period G of the 2011 data sample the distributions of pre-selected J/ψ and Λ invariant masses are shown in Figure 3.4.

3.4.3 Reconstruction of $\Lambda_b \to J/\psi(\mu^+\mu^-)\Lambda(p\pi^-)$

The muon and hadron track pairs pre-selected with the criteria described in the previous section are then refitted with a constraint of a $\Lambda_b \to J/\psi(\mu^+\mu^-)\Lambda(p\pi^-)$

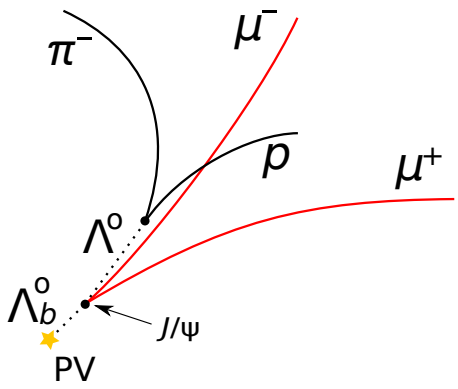

Figure 3.5: Λ_b decay topology.

topology. The muons are constrained to intersect at a single vertex while their invariant mass is set equal to the known mass of the J/ψ, $m_{J/\psi} = 3096.92$ MeV [15]. The two hadronic tracks are constrained to a second vertex and their invariant mass is fixed to the mass of the Λ, $m_{\Lambda^0} = 1115.68$ MeV [15]. The combined momentum of the refitted V^0 track pair is constrained to point to the di-muon vertex in three dimensions. The decay topology is schematically illustrated in Figure 3.5. The fit is performed on all four tracks simultaneously, taking into account the constraints described above (cascade topology fit) and the full track error matrices. The quality of the fit is characterized by the value of χ^2/N_{dof}, where a global χ^2 involving all four tracks is used. The corresponding number of degrees of freedom, N_{dof}, is six. Furthermore, for each track quadruplet, that can be successfully fitted to the Λ_b decay topology, a $B_d^0 \to J/\psi(\mu^+\mu^-)K_S^0(\pi^+\pi^-)$ topology fit is attempted (i.e. a pion mass is assigned to the hadronic tracks and the V^0 mass is constrained to the mass of K_S^0, $m_{K_S} = 497.65$ MeV [15]). This is to label possible B_d^0 decays misidentified as Λ_b.

The Λ_b candidates are then subjected to the following selections:

- The global $\chi^2/N_{\text{dof}} < 3$;
- The transverse momentum of the cascade-refitted V^0, $p_{\text{T},V^0} > 3.5$ GeV;
- The transverse decay length of the cascade-refitted V^0 vertex measured from the Λ_b vertex, $L_{xy,V^0} > 10$ mm;

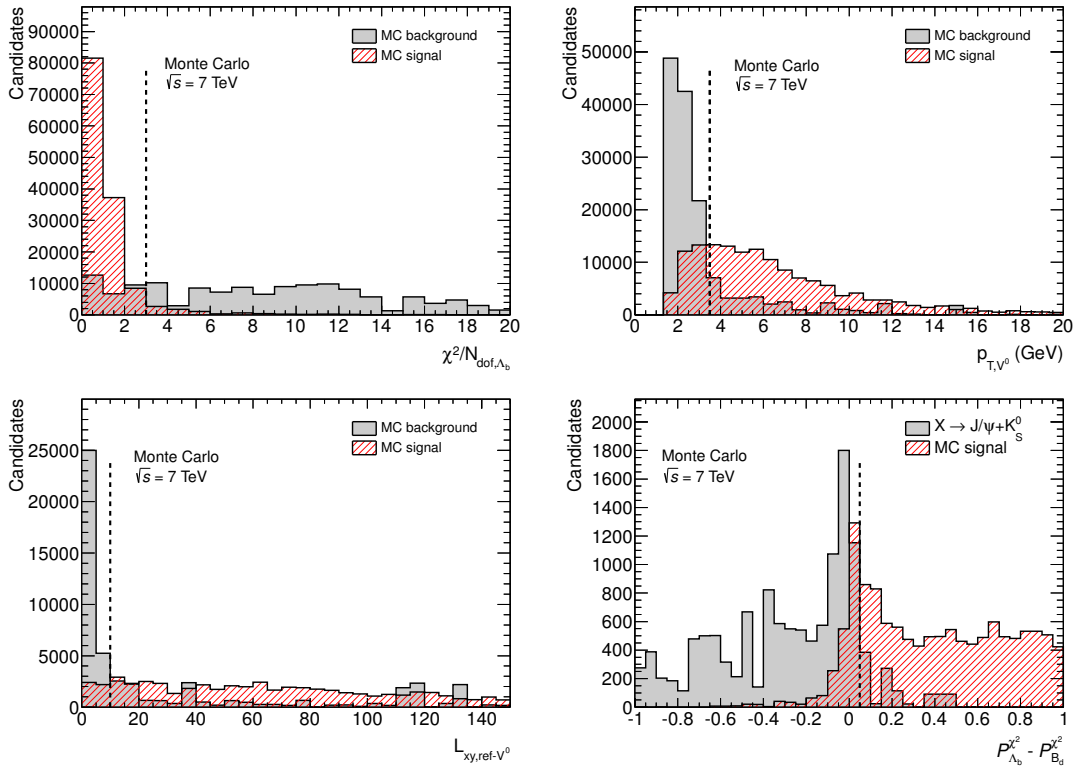

Figure 3.6: Monte Carlo signal and background distributions: $\chi^2/N_{\rm dof}$ (top left), refitted V^0 transverse momentum, p_{T,V^0} (top right), Λ decay distance (measured from the Λ_b vertex), L_{xy,Λ^0} (bottom left), and the difference between the Λ_b and B_d^0 fit probabilities, $\mathcal{P}_{\Lambda_b^0} - \mathcal{P}_{B_d}$ (bottom right). The cut values are indicated by vertical dotted lines.

- The invariant mass must be in the range 5.38 GeV $< m_{J/\psi\Lambda^0} <$ 5.90 GeV;
- If the four tracks forming a Λ_b candidate also result in an acceptable B_d^0 fit, the candidate must have a difference of cumulative χ^2 probabilities of the two fits, $\mathcal{P}_{\Lambda_b^0} - \mathcal{P}_{B_d} > 0.05$.

The selection cuts described above are determined using the MC samples. Distributions of the cut variables for MC signal and background are shown in Figure 3.6. The contribution of the B_d^0 decays to the MC background is shown in Figure 3.7. The figure shows the relative contribution of the MC signal and B_d^0 background before and after the B_d^0 removal. Note that although most of the B_d^0 background is removed, the procedure is not 100% efficient.

With these criteria, 4074 Λ_b and 4081 $\bar{\Lambda}_b$ candidates (including background) are selected. No track quadruplet is successfully fitted as both a Λ_b and a $\bar{\Lambda}_b$

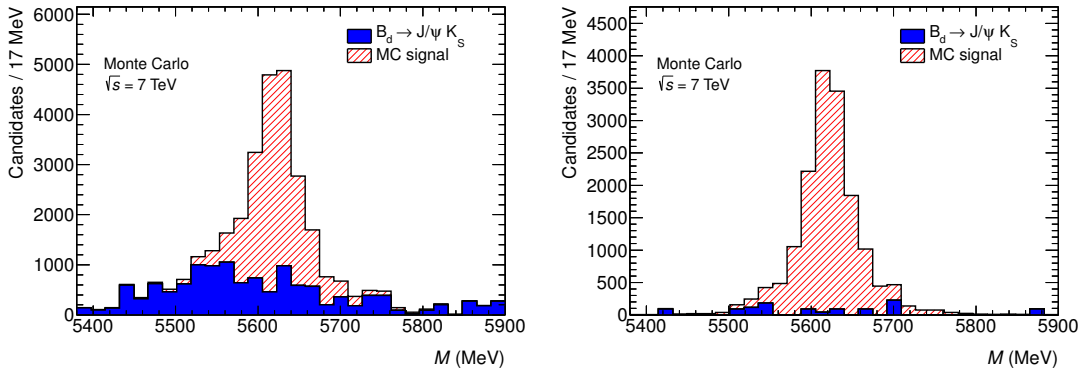

Figure 3.7: Relative contributions of the Monte Carlo signal and the B_d^0 background before (left) and after (right) the B_d^0 removal.

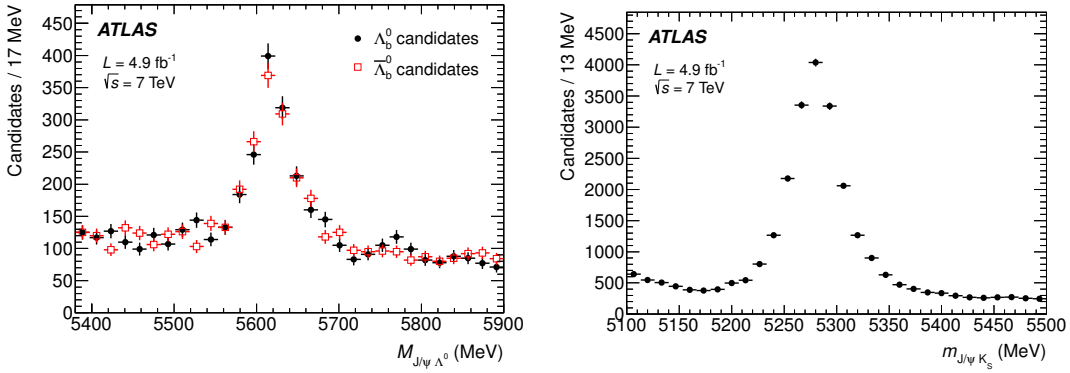

Figure 3.8: Invariant mass distribution of the selected Λ_b and $\bar{\Lambda}_b$ (left) and B_d^0 (right) candidates.

decay. The mass distributions of the selected candidates are shown in Figure 3.8 (left) and the transverse momentum distributions of Λ_b, the muons, the proton, and the pions from the decay chain are shown in Figure 3.9. In the rest of this chapter the Λ_b and $\bar{\Lambda}_b$ samples are combined, unless explicitly stated otherwise.

The $B_d^0 \to J/\psi(\mu^+\mu^-)K_S^0(\pi^+\pi^-)$ channel has the same decay topology as $\Lambda_b \to J/\psi(\mu^+\mu^-)\Lambda(p\pi^-)$ and can be used to cross-check the Λ_b results and to determine the ratio of the Λ_b and B_d^0 lifetimes. The B_d^0 channel is subjected to exactly the same kinematic cuts as for the Λ_b channel, with the only difference being the mass range used for the K_S^0 pre-selection, 440 MeV $< m_{\pi^+\pi^-} <$ 570 MeV, the B_d^0 invariant mass range, 5.1 GeV $< m_{J/\psi K_S^0} <$ 5.5 GeV, and the Λ_b contamination removal criterion, $\mathcal{P}_{B_d} - \mathcal{P}_{\Lambda_b^0} > 0.05$. Using these criteria 27594 of B_d^0 candidates

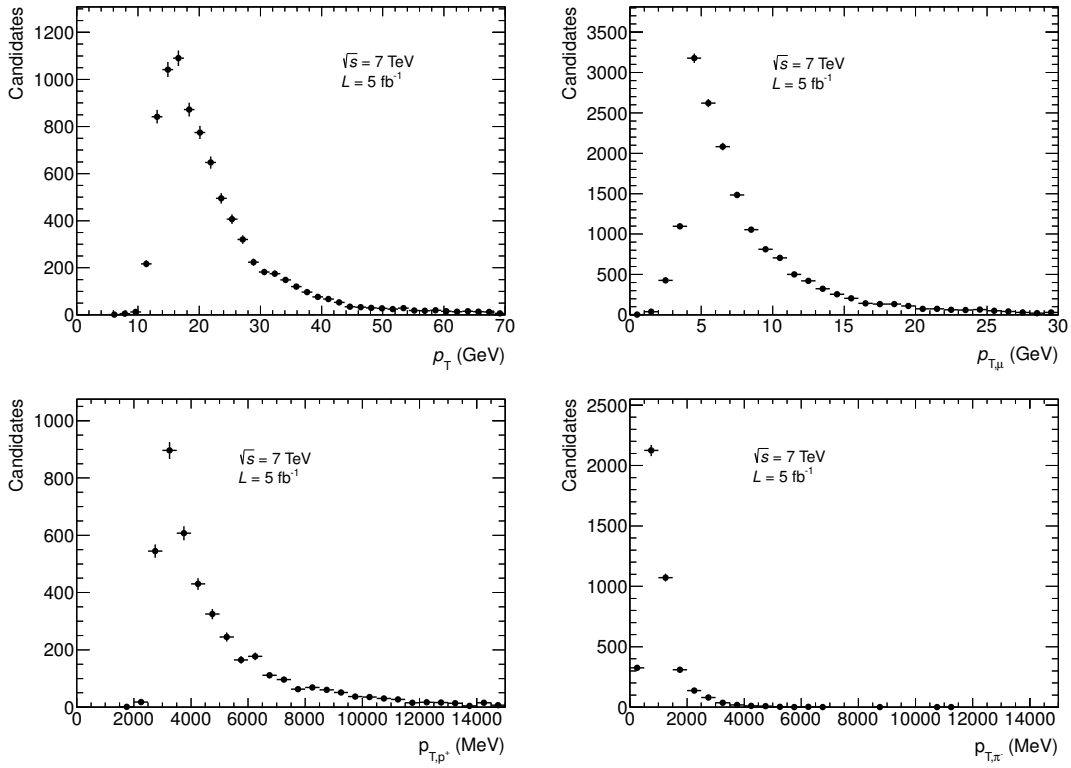

Figure 3.9: Transverse momentum distributions for Λ_b (top left), muons (top right), protons (bottom left), and pions (bottom right).

are selected. The invariant mass distribution is shown in Figure 3.8 (right).

3.4.4 Primary Vertex Selection

The distribution of the multiplicity of the reconstructed collision vertices is shown in Figure 3.10 (left). On average there are 6.8 collision vertices per event in the selected data resulting from multiple collisions at each LHC bunch crossing (pileup events). The collision vertex that lies closest to the direction of the reconstructed Λ_b momentum is used as the primary vertex. In 95% of the cases the chosen vertex has the largest sum of squares of transverese momenta of the tracks used to fit the vertex. This is illustrated in Figure 3.10 (right) where the index of the collision vertex that is used as the primary vertex is shown. The collision vertices are ordered by the sum of squares of track transverse momenta, i.e. the vertex with index 0 has the largest sum-p_T^2.

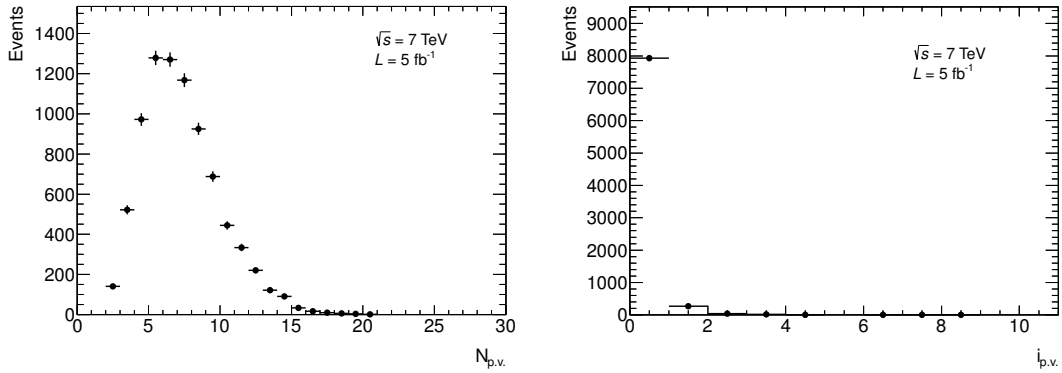

Figure 3.10: Distribution of the collision vertex multiplicity (left) and the index of the selected primary vertex (right).

3.5 Mass and Proper Decay Time Fit

The proper decay time of the Λ_b candidate is calculated from the measured decay distance and the candidate's momentum as follows:

$$\tau = \frac{L_{xy} m^{\mathrm{PDG}}}{p_{\mathrm{T}}},$$

where $m^{\mathrm{PDG}} = 5619.4$ MeV [15], p_{T} is the reconstructed Λ_b transverse momentum, and L_{xy} is the Λ_b transverse decay distance measured from the primary vertex (PV).

An unbinned maximum likelihood fit is used to determine the Λ_b mass and lifetime. The mass and proper decay time are fitted using a likelihood function defined as follows:

$$\begin{aligned} L &= \prod_{i=1}^{N} \Big[f_{\mathrm{sig}} \mathcal{M}_{\mathrm{s}}(m_i|\delta_{m_i}) \mathcal{T}_{\mathrm{s}}(\tau_i|\delta_{\tau_i}) w_{\mathrm{s}}(\delta_{m_i}, \delta_{\tau_i}) + \\ &\quad (1 - f_{\mathrm{sig}}) \mathcal{M}_{\mathrm{b}}(m_i|\delta_{m_i}) \mathcal{T}_{\mathrm{b}}(\tau_i|\delta_{\tau_i}) w_{\mathrm{b}}(\delta_{m_i}, \delta_{\tau_i}) \Big], \end{aligned}$$

where f_{sig} denotes the fraction of signal candidates; m_i is the invariant mass of the i-th candidate and τ_i is its proper decay time. The corresponding errors, δ_{m_i} and δ_{τ_i}, are estimated on a candidate-by-candidate basis by the cascade topology fit. $\mathcal{M}_{\mathrm{s}}$ and $\mathcal{M}_{\mathrm{b}}$ are probability density functions (PDFs) describing the signal and background mass dependence; $\mathcal{T}_{\mathrm{s}}$ and $\mathcal{T}_{\mathrm{b}}$ describe the dependence on the proper decay time. The invariant mass and proper decay time error distributions,

$w_{\mathrm{s(b)}}(\delta_m, \delta_\tau) = w'_{\mathrm{s(b)}}(\delta_m) w''_{\mathrm{s(b)}}(\delta_\tau)$, are extracted from data. It has been verified that using separate PDFs for the signal and background component produces the same result as when a single PDF is used, i.e. $w \equiv w_{\mathrm{s}} = w_{\mathrm{b}}$. For this reason the latter (simpler) case is used.

The background can be divided into two categories: prompt and non-prompt background. The prompt background consists of J/ψ candidates produced directly in the pp collision that are randomly combined with V^0 candidates, which also include fake combinatorial Λ or K^0_S candidates. The prompt background decay length is only due to the finite resolution of the vertex reconstruction. The non-prompt background includes events where the J/ψ candidate originates in a decay of a b-hadron. This type of background has a lifetime due to its origin in long-lived b-hadrons [e.g. $B^0_d \to J/\psi(\mu^+\mu^-)K^0_S(\pi^+\pi^-)$, with the K^0_S meson misidentified as Λ, forming a non-prompt background for Λ_b].

The signal component of the mass PDF, $\mathcal{M}_{\mathrm{s}}$, is a Gaussian function with a mean equal to m_{Λ_b} and width $S_m\delta_m$. The mass error scale factor, S_m, determines how much the errors δ_{m_i} are overestimated or underestimated. The background component is a first order polynomial with a slope b defined as follows:

$$\mathcal{M}_{\mathrm{bkg}}(m|\delta_m) = \frac{1}{\Delta m}\left[1 + b\,(m - m_{\mathrm{C}})\right], \tag{3.2}$$

where $\Delta m = m_{\max} - m_{\min}$ and $m_{\mathrm{C}} = (m_{\max} + m_{\min})/2$, with $m_{\max}$ and $m_{\min}$ being the edges of the invariant mass fit range. In case of B^0_d fit an additional background term is added to the formula (3.2):

$$\mathcal{M}_{\mathrm{bkg,4}}(m|\delta_m) = \mathcal{N}\frac{1}{e^{\frac{m-m_{\mathrm{bkg,4}}}{\sigma_{\mathrm{bkg,4}}}} + 1}, \tag{3.3}$$

where $m_{\mathrm{bkg,4}}$ and $\sigma_{\mathrm{bkg,4}}$ are parameters of the fit. This term describes a non-linear increase of background for $m_{J/\psi K^0_S} < 5150$ MeV (see Figure 3.8, right). The factor $\mathcal{N}$ normalizes the function to 1 in the fitted mass range. Parameters $m_{\mathrm{bkg,4}}$ and $\sigma_{\mathrm{bkg,4}}$ determine the position and the slope of the non-linear background component, respectively. This background component can be attributed to the decays of B^0_d with incompletely reconstructed final state (i.e. $B^0_d \to J/\psi K^0_S + X$, with X being one or more pions).

Using the estimated decay time error, δ_τ, the proper decay time resolution is

modeled with a Gaussian function:

$$R(\tau - \tau'|\delta_\tau) = \frac{1}{\sqrt{2\pi} S_\tau \delta_\tau} \, e^{-\frac{(\tau-\tau')^2}{2(S_\tau \delta_\tau)^2}}, \tag{3.4}$$

where S_τ denotes the proper decay time error scale factor, τ and τ' stand for the reconstructed and true proper decay times, respectively.

The signal and non-prompt background proper decay time distributions are modeled as exponential functions, $E(\tau'; \tau_B)$, for $\tau' > 0$; with τ_B being the fitted parameter denoting either the Λ_b lifetime, or the pseudo-lifetime of the long-lived background. The prompt background component is modeled by a sum of two functions: a Dirac δ-function, $\delta_{\text{Dirac}}(\tau')$, and a symmetric exponential (Laplace distribution), $E_{\text{sym}}(\tau')$, to account for the non-Gaussian tails of the prompt background observed in data.

The functions are convolved with the resolution model (3.4) to obtain the PDFs of the measured proper decay time:

$$\begin{aligned} \mathcal{T}_{\text{s}}(\tau|\delta_\tau) &= \varepsilon(\tau')^{-1} E(\tau'; \tau_{\Lambda_b}) \otimes R(\tau - \tau'|\delta_\tau), \\ \mathcal{T}_{\text{b}}(\tau|\delta_\tau) &= \Big[f_1 \mathcal{T}_{\text{p}}(\tau') + (1 - f_1) \mathcal{T}_{\text{np}}(\tau') \Big] \otimes \\ &\quad R(\tau - \tau'|\delta_\tau), \end{aligned} \tag{3.5}$$

with the non-prompt and prompt components defined as

$$\begin{aligned} \mathcal{T}_{\text{np}}(\tau') &= f_2 E(\tau'; \tau_{\text{bkg},1}) + (1 - f_2) E(\tau'; \tau_{\text{bkg},2}), \\ \mathcal{T}_{\text{p}}(\tau') &= f_3 \delta_{\text{Dirac}}(\tau') + (1 - f_3) E_{\text{sym}}(\tau'; \tau_{\text{bkg},3}). \end{aligned}$$

The efficiency correction function, $\varepsilon(\tau')$, in Eq. (3.5) accounts for the decay-time-dependent selection bias, explained in Section 3.5.2.

3.5.1 Parameters Determined from the Fit

The full PDF has 12 free parameters:

- the Λ_b mass and lifetime, m_{Λ_b} and τ_{Λ_b};
- the fraction of signal events, f_{sig};
- the error scale factors, S_m and S_τ;

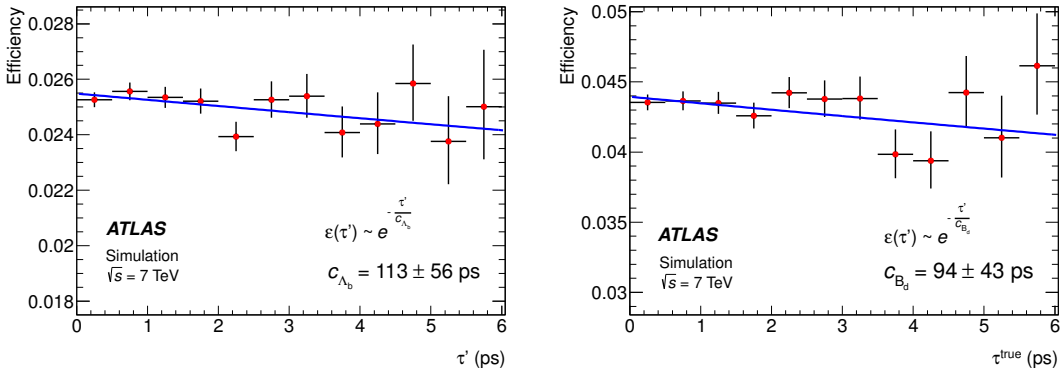

Figure 3.11: Extraction of the efficiency correction for Λ_b (left) and B_d^0 (right). The MC efficiency is fitted with an exponential function. The y-axis has a suppressed zero. The displayed error is statistical only.

- the slope of the mass dependence of the background, b;
- the pseudo-lifetimes of the long-lived background, $\tau_{\mathrm{bkg},1}$ and $\tau_{\mathrm{bkg},2}$; the exponential slope of the non-Gaussian prompt background, $\tau_{\mathrm{bkg},3}$;
- and the relative fractions of the various background contributions, f_1, f_2, and f_3.

Other quantities are calculated from the fit parameters. The number of signal and background candidates, N_{sig} and N_{bkg}, are calculated as $N_{\mathrm{sig}} = f_{\mathrm{sig}}N$ and $N_{\mathrm{bkg}} = (1 - f_{\mathrm{sig}})N$, where N is the total number of candidates. The mass and proper decay time resolutions are calculated from the fit parameters, too. By analogy with a Gaussian distribution, the mass resolution, σ_m, is defined as half of that mass range for which the integral of $\mathcal{M}_{\mathrm{s}}$ retains 68.3% of the number of signal events symmetrically around the fitted Λ_b mass. The proper decay time resolution, σ_τ, is determined in the same fashion by integrating the prompt background PDF.

3.5.2 Efficiency Correction

Two sources are responsible for the selection bias in the Λ_b decay time: the V^0 reconstruction efficiency and the trigger selection. The efficiency correction, $\varepsilon(\tau')$, is determined using the MC sample which is weighted to reproduce biases observed in data, as explained in the following sections. It is modeled as a simple exponential,

$$\varepsilon(\tau') \propto e^{-\tau'/c_{\Lambda_b}}, \tag{3.6}$$

where c_{Λ_b} denotes the slope of the efficiency correction. The exponential form is chosen for $\varepsilon(\tau')$ because it describes the MC well and is particularly easy to convolve with the resolution model. The slope of the exponential, c_{Λ_b}, is extracted from a fit to the MC decay time efficiency plot shown in Figure 3.11. The extracted value is $c_{\Lambda_b} = 113 \pm 56$ ps for Λ_b and $c_{B_d} = 94 \pm 43$ ps for B_d^0. The Λ_b and B_d^0 lifetimes are biased toward smaller values. In the MC simulation, the bias correction accounts for a Λ_b lifetime shift of 26 fs (25 fs for B_d^0), which can be broken into 10 fs due to the V^0 reconstruction efficiency and 16 fs due to the trigger (for B_d^0 the corresponding numbers are 11 fs and 14 fs), as explained in the following sections.

Bias Due to the V^0 Reconstruction Efficiency

The V^0 reconstruction efficiency drops with the distance of the decay vertex from the center of the detector, R_{xy,V^0}, as tracks from displaced vertices have fewer hits than those decaying close to the center of the detector (see Figure 3.12, left). This inefficiency in V^0 reconstruction projects directly into the Λ_b reconstruction efficiency, because the V^0 and Λ_b decay distances are correlated. One can easily imagine this correlation if one assumes that the Λ and Λ_b momenta are almost parallel: then the decay distance of Λ_b can be expressed as $L_{xy,\Lambda_b} \approx R_{xy,V^0} - L_{xy,V^0}$ (see Figure 3.12, right). If the detector is inefficient for large R_{xy,V^0}, it will favour cases with smaller L_{xy,Λ_b}. Similarly, the cut $L_{xy,V^0} > 10$ mm favours cases where L_{xy,Λ_b} is small. Under normal circumstances this bias is quite small. However, the effect can be enhanced by cutting tightly on R_{xy,V^0} or by increasing the value of the L_{xy,V^0} cut.

To study the bias due to the V^0 reconstruction separately from the bias caused by the trigger one has to disable the trigger selection in the MC. As a consequence, the muon p_{T} distribution will not agree with data. To ensure that the kinematic distribution of the Λ_b candidates in the MC sample is similar to the ones in data the weighting procedure is used. Using the signal MC a 2D histogram of the muon momenta, p_{T,μ^+} and p_{T,μ^-}, is filled. For data, the same histogram is filled separately for the signal region (5520–5720 MeV for Λ_b and 5200–5360 MeV for B_d^0) and for the sidebands. It is assumed that the background muon momentum distribution does not change (or changes linearly) with the b-hadron invariant mass, i.e. that the p_{T} distribution of background muons in the signal region is the same as that in the sidebands. Then one can subtract the sideband distributions

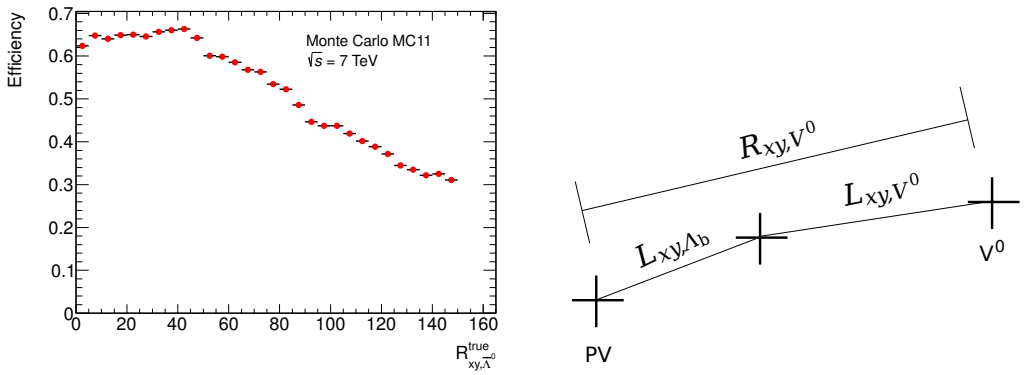

Figure 3.12: Reconstruction and selection efficiency of $\bar{\Lambda}$ as a function of the distance from the center of the detector (left). The cut of $p_{\mathrm{T}} > 400$ MeV was applied on the generator-level proton and pion tracks to remove the inefficiency caused by the reconstruction tracking p_{T} threshold. Definition of the Λ_b and V^0 decay distances (right).

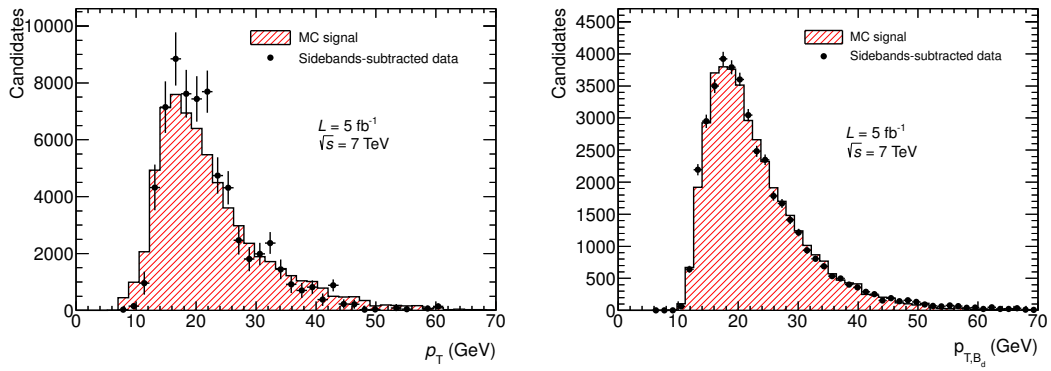

Figure 3.13: Comparison of the p_{T} distributions for the sideband-subtracted data and the weighted signal-only MC for Λ_b (left) and B_d^0 (right).

from the signal-region to get an estimate of the pure signal distribution. The weight of the subtracted histogram is calculated as follows:

$$w_{\mathrm{sub}} = -(1 - f'_{\mathrm{sig}}) \frac{N_{\mathrm{center}}}{N_{\mathrm{sb}}}, \tag{3.7}$$

where N_{center} and N_{sb} are the observed numbers of events in the signal region and the sidebands, while f'_{sig} is the signal fraction in the signal region extracted from the invariant mass fit. The muon p_{T} weight matrix is obtained by dividing the data histogram by the MC one. Figure 3.13 shows the comparison of the b-hadron p_{T} distributions for data and weighted MC.

Trigger Bias of the Muon Transverse Impact Parameter

It has been observed that the muon trigger biases the transverse impact parameter of muons, d_0, toward smaller values. Since muon tracks are used to determine the position of the Λ_b vertex this causes a bias in the measured decay distance of Λ_b. This bias is caused by the level-2 muon trigger. Although the trigger is simulated in the MC, its impact on the muon transverse impact parameter, d_0, is not modelled realistically (the bias is too large in the used MC simulation). Therefore, a tag-and-probe method using J/ψ is implemented to measure the muon trigger selection efficiency as a function of d_0. The procedure can be described in the following steps (illustrated in Figure 3.14):

1. The J/ψ sample is collected using the single muon trigger EF_mu18. This is the lowest threshold single muon trigger that was unprescaled in the 2011 data running.

2. The J/ψ candidate is reconstructed in the event using the offline reconstruction software. One of the J/ψ muons is matched to the trigger object EF_mu18. The matching is done using a $\Delta R < 0.003$ criterion. This muon is called *Tagged muon*. The other muon is called *Probe muon*. If both J/ψ muons are matched to the EF_mu18 then both muons will also be used as probes. Since no trigger is required to explicitly trigger on the probe muons, they represent an unbiased sample and can be used to determine the efficiency.

3. A histogram distribution of the transverse impact parameter, d_0, of all probe muons is made. This is used as the denominator of the efficiency plot.

4. Triggered probe muons are selected by requiring that they match the EF_mu4_Jpsimumu trigger object. The other muon of the EF_mu4_Jpsimumu is required to match the tag muon. If the probe muon fires EF_mu18, it will also fire EF_mu4 and therefore this matching criterion does not further decrease the selection efficiency.

5. The efficiency function is obtained by dividing the d_0 distribution of the trigger-matched probe muons by the denominator plot from step 3. Since the EF_mu4_Jpsimumu trigger performs a vertex fit the efficiency obtained this way will also include the efficiency of the trigger vertex fit. It is assumed

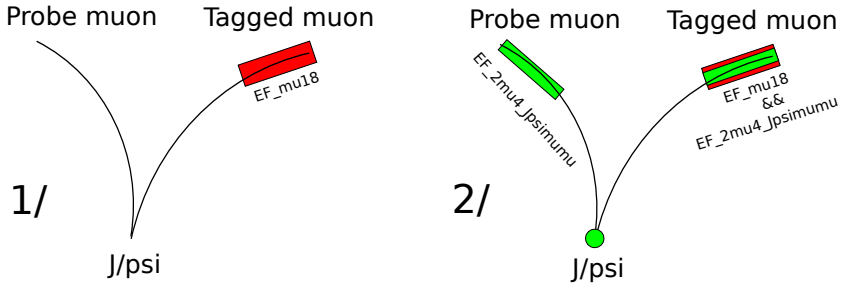

Figure 3.14: Tag-and-probe method with J/ψ to measure a single-muon trigger efficiency. The sample is collected by the EF_mu18 trigger which is matched to the tag muon (left). The other J/ψ muon is used as a probe (right) to measure an efficiency of EF_2mu4_Jpsimumu trigger.

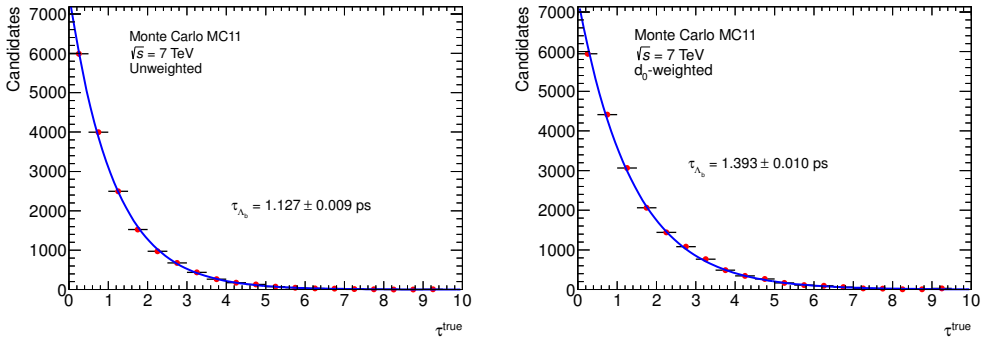

Figure 3.15: MC Λ_b lifetime fit for the sample selected by the di-muon trigger EF_2mu4_Jpsimumu. Fit to the unweighted events (left) and d_0-weighted events (right).

that vertexing does not have a significant impact on d_0, which is confirmed using the MC simulation.

The trigger selection efficiency as a function of the muon d_0 is measured using the tag-and-probe method in both data and MC samples, in 5 bins of muon p_{T} separately in the barrel and end-cap regions. A comparison between the data and MC is shown in Figures A.1 and A.2, where a clear discrepancy is visible. Therefore, the MC events are weighted to achieve an agreement with the data. The MC weighting procedure consists of 2 steps: first the MC data are weighted to remove the d_0 bias completely. This is to confirm that the Λ_b lifetime shift observed in the MC indeed comes from the d_0 bias. Then, the MC is weighted to achieve an agreement with data and this sample is used to estimate the magnitude of the shift and corresponding the systematic error.

From the d_0-efficiency plots in Figures A.1 and A.2 the weighting functions are determined. The weighting function is parametrized as a linear function of d_0:

$$w(d_0) = a_0(1 + a_1 d_0), \tag{3.8}$$

where a_1 is the magnitude (slope) of the correction. For the "no-bias" weights the slope, a_1, will correspond to the negative value of the slope obtained by fitting efficiency plots in Figures A.1 and A.2.

For events selected by the di-muon triggers the event weight is determined as the product of the weights (3.8) for both of the J/ψ muons. In case of events triggered by single-muon triggers, the event is weighted using the impact parameter of the leading J/ψ muon. Figure 3.15 shows the true Λ_b proper decay time distribution in the MC sample triggered by EF_2mu4_Jpsimumu before and after the d_0 weighting. The distributions are fitted by an exponential function to extract the lifetime. While in the unweighted sample (Figure 3.15, left) the fitted lifetime shows a large shift, the lifetime of the weighted sample (right) agrees with the generated lifetime, $\tau_{\Lambda_b}^{\mathrm{MC}} = 1.391$ ps.

For the single-muon triggers the correction does not work so well, since there is an ambiguity in which muon has triggered the event (the assumption that it was the leading one may not be always correct) and also the probability that the event is triggered by a third, non-J/ψ, muon is larger. Therefore, the weight (3.8) over-corrects the bias. One has to adjust the slope of the correction a_1 for single muon triggers so that an agreement with the generated Λ_b lifetime is achieved. This is done for each trigger item in the menu, so that when the full trigger menu with appropriate prescale factors is used, the fitted Λ_b lifetime in the MC agrees with the generated value.

Once this closure test is concluded, weights that correct d_0 to the bias observed in data are used instead, while using the same adjustment factors for single-muon triggers that were determined in the previous step. The new weights, $w(d_0)$, are extracted by dividing the data and MC plots in Figures A.1 and A.2 and fitting the ratio with a linear function. The MC sample weighted this way is used to determine the lifetime shift due to the trigger selection. Although this method is data-driven, it still relies on the MC for determination of the adjustment factors for single-muon triggers.

Table 3.4: Results of the maximum likelihood fit for Λ_b. The uncertainties shown here are statistical only. The number of degrees of freedom used for the χ^2 calculation is $N_{\mathrm{dof}} = 61$.

Parameter	**Value**	**Par.**	**Value**	**Par.**	**Value**
m_{Λ_b} (MeV)	5619.7 ± 0.7	f_{sig}	0.268 ± 0.007	N_{sig}	2184 ± 57
τ_{Λ_b} (ps)	1.449 ± 0.036	f_1	0.61 ± 0.01	N_{bkg}	5970 ± 160
b (GeV^{-1})	-0.145 ± 0.003	f_2	0.70 ± 0.04	σ_m (MeV)	31.1 ± 0.8
$\tau_{\mathrm{bkg},1}$ (ps)	1.31 ± 0.06	f_3	0.91 ± 0.02	σ_τ (ps)	0.117 ± 0.003
$\tau_{\mathrm{bkg},2}$ (ps)	0.26 ± 0.05	S_m	1.18 ± 0.03		
$\tau_{\mathrm{bkg},3}$ (ps)	0.36 ± 0.05	S_τ	1.05 ± 0.02	χ^2/N_{dof}	1.09

Table 3.5: Results of the maximum likelihood fit for B_d^0. The uncertainties shown here are statistical only. The number of degrees of freedom used for the χ^2 calculation is $N_{\mathrm{dof}} = 92$.

Parameter	**Value**	**Par.**	**Value**	**Par.**	**Value**
m_{B_d} (MeV)	5279.6 ± 0.2	f_{sig}	0.635 ± 0.004	N_{sig}	17530 ± 110
τ_{B_d} (ps)	1.509 ± 0.012	f_1	0.57 ± 0.01	N_{bkg}	10069 ± 65
b (GeV^{-1})	-0.156 ± 0.004	f_2	0.78 ± 0.05	σ_m (MeV)	27.8 ± 0.2
$\tau_{\mathrm{bkg},1}$ (ps)	1.49 ± 0.06	f_3	0.86 ± 0.02	σ_τ (ps)	0.107 ± 0.003
$\tau_{\mathrm{bkg},2}$ (ps)	0.47 ± 0.09	S_m	1.11 ± 0.01		
$\tau_{\mathrm{bkg},3}$ (ps)	0.32 ± 0.03	S_τ	1.06 ± 0.02	χ^2/N_{dof}	1.03

The lifetime shift attributed to the trigger bias estimated using this method is 16 fs for the Λ_b and 14 fs for B_d^0.

3.6 Extraction of the Lifetime and Mass

3.6.1 Results of the Maximum Likelihood Fit

The results of the maximum likelihood fit are listed in Table 3.4 for Λ_b and Table 3.5 for B_d^0. The tables show the fitted parameters, quantities calculated from these parameters, and a χ^2/N_{dof} value which quantifies the fit quality. The χ^2/N_{dof} value is calculated from the dataset binned in mass and decay time with 61 degrees of freedom in case of Λ_b and 92 in case of B_d^0. The sizes of the bins are commensurate with the measured mass and decay time resolutions and only bins with more than 11 entries are used for the χ^2 calculation. This requirement is imposed so

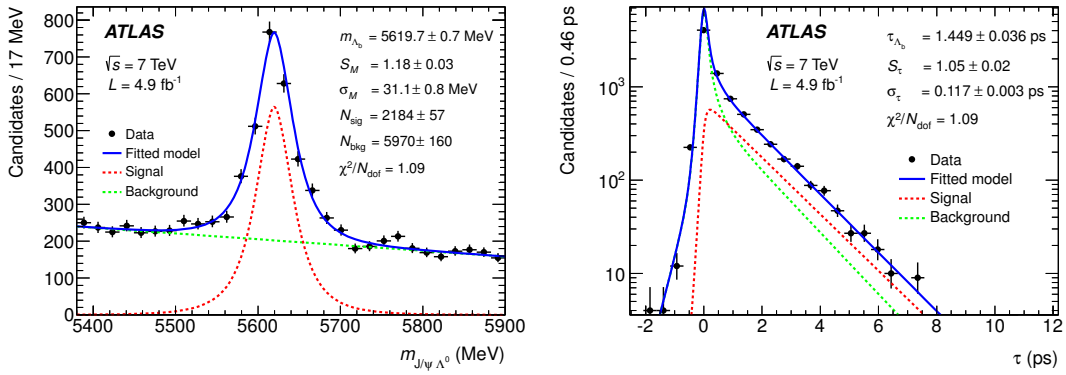

Figure 3.16: Projections of the fitted PDF onto the mass (left) and the proper decay time (right) axes for Λ_b candidates. The errors of the listed fit result values are statistical only. The $\chi^2/N_{\rm dof}$ value is calculated from the dataset binned in mass and decay time with the number of degrees of freedom $N_{\rm dof} = 61$.

that the error on the number of entries in each bin can be taken as Gaussian. The lifetime result is corrected for the selection bias (see Section 3.5.2). An estimate of the correlation matrix is shown in Table A.1. The estimated correlation between the mass and lifetime is small, 0.002. Projections of the PDF onto the mass and proper decay time axes are shown in Figure 3.17 for Λ_b and Figure 3.17 for B_d^0.

3.6.2 Systematic Uncertainties

Systematic uncertainties are estimated by changing various parameters of the analysis and observing the shift in the extracted mass and lifetime. The shift with respect to the baseline result is then quoted as a systematic uncertainty. The non-negligible systematic uncertainties are summarized in Table 3.6. The individual errors are added in quadrature, yielding total systematic uncertainties of the Λ_b lifetime and mass measurements, $\sigma_\tau^{\rm syst} = 17$ fs and $\sigma_m^{\rm syst} = 1.1$ MeV, respectively. The estimated systematic uncertainties of B_d^0 measurement are $\sigma_\tau^{\rm syst} = 18$ fs and $\sigma_m^{\rm syst} = 1.0$ MeV. Details of the determination of the systematic uncertainties follow:

Event Selection and Reconstruction Bias

In this section, a systematic uncertainty due to the selection and reconstruction bias is discussed. Its impact on the decay time is studied first. Two effects that lead to a decay time-dependent selection bias have been identified: the dominant

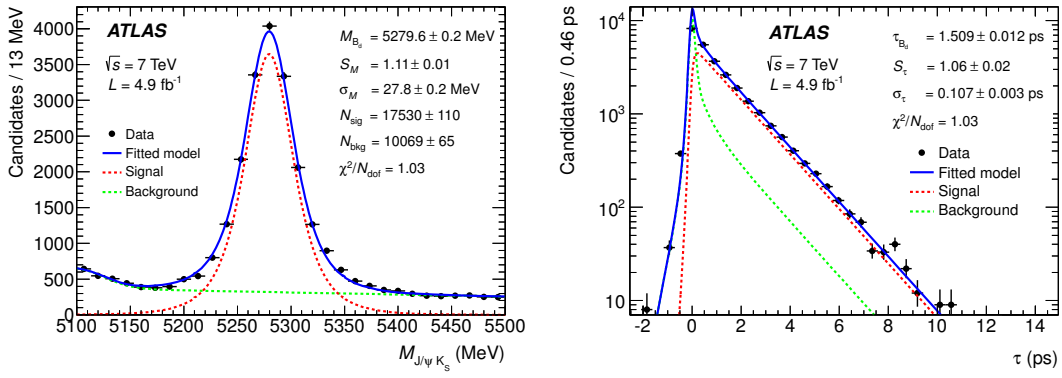

Figure 3.17: Projections of the fitted PDF onto the mass (left) and the proper decay time (right) axes for B_d^0 candidates. The errors of the listed fit result values are statistical only. The χ^2/N_{dof} value is calculated from the dataset binned in mass and decay time with the number of degrees of freedom $N_{\text{dof}} = 92$.

contribution comes from the muon trigger, which slightly biases the transverse impact parameter of muons, d_0, toward smaller values. The second bias comes from the V^0 reconstruction. The event selection bias is corrected using the MC simulation, determining the efficiency as a function of the decay time, as described in Section 3.5.2. Three components of the systematic uncertainty are considered:

1. Uncertainty of the efficiency correction function fit;
2. Uncertainty of the MC re-weighting;
3. Uncertainty of the V^0 selection bias estimation.

The first uncertainty relates to the precision with which the correction function is determined. The slope of the correction function, c_{Λ_b}, is fitted with a statistical accuracy of about 50% ($c_{\Lambda_b} = 113 \pm 56$ ps and $c_{B_d} = 94 \pm 43$ ps). Using standard error propagation, this statistical uncertainty is propagated to the uncertainty of the lifetime measurement:

$$\sigma_{\tau,c} \approx \left(\frac{\tau_B}{c}\right)^2 \sigma_c, \tag{3.9}$$

where σ_c is the estimated statistical uncertainty of the correction factor c. Formula (3.9) is an approximation assuming that $c \gg \tau_B$, which is satisfied in this case. Plugging the values for Λ_b and B_d^0 into the formula gives the corresponding lifetime uncertainties, 9 fs and 11 fs, respectively.

To ensure that the MC trigger simulation describes the data well, the MC is re-weighted using the output from the tag-and-probe measurements of single-muon

Table 3.6: Summary of the systematic uncertainties of the lifetime measurement, $\sigma_\tau^{\text{syst}}$, and the mass measurement, σ_m^{syst}, for Λ_b and B_d^0.

Syst. uncertainty	**Lifetime (fs)**		**Mass (MeV)**	
	$\boldsymbol{\Lambda_b}$	$\boldsymbol{B_d^0}$	$\boldsymbol{\Lambda_b}$	$\boldsymbol{B_d^0}$
Selection/reco. bias	12	15	0.9	0.9
Background fit models	9	10	0.2	0.1
Physics background	7	0	0.2	0.0
Residual misalignment	1	1	0.0	0.0
Extra material	3	3	0.2	0.2
Tracking p_{T} scale	0	0	0.5	0.5
Total systematic error	17	18	1.1	1.0

trigger efficiencies. The second uncertainty in the list quantifies the precision of this re-weighting. The used weighting functions are parameterized as linear functions of muon impact parameter, $w(d_0) \propto 1 + ad_0$, and their slope, a, is determined by a linear fit in bins of the muon p_{T} and η. To assess the systematic uncertainty on the trigger bias correction, the weighting parameters a are varied by their estimated errors. This produces a lifetime shift of 7 fs (for both Λ_b and B_d^0), which is used as an estimate of this systematic uncertainty.

Finally, the effect of the V^0 selection is estimated. The V^0 selection bias is caused by the fact that the Λ_b and Λ transverse decay distances are correlated (Figure 3.12, right). As a consequence, selection cuts applied on Λ transverse decay distance will affect indirectly the Λ_b distance, too. The transverse decay distance depends on the particle's decay time and its transverse momentum, since faster particles will travel larger distances before decaying. Since the MC simulation is used to correct for the V^0 selection bias, one has to make sure that the Λ_b p_{T} distribution is modeled correctly in MC. The comparison is shown in Figure 3.13. The mean Λ_b p_{T} in the MC sample agrees with the mean p_{T} in data within 0.7 GeV. Using the kinematic weighting, this agreement is made worse by about a factor of 3, which in turn results in a decay time shift of 4 fs for Λ_b and 7 fs for B_d^0. These values are taken as estimates of the uncertainty of the V^0 bias correction.

Adding these three contributions together, the total systematic uncertainty due to the selection bias is obtained: 12 fs for Λ_b and 15 fs for B_d^0.

Reconstruction Bias

Apart from the selection bias, discussed in the previous paragraphs, the measurement can also be affected by the reconstruction bias. This means that the measured quantities, the proper decay time and the invariant mass, can be systematically shifted towards larger or smaller values. At the first approximation this bias can be estimated using the MC simulation by looking at the decay time and mass resolution plots, however, this test only probes effects modeled in the MC simulation. Additional, more sophisticated tests aimed to study specific effects are performed, too, and are described separately in the following paragraphs.

The reconstruction bias is determined using a double-Gaussian fit to the distributions of $\Delta\tau = \tau^{\mathrm{MC}} - \tau$ and $\Delta m = m^{\mathrm{MC}} - m$, where τ^{MC} and m^{MC} denote the generator-level values of the decay time and mass, while τ and m stand for the reconstructed ones. The bias is determined as a mean of the fitted double-Gaussian, as shown in Figure 3.18. A shift of -0.9 ± 0.3 MeV is observed, meaning that the reconstructed mass is slightly overestimated. This mass shift is caused by the muon trigger p_{T} thresholds: muons with larger p_{T} have higher probability of being selected than low-p_{T} muons. As a consequence, muons whose p_{T} is mis-measured larger than the true value have higher probability of being reconstructed than muons whose p_{T} is mis-measured smaller, which creates a small asymmetry of the mass peak. By applying cut on true muon p_{T} which is above the muon trigger efficiency turn-on curve (e.g. 6 GeV for EF_2mu4_Jpsimumu trigger) one can remove the mass bias in MC, however, such a cut is not possible in data. The reconstruction bias on the decay time, 2 fs, is negligible compared to the systematic uncertainties due to the V^0 and trigger selection, described in the previous paragraph.

For each candidate, a proper decay time error, δ_τ, and a mass error, δ_m, are estimated by the cascade topology fitter. The MC sample is used to test the goodness of the error estimate by plotting the pull distributions for the mass and proper decay time (see Figure 3.19). The pulls are defined as $\Delta_\tau/\delta_\tau = \frac{\tau^{\mathrm{MC}}-\tau}{\delta_\tau}$ and $\Delta_m/\delta_m = \frac{m^{\mathrm{MC}}-m}{\delta_m}$. A Gaussian function is fitted to the distributions. The value of the decay time pull distribution width, 1.028 ± 0.007, indicates that the decay time errors are estimated correctly. The width of the mass pull distribution, 1.134 ± 0.008, is slightly larger than one, however, the number is consistent with the scale factor, S_m (see Table 3.4), which means that the fit is performed correctly.

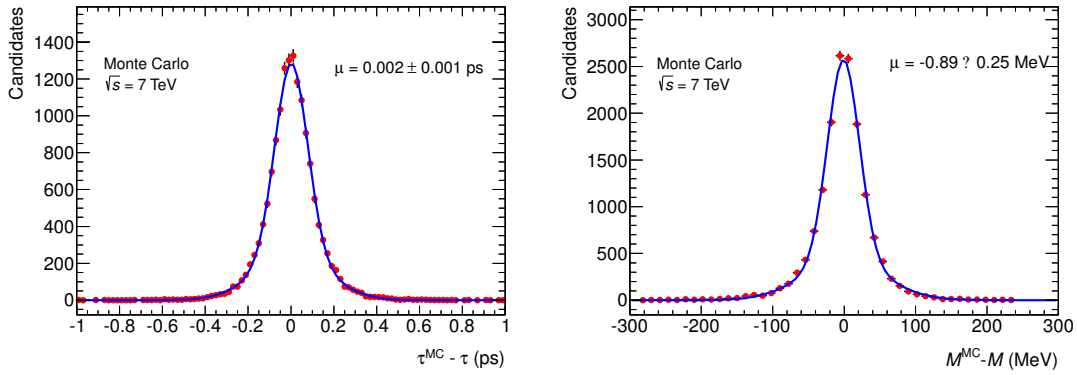

Figure 3.18: The proper decay time (left) and mass (right) resolution of the MC candidates.

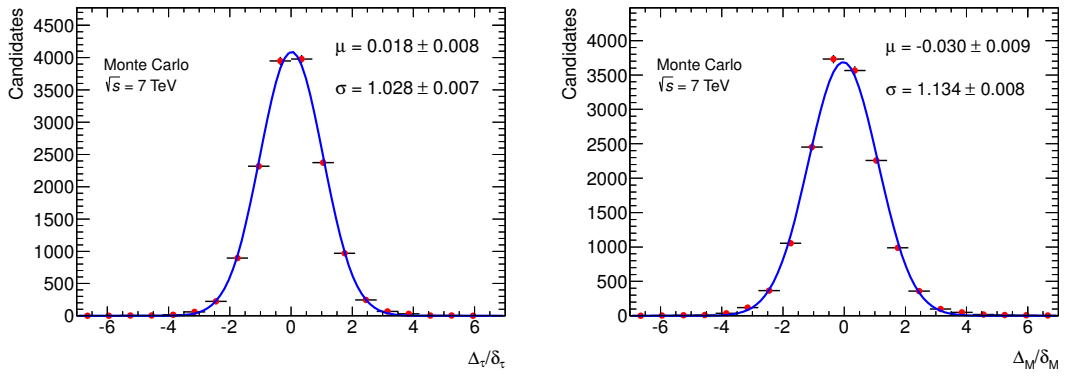

Figure 3.19: The proper decay time (left) and mass (right) pull distribution of the Monte Carlo candidates.

Background Fit Models

Alternative background models are used to assess the sensitivity of the results to the choice of background parameterization. A second-order polynomial and an exponential mass dependence of the $\mathcal{M}_{\rm b}$ PDF are tested. In addition the decay time dependence is modified by adding a third exponential into the non-prompt background component, $\mathcal{T}_{\rm np}$. The alternative background PDFs fit the data well. These changes result in a lifetime shift of 2 fs and a mass shift of 0.2 MeV. In the background fit model the decay time and mass are assumed to be uncorrelated. To test this assumption the fit's mass range limits, $m_{\rm min}$ and $m_{\rm max}$, are varied independently by 60 MeV (Figure 3.20). This changes the relative contribution of the background from the left and right sidebands, and the mass and lifetime

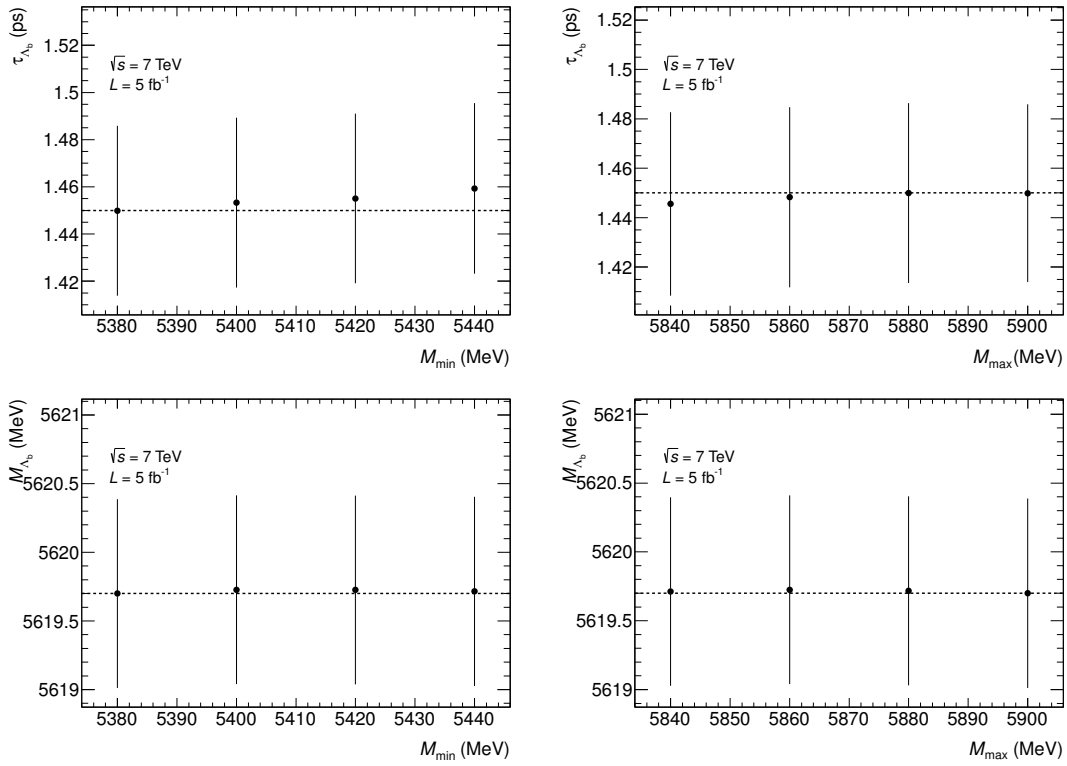

Figure 3.20: Dependence of the fitted lifetime (top) and mass (bottom) on the chosen value of the mass range, $m_{\min}$ (left) and $m_{\max}$ (right). The baseline result is indicated by a dotted line.

are extracted again for these new mass ranges. While the change of $m_{\max}$ has a minimal impact on the extracted mass and lifetime, the change of $m_{\min}$ produces a lifetime shift of 9 fs. This value is added to the total systematic error due to background modeling.

Physics Background: B_d^0 and Λ_b Contamination

The number of B_d^0 candidates misidentified as Λ_b is estimated by a fit to the mass distribution of the candidates which fall in the Λ_b signal region, 5.52 GeV $< m_{J/\psi\Lambda^0} <$ 5.72 GeV, under the hypothesis that they are $B_d^0 \to J/\psi(\mu^+\mu^-)K_S^0(\pi^+\pi^-)$ decays (see Figure 3.21, left). A fit to a Gaussian peak on a linear background yields 82 ± 46 B_d^0 candidates. Since these candidates are treated as Λ_b, their pseudo-lifetime is scaled-up by the ratio of the Λ_b and B_d^0 masses,

$$\tau^*_{B_d} = \tau_{B_d} m^{\rm PDG}_{\Lambda_b} / m^{\rm PDG}_{B_d} = 1617 \text{ fs}$$

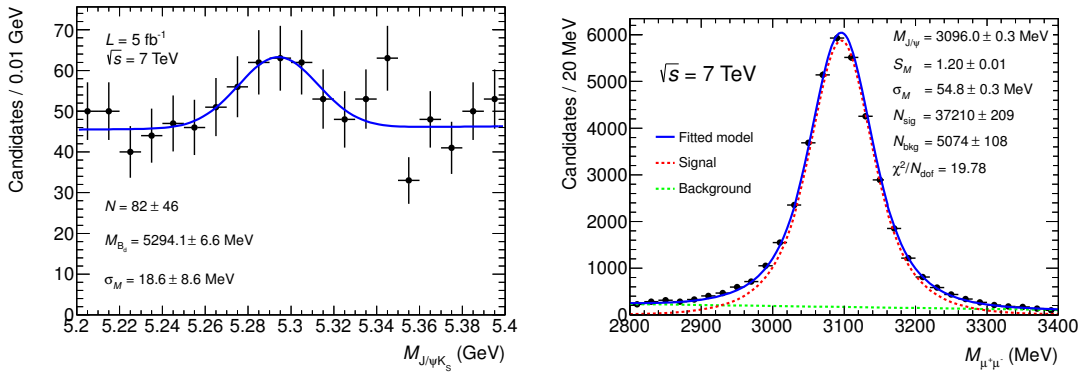

Figure 3.21: Invariant mass of Λ_b candidates reconstructed under B_d^0 hypothesis (left). Fit to the J/ψ invariant mass distribution (right).

(the decay time change due to the difference in p_{T} reconstructed under the two hypotheses is negligible). If all such background candidates contributed to the fitted Λ_b lifetime, the shift to the Λ_b lifetime could be estimated using a simple formula:

$$\tau_{\mathrm{mea}} = \frac{1}{N_{\mathrm{mea}}}((N_{\mathrm{mea}} - N_{B_d})\tau_{\Lambda_b} + N_{B_d}\tau^*_{B_d}),$$

where N_{mea} is the measured number of Λ_b candidates (from the fit), N_{B_d} is the estimated B_d^0 contamination, and τ_{Λ_b} is the Λ_b lifetime. Using the above formula, a shift do to the B_d^0 contamination is estimated 7 fs. This is quoted as a conservative estimate of the systematic uncertainty. The error on the mass measurement is estimated by relaxing the $\mathcal{P}_{\Lambda_b^0} - \mathcal{P}_{B_d}$ cut to double the estimated B_d^0 background. This results in a Λ_b mass shift of 0.2 MeV.

The Λ_b contamination in the B_d^0 sample is negligible, because the B_d^0 production cross-section is much larger than that of Λ_b.

Residual Misalignment of the ID

The distribution of the transverse impact parameter, d_0, of tracks originating from the PV is used to estimate the geometrical distortions due to residual misalignment, as described in Section 3.3.1. The geometry in the MC simulation is distorted by adjusting the positions of the ID modules so that the d_0 of tracks coming from the PV is biased by the same amount as observed in data. The mass-lifetime fit is performed with simulated data using the default (ideal) geometry and the sample with geometry distortions. A shift of 1 fs is observed between the two

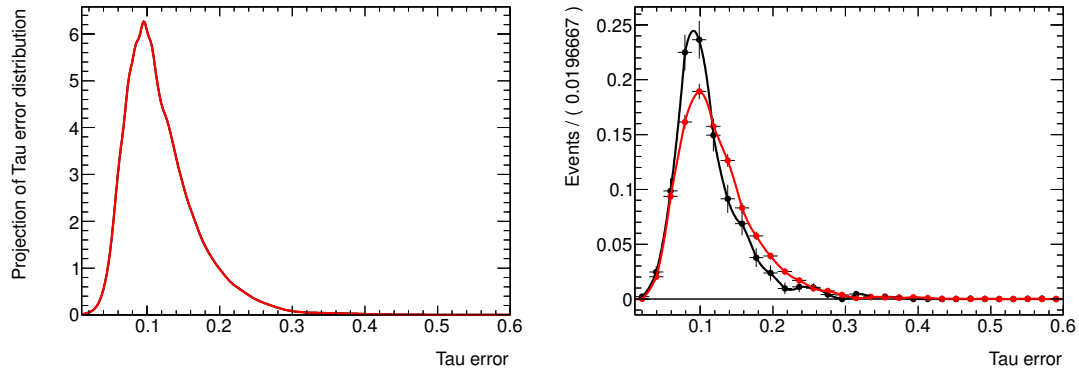

Figure 3.22: Proper decay time error distribution of all candidates (left) and distributions modeled separately for background (right, red curve) and signal (right, black curve).

measurements and is assigned as a systematic error due to residual misalignment. No significant mass shift is observed.

Uncertainty in the Amount of ID Material

Inaccurate modeling of the amount of material in the ID could affect the measurement since the tracking algorithm estimates the particle energy loss using a material map. To explore this uncertainty, the MC simulation is repeated with 20% more material in the ID silicon detectors (Pixel and SCT) and their supporting services, which is large compared to the estimated uncertainty of 6%(9%) in the Pixel (SCT) detectors (see Ref. [32]). The resulting shifts of 3 fs in lifetime and 0.2 MeV in mass are conservative estimates of the systematic uncertainties from this source.

Uncertainty in the Tracking Momentum Scale

The K^0_S mass value is used to estimate the uncertainty in the track momentum determination. The K^0_S mass extracted from a fit to the invariant mass agrees with the PDG's world average within 0.03%. Such a shift corresponds to a track momentum scale shift of 0.05%. The momentum scale can be further tested using the reconstructed J/ψ mass (Figure 3.21, right). The observed mass shift corresponds to a momentum scale error of -0.03%, in agreement with the assumption of $\pm 0.05\%$. The J/ψ selection described in section 3.4 is used, with an additional

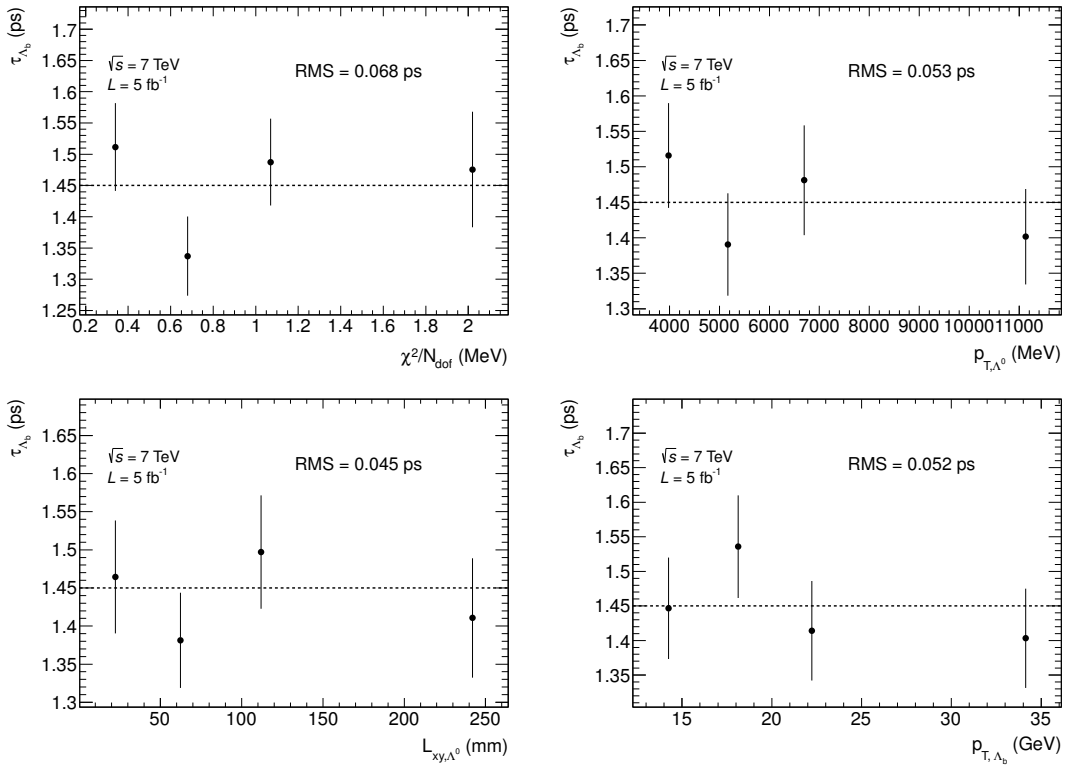

Figure 3.23: Λ_b lifetime extracted for different ranges of the cut variables. Dependence on the fit quality, $\chi^2/N_{\rm dof}$ (top left), Λ transverse momentum, $p_{\rm T,\Lambda^0}$ (top right), Λ decay distance, L_{xy,Λ^0} (bottom left), and Λ_b transverse momentum, $p_{\rm T,\Lambda_b}$ (bottom right) is shown.

cut $\chi^2/N_{\rm d.o.f.} < 3$. Shifting the momenta of all tracks in the MC simulation by this amount yields a Λ_b mass shift of 0.5 MeV. No significant lifetime shift is observed.

Choice of the PV

The collision vertex closest in 3D to the reconstructed Λ_b (B_d^0) direction is used as the primary vertex. Using the vertex that has the largest sum of squares of its tracks does not produce any significant change in the lifetime result.

Decay Time Error Distribution Models

In the PDF model it is assumed that the decay time error distribution, $w(\delta_\tau)$, is the same for signal and background. To test this assumption, the PDF is modified using separate PDFs for signal and background, $w_{\rm sig}(\delta_\tau)$ and $w_{\rm bkg}(\delta_\tau)$. The background distribution is taken from the data sidebands, with division between the

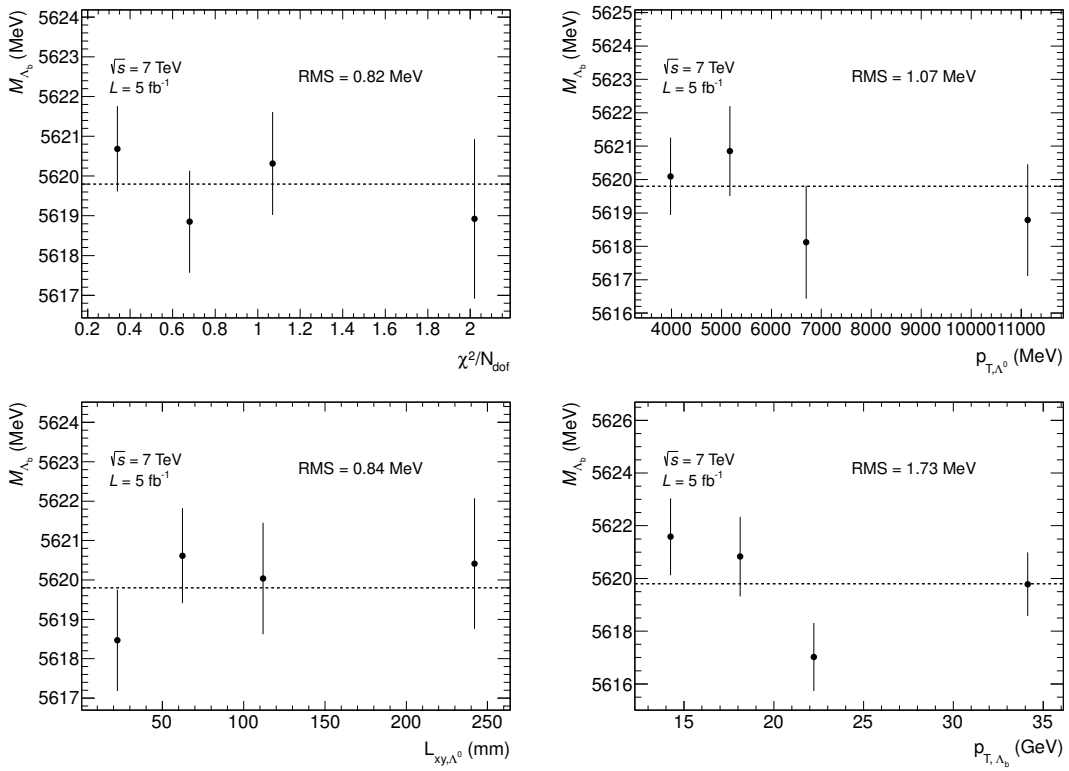

Figure 3.24: Λ_b mass extracted for different ranges of the cut variables. Dependence on the fit quality, $\chi^2/N_{\rm dof}$ (top left), Λ transverse momentum, $p_{\rm T,\Lambda^0}$ (top right), Λ decay distance, L_{xy,Λ^0} (bottom left), and Λ_b transverse momentum, $p_{\rm T,\Lambda_b}$ (bottom right) is shown.

sidebands and the signal region at 5520 and 5720 MeV. The signal distribution is modeled using data in the signal region, with the sidebands distribution subtracted. The subtraction weight is defined as $w_{\rm sub} = -\frac{N_{\rm S+B}}{N_{\rm B}}(1 - f'_{\rm sig})$, where $N_{\rm B}$ is the number of candidates in the sidebands, $N_{\rm S+B}$ is the number of candidates in the signal region, and $f'_{\rm sig}$ is the signal fraction in the signal region, determined from the fit. Figure 3.22 shows the proper decay time error distribution determined from all candidates (left) and using separate background and signal models (right). The Λ_b lifetime and mass are extracted again, however, no significant shift is observed.

3.6.3 Cross-checks

B_d^0 Lifetime and Mass

Unlike in the case of Λ_b, the B_d^0 lifetime is known with a good precision from earlier measurements on B-factories. Therefore, the $B_d^0 \to J/\psi(\mu^+\mu^-)K_S^0(\pi^+\pi^-)$ serves as an excellent cross-check for the Λ_b measurement. The B_d^0 channel is subjected to exactly the same kinematic cuts as for the Λ_b channel, and therefore suffers from similar systematic effects. The measured values of the B_d^0 lifetime and mass, $\tau_{B_d} = 1.509 \pm 0.012(\text{stat}) \pm 0.018(\text{syst})$ ps and $m_{B_d} = 5279.6 \pm 0.2(\text{stat}) \pm 1.0(\text{syst})$ MeV, are consistent with the world averages, $\tau_{B_d}^{\text{PDG}} = 1.519 \pm 0.007$ ps and $m_{B_d}^{\text{PDG}} = 5279.50 \pm 0.30$ MeV [15].

Checks on the Λ_b Maximum Likelihood Fit Stability

To check that the result does not depend on the value of the selection cuts (and other variables) consistency checks are performed. The data sample is divided into 4 statistically independent sub-samples in bins of cut variables. The ranges of the bins are chosen so that each sub-sample contains roughly the same number of signal candidates (based on the invariant mass fit). The maximum likelihood fit is performed for each sub-sample. If the differences of the obtained fit results are only due to statistical fluctuations, the standard deviation of these results should be approximately equal to 2-times the statistical error of the baseline result (the factor of 2 accounts for the fact that the sub-sample's statistics is about 4-times smaller).

The data sample is divided into bins of χ^2/N_{dof}, p_{T,Λ^0}, L_{xy,Λ^0}, and transverse momentum of Λ_b, p_{T,Λ_b^0}. The results of the fits are shown in Figures 3.23 and 3.24. The standard deviation is calculated for each set of results and is displayed in the corresponding plots. When scaled down by a factor of 2, all standard deviation values are smaller than estimated uncertainty of the measurement, which confirms the consistency of the results.

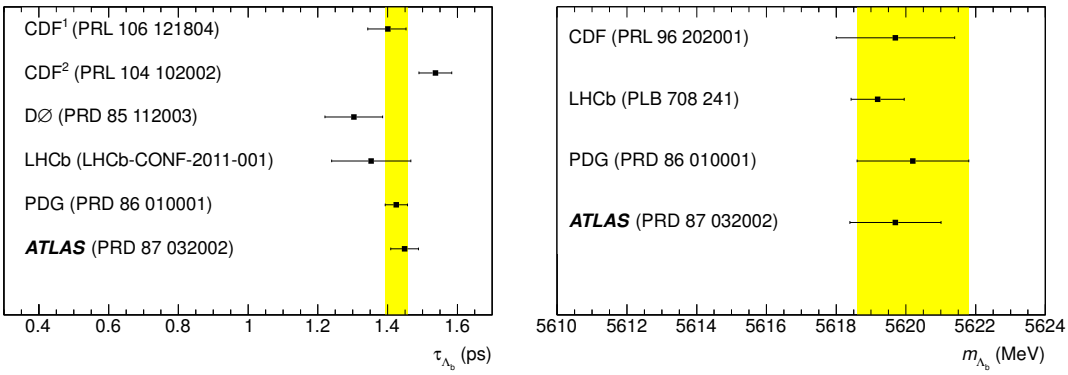

Figure 3.25: Comparison of the ATLAS values of the Λ_b lifetime (left) and mass (right) to the results of the CDF, DØ and LHCb experiments. The CDF[1] measurement uses the decay $\Lambda_b^0 \to \Lambda_c \pi$, the other measurements use $\Lambda_b \to J/\psi(\mu^+\mu^-)\Lambda(p\pi^-)$ decay channel.

3.7 Results and Conclusions of the Λ_b Measurements

The Λ_b lifetime and mass are measured to be

$$\begin{aligned} \tau_{\Lambda_b} &= 1.449 \pm 0.036(\text{stat}) \pm 0.017(\text{syst}) \text{ ps}, \\ m_{\Lambda_b} &= 5619.7 \pm 0.7(\text{stat}) \pm 1.1(\text{syst}) \text{ MeV}. \end{aligned}$$

These results agree with the world average values of the Λ_b lifetime, $\tau_{\Lambda_b}^{\text{PDG}} = 1.425 \pm 0.032$ ps and mass, $m_{\Lambda_b}^{\text{PDG}} = 5619.4 \pm 0.7$ MeV [15], and with a recent determination of the Λ_b mass by the LHCb experiment, $m_{\Lambda_b}^{\text{LHCb}} = 5619.19 \pm 0.70(\text{stat}) \pm 0.30(\text{syst})$ MeV [16]. A comparison of the ATLAS results with selected measurements of other experiments is shown in Figure 3.25.

The ratio of the Λ_b and B_d^0 lifetimes is determined to be

$$R = \tau_{\Lambda_b}/\tau_{B_d} = 0.960 \pm 0.025(\text{stat}) \pm 0.016(\text{syst}).$$

The statistical and systematic uncertainties are propagated from the uncertainties of the lifetime measurements. The systematic uncertainties are conservatively assumed to be uncorrelated. This value lies between the recent determination by DØ, $R^{\text{DØ}} = 0.864 \pm 0.052(\text{stat}) \pm 0.033(\text{syst})$ [19], and the measurement by CDF, $R^{\text{CDF}} = 1.020 \pm 0.030(\text{stat}) \pm 0.008(\text{syst})$ [18]. It agrees with the heavy quark expansion (HQE) calculations with the leading spectator quark contribution, which

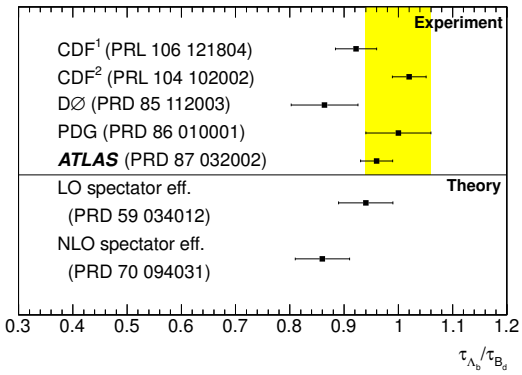

Figure 3.26: Comparison of the ATLAS value of the Λ_b to B_d^0 lifetime ratio and the results of the CDF and DØ experiments. The experimental values are also compared with the two selected theoretical predictions, one including only the leading order spectator quark effects (LO spectator eff.) and the more recent prediction with the next-to-leading order spectator effects calculations (NLO spectator eff.)

predict the value between 0.93 and 0.95 [20, 21, 22, 23] and is compatible with the most recent HQE prediction including next-to-leading-order (NLO) spectator quark contribution and improved pQCD calculations, predicting a ratio of 0.86 ± 0.05 [24]. The comparison is shown in Figure 3.26.

The ATLAS result suggests that the role of the spectator quarks in the Λ_b decay is less significant than it would seem from the latest HQE calculations (which include the NLO spectator quark contribution) and is in a better agreement with the previous LO calculations. Given the complicated history of the Λ_b lifetime measurements (outlined in Section 3.1.1), one has to wonder whether the current value of the theoretical prediction is not just a consequence of theorists' struggle to achieve agreement with the old LEP and Tevatron measurements, which measured the value of about 0.8. On the other hand, one should keep in mind that the current experimental value is compatible with both predictions within a 2-σ error margin.

The framework of HQE is an essential tool in b-physics phenomenology. It enables theorists to make fairly precise and testable theoretical predictions of various observables, which in turn allow experimentalists to search for an indirect evidence of new physics. The great advantage of the indirect searches (e.g. measurements of anomalous CP violation and rare or semi-rare decays) is that they are sensitive to effects of new particles that couple to the standard model (SM) sector, even if they are too heavy to be produced directly. These particles manifest themselves indirectly through the higher-order (loop) corrections to the exclusive

decay rates, significantly modifying for instance the rate of the SM-suppressed rare decays $B_s \to \mu\mu$ and $B_d \to \mu\mu$.

Although the inclusive decay rates themselves are not sensitive to new physics (since they are dominated by the tree-level contributions), their measurement provides an excellent testing ground for the necessary theoretical framework. While the HQE calculations have been very successful in predicting lifetime ratios of the B meson lifetimes (i.e. τ_{B_u}/τ_{B_d} and τ_{B_s}/τ_{B_d}), it is only with the recent measurements from Tevatron and now ATLAS, that some agreement with the theoretical prediction is seen also for the Λ_b to B_d^0 ratio. There is no doubt that with increased data statistics accumulated over the future extended period of the LHC running, ATLAS and other LHC experiments will be able to further improve the precision of the Λ_b lifetime measurement and definitively resolve the Λ_b controversy.

Chapter 4

Λ Polarization in Minimum Bias and Di-jet Events

4.1 Introduction

A large polarization of hyperons observed in inclusive proton-proton and proton-nucleon collisions below 1 TeV is still one of the largest mysteries of spin physics. The puzzlement derives from the fact that a single particle like the Λ can emerge with a large polarization even in the midst of a host of other accompanying final state particles that could share or dilute the polarization. Furthermore, perturbative QCD (pQCD) calculations predict polarization much smaller than the values observed in fixed target experiments. This suggests that the polarization, in fact, originates in a non-perturbative regime of the QCD (fragmentation and hadronization) or altogether new physics.

In this analysis, the polarization of the lightest strange hyperon, Λ, is studied. It's decay $\Lambda \to p\pi^-$ is fully reconstructible and the polarization can be extracted from the angular distribution of the final state particles. An example of a reconstructed event is shown in Figure 4.1. In the Λ rest frame, the angle θ^* between the proton and an analyzing direction $\hat{n}$ will follow the probability distribution:

$$w(\cos\theta^*) = \frac{1}{2}\left(1 + \alpha P \cos\theta^*\right), \tag{4.1}$$

where $\alpha = 0.642$ [15] is the decay asymmetry of the parity violating weak decay $\Lambda \to p\pi^-$ and P is polarization in the direction of $\hat{n}$. Therefore, the polarization can be extracted by analyzing the decay angular distribution. The analysis

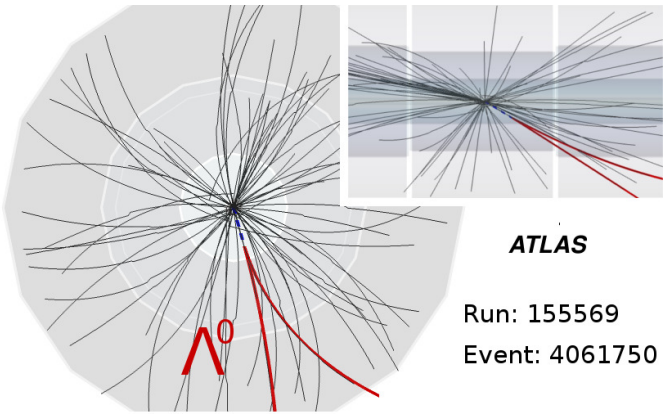

Figure 4.1: Example of $\Lambda \to p\pi^-$ decay in the inner tracker in xy and zR projections (inset). Highlighted tracks are vertex-refitted proton and pion candidate tracks. Three concentric rings represent 3 sub-detectors of the inner detector: pixel, silicon micro-strip, and transition radiation trackers.

reported here uses so called Method of moments to extract the value of polarization from the angular distribution. It exploits the fact that the first moment (i.e. the expectation value) of the distribution is proportional to the polarization. This method, although trivial in case of theoretical distribution (4.1), becomes more complicated when the detector effects and background has to be taken into account. It is explained in details in Section 4.2.

4.1.1 Theoretical Considerations

Derivation of the Decay Angle Distribution

A convenient description of an ensemble of spin 1/2 particles is offered by a density matrix framework (cf. e.g. Ref [33]). The density matrix describing the spin state of an ensemble of Λ hyperons in their rest-frame will look as follows:

$$\rho = \frac{1}{2}(\mathbb{I} + \vec{P} \cdot \vec{\sigma}), \tag{4.2}$$

where $\mathbb{I}$ stands for a 2×2 unit matrix, $\vec{P}$ is the polarization vector and $\vec{\sigma}$ is a vector of the Pauli matrices, σ_1, σ_2, and σ_3. If the coordinate system is chosen to have a z-axis aligned with the polarization direction, the density matrix becomes rather simple:

$$\rho = \frac{1}{2}(\mathbb{I} + P\sigma_3) = \begin{pmatrix} 1+P & 0 \\ 0 & 1-P \end{pmatrix}, \tag{4.3}$$

where P stands for the magnitude of the polarization vector. Since Λ decays into a spin-1/2 proton and a spin-less pion, there are only two possible combinations of final state helicities. Dynamics of the decay can therefore be described in terms of two helicity amplitudes, h_λ, where $\lambda = \pm 1/2$ is the helicity of the final state proton. The decay amplitude in the Λ rest frame can be obtained by applying the Wigner-Eckart theorem to the S-matrix element [34]:

$$\mathcal{M}_{s_z\lambda}(\phi^*, \theta^*) = \langle s_z|S|\theta^*, \phi^*; \lambda\rangle = h_\lambda D^{1/2}_{s_z\lambda}(\phi^*, \theta^*, 0), \tag{4.4}$$

where $\langle s_z|$ denotes the initial state with the spin projection s_z and $|\theta^*, \phi^*; \lambda\rangle$ denotes the final state with the helicity λ where the proton goes off at a polar angle θ^* and an azimuthal angle ϕ^*. $D^{1/2}_{s_z\lambda}(\phi^*, \theta^*, 0)$ stands for the Wigner D-matrix for spin 1/2. A density matrix for the final state proton can be obtained by applying similarity transformation to the Λ density matrix (4.3) using the amplitudes (4.4):

$$\rho_f(\phi^*, \theta^*) = \mathcal{M}(\phi^*, \theta^*)\, \rho\, \mathcal{M}^\dagger(\phi^*, \theta^*). \tag{4.5}$$

A concrete form of the Wigner matrix can be found e.g. in Ref [15]:

$$D^{1/2}(\phi^*, \theta^*, 0) = \begin{pmatrix} e^{-i\frac{\phi^*}{2}} \cos\frac{\theta^*}{2} & -e^{-i\frac{\phi^*}{2}} \sin\frac{\theta^*}{2} \\ e^{+i\frac{\phi^*}{2}} \sin\frac{\theta^*}{2} & e^{+i\frac{\phi^*}{2}} \cos\frac{\theta^*}{2} \end{pmatrix}, \tag{4.6}$$

which plugged into the formulas (4.4 and 4.5) gives a concrete form of the final state density matrix:

$$\rho_f(\phi^*, \theta^*) = \frac{1}{2} \begin{bmatrix} |h_{+1/2}|^2(1 + P\cos\theta^*) & h_{1/2}h^*_{-1/2} P e^{-i\phi^*} \sin\theta^* \\ h_{1/2}h^*_{-1/2} P e^{+i\phi^*} \sin\theta^* & |h_{-1/2}|^2(1 - P\cos\theta^*) \end{bmatrix}. \tag{4.7}$$

The probability density function of the decay angles θ^* and ϕ^* can now be calculated as a trace of this density matrix. It is clear that this probability will not depend on ϕ^*, since that appears only in non-diagonal elements:

$$w(\theta^*) = \mathrm{Tr}\rho_f(\theta^*, \phi^*) = \frac{1}{2}\left[|h_{1/2}|^2 + |h_{-1/2}|^2 + (|h_{1/2}|^2 - |h_{-1/2}|^2) P\cos\theta^*\right]. \tag{4.8}$$

The formula can be further simplified using the normalization condition for helicity amplitudes, $|h_{+1/2}|^2 + |h_{-1/2}|^2 = 1$, and a definition of the Λ decay asymmetry

parameter, $\alpha = |h_{+1/2}|^2 - |h_{-1/2}|^2$. Plugging in these relations one gets the well-known formula (4.1) for the decay angle distribution.

Symmetry Under the Parity Transformation

Λ hyperons studied in this analysis are produced via the strong interaction, which is believed to conserve parity. Since the initial state is symmetric under the parity operation (two unpolarized protons colliding in a center-of-mass frame), and assuming that parity is conserved by a Λ production mechanism, the final state has to be invariant under the parity operation, too. As a consequence, the longitudinal polarization has to be zero and only non-zero polarization can be observed in a direction perpendicular to the Λ momentum. This claim can be understood if one looks at a behavior of the longitudinal polarization under the parity transformation: let $\vec{p}$ be a Λ momentum and $\vec{P}$ its polarization vector. Then longitudinal polarization, L, can be expressed as a projection of the polarization vector into the direction of Λ:

$$L = \frac{\vec{p}}{|p|} \cdot \vec{P}. \tag{4.9}$$

Under the parity transformation, the Λ momentum changes orientation, however, the polarization vector does not since it is an axial vector. Consequently, the longitudinal polarization changes sign. This means that the longitudinal polarization has to be zero if parity is to be conserved, i.e. product $\vec{p} \cdot \vec{P} = 0$. This condition still allows for the transverse polarization to be present.

Polarization in the Beam-Λ Reference Frame

Traditionally, the transverse polarization is measured in the direction of the normal to the the scattering plane, defined as a cross-product of the beam direction, $\vec{p}_{\text{beam}}$, and the Λ momentum: $\hat{n} \propto \vec{p}_{\text{beam}} \times \vec{p}$ (see Figure 4.2). The same as in the case of the longitudinal polarization, the transverse polarization, P, is defined as a projection of the polarization vector, $\vec{P}$, into the analyzing direction:

$$P = \hat{n} \cdot \vec{P}. \tag{4.10}$$

Since the LHC collides two identical protons in the center-of-mass frame, the choice of the beam direction is completely arbitrary. This symmetry further constrains behavior of the transverse polarization. If the opposite beam direction is chosen in

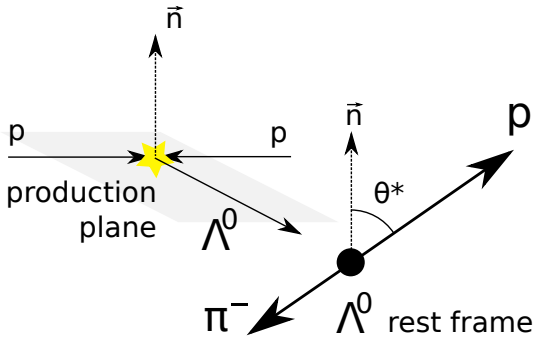

Figure 4.2: Traditional definition of the decay angle as an angle between the normal to the scattering plane and the decay proton, measured in the Λ rest frame (left).

definition of $\hat{n}$, the sign of the numerical value of the polarization, P, will change, because $\hat{n}$ is involved in the definition of P (Eqn. 4.10). Since the beam direction is also used to define rapidity of Λ, y, the alternative choice of the beam direction will change the sign of rapidity, too. Due to the arbitrariness of the choice of the positive beam direction, it should not have any impact of the physics result and therefore the following symmetry has to hold for the transverse Λ polarization:

$$P(y) = -P(-y), \tag{4.11}$$

which means that polarization defined in the beam-Λ reference frame has to be an odd function of Λ rapidity. Since the detector coverage is symmetric in rapidity, polarization of the sample reconstructed in the entire volume of the detector must therefore be zero. In order to measure potentially non-zero value, the analyzing direction definition used in this study depends on the rapidity of the outgoing Λ hyperon:

$$\begin{aligned} \hat{n} &\propto \hat{z} \times \vec{p} && \text{for } \Lambda \text{ with positive rapidity and} \\ \hat{n} &\propto -\hat{z} \times \vec{p} && \text{for } \Lambda \text{ with negative rapidity.} \end{aligned}$$

This definition follows the convention used in the fixed target experiments, where the incoming beam direction vector always points to the same hemisphere as Λ.

The traditional choice of the analyzing direction (Figure 4.2) assumes that the polarization is correlated to the Λ transverse momentum, as p_{T} always lies in the scattering plane and determines orientation of the normal $\hat{n}$. Such a reference frame is motivated by measurement of the polarization originating in the hard scattering process (e.g. $q\bar{q} \to s\bar{s}$, $gg \to s\bar{s}$, etc.) Polarization of the s quark, and

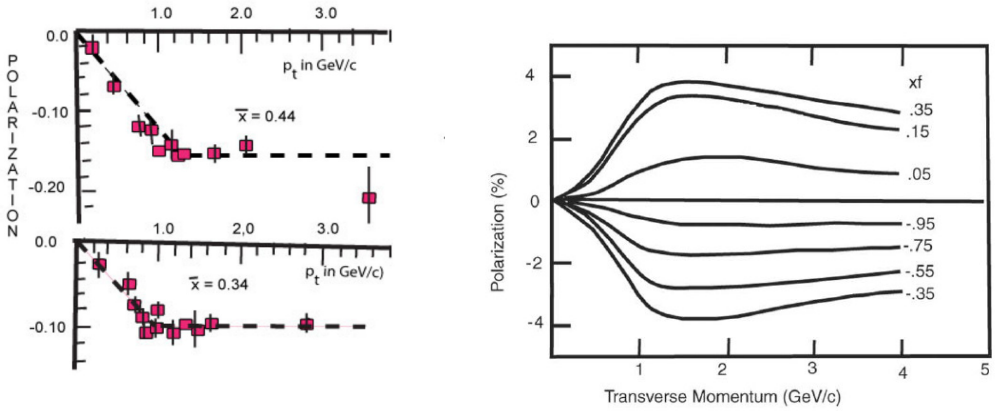

Figure 4.3: Dependence of the polarization in inclusive Λ production in $p-p$ and $p-Be$ collisions at 400 GeV as a function of p_{T} for the two x_F bins (left). Figure taken from Ref. [43]. Polarization of s quark in pQCD calculations [35] (right).

consequently that of Λ, produced in such a process, is calculable in the framework of the pQCD. These calculations were performed e.g. by the authors of Ref. [35], however, the obtained results are significantly smaller than values measured experimentally (e.g. Ref. [36, 37, 38, 39, 40, 41, 42]). A comparison between the experimentally measured Λ polarization in a fixed target experiment [38] and pQCD prediction of the expected s quark polarization is shown in Figure 4.3, where a stark disagreement can be seen. One therefore has to look for alternative explanations of the observed results.

Figure 4.3 shows principal features of the polarization dependence on event kinematics observed by all the experiments:

- the polarization increases with p_{T} until it reaches a saturation value of about 1 GeV;
- the polarization decreases with decreasing value of Feynman-x variable, x_{F}, defined as $x_{\mathrm{F}} = p_z/p_{\mathrm{beam}}$, where p_z is the longitudinal component of the Λ momentum;
- the polarization does not depend strongly on the beam energy (at least in the tested range of about 400–800 GeV).

Several models have been proposed to explain these features, including the polarization plateau at fixed x_F seen in the p_{T}-dependence of the polarization. While some models have been successful in explaining the behavior of one member

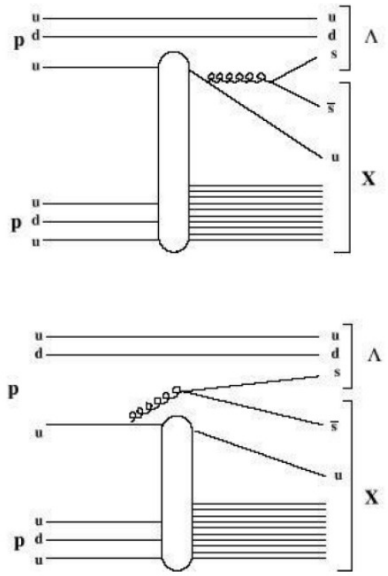

Figure 4.4: Strange quark production through gluon bremsstrahlung [37].

of the hyperon family, no one model has been successful in explaining the behavior of all. In the static quark model, Λ baryon consists of u, d, and s quarks. The ud quarks form a spin singlet, and therefore the Λ polarization is assumed given solely by the polarization of the s quark. Although this assumption is used by many models describing the origin of the Λ polarization, it is not inherently needed for the measurements presented in this document.

As pointed out in Ref. [44], the older models have been based either on gluon bremsstrahlung, the polarization vs. p_{T} distribution of sea quarks, or the production of $s\overline{s}$ pairs in color force fields. An example of the bremsstrahlung picture is illustrated in Figure 4.4 [37]. Here, just as in the case of electron bremsstrahlung, the polarization of the final state particles could be significant and dependent on p_{T}. This model, however, suffers from the lack of definitive predictive ability.

The second class of models assumes that collisions occur involving $s\overline{s}$ pairs spontaneously created from the vacuum. The s-quark becomes polarized in the collision with the incoming beam proton, and then recombines with a singlet (ud) pair to form the outgoing polarized Λ – polarization of the scattered s quark being transferred into the Λ hyperon. Although this model does not explain how the original s quark gets polarized, it allows for cross-comparison of polarization data for various baryons. Some support for this picture comes from the suggestion of Neal and de la Cruz Burelo [45] that there is a direct relationship between $p - p$

and Λ polarizations, based on an universal relationship between $q - q$ scattering and polarization.

Another model is that of DeGrand [46, 47]. This model attributes hyperon polarization to a Thomas precession effect connected with the merging of a sea s-quark in one of the colliding protons with the (ud) pair from the second colling proton in a way that the s-quark must be accelerated in order to form the ultimate Λ. The polarization dependence of p_{T} thus occur because the related s-quark boost is different for different Λ p_{T}. This model permits an integrated explanation of the polarization for a number of hyperons, not just the Λ. On the other hand, some of the assumptions made in the model have been drawn into question in the literature, see e.g. Ref [48].

A more speculative possibility is that in the new energy regime of the LHC quark internal structure might be revealed. In that case, the s quark scattering in the $p - p$ collision could be understood as scattering of individual strongly bound constituents of the s-quark (the same way as proton elastic scattering can be understood as a scattering of a single constituent quark which than drags with itself the rest of the proton). If the single constituent interaction decreases with p_{T}, for larger values of p_{T} the multiple-constituent interaction may start playing a non-negligible role. Should this occur, abrupt changes in the polarization magnitude could occur as a function of p_{T} and could even be visible as a slope change in the polarization as a function of x_{F}, even near $x_{\mathrm{F}} = 0$. Such a model has been motivated by the models of Neal and Nielsen [49, 50] who have argued that the polarization structure in $p - p$ elastic scattering provided retrospectively the first evidence for the existence of quarks inside protons.

Another explanation is provided by Lund model of the Λ polarization [51].

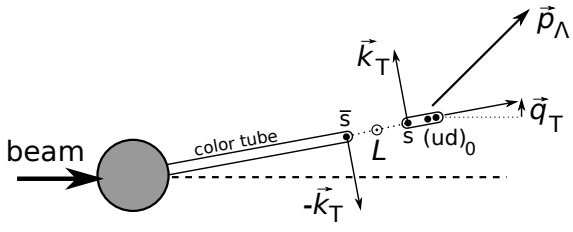

Figure 4.5: Lund model of polarization. $s\bar{s}$ quarks are produced by breaking of the color tube and they carry transverse momenta $\vec{k}_{\mathrm{T}}$ and $-\vec{k}_{\mathrm{T}}$. This creates an orbital momentum L which is than compensated by the alignment of the quarks spins thus creating polarization.

This semi-classical model assumes that Λ originates from the ud remnant of the original proton that gets combined with the s quark from $s\bar{s}$ pair created by fragmentation of the color field (color tube) connecting the ud remnant with the interaction center, as illustrated in Figure 4.5. In the fragmentation process the s and $\bar{s}$ gain momenta $\vec{k}_{\mathrm{T}}$ and $-\vec{k}_{\mathrm{T}}$ transverse to the direction of the color tube, which gives the quarks an orbital momentum L. As the total angular momentum of the system has to be zero, spins of the s and $\bar{s}$ quarks get aligned to compensate the orbital momentum (in Figure 4.5 spins of the s-quarks would point into the paper to compensate L pointing outwards). If the transverse momentum of the ud remnant is smaller or at least comparable to the transverse momentum of the s-quark, i.e. $k_{\mathrm{T}} \gtrsim q_{\mathrm{T}}$, then the transverse momentum of the final Λ particle, p_{T}, will be correlated to the s-quark momentum $\vec{k}_{\mathrm{T}}$. In such a case, the Λ transverse momentum and the orientation of the spin will be correlated as well and the transverse polarization can be observed. The reader should note that the condition $k_{\mathrm{T}} \gtrsim q_{\mathrm{T}}$ is essential, because vectors $\vec{k}_{\mathrm{T}}$ and $\vec{q}_{\mathrm{T}}$ can point in completely different directions. This condition is satisfied at fixed target experiments, where the collected Λ candidates have large Feynman-x variable, $x_{\mathrm{F}} = p_z/p_{\mathrm{beam}}$ (p_z is the longitudinal component of the Λ momentum).

More recent quantum mechanical models have been advanced using the assumption of factorization of scattering amplitudes into components representing unpolarized parton densities, partonic cross sections, and spin dependent fragmentation functions [52, 53, 54, 55]. The reach of the LHC in terms of energy and momentum makes the factorization approach seem justified. A interesting feature of these models is the potential universality of the fragmentation functions across a variety of interactions.

More details on the various models can be found for instance in Ref. [56, 57, 44].

Polarization in the Di-jet Reference Frame

In the ATLAS experiment, Λ candidates with large x_{F} cannot be reconstructed because of the limited rapidity acceptance of the detector. On the other hand, due to a jet reconstruction capability, one can learn additional information about the parton momenta, which were not accessible in the previous experiments. A novel scheme has been proposed by Daniel Boer et al. [54] who suggest that the spin properties of the non-perturbative fragmentation process can be studied in events where Λ is produced inside one of the jets of a di-jet event. If both jets are

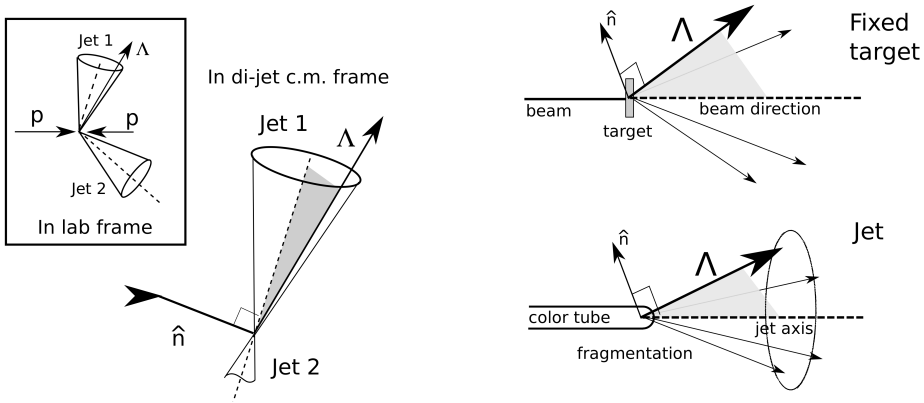

Figure 4.6: Definition of the scattering plane in the di-jet event with Λ hyperon in one jet (left). Analogy between the definition of the scattering plane in the fixed target experiment and inside a jet (right).

reconstructed, the underlying parton momenta are known (neglecting the higher order correction to the QCD scattering process). Let us denote K_{j} a 4-momentum of the jet containing Λ, $K_{\mathrm{j}'}$ the 4-momentum of the other jet, and $\vec{k}_{\mathrm{j}}$ and $\vec{k}_{\mathrm{j}'}$ the corresponding 3-momenta. One can then define a new analyzing direction using the jet axis, $\vec{k}_{\mathrm{j}}$, and the Λ momentum, $\vec{p}$, as a cross-product of the two, $\hat{n} \propto \vec{k}_{\mathrm{j}} \times \vec{p}$, where both directions are expressed in the di-jet rest frame (Figure 4.6, left). The reader should note that the jet direction may be thought of as the beam direction in a fixed target experiment and the angle between the Λ and the jet direction is similar to the scattering angle, as shown in Figure 4.6, right. Taking this analogy further, one can imagine that in the limit of large x_{F} the outgoing parton momentum (jet axis) will be close to the beam axis and two frames will become identical.

Boer's paper [54] does not give a dynamical explanation of how the polarization could arise in the fragmentation process, however, it provides a phenomenological framework for its description in terms of polarizing fragmentation functions. These are generic functions of z and k_{T}^2, where z is the momentum fraction defined as $z = \frac{K \cdot K_{\mathrm{j}'}}{K_j \cdot K_{\mathrm{j}'}}$, with K being the Λ's 4-momentum, and k_{T} the Λ transverse momentum relative to the jet axis. The polarizing fragmentation functions parametrize the probability that unpolarized parton, such as quark or gluon, fragments into a polarized Λ hyperon. Using the factorization theorem, the Λ polarization can be

expressed, assuming dominance of gluons, as follows [54]:

$$P_{\text{theor}}(z, k_{\text{T}}, y_{\text{j}}) = \frac{D_T^g(z, k_{\text{T}})}{D^g(z, k_{\text{T}})} + a(y_{\text{j}}) \frac{\tilde{D}_T^g(z, k_{\text{T}})}{D^g(z, k_{\text{T}})}, \tag{4.12}$$

where D_T^g and $\tilde{D}_T^g$ are polarizing fragmentation functions of gluons, D^g are ordinary (unpolarized) fragmentation functions measured by previous experiments, $a(y_{\text{j}})$ is a function defined as $a(y_{\text{j}}) = -\frac{1}{2}\frac{1+y_{\text{j}}^2+(1-y_{\text{j}})^2}{1+y_{\text{j}}^4+(1-y_{\text{j}})^4}$, and $y_{\text{j}} = \frac{1}{e^{\eta_j - \eta_{j'}}+1}$. The di-jet variable y_{j} can also be expressed in terms of Mandelstam variables s and t: $y_{\text{j}} = -\frac{t}{s}$.

The polarization cannot be experimentally measured fully differential in all the variables due the lack of statistics, however, it can be measured in bins of z and k_{T}. To compare the measurement to the theoretical prediction (or fit the fragmentation functions to the measured results), one has to integrate the function (4.12) over the Λ phase-space. Let $P_{\text{mea}}(z_i)$ is the measured polarization in i-th bin of z. Then $P_{\text{mea}}(z_i)$ should be compared to the following integral:

$$P_{\text{theor}}(z_i) = \int_{z_{\text{min}}}^{z_{\text{max}}} \mathrm{d}z \iint \mathrm{d}k_{\text{T}} \mathrm{d}y_{\text{j}} \; w(z) w(k_{\text{T}}) w(y_{\text{j}}) \; P_{\text{theor}}(z, k_{\text{T}}, y_{\text{j}}), \tag{4.13}$$

where $w(z)$, $w(k_{\text{T}})$, and $w(y_{\text{j}})$ are distributions of kinematic variables observed in the data sample, and z_{min} and z_{max} are the limits of the i-th z bin. The kinematic variables should be corrected to the hadron level so that the detector effects are not included in the calculations.

Ref [58] gives evaluation of the Λ polarization as a function of z for polarizing fragmentation functions extracted from the low energy data (see Figure 4.7, taken from the cited reference). It predicts very small polarization for smaller values of z. However, the polarizing fragmentation functions were fitted from low energy data, where only valence quarks matter. At the LHC it does not have to be so, as the dominant contribution is from sea quarks and gluons.

Some insight into the dynamical process that could cause Λ spin asymmetry in jets is given in Ref [59] (although the paper focuses on a different topic). The model outlined there is similar to the Lund model in some aspects. It assumes the $s\bar{s}$ quarks are produced in the fragmentation of the uniformly expanding color tube stretched between the outgoing partons. However, unlike in the Lund model, the outgoing partons are either quarks or gluons (not the ud singlet). The color

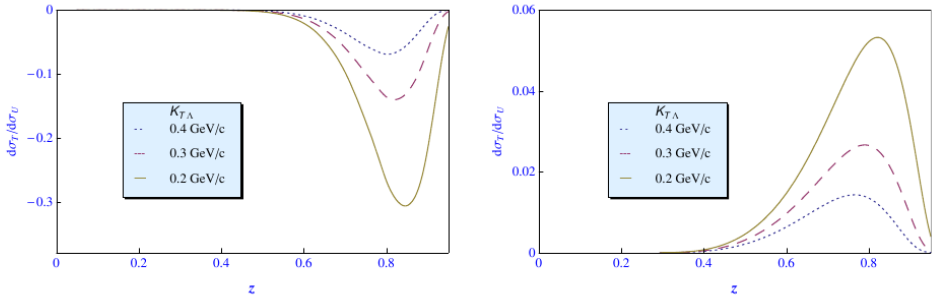

Figure 4.7: The Λ polarization prediction for $\sqrt{s} = 14$ TeV using the polarizing fragmentation functions extracted from the low energy data. The result depends on the choice of the unpolarized fragmentation function parametrization. The results for two choices of the parametrization are shown. The plot was taken from Ref [58].

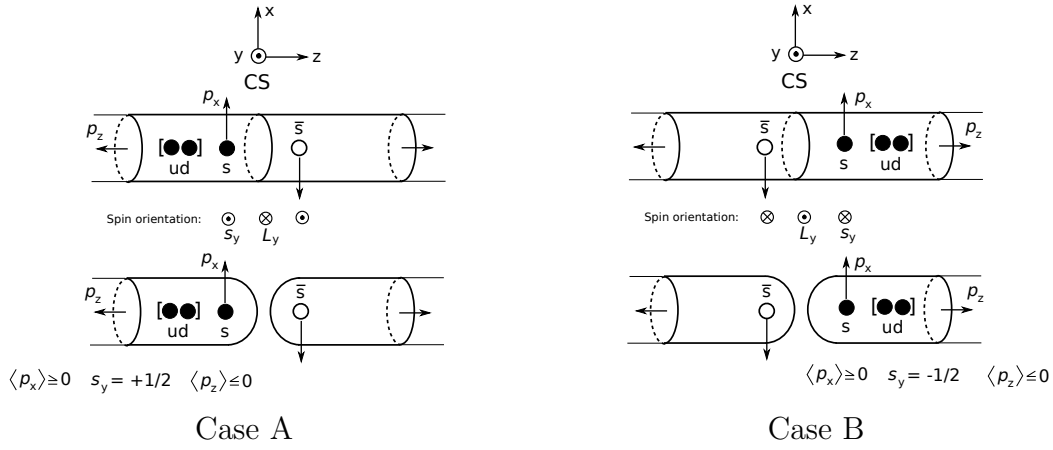

Figure 4.8: Fragmentation of the color tube through creation of $s\bar{s}$ pair in a vacuum state $^3P_0$.

tube is broken into two fragments through creation of the $s\bar{s}$ quark pair which is in a vacuum state $^3P_0$, with the orbital momentum $L = 1$ and spins of the s-quarks pointing in the opposite direction to L. This process is illustrated in Figure 4.8. The coordinate system is chosen such that the z-axis points in the direction of the tube, x-axis points in the direction of the s-quark transverse momentum (transverse w.r.t. the axis of the tube) and y forms an orthogonal basis. The reference frame is stationary w.r.t. the surface marked "CS" in the drawing and since the tube is uniformly expanding it means that the hadrons condensing from the left part of the tube will have longitudinal momentum $p_z \leq 0$ while the particles in the right half will have $p_z \geq 0$. There are two possible scenarios that can occur, denoted as "Case A" and "Case B" in Figure 4.8. In Case A

the s quarks have mean longitudinal momentum $\langle p_z \rangle \leq 0$ while in Case B their momentum is $\langle p_z \rangle \geq 0$. Furthermore, the polarization of the s-quark is opposite since the spins point in opposite direction in the two cases. If both scenarios have the same probability the polarization of the Λ hyperon will be zero. This is to be expected for data where Λ carries a low fraction of the parton momentum, z. For events with large z, however, Case B will be favored as s quarks in that case have larger longitudinal momenta. The reader should note, that the assumption that $s\bar{s}$ pairs are produced in the P-state is crucial for this model. If pairs were produced for instance in the S-state their orbital momenta would be 0 and there would be no spin-momentum correlation. Also a pair production through a gluon splitting, $g \to s\bar{s}$, will create s quarks with small polarization, as predicted by pQCD. Note that this model, similarly to the Lund model, have some restrictions on values of s quarks momentum relative to the tube's axis (denoted p_x in Figure 4.8). If the tube was aligned with the jet axis, the value of p_x would correspond to the Λ's transverse momentum relative to the jet axis, k_{T}. However, partons that are connected by the tube will likely already have some transverse momenta of their own from the initial parton shower. Therefore, it is important, like in the Lund model, that $p_z \gtrsim k_{\mathrm{T,part}}$, where $k_{\mathrm{T,part}}$ is the relative transverse momentum of the partons from the parton shower. One can thus expect to see larger polarization for events with large k_{T}, where it is more likely that directions of p_x and $k_{\mathrm{T,part}}$ are aligned and the polarization effect is therefore enhanced. This qualitative analysis suggest that polarization should be zero for small z and increase with growing z and k_{T}.

Naive Extrapolation of the Previous Results into the Di-jet Frame

Results of fixed-target experiment measurements of inclusive Λ polarization as a function of the Feynman-x variable, x_{F}, and transverse momentum, p_{T}, is published for instance in Ref [43] (see Figure 4.3, left). The analyzing direction in these measurements is defined in the beam-Λ reference frame, i.e. $\hat{n} \propto \vec{p}_{\mathrm{beam}} \times \vec{p}$. The observed results can be approximated by a simple function

$$P_{\mathrm{old}}(x_{\mathrm{F}}, p_{\mathrm{T}}) = 0.392\, x_{\mathrm{F}} \left[\frac{p_{\mathrm{T}}}{1.1\ \mathrm{GeV}}\, \Theta(1.1\ \mathrm{GeV} - p_{\mathrm{T}}) + \Theta(p_{\mathrm{T}} - 1.1\ \mathrm{GeV}) \right], \quad (4.14)$$

where Θ is the Heaviside step function. It is assumed that polarization increases linearly with x_{F}. The p_{T} dependence is also linear until the saturation value of

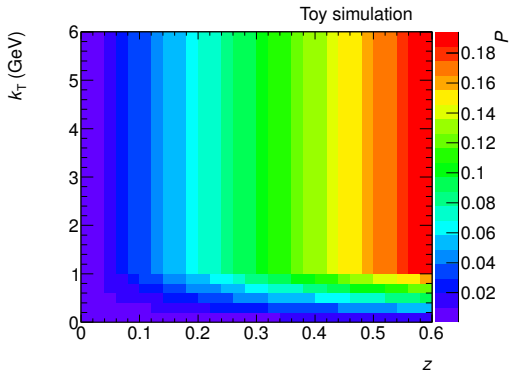

Figure 4.9: Naive extrapolation of results of the previous polarization measurement [43] into the di-jet reference frame.

1.1 GeV is reached beyond which the polarization becomes independent on p_{T}.

The most naive extrapolation of these previous results to the di-jet reference frame can be done by replacing variable x_{F} by z and p_{T} by k_{T}:

$$P(z, k_{\mathrm{T}}) \equiv P_{\mathrm{old}}(z, k_{\mathrm{T}}). \tag{4.15}$$

This function is visualized in Figure 4.9. One can then use the parametrization (4.15) to predict values of the polarization expected in ATLAS data, using the toy MC method to calculate integrals (4.13). Since this simple model does not depend on y_{j}, only integration over z and k_{T} is performed. Histograms of kinematic distributions of ATLAS data, Figures B.11 and B.12, are used to model distributions $w(z)$ and $w(k_{\mathrm{T}})$. An uncertainty of the polarization prediction is estimated by performing 100 pseudo-experiments varying each bin content of the distributions $w(z)$ and $w(k_{\mathrm{T}})$ by a random shift following a Gaussian distribution with width corresponding to the bin error. The results are shown in Figure 4.10. The predicted values of the polarization are too small to be distinguishable from zero with the current data sample. However, it is conceivable that with the increased statistics (data collected after the LHC shutdown) precise-enough measurement will be possible, especially if the z coverage can be extended towards larger values.

4.2 Measurement Strategy

The angular distribution (4.1) can never be seen in real data, since detector acceptance, efficiency and resolution will distort the observed distribution. Denoting

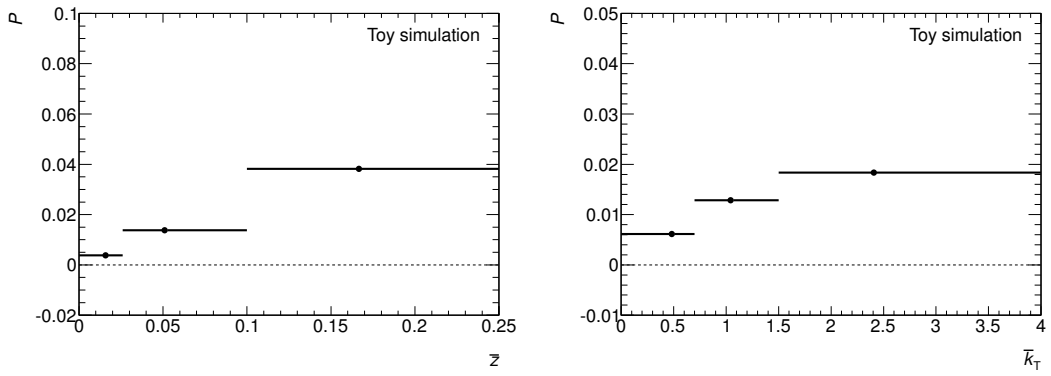

Figure 4.10: Naive extrapolation of the previous polarization results expressed as a function of the momentum fraction, z (left), and the relative transverse momentum, k_{T} (right).

$\cos\theta^*_{\mathrm{true}} \equiv t'$ the real decay angle without the detector distortions, the formula (4.1) will read $w(t') = (1/2)\,(1 + \alpha P t')$ in this notation. An expectation value (1st moment) of this distribution is directly proportional to the polarization:

$$E_P^{\mathrm{true}} = \int \mathrm{d}t'\, t\, \frac{1}{2}(1 + \alpha P t') = \frac{1}{3}\alpha P, \tag{4.16}$$

where $\alpha = 0.642$ [15] is the decay asymmetry of the parity violating weak decay $\Lambda \to p\pi^-$. Unfortunately, in reality detector effects are not negligible and one has to modify the PDF in terms of the observed decay angle, $\cos\theta^* \equiv t$, as follows:

$$w(t) = \frac{1}{2\varepsilon_{\mathrm{T}}}\left[(1 + \alpha P t')\ \varepsilon(t')\right] \otimes R(t, t'), \tag{4.17}$$

where $\varepsilon(t')$ is the reconstruction efficiency, $R(t, t')$ is the resolution function, which is convolved with the true decay angle distribution, and ε_{T} is the total efficiency normalizing the modified PDF. The expectation value of PDF (4.17) will now look as follows:

$$\begin{aligned} E_P &= \frac{1}{2}\iint \mathrm{d}t\ \mathrm{d}t'\ t\ R(t,t')\ \varepsilon(t')\ \left[1 + \alpha P t'\right] = \\ &= \underbrace{\frac{1}{2\varepsilon_{\mathrm{T}}}\iint \mathrm{d}t\ \mathrm{d}t'\ t\ R(t,t')\ \varepsilon(t')}_{C_0} + P\ \underbrace{\frac{\alpha}{2\varepsilon_{\mathrm{T}}}\iint \mathrm{d}t\ \mathrm{d}t'\ t\ t'\ R(t,t')\ \varepsilon(t')}_{C_1} = \\ &= C_0 + C_1 P. \end{aligned} \tag{4.18}$$

Note that one simplification was made when deriving the formula (4.18), namely that the total efficiency does not depend on polarization, i.e. $\varepsilon_{\mathrm{T}}(P) \equiv \varepsilon_{\mathrm{T}}$ is constant. This is not generally true, however, it is reasonably well satisfied in the the analyzed data. An impact of this assumption on the final result is estimated as a systematic uncertainty. The constants C_0 and C_1 can be expressed in terms of the expectation values of the PDFs with known polarization:

$$\begin{aligned} C_0 &= E_0, \\ C_1 &= E_1 - E_0, \end{aligned}$$

where E_0 and E_1 are expectation values of PDF (4.18) for $P = 0$ and $P = 1$, respectively. These values can be estimated using the Monte Carlo (MC) simulation. The MC events used in this analysis are weighted (see following section for description of the weighting procedure), therefore, the expectation value is estimated as a weighted average:

$$E_P^{\mathrm{MC}} = \frac{\sum w_i^P t_i}{\sum w_j^P}, \tag{4.19}$$

where t_i is the value of the reconstructed decay angle in the i-th event and w_i^P is the weight of that event. The MC samples weighted to polarization $P = 0$ and $P = 1$ are used to determine values of the constants C_0 and C_1. The final piece of the polarization extraction is the description of background. The presence of background in analyzed data modifies the expectation value as follows:

$$E_P = f_{\mathrm{sig}} \left[E_0^{\mathrm{MC}} + (E_1^{\mathrm{MC}} - E_0^{\mathrm{MC}}) P \right] + (1 - f_{\mathrm{sig}}) E_{\mathrm{bkg}}, \tag{4.20}$$

where f_{sig} is the signal fraction and E_{bkg} is the decay angle expectation value of background events. To determine the value of the background expectation value, the formula (4.20) is expressed as a function of the invariant mass of the proton-pion pair. For the invariant mass far from the Λ mass the signal fraction is small and therefore the expectation value is dominated by background, while in the signal region the main contribution is from the signal decays. It is assumed, that the background expectation value changes linearly and can be therefore interpolated into the central region. Using this assumption, the decay angle expectation value

as a function of the invariant mass can be expressed as:

$$E_P(m_{p\pi}) = f_{\text{sig}}(m_{p\pi}) \left[E_0^{\text{MC}} + (E_1^{\text{MC}} - E_0^{\text{MC}})P\right] + [1 - f_{\text{sig}}(m_{p\pi})][b_0 + b_1(m_\Lambda - m_{p\pi})], \tag{4.21}$$

where b_0 and b_1 describe the mass dependence of the background expectation value. The formula (4.21) is used to extract the value of polarization from data. The procedure can be described in the following steps:

- The MC is weighted for polarization $P = 0$ and $P = 1$ and the expectation values E_0^{MC} and E_1^{MC} are calculated as a weighted average of the MC decay angle values;
- Data sample is divided into 7 slices of the invariant mass and the decay angle expectation value is calculated in each slice as an average of decay angle values;
- In each mass bin the signal fraction is estimated using the fit to the invariant mass distribution;
- The χ^2 fit method is used to fit the function (4.21) to the the data expectation values in the mass bins, using the signal fraction in each bin from the previous step. The extracted parameters are polarization, P, and the background parameters, b_0 and b_1;
- Systematic uncertainties are estimated by modifying various aspects of the analysis and observing their impact on the final result.

In this document results of two analyses are presented. Firstly, the Λ polarization in the beam-Λ reference frame is measured. In this frame the polarization in direction $\hat{n} \propto \vec{p}_{\text{beam}} \times \vec{p}$ (where $\vec{p}_{\text{beam}}$ is direction of the beam and $\vec{p}$ is the Λ momentum) is measured. This measurement is done using inclusive Λ events selected by the minimum bias trigger. The second measurement is of the Λ polarization in the di-jet frame, using di-jet events where one of the jets contains Λ. In this case, the analyzing direction is defined as $\hat{n} \propto \vec{k}_{\text{j}} \times \vec{p}$, where $\vec{k}_{\text{j}}$ is the momentum of the jet containing Λ, expressed in the di-jet center-of-mass frame.

All the steps mentioned above are described in detail in the following sections.

4.3 Data Samples and the Trigger Selection

The Λ polarization in the beam-Λ reference frame is measured using the 2010 data. Events that have at least one hit in the minimum bias trigger scintillators are selected. The 2010 minimum bias data sample selected by this trigger corresponds to an integrated luminosity of about 762 μb^{-1}. The Λ polarization in the di-jet reference frame uses data collected in 2011 that correspond to an integrated luminosity of about 5 fb^{-1}. Single-jet calorimeter triggers are used to select the di-jet data. ATLAS has a three-layer trigger system, with the first layer being hardware based, the other two (together called the High-Level Trigger or HLT) are software based. The jet trigger reads data from electromagnetic and hadronic calorimeters, performing fast jet calorimeter shower reconstruction (anti-k_{T} jet algorithm with the distance parameter of 0.4) [11]. Compared to the offline jet reconstruction it uses a simplified jet energy scale calibration. The level-1 trigger has access only to the limited granularity of the calorimeter, HLT then uses the full granularity. The trigger selection is based on the transverse energy cut, E_{T}, that has to be satisfied by at least one trigger-reconstructed jets in the event. Several different E_{T} thresholds are available, ranging from 10 GeV to 425 GeV. Since the output rate of the low-threshold jet triggers is too high for all the events to be recorded, rate of these triggers has to be reduced by so called prescale factor. For triggers with the prescale factor of X, on average only every X-th accepted event is recorded. The triggers used for the di-jet analysis are shown in Figure 4.11. The left plot shows the number of events accepted by a given trigger, the right plot shows the corresponding average prescale factor. One event can be accepted by multiple triggers. Only events after the final selection (described in the following sections) are counted in Figure 4.11. A single minimum bias trigger, `MBTS_1`, is used for the inclusive Λ selection. This trigger was prescaled in the later periods of 2010 data taking.

4.4 Monte Carlo Samples

For the measurement of the polarization in the beam-Λ reference frame, the 20 M of MC events[1] generated by Pythia [27] are used. For the di-jet analysis, QCD di-jet Monte Carlo samples are used. The number of events, cross section and

[1] mc10_7TeV.105001.pythia_minbias.merge.AOD.e574_s932_s946_r1649_r1700/

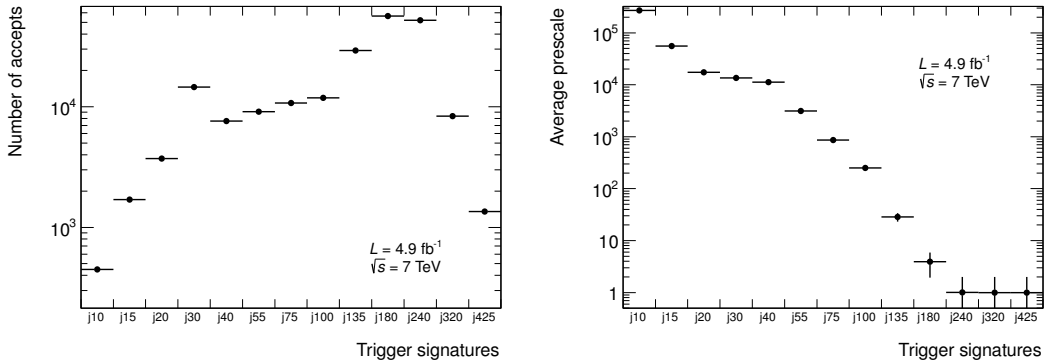

Figure 4.11: Number of events accepted by a given trigger (left) and the corresponding average trigger prescale factors (right).

generator-level selection cuts for these samples are listed in Table 4.1. Samples are generated by MC generator Pythia[2] [27] and Herwig[3] [60] and the Geant 4 package [61] is used to simulate propagation of particles through the detector. Geant 4 also simulates decays of long-lived unstable particles, such as pions, kaons, or Λ. The samples are then reconstructed using the same software as that used for the data reconstruction. The di-jet samples are generated in slices of the outgoing parton transverse momentum, $p_{\mathrm{T}}^{\mathrm{part}}$, each sample having the same statistics but different cross section (also listed in Table 4.1). Before they can be used, each sample has to be weighted by a factor proportional to the corresponding cross section. For the inclusive Λ measurement the single minimum bias sample is used and therefore no such wighting is required. The data and MC events are selected using the same triggers, however, in the MC all the triggers are unprescaled. That is not a problem for the minimum bias analysis, where only one trigger is required. However, the di-jet MC events have to be weighted to simulate the effect of the prescale factors.

[2]Pythia samples:
mc11_7TeV.105011.J2_pythia_jetjet.merge.AOD.e815_s1273_s1274_r2923_r2900/,
mc11_7TeV.105012.J3_pythia_jetjet.merge.AOD.e815_s1273_s1274_r2923_r2900/,
mc11_7TeV.105013.J4_pythia_jetjet.merge.AOD.e815_s1273_s1274_r2923_r2900/,
mc11_7TeV.105014.J5_pythia_jetjet.merge.AOD.e815_s1273_s1274_r2923_r2900/,
mc11_7TeV.105015.J6_pythia_jetjet.merge.AOD.e815_s1273_s1274_r2923_r2900/

[3]Herwig samples:
mc11_7TeV.113206.HerwigppJetsJ2.merge.AOD.e873_s1349_s1300_r2923_r2900/,
mc11_7TeV.113207.HerwigppJetsJ3.merge.AOD.e873_s1349_s1300_r2923_r2900/,
mc11_7TeV.113208.HerwigppJetsJ4.merge.AOD.e873_s1349_s1300_r2923_r2900/,
mc11_7TeV.113209.HerwigppJetsJ5.merge.AOD.e873_s1349_s1300_r2923_r2900/,
mc11_7TeV.113210.HerwigppJetsJ6.merge.AOD.e873_s1349_s1300_r2923_r2900/

Table 4.1: Di-jet Monte Carlo samples. An abbreviation "Py." stands for Pythia and "Hw." for Herwing generator.

Name	No. of events		Cross section		Parton momentum cuts
	Py.	Hw.	Py.	Hw.	
J2	2.8 M	1 M	48.04 mb	46.64 mb	$35 < p_{\mathrm{T}}^{\mathrm{part}} < 70$ GeV
J3	2.8 M	1 M	2.54 mb	2.45 mb	$70 < p_{\mathrm{T}}^{\mathrm{part}} < 140$ GeV
J4	2.8 M	1 M	0.0996 mb	0.0957 mb	$140 < p_{\mathrm{T}}^{\mathrm{part}} < 280$ GeV
J5	2.8 M	1 M	2.29 nb	2.48 nb	$280 < p_{\mathrm{T}}^{\mathrm{part}} < 560$ GeV
J6	2.8 M	1 M	0.0355 nb	0.0341 nb	$560 < p_{\mathrm{T}}^{\mathrm{part}} < 1120$ GeV

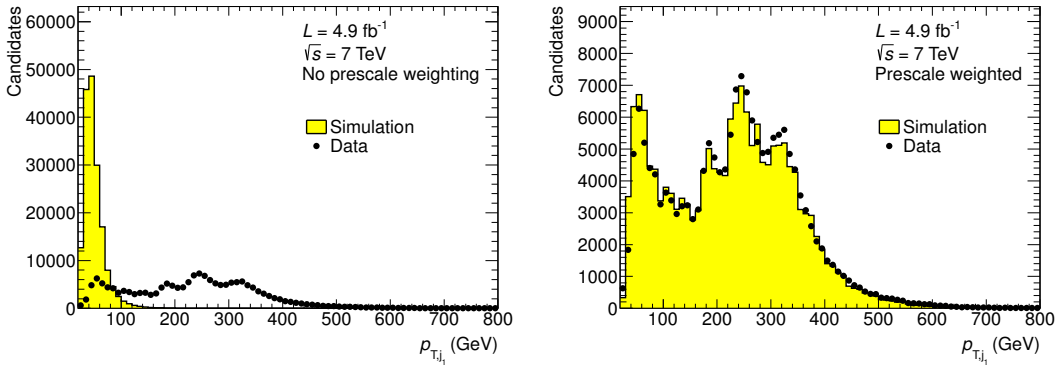

Figure 4.12: Effect of the MC prescale weighting. Comparison between the data and MC leading jet p_{T} spectrum without the prescale weighting (left) and after the prescale weighting (right).

Let PS_i be the prescale factors of all triggers active in some event. Then the probability that the event will not be recorded due to the prescale factor is $1-\frac{1}{PS_i}$. For all the active triggers this probability can be calculated as a product of all the individual probabilities, $\prod_i \left(1-\frac{1}{PS_i}\right)$, and therefore probability that the event is recorded equals to

$$p_{\mathrm{recorded}} = 1 - \prod_i \left(1 - \frac{1}{PS_i}\right), \tag{4.22}$$

where i runs over all the active triggers in the event. The probability p_{recorded} is used to weight each MC event using the average prescale factors, PS_i, measured in data (Figure 4.11, right). The effect of the MC prescale weighting on the leading jet p_{T} spectrum is illustrated in Figure 4.12. The left plot shows the data and MC distribution without the prescale weighting, while the right plot shows the same distributions after the MC events were weighted using the prescale weights (4.22).

The plots show that the agreement between data and MC is much better after the prescale weighing.

In addition to the QCD samples, 50 million events of single-Λ MC[4] are used. This single-particle sample contains Λ and $\bar{\Lambda}$ hyperons uniformly distributed in transverse momentum, p_{T}, and pseudo-rapidity, η, such that 0.5 GeV$< p_{\mathrm{T}} <$50 GeV and $-2.5 < \eta < 2.7$. It is used to create a Λ reconstruction efficiency map used for the MC decay angle re-sampling (described in the following sections).

4.5 Event Selection

Events passing the trigger selection described above are analyzed. It is also required that events contain at least one reconstructed collision vertex built from at least 3 inner detector tracks. If there are more than one collision vertex in the event, the one with the largest sum of p_{T}^2 of its tracks is used as the primary vertex (PV). For the di-jet analysis it is further required that the event contains at least two jets, where either a leading or a sub-leading jet contains a Λ hyperon. The di-jet and Λ reconstruction and selection is described in the following sections.

4.5.1 Λ Reconstruction and Selection

Long-lived 2-prong decay candidates (V^0's) are reconstructed using the standard ATLAS V^0 finding tool. It reconstructs decays $V^0 \to f^+f^-$, where $f^{\pm}$ are charged tracks, that are re-fitted with a common vertex constraint. The invariant mass of the V^0 candidate is calculated using the following hypotheses: $\Lambda \to p\pi^-$, $\bar{\Lambda} \to p^-\pi^+$, $K_S^0 \to \pi^+\pi^-$, and $\gamma \to e^+e^-$. For example, the $\Lambda \to p\pi^-$ hypothesis means that the proton mass is assigned to the positive and the pion mass to the negative re-fitted track when the V^0 invariant mass is calculated. Since ATLAS does not have a good particle identification capability, the invariant mass is the main criterion to distinguish between different V^0 decays. The 2010 data were reconstructed with the requirement on the track transverse momentum, $p^{\mathrm{trk}} >$ 50 MeV, while in the 2011 reconstruction this cut has been increased to $p^{\mathrm{trk}} >$ 400 MeV. As a consequence, the 2010 Λ reconstruction efficiency is better than the one in 2011.

[4]Generator job option: MC11.107156.singlepart_Lambda_pt0p5-50.py

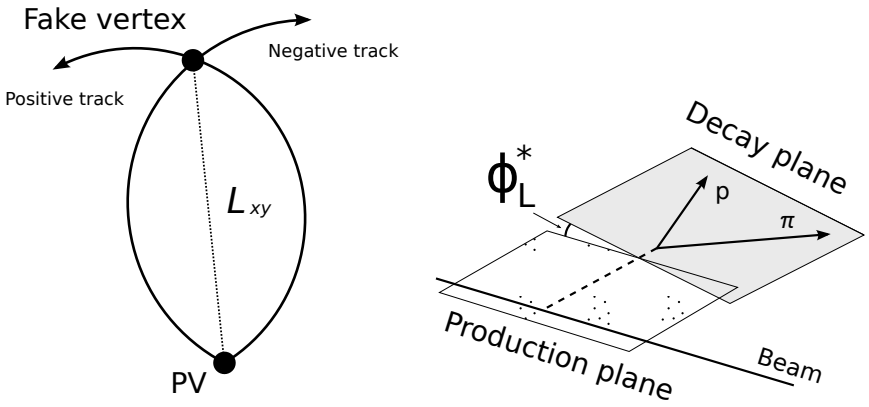

Figure 4.13: Two possible vertex solutions for intersecting helicalal trajectories with the same pseudo-rapidity (left). The definition of the angle between the Λ production and decay planes, ϕ^*_{L} (right).

The MC sample is used to determine values of the cuts employed to separate signal Λ from the background with a good purity. In the MC simulation, the signal candidates can be identified using the hit-based matching between the reconstructed tracks and the generator-level particles. Two types of the Λ background are conceived: combinatorial and physics background. The combinatorial background are random combinations of oppositely charged tracks, usually coming from the primary vertex, that mimic a Λ decay. The physics background consists of K^0_S decays or $\gamma \to e^+e^-$ conversions that are misidentified as Λ. The same selection criteria are used for Λ in minimum bias and di-jet events.

The candidates must pass the following criteria:

- Already at the V^0 reconstruction phase the candidates are pre-selected by requiring that the decay distance, $L_{xy} > 15$ mm. The decay distance is measured from the primary vertex. This cut is superseded by a tighter requirement on the decay distance significance (listed below), however, such a pre-selection is crucial for reducing immense number of combinatorial background candidates before they are stored in the output file. The effect of

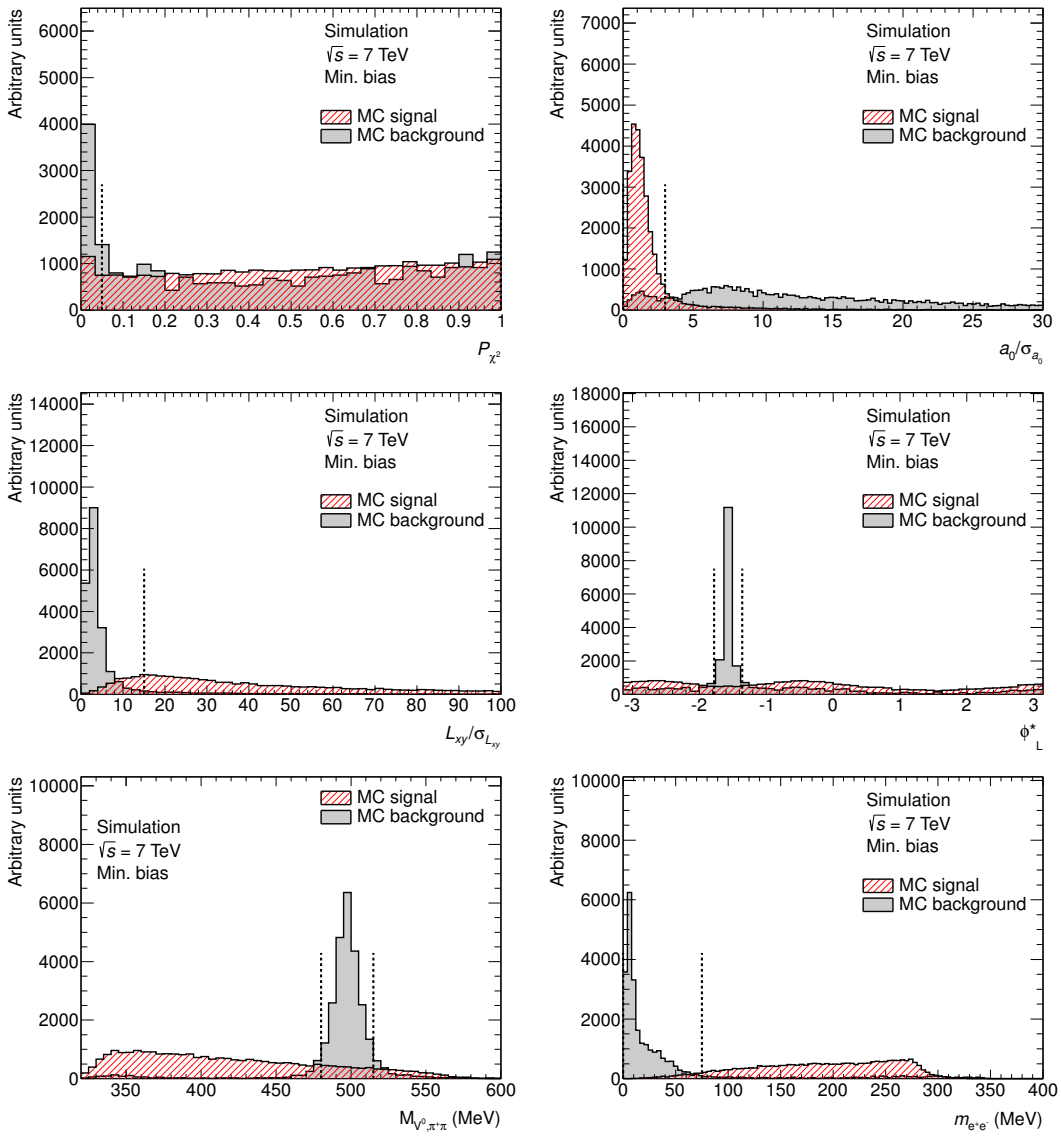

Figure 4.14: Distributions of selection variables for MC signal and background candidates in minimum bias sample. Plots are normalized to the same area. Plots show candidates after the final selection safe for the cut on the variable whose distribution is being displayed. The cumulative χ^2 probability of the vertex fit (top-left), Λ impact parameter significance (top-right), decay distance significance (middle-left), the angle between the Λ production and decay planes (bottom-right), are shown. Cuts are indicated by dashed lines.

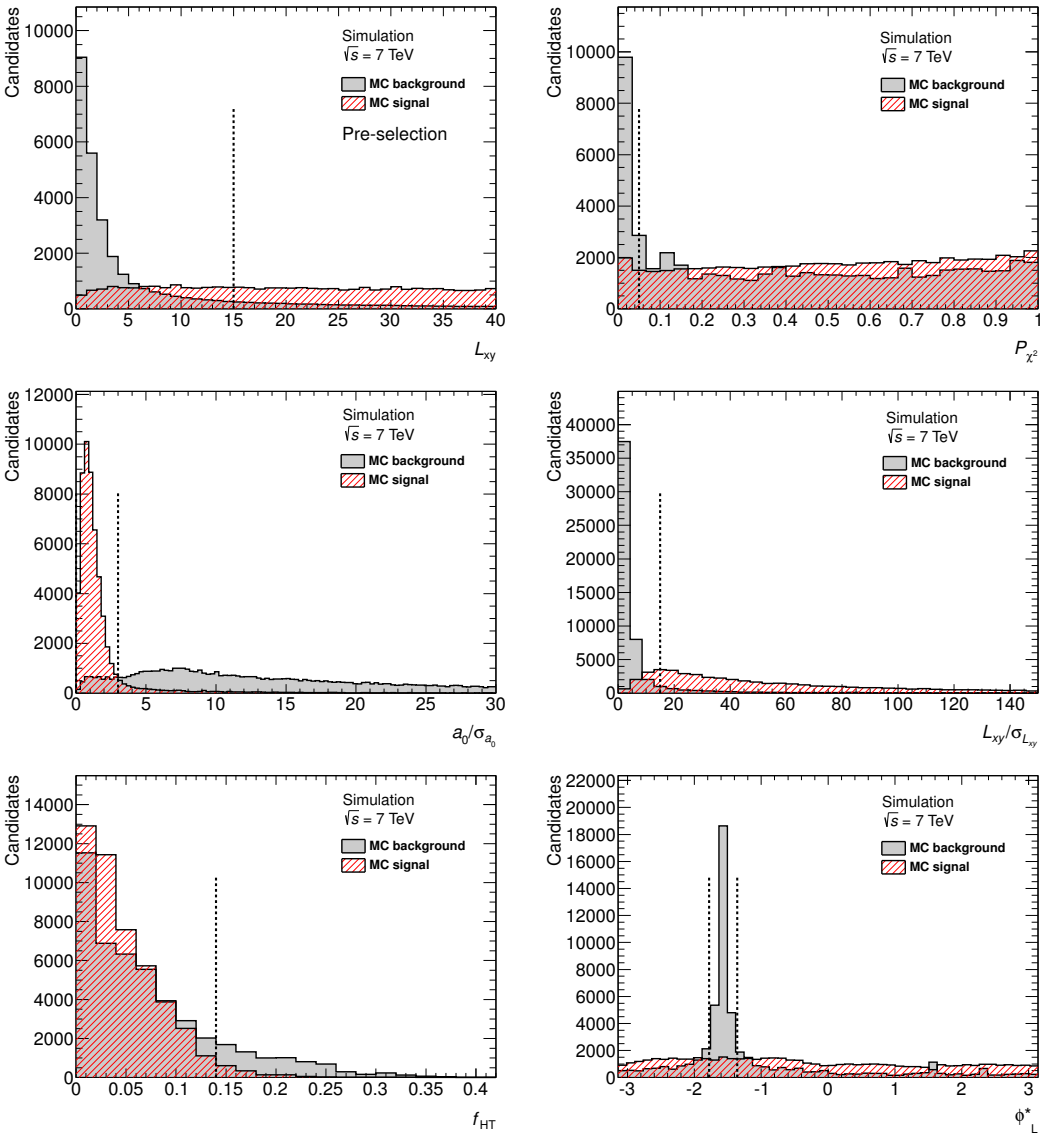

Figure 4.15: Distributions of selection variables for MC signal and background candidates. Plots are normalized to the same area. The top-left plot shows a distribution of decay distance L_{xy} for all the MC candidates before any selection. All the remaining plots show candidates after the final selection, safe for the cut on the variable whose distribution is being displayed. Cumulative χ^2 probability of the vertex fit (top-right), Λ impact parameter significance (middle-left), decay distance significance (middle-right), fraction of high-threshold TRT hits (bottom-left), and angle between the Λ production and decay planes (bottom-right) and distributions of the invariant mass under K^0_S mass hypothesis (bottom-left) and γ hypothesis (bottom-right) are shown. Cuts are indicated by dashed lines.

this cut is illustrated in Figure 4.15, top-left, where the distribution of MC signal and background is shown before any selection is applied.

- The invariant mass under the Λ or $\bar{\Lambda}$ hypothesis must lie in the mass range, 1100 MeV $< m_{p\pi} <$ 1132 MeV;

- The cumulative χ^2-probability of the V^0 vertex fit, $\mathcal{P}_{\chi^2} > 0.05$;

- Both tracks must have at least 3 silicon hits, i.e. hits in the Pixel or SCT detectors;

- The Λ impact parameter significance, $a_0/\sigma_{a_0} < 3$. The impact parameter is defined as a distance between the reconstructed Λ trajectory (i.e. straight line) and the primary vertex. The uncertainty of the impact parameter, σ_{a_0}, is calculated from the covariance matrices estimated by the primary vertex and the V^0 vertex fitters. This cut selects Λ's that originate in the primary vertex;

- The Λ transverse decay distance significance, $L_{xy}/\sigma_{L_{xy}} > 15$. The decay distance is measured from the primary vertex.

- The Transition Radiation Tracker (TRT) is used to suppress background from γ conversions by requiring that the fraction of the high-threshold TRT hits on both V^0 tracks, $f_{HT} < 0.14$. Since electrons with the same momentum produce more transition radiation than protons or pions, statistically, their tracks will have larger fraction of the high-threshold TRT hits;

- Physics background from K^0_S decays and γ conversions is removed mainly by applying a veto cut on the invariant mass under respective mass hypotheses, i.e. candidate is removed if 480 MeV$< m_{\pi\pi} <$ 515 MeV or if $m_{ee} <$ 50 MeV;

- Charged particles in the solenoidal magnetic field of the inner detector make helical trajectories. If two tracks have the same pseudo-rapidity they may, under right circumstances, intersect in two points (see Figure 4.13, left). This may cause an ambiguity in the vertex finding procedure, since the vertex fitter has no way of deciding which of the intersections is the real decay vertex. As a consequence, pairs of tracks originating in the primary vertex can be refitted to a fake vertex with a large decay distance and pass the selection cuts on L_{xy} and $L_{xy}/\sigma_{L_{xy}}$. These pathological cases are excluded

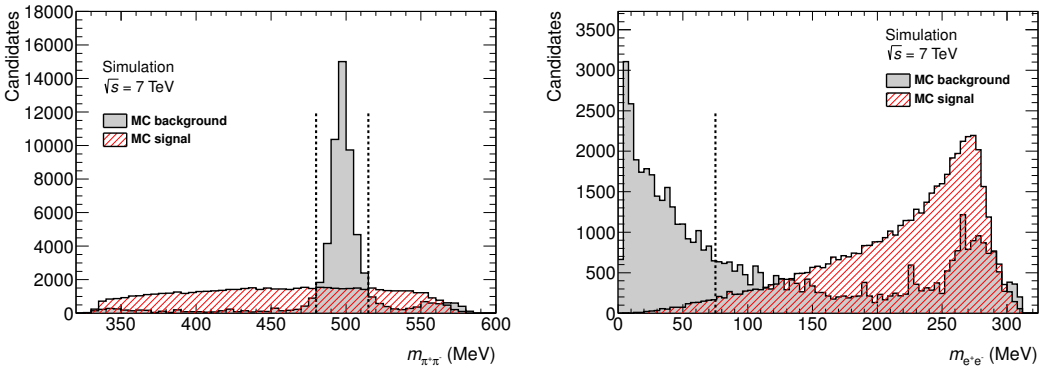

Figure 4.16: Distributions of the invariant mass under K^0_S mass hypothesis (left) and γ hypothesis (right) in the di-jet MC sample. Plots show candidates after the final selection, safe for the cut on the variable whose distribution is being displayed. Cuts are indicated by dashed lines.

using variable ϕ^*_{L}, which is defined as an angle between the Λ production and decay planes (see Figure 4.13, right). The problematic cases occur when ϕ^*_{L} is close to $-\pi/2$ for Λ candidates and $+\pi/2$ for $\bar{\Lambda}$ and they are rejected by requiring $|\phi_{\mathrm{L}} + \pi/2| > 0.21$ and $|\phi_{\mathrm{L}} - \pi/2| > 0.21$, respectively.

- For the di-jet analysis, a distance $\Delta R = \sqrt{\Delta\eta^2 + \Delta\phi^2}$ between the leading or sub-leading jet axis and Λ must be in range $0.06 < \Delta R < 0.5$. The lower limit ensures that the analyzing direction, $\hat{n}$, can be well defined and is chosen to be 3-times the resolution of ΔR, estimated from MC.

For the selection variables listed above, distributions of the MC signal and background candidates, together with the selection cuts, are shown in Figures 4.14 for the minimum bias sample and in Figures 4.15 and 4.16 for the di-jet sample. With these selection criteria 453986 Λ and 401400 $\bar{\Lambda}$ candidates have been selected in the minimum bias data.

Due to the detector acceptance the p_{T} range of the reconstructed Λ candidates is limited only to ∼200 GeV. This is caused mainly by the limited volume of the inner detector. The Λ candidate can only be reconstructed if it decays within a cylinder with $\sim$ 50 cm radius, where the silicon detectors are located. This means that candidates with higher momenta will have lower chance of being reconstructed, since their decay distance is larger due to their Lorentz boost. This is illustrated in Figure 4.17, left, where a probability of Λ decaying within the volume of the Inner Detector is shown. In addition, decay candidates with a large momentum will have small opening angle, $\psi_{p\pi}$, again due to their Lorentz boost.

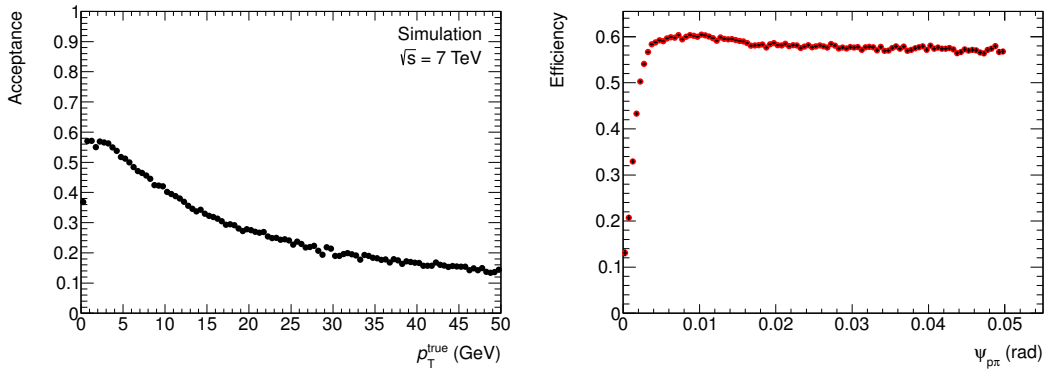

Figure 4.17: Probability of the Λ decaying withing the volume of the Inner Detector (left). Reconstruction efficiency as a function of the $\Lambda \to p\pi^-$ opening angle, $\psi_{p\pi}$ (right).

If the opening angle is too small, the detector is no longer capable to resolve the proton and pion tracks, which also leads to a drop of efficiency. This is illustrated in Figure 4.17, right, where the reconstruction efficiency for small opening angles is shown.

4.5.2 Jet Reconstruction and Selection

An anti-k_T jet reconstruction algorithm with the distance parameter of 0.4 and the local cluster weighting (LCW) calibration is used to reconstruct jets [62]. The jets are reconstructed from the topologically connected calorimeter cells that contain certain signal above noise (topo-clusters). Topo-clusters are reconstructed at the EM scale (with correctly measured energy from electromagnetic showers in calorimeter) and are then calibrated using the LCW method to account for the hadronic component of the shower. The LCW-calibrated jets have better resolution than jets reconstructed at EM scale. In the MC samples, true jets are reconstructed by running the same jet algorithm on non-decaying MC true particles.

In this analysis, events that contain at least two calorimeter jets where one of the two leading jets contains Λ or $\bar{\Lambda}$ hyperon are accepted. Both jets must satisfy ATLAS loose jet quality requirements [63]. Bad jets, i.e. the jets that satisfy the following criteria, are rejected:

- The jet is rejected if its energy fraction in the hadronic calorimeter end-cap (HEC), $f_{\mathrm{HEC}} > 0.5$, and the jet quality in HEC, $|q_{\mathrm{HEC}}| > 0.5$, and the normalized mean jet quality in liquid argon calorimeter (LAr), $\bar{q}_{\mathrm{LAr}} > 0.8$.

The jet quality variable, q, is calculated as a fraction of the jet energy corresponding to the calorimeter cells with a Q-factor larger than 4000, where the Q-factor measures difference between the measured and predicted pulse shape that is used to measure the cell energy – the smaller the Q factor, the better agreement between the measured and predicted pulse shape. The mean jet quality, $\bar{q}$, is calculated as the energy-squared mean cell quality. These criteria remove jets with spikes in HEC;

- The jet is rejected if negative energy in the jet, $|E_{\text{neg}}| > 60$ GeV;
- The jet is rejected if the energy fraction in electromagnetic (EM) calorimeter, $f_{\text{EM}} > 0.95$, and the jet quality in the LAr calorimeter, $|q_{\text{LAr}}| > 0.8$, and the normalized mean jet quality in the LAr calorimeter, $\bar{q}_{\text{LAr}} > 0.8$. These criteria remove the EM calorimeter coherent noise;
- The jet with pseudo-rapidity, $|\eta_{\text{j}}| < 2$, is rejected if the energy fraction in the EM calorimeter, $f_{\text{EM}} < 0.05$ and the jet charge fraction, $f_{\text{ch}} < 0.05$; or if the maximum energy fraction in one calorimeter layer, $f_{\text{max}} > 0.99$. The jet charge fraction is calculated as the ratio of the sum p_{T} of tracks associated to the jets divided by the calibrated jet p_{T}. These criteria remove non-collision and cosmic background.
- For the jet with pseudo-rapidity, $|\eta_{\text{j}}| \geq 2$, the non-collision and cosmic background is removed by requiring only that the energy fraction in electromagnetic calorimeter, $f_{\text{EM}} < 0.05$.

Furthermore, both jets have to satisfy the following additional requirements:

- The momentum of leading and sub-leading jets, $p_{\text{T,j}} > 20$ GeV. The jet momentum after the LCW calibration is used;
- Their pseudo-rapidity, $|\eta_{\text{j}}| < 2.8$;
- The transverse opening angle between the jets, $\phi_{\text{j}_1,\text{j}_2} > 2$. This is to select jets that are back-to-back in the transverse plane;
- More than 75% of tracks associated to the jets must come from the primary vertex, $f_{\text{PV}} > 0.75$. This cut reduces contribution of jets coming from the pile-up events;

With these selection criteria, together with the Λ selection described in the previous section, 90472 Λ and 84517 $\bar{\Lambda}$ candidates have been selected in the di-jet data.

4.6 Fit to the Invariant Mass

The invariant mass distribution in range 1100 MeV $< m <$ 1132 MeV is fitted with a 2-component mass PDF:

$$\mathcal{M}(m) = f_{\text{sig}}\mathcal{M}_{\text{sig}}(m) + (1 - f_{\text{sig}})\mathcal{M}_{\text{bkg}}(m), \tag{4.23}$$

where $\mathcal{M}_{\text{sig}}(m)$ and $\mathcal{M}_{\text{bkg}}(m)$ denote the signal and background components, respectively. The signal component is defined as a double asymmetric gaussian, i.e.:

$$\mathcal{M}_{\text{sig}}(m) = f_1\mathcal{G}(m - m_\Lambda, \sigma_1^{\text{L}}, \sigma_1^{\text{R}}) + (1 - f_1)\mathcal{G}(m - m_\Lambda, \sigma_2^{\text{L}}, \sigma_2^{\text{R}}), \tag{4.24}$$

where $\mathcal{G}(m - m_\Lambda, \sigma^{\text{L}}, \sigma^{\text{R}})$ is an asymmetric gaussian with mean, m_Λ, and left and right widths, σ^{L} and σ^{R}. f_1 is the relative contribution of the first gaussian. The asymmetric gaussian is used in order to model peak asymmetry caused by the p_{T} cuts imposed on proton and pion tracks by the reconstruction software ($p_{\text{T}}^{\text{trk}} > 50$ MeV for 2010 and $p_{\text{T}}^{\text{trk}} > 400$ MeV for 2011 data). Since Λ is a long-living particle, its natural width is negligible and the observed width of the mass peak is caused solely by the fluctuations of the reconstructed mass due to the finite detector resolution. Because of the tracking cut, fluctuations towards larger Λ mass are slightly more probable than fluctuations toward lower Λ mass, causing a small asymmetry in the mass peak.

The background component is modeled as a second-order polynomial PDF:

$$\mathcal{M}_{\text{bkg}}(m) = \frac{1}{\Delta m + \frac{b_2 \Delta m_3}{3}} \left[1 + b_1(m - m_c) + b_2(m - m_c)^2\right], \tag{4.25}$$

where $m_c = (m_{\max} + m_{\min})/2$, $\Delta m = m_{\max} - m_{\min}$, and $\Delta m_3 = (m_{\max} - m_c)^3 - (m_{\min} - m_c)^3$, with $m_{\max}$ and $m_{\min}$ being edges of the fitted mass range. The mass fit PDF has the following free parameters:

- The Λ mass, m_Λ;

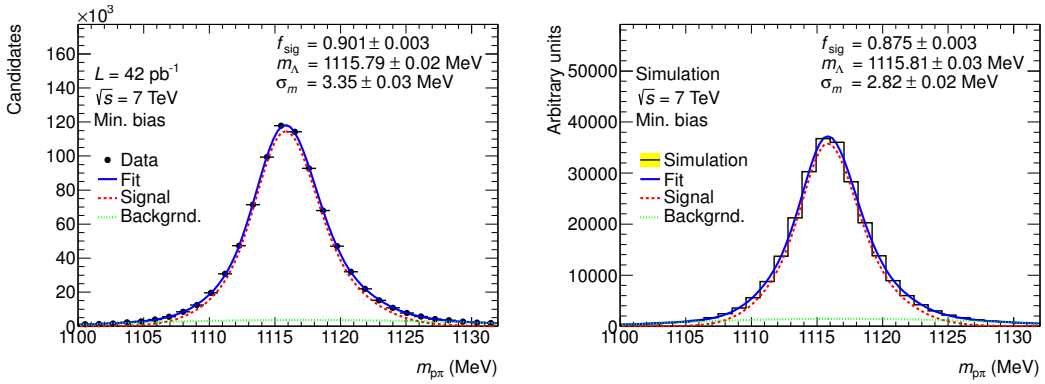

Figure 4.18: Result of the fit to the invariant mass distribution for minimum bias data (left) and MC (right). The fitted function and its components are drawn in blue, red, and green lines. The mass resolution, σ_m, is calculated from the fitted parameters.

- The signal fraction, f_{sig};
- The widths of the double asymmetric gaussian, $\sigma^{\text{L}}_{1,2}$ and $\sigma^{\text{R}}_{1,2}$;
- The relative contribution of the first gaussian, f_1;
- And the background coefficients, b_1 and b_2.

An invariant mass resolution can be calculated as a square-root of the variance of the signal PDF (4.24):

$$\sigma_m = \sqrt{\frac{1}{2}\left[f_1\left(\sigma_1^{\text{L}\,2} + \sigma_1^{\text{R}\,2}\right) + (1-f_1)\left(\sigma_2^{\text{L}\,2} + \sigma_2^{\text{R}\,2}\right)\right]}. \tag{4.26}$$

The results of the mass fit are shown in Figure 4.18 for minimum bias data and in Figure 4.19 for di-jet data. The most important results of the fit are summarized in Table 4.2. A small discrepancy between data and MC is observed in the fitted values of the Λ mass, m_Λ, and the mass resolution, σ_m. These values are used to estimate systematic uncertainty due to the track momentum scale and resolution, as is discussed in the following sections. A small discrepancy in the value of the signal fraction between data and MC has no bearing on the final polarization result since MC background is not used in this analysis.

Fit to the Λ invariant mass is used to determine the signal fraction in mass bins used for the calculation of the decay angle expectation value, as described in Section 4.2. The signal fraction in the mass bin of size 2Δ is calculated as a ratio

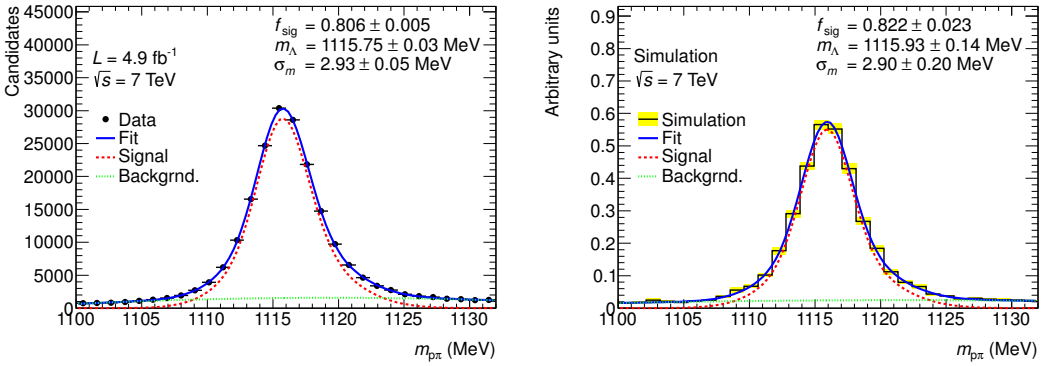

Figure 4.19: Result of the fit to the invariant mass distribution for di-jet data (left) and MC (right). The fitted function and its components are drawn in blue, red, and green lines. The mass resolution, σ_m, is calculated from the fitted parameters.

Table 4.2: Selected results of the Λ invariant mass fit. The Λ mass, m_Λ, the mass resolution, σ_m, and the signal fraction , f_{sig}, are listed. Displayed errors are statistical only.

Param.	**Min. bias**		**Di-jet**	
	Data	**MC**	**Data**	**MC**
f_{sig}	0.901 ± 0.003	0.875 ± 0.003	0.806 ± 0.005	0.822 ± 0.023
m_Λ (MeV)	1115.79 ± 0.02	1115.81 ± 0.03	1115.75 ± 0.03	1115.93 ± 0.14
σ_m (MeV)	3.35 ± 0.03	2.82 ± 0.02	2.93 ± 0.06	2.90 ± 0.20

of two integrals:

$$f_{\text{sig}}(m) = \frac{\int_{m-\Delta}^{m+\Delta} \mathrm{d}m' \; \mathcal{M}_{\text{sig}}(m')}{\int_{m-\Delta}^{m+\Delta} \mathrm{d}m' \; \mathcal{M}(m')}, \tag{4.27}$$

where m is the center of the mass bin. The function (4.27) is visualized in Figure 4.20 for the mass bin size of $2\Delta = 4.57$ MeV.

4.7 Monte Carlo Simulation

The method of moments, used to extract polarization (described in Section 4.2) relies on MC for correction of the efficiency and resolution effects. Therefore, it is important to have a good agreement between data and MC. Furthermore, ideally MC statistics should be larger than that of data so that the result is not

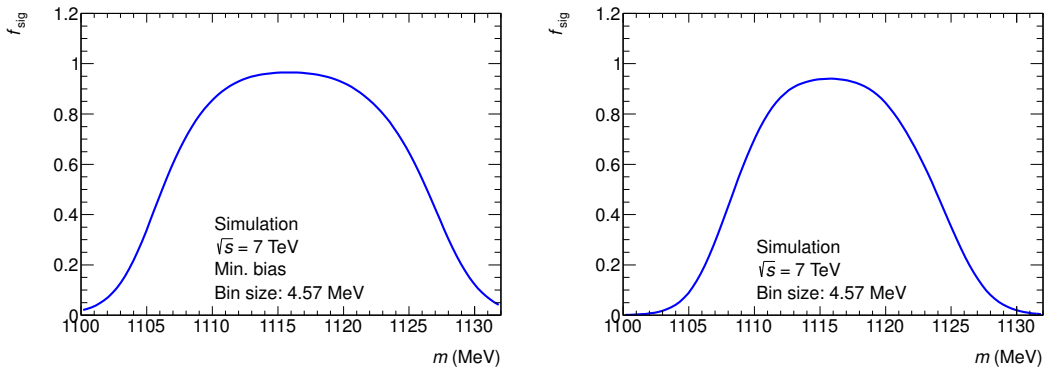

Figure 4.20: Signal fraction as a function of center of the mass bin, m. The left plot shows the signal fraction for minimum bias while the right plots shows the signal fraction for di-jet data.

dominated by the systematic uncertainty. While the agreement between data and MC is reasonable good and can be improved by an event weighting, the di-jet MC sample lacks the statistics needed to achieve desired precision of the measurement. Therefore, in this analysis Pythia and Herwig di-jet samples are combined to reduce an uncertainty stemming from the lack of MC statics. Furthermore, the di-jet MC events are re-sampled using the efficiency map (see Section 4.7.4) to reduce this uncertainty even further.

Although the Pythia minimum bias MC sample is smaller than one could hope for, it is large enough to perform the measurement with a reasonable precision of a few per-cent.

4.7.1 Kinematic and Pile-up Weighting

The aim of the MC weighting is to make distributions of kinematic variables agree between data and MC. For a single variable, an event weight function can be calculated as a ratio of the data and MC distributions, normalized to the same area. The obtained weight function, $w(x)$, can be used to correct the MC distribution of variable x by assigning weight of $w(x_i)$ to each event, where x_i is the value of x in i-th event. If more variables need to be weighted and if the weights are not correlated, the final weight function can be expressed as a product of single-variable weight functions (partial weights).

In this analysis the minimum bias MC sample is weighted using the following variables:

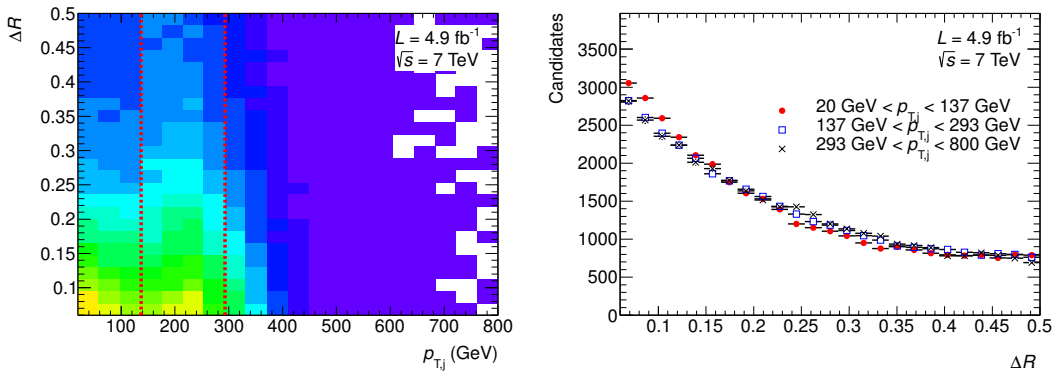

Figure 4.21: Distribution of the transverse momentum of the Λ-containing jet, $p_{\mathrm{T,j}}$, vs. the Λ-jet distance, ΔR, (left) and the ΔR distribution in slices of jet transverse momentum (right). The red dashed lines indicate the slices of jet p_{T}.

1. The Λ transverse momentum, p_{T}, to correct the Λ kinematics in MC;
2. The Λ rapidity, y, to correct the Λ kinematics in MC;
3. And the longitudinal position of the PV, z_{PV}, to adjust the beam-spot size (i.e. the region of intersecting beams where collisions can occur.)

The di-jet MC sample is weighted using the following variables:

1. The leading jet transverse momentum, $p_{\mathrm{T,j1}}$ to remove remaining discrepancies in the jet p_{T} spectra after the prescale weighting (see Figure 4.12, right);
2. The distance between Λ and jet direction, ΔR, which is not modeled well by the MC generators;
3. The number of collision vertices, N_{PV}, to adjust the correct amount of pile-up events in MC;
4. And the longitudinal position of the PV, z_{PV}.

The correlation between the partial weights is assumed to be small, which is verified in the analyzed data. Figure 4.21 shows the jet transverse momentum vs. distance ΔR distribution and the ΔR distribution in slices of jet p_{T}, illustrating that the correlation is indeed small. Furthermore, the kinematic (p_{T}, η, ΔR) and the PV (N_{PV}, z_{PV}) variables are uncorrelated by definition. Therefore, the final weight function can be expressed as a product of the partial weights,

$w(p_{\mathrm{T}}, \eta, z_{\mathrm{PV}}) = w(p_{\mathrm{T}})\, w(\eta)\, w(z_{\mathrm{PV}})$ for the minimum bias and $w(p_{\mathrm{T,j_1}}, \Delta R, N_{\mathrm{PV}}, z_{\mathrm{PV}}) = w(p_{\mathrm{T,j_1}})\, w(\Delta R)\, w(N_{\mathrm{PV}})\, w(z_{\mathrm{PV}})$ for the di-jet MC. The partial weight functions are obtained through an iterative procedure, which can be illustrated using the di-jet MC weighting as an example: in the first iteration weight $w(p_{\mathrm{T,j_1}})$ is obtained as a ratio of the data and MC jet p_{T} distributions. In the second iteration this weight is applied to the MC events and using this re-weighted sample the function $w(\Delta R)$ is calculated. In the third iteration the sample is weighted by a product $w(p_{\mathrm{T,j_1}})\, w(\Delta R)$ and the partial weight $w(N_{\mathrm{PV}})$ is obtained. In the fourth iteration, the partial weight $w(z_{\mathrm{PV}})$ is obtained from the sample weighted by the previously extracted weights, $w(p_{\mathrm{T,j_1}})\, w(\Delta R)\, w(N_{\mathrm{PV}})$. Then the whole procedure is repeated, always using the product of all the partial weights from the previous steps before a new partial weight is calculated. The whole procedure is terminated when the agreement between all the weighted distributions and data is achieved.

Distributions of weighted variables for minimum bias MC sample, p_{T} and y, are shown in Figures 4.22, top. Distributions of weighted variables for di-jet MC sample, $p_{\mathrm{T,j_1}}$, ΔR, and N_{PV}, are shown in Figure 4.23, top-left, top-right, and middle-left, respectively. Distributions of other variables in Figures 4.22–4.24 illustrate good agreement between MC and data after the MC weighting in both the minimum bias and di-jet samples. The minimum bias sample variables are shown in Figure 4.22, which in addition to the weighted variables displays distributions of the Λ transverse decay distance, L_{xy}, Feynman-x variable, x_{F}, and the number of silicon hits on proton and pion tracks, $N_{\mathrm{Si},p}$ and $N_{\mathrm{Si},\pi}$. The di-jet sample variables are shown in Figures 4.23–4.25, which contain distributions of the Λ transverse momentum, p_{T}, its rapidity, y, and decay distance, L_{xy} (Figure 4.23); distributions of proton impact parameter, $d_{0,p}$, the number of silicon hits on its track, $N_{\mathrm{Si},p}$, the same variables for the pion track, i.e. $d_{0,\pi}$ and $N_{\mathrm{Si},\pi}$, the Λ relative transverse momentum w.r.t. the jet axis, k_{T}, and the jet Λ momentum fraction, z (Figure 4.24). Finally, in Figure 4.25, the transverse momentum of the sub-leading jet, $p_{\mathrm{T,j_1}}$, the pseudo-rapidity of both leading and sub-leading jet, $\eta_{\mathrm{j_1}}$ and $\eta_{\mathrm{j_2}}$, and the difference in their transverse momenta, $\Delta p_{\mathrm{T,j_1j_2}}$, their pseudo-rapidity, $\Delta\eta_{\mathrm{j_1j_2}}$, and the azimuthal angle, $\Delta\phi_{\mathrm{j_1j_2}}$, are shown.

The χ^2 test probability, P_{χ^2}, is used to quantify the level of agreement between the data and MC distributions. The plots show a good agreement between data and MC, the lowest probability is observed for the Λ rapidity, y, and jets pseudo-rapidity, η_{j_1} and η_{j_2}, distributions. This is taken into account in the systematic

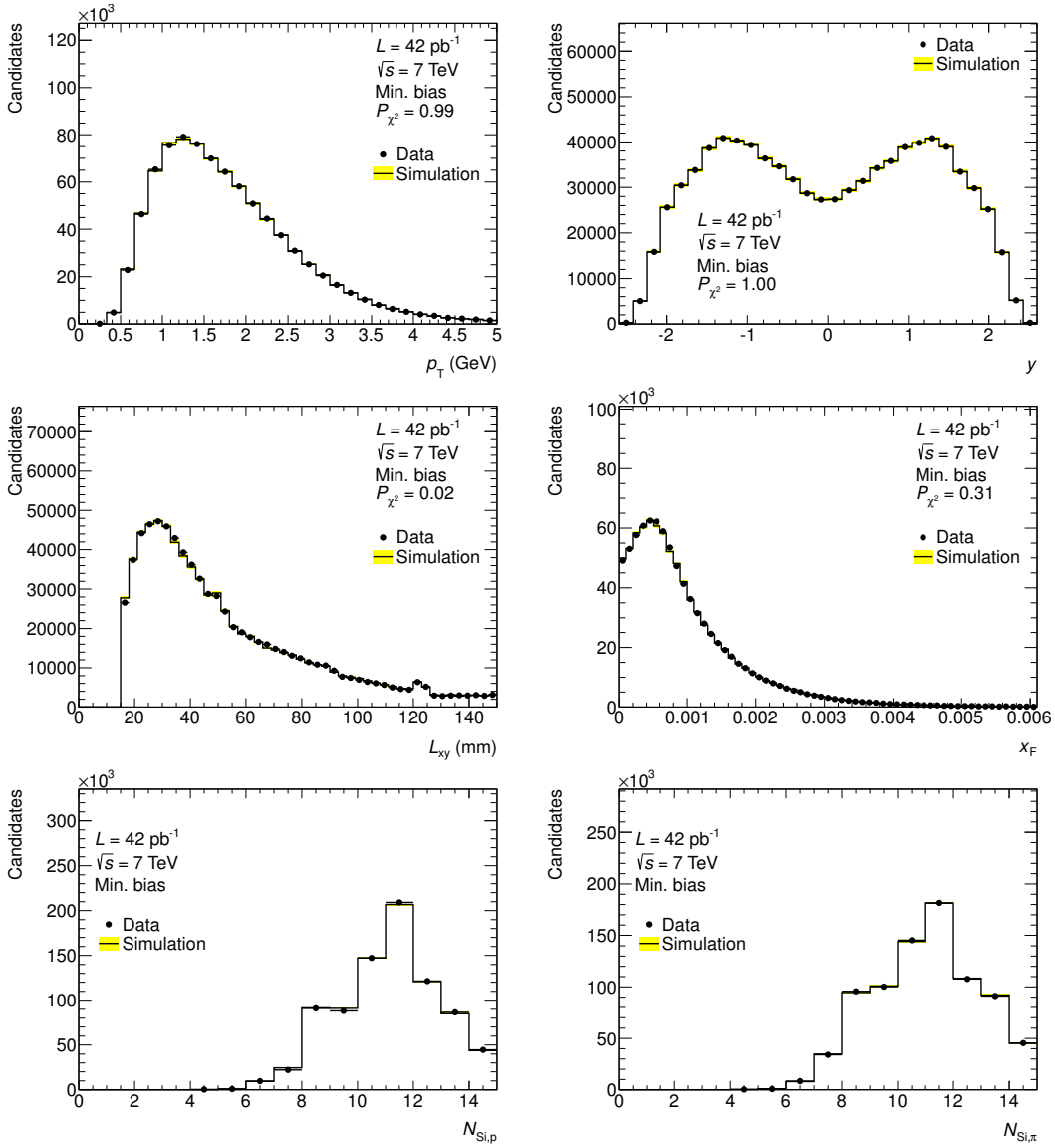

Figure 4.22: Minimum bias data and MC comparison after MC weighting. Distribution of the Λ transverse momentum, p_{T} (top-left), the Λ rapidity, y (top-right), the decay distance, L_{xy} (middle-left), the Feynman-x variable, x_{F} (middle-right), and the number of proton and pion track silicon hits, $N_{\mathrm{Si},p}$ (bottom-left) and $N_{\mathrm{Si},\pi}$ (bottom-right), respectively. Plots are normalized to the same area. The level of agreement between the MC and data distributions is quantified by the χ^2-test probability value, P_{χ^2}.

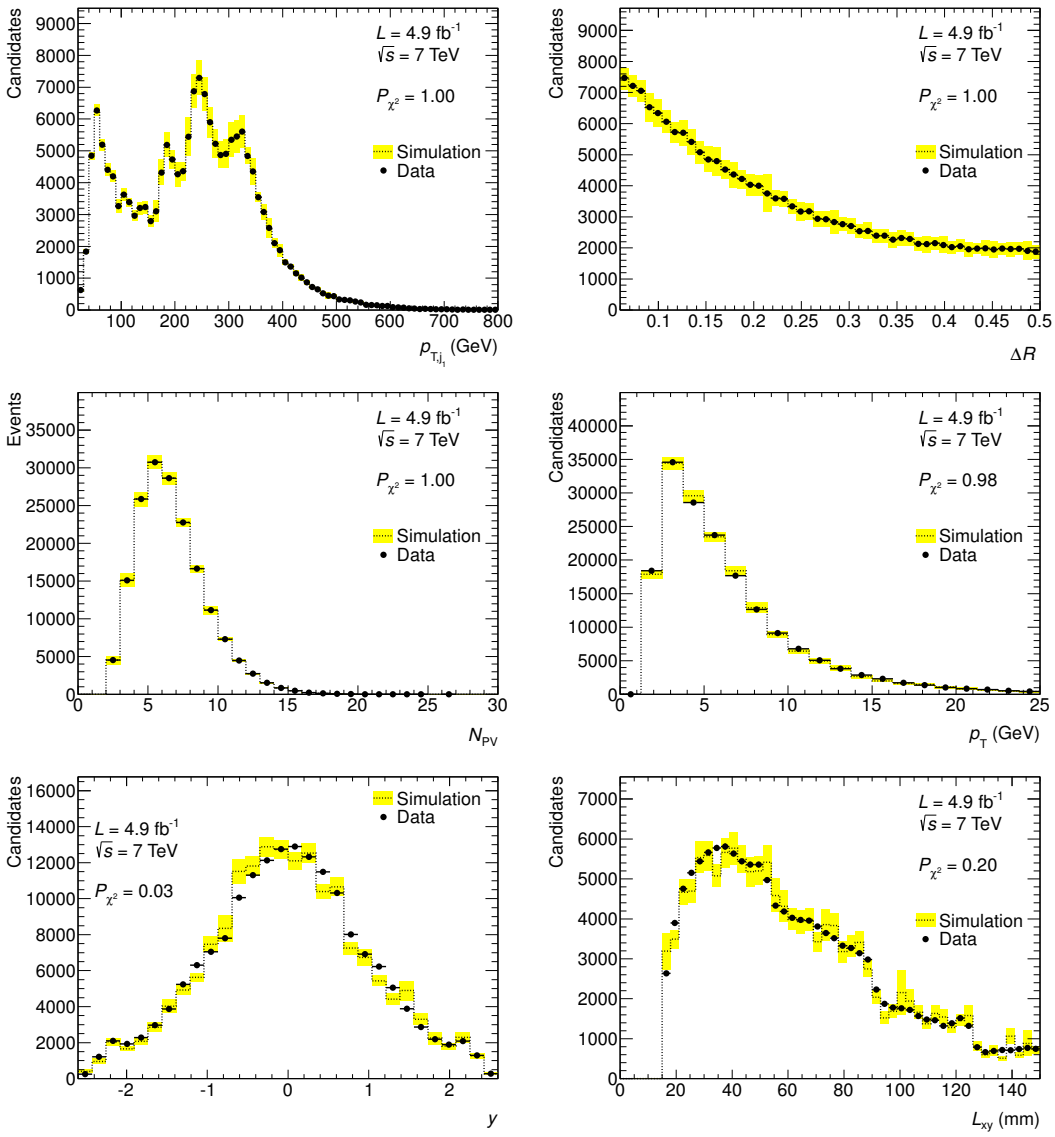

Figure 4.23: Di-jet data and MC comparison after MC weighting. Distributions of the leading jet transverse momentum, $p_{\mathrm{T,j1}}$ (top-left), the distance between the Λ and the jet axis, ΔR (top-right), the number of collision vertices, N_{PV} (middle-left), Λ transverse momentum, p_{T} (middle-right), its pseudo-rapidity, η (bottom-left), and the decay distance, L_{xy} (bottom-right), are shown. Plots are normalized to the same area. The level of agreement between the MC and data distributions is quantified by the χ^2-test probability value, P_{χ^2}.

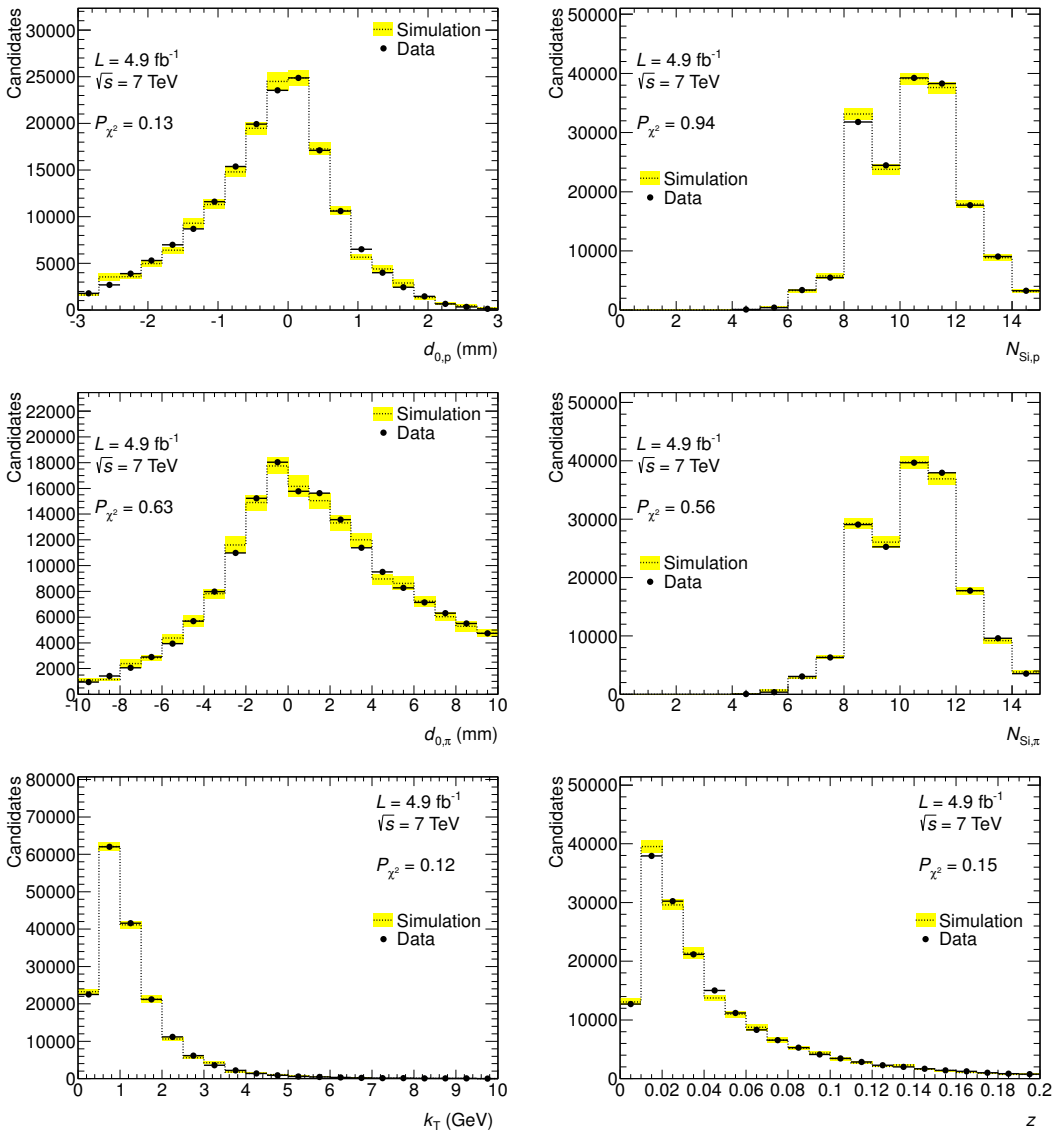

Figure 4.24: Di-jet data and MC comparison after MC weighting. Distributions of the proton impact parameter, $d_{0,p}$ (top-left), the number of silicon hits on its track, $N_{\mathrm{Si},p}$ (top-right), the same variables for the pion track, $d_{0,\pi}$ (middle-left) and $N_{\mathrm{Si},\pi}$ (middle-right), the relative transverse momentum of Λ w.r.t. the jet axis, k_{T} (bottom-left), and the jet momentum fraction, z (bottom-right), are shown. Plots are normalized to the same area. The level of agreement between the MC and data distributions is quantified by the χ^2-test probability value, P_{χ^2}.

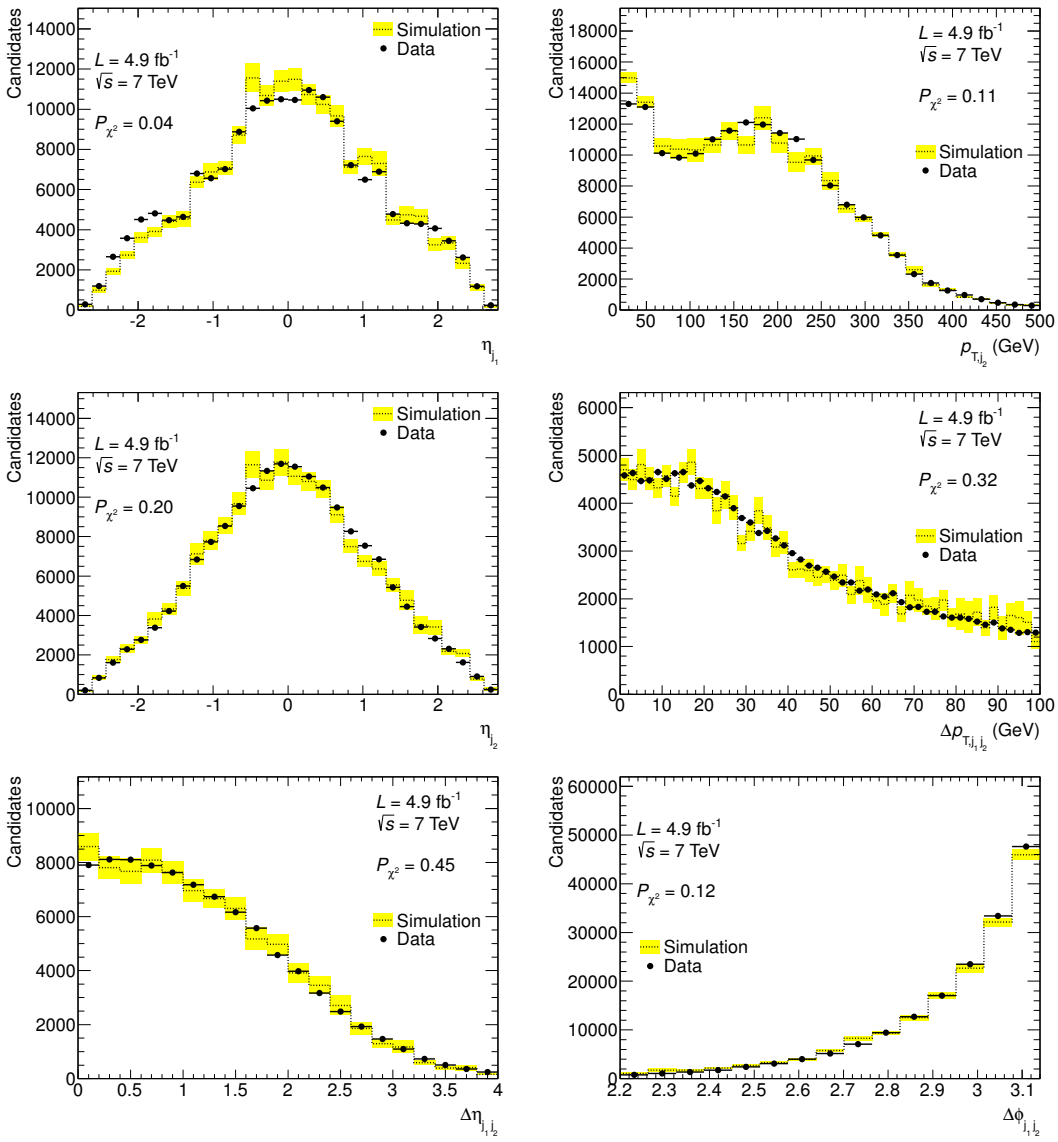

Figure 4.25: Data and MC comparison after MC weighting. Distributions of the transverse momentum of the sub-leading jet, $p_{\mathrm{T,j_1}}$ (top-left), the pseudo-rapidity of both leading jets, $\eta_{\mathrm{j_1}}$ (top-right) and $\eta_{\mathrm{j_2}}$ (middle-left), and the difference in the leading jets transverse momentum, $\Delta p_{\mathrm{T,j_1 j_2}}$ (middle-right), their pseudo-rapidity, $\Delta\eta_{\mathrm{j_1 j_2}}$ (bottom-left), and the azimuthal angle, $\Delta\phi_{\mathrm{j_1 j_2}}$ (bottom-right), are shown. Plots are normalized to the same area. The level of agreement between the MC and data distributions is quantified by the χ^2-test probability value, P_{χ^2}.

uncertainty estimation. Good agreement between data and MC means that MC models data well and it can be used to quantify the efficiency and resolution effects. Of particular importance are plots showing the number of silicon hits, N_{Si} on the on the proton and pion tracks (Figures 4.22 and 4.24), since they confirm that the tracking performance is modeled well. Also, distributions of the proton and pion track impact parameters, d_0, which have been found to be correlated to the decay angle $\cos\theta^*$, are well reproduced by MC (Figure 4.24, top-left and middle-left).

4.7.2 Pythia and Herwig Comparison

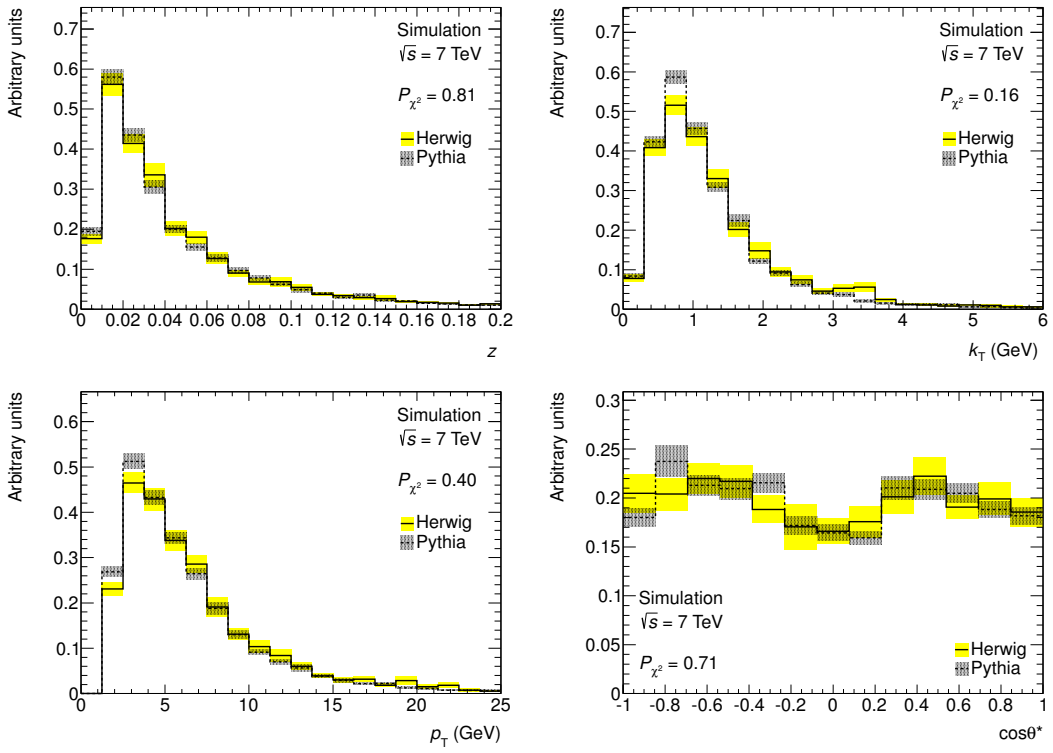

Figure 4.26: Comparison of kinematic distributions generated by Pythia and Herwig MC generators. Distributions of the Λ momentum fraction, z, (top left) the transverse momentum relative to the jet axis, k_{T}, (top right) the Λ transverse momentum, p_{T}, (bottom left) and the decay angle, $\cos\theta^*$, (bottom right) are shown. The modified χ^2-test is used to compare the distributions and the corresponding χ^2 probability is displayed in the plots.

Since both Pythia and Herwig generators are used to generate di-jet MC samples and the respective samples are combined into a single one it is important to make sure that both generators produce the same (or similar) kinematic distri-

butions after re-weighting. Although the Herwig sample has about a third of the statistics of the Pythia one, there is a good agreement between the two samples, allowing for the statistical fluctuations. A comparison of distributions of the jet Λ momentum fraction, z, the Λ transverse momentum relative to the jet axis, k_{T}, the Λ transverse momentum, p_{T}, and the decay angle, $\cos\theta^*$, are shown in Figure 4.26. The distributions after the kinematic weighting are shown. The figure shows a good agreement between the distributions within the statistical precision.

4.7.3 Polarization Weighting

The Pythia (Herwig) generator and Geant 4 simulation do not model spin effects. This means that unstable particles, such as Λ, are decayed with a uniform angular distribution. To build the polarized MC sample a method of event weighting has to be used again. Since the original sample is unpolarized, the event weight is simply

$$w_P(\cos\theta_i^{*\mathrm{true}}) = 1 + \alpha P \cos\theta_i^{*\mathrm{true}}, \tag{4.28}$$

where $\cos\theta_i^{*\mathrm{true}}$ stands for the true decay angle in the i-th event. True quantities, i.e. true Λ momentum and true jet momenta, must be used since the distribution of the reconstructed angle, $\cos\theta^*$, is distorted by the detector resolution effects and no longer follows the theoretical distribution (4.1), from which the weight is derived. Using the true quantities ensures that the extracted polarization is already corrected to the true particle level. Figure 4.27 shows that the polarization weighting does not affect distributions of other weighted variables, $p_{\mathrm{T,j_1}}$ and ΔR.

4.7.4 Re-sampling

If the di-jet MC sample was used directly to calculate $\cos\theta^*$ expectation values, E_0^{MC} and E_1^{MC} (which are used to correct for the efficiency and resolution effects) the precision of the di-jet polarization measurement would be quite poor due to the limited MC statistics. Therefore, a detailed Λ reconstruction efficiency and resolution map is used to increase the number of signal MC events and thus improving the measurement's precision. The idea behind the MC re-sampling is that since the Λ and jet reconstruction algorithms are independent of each other, knowing the Λ reconstruction efficiency and resolution functions is sufficient to model the shape of the $\cos\theta^*$ distribution. The advantage of this approach is that

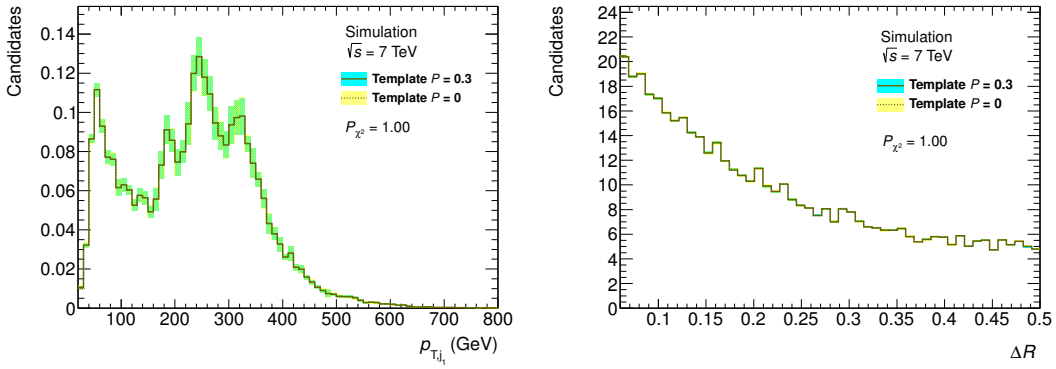

Figure 4.27: Effect of the polarization weighting on the other weighted variables. Distributions of leading jet transverse momentum (left) and the distance between Λ and the jet axis (right) before and after the polarization weighting is shown. The overlaid distributions agree with the probability, $P_{\chi^2} = 1$.

while production of the di-jet sample is computationally heavy, production of a single Λ sample is fast and a large-statistics sample can be created in a couple of days.

The MC sample of 50 M events of Λ and $\bar{\Lambda}$ particles is used to create the efficiency and resolution map. The MC particles are produced uniformly in p_{T}, covering the whole volume of the detector, and are reconstructed using the standard ATLAS reconstruction software. Using this sample, the reconstruction efficiency is calculated in 30×30 bins of true longitudinal decay angles, $\cos\theta_{\mathrm{L}}^{*\mathrm{true}}$ and $\phi_{\mathrm{L}}^{*\mathrm{true}}$, defined as an angle between the decay proton and Λ direction in the Λ rest-frame and an angle between the production and decay planes (see Figure 4.13, right), respectively. These maps are created in 1 GeV-slices of Λ p_{T}, separately in the barrel and end-cap regions of the detector, i.e. for $|\eta| < 1.1$ and $|\eta| > 1.1$, respectively. Figure 4.28 shows an example of two maps for two p_{T} ranges, 4.5 GeV $< p_{\mathrm{T}} <$ 5.5 GeV and 13.5 GeV $< p_{\mathrm{T}} <$ 14.5 GeV, the first one in the end-cap, the one second in the barrel part of the detector.

Resolution maps are created in the same slices of Λ p_{T} and η. These maps are two-dimensional distributions of $\theta_{\mathrm{L}}^{*\mathrm{true}}$ vs $\theta_{\mathrm{L}}^{*\mathrm{true}} - \theta_{\mathrm{L}}^{*}$ and $\phi_{\mathrm{L}}^{*\mathrm{true}}$ vs $\phi_{\mathrm{L}}^{*\mathrm{true}} - \phi_{\mathrm{L}}^{*}$, where θ_{L}^{*} and ϕ_{L}^{*} stand for the reconstructed values of the decay angles. An example is shown in Figure 4.29. These distributions serve to model θ_{L}^{*} and ϕ_{L}^{*} resolution given the true values of these decay angles.

The procedure of the MC re-sampling can be summarized in the following steps:

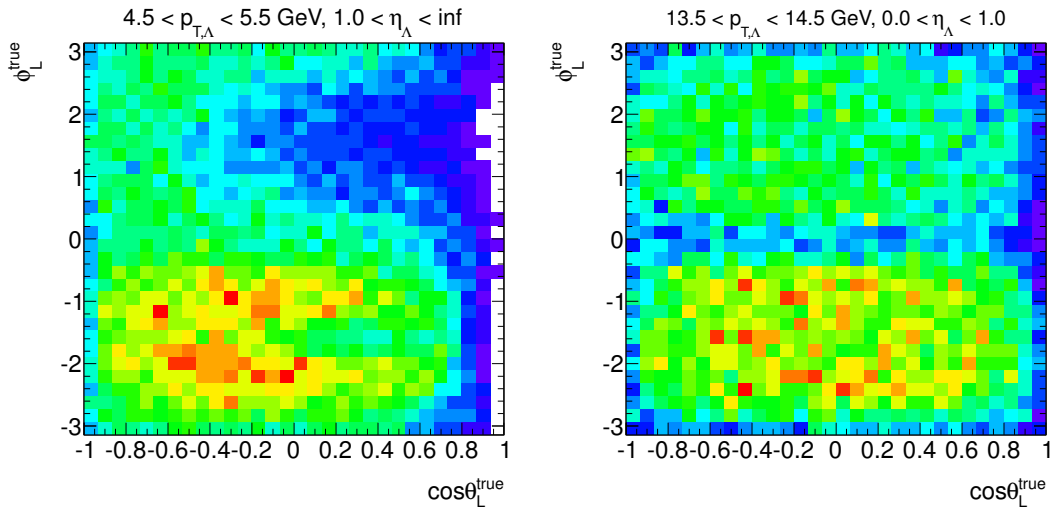

Figure 4.28: Example of the Λ efficiency maps for two ranges of Λ p_{T}, in end-cap (left) and barrel (right) part of the detector.

- Candidates from the di-jet MC sample are used as seeds for the re-sampling. For each signal candidate the values of true and reconstructed 4-momenta are known.

- Taking the seed's true 4-momentum the corresponding efficiency and resolution map is looked up. For example, if the true Λ carried transverse momentum of 4.7 GeV and pointed to the end-cap region of the detector, the map shown on Figure 4.28, left, would be used.

- True longitudinal decay angles, $\cos\theta_{\mathrm{L}}^{*\mathrm{true}}$ and $\phi_{\mathrm{L}}^{*\mathrm{true}}$, are randomly generated using the chosen efficiency map as the generator's PDF. This will ensure that the generated decay angle distribution will correspond to the unpolarized Λ's after the reconstruction. For each seed about 200 new candidates is thus generated.

- Reconstructed longitudinal decay angles, θ_{L}^{*} and ϕ_{L}^{*}, are then obtained by smearing the true values by amount extracted from the corresponding resolution map.

- These new candidates are used to calculated the MC decay angle moments, E_0^{MC} and E_1^{MC}.

Since the same reconstruction software is used for both the single-particle and di-jet MC samples, the reconstruction performance should be the same in both

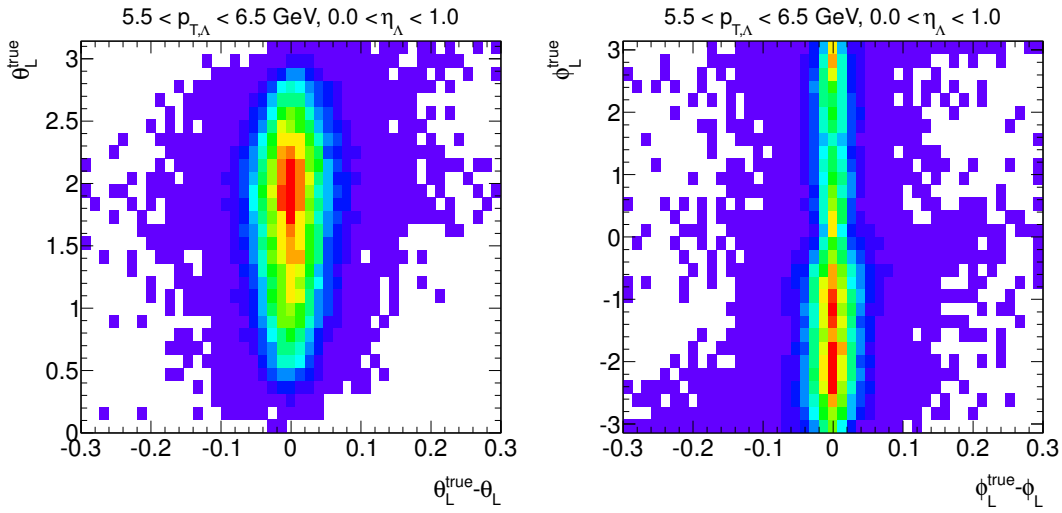

Figure 4.29: Example of the Λ resolution map for θ^*_{L} (left) and ϕ^*_{L} (right) decay angles.

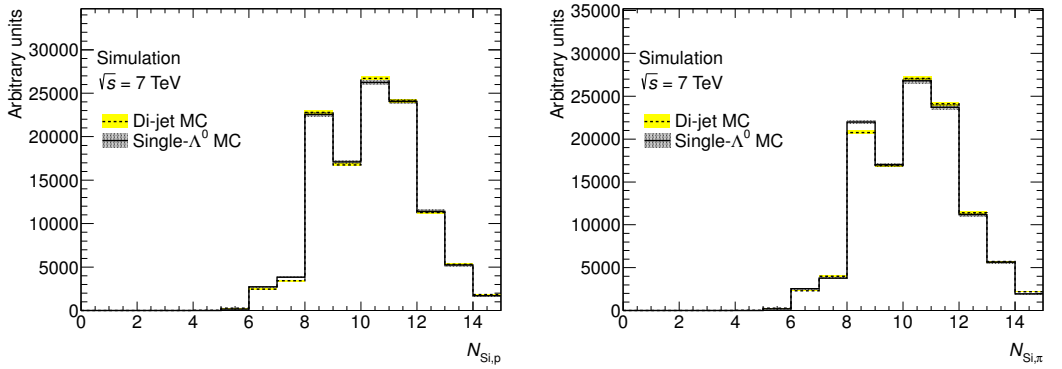

Figure 4.30: Comparison of distributions of the number of silicon hits for proton (left) and pion (right) candidates in the single-Λ and di-jet samples.

cases. However, some difference could stem from different track occupancy in the two samples: while there are virtually no tracks in the single-particle samples, in the di-jet sample the Λ is reconstructed among a host of jet particles. However, if there was a significant difference in the tracking performance in these two cases, one would expect to see a large difference in the number of hits on proton and pion tracks. Such a comparison is shown in Figure 4.30, where distributions of the number of silicon hits for proton and pion candidates are shown. The plots show a good agreement between the single-Λ and di-jet MC distributions. Figure 4.31 shows a resolution of the proton and pion p_{T}, σ_{rel}, as a function of true p_{T}, determined using the full di-jet and the single-particle MC samples. The σ_{rel}

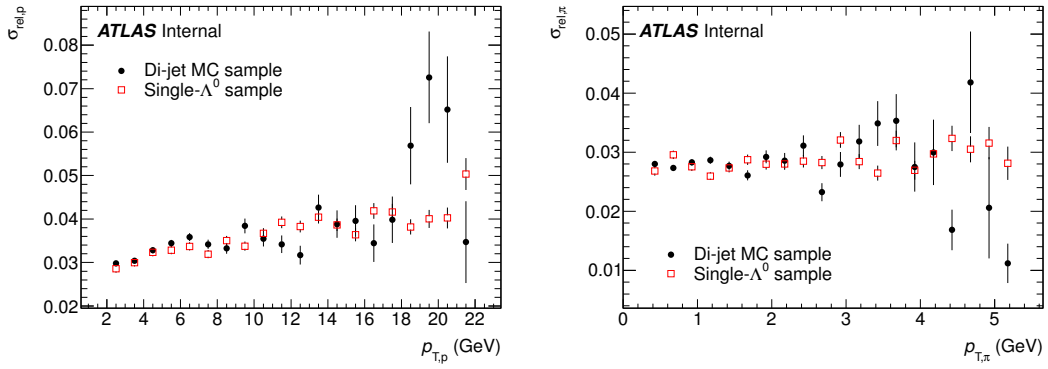

Figure 4.31: Track p_{T} reconstruction resolution as a function of true transverse momentum, $p_{\mathrm{T}}^{\mathrm{true}}$, determined using the full di-jet and single-particle MC samples for proton (left) and pion (right) tracks.

is calculated as a root mean square of the distribution of normalized p_{T} residuals,

$$r = \frac{p_{\mathrm{T}}^{\mathrm{true}} - p_{\mathrm{T}}}{p_{\mathrm{T}}^{\mathrm{true}}}.$$

The plots do not show any large difference in the p_{T}-dependence of the track momentum resolution between the two samples.

Using the procedure described above one can generate virtually any number of candidates, however, the method have some limitations. Firstly, precision of the MC moments $E_{0,1}^{\mathrm{MC}}$ is determined by the precision of the efficiency and resolution map, therefore, even with the infinite number of candidates, one would not get a perfect value. The re-sampling factor of 200 was determined as a number at which estimated precision is no longer improving. Secondly, the procedure re-samples only the decay angles while keeping the original Λ and di-jet kinematics. Therefore, the final result precision is still affected by the limited statistics of the original di-jet sample, however, it was observed that this effect is much smaller than uncertainty due to the statistical fluctuations of the decay angle.

The re-sampling method is validated using the unweighted di-jet MC sample. If none of the event weights are applied (i.e. no prescale weighting, no kinematic and pileup weighting, and no polarization weighting) the di-jet MC samples contain together 33276 events. The unweighted MC is used since it provides largest possible statistics, however, this MC sample does not agree with real data and is used only to validate the re-sampling method. Using this sample as a seed, $\cos\theta^*$ is re-sampled and the distribution is compared to the original one in Figure 4.32.

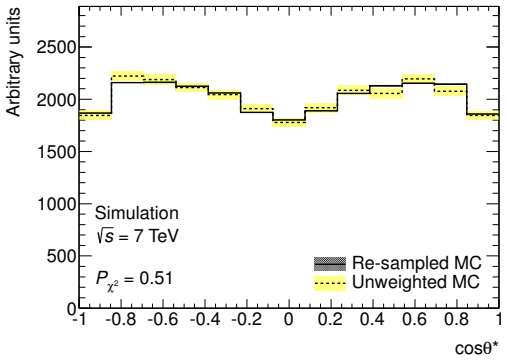

Figure 4.32: Comparison of the $\cos\theta^*$ distribution created from the unweighted di-jet MC sample and the re-sampled $\cos\theta^*$ distribution.

The χ^2-test applied to the overlaid histograms yields probability of 0.51, which corresponds to a good agreement.

4.7.5 Symmetry Between Λ and $\bar{\Lambda}$

Despite the similarity of the Λ and $\bar{\Lambda}$ decays, there are differences between Λ and $\bar{\Lambda}$ reconstruction performance. The most important difference is caused by an orientation of the inner detector magnetic field, which causes trajectories of charged particles to bend and thus enabling measurement of their transverse momenta. Tracks of the final state particles, $p\pi^-$ and $\bar{p}\pi^+$, bend in opposite directions which causes difference in the reconstruction performance of Λ and $\bar{\Lambda}$. There is, however, a symmetry between Λ and $\bar{\Lambda}$ decay topologies given by the orientation of the z-axis of the coordinate system, since the magnetic field is axially symmetric. This means that Λ kinematic variables calculated in the coordinate system with the z-axis aligned with the orientation of the magnetic field will correspond to the $\bar{\Lambda}$ kinematic variables calculated in the coordinate system with the z-axis anti-aligned with the orientation of the magnetic field. In practice, change of the z-axis orientation will change signs of decay angles, $\cos\theta^*$ and ϕ^*_{L}. This symmetry can be exploited to increase the size of the MC sample: Λ and $\bar{\Lambda}$ MC samples can be combined if the orientation of the z-axis is flipped for $\bar{\Lambda}$ particles, when the decay angles are calculated.

This symmetry would be perfect if the detector was perfectly axially symmetric. However, this is not the case since the pixel and SCT modules in the inner detector are tilted wrt. the radial direction (Figure 4.33). This means that an angle of

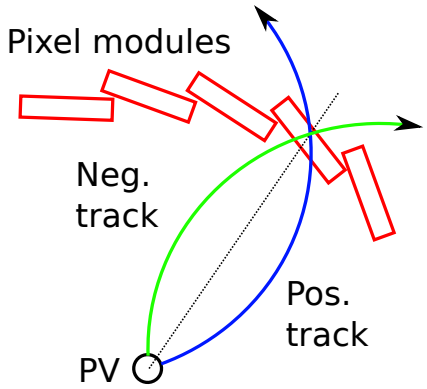

Figure 4.33: Tilt of the pixel and SCT modules in the inner detector.

impact for positive tracks is different than an angle of impact for negative ones. This means that positive and negative tracks can have a different pixel or strip cluster size and therefore a different hit reconstruction efficiency. This effect is mostly important for low p_{T} tracks that have large curvature. Finally, there is a difference in cross section for a proton and anti-proton interaction with detector material. However, this difference will be very small for protons with typical momentum of few GeV that are used in this analysis.

Despite these differences, the Λ and Λ MC samples can still be combined if the differences between the particle and anti-particle reconstruction performance do not affect the decay angle distribution. Figure 4.34 show a comparison of the decay angle distribution for low-p_{T} and high-p_{T} Λ and $\bar{\Lambda}$ candidates. The plots show a good agreement between the Λ and $\bar{\Lambda}$ distribution. The difference in the expectation values of these distributions, which are used as parameters in the polarization extraction fit, are smaller than the estimated statistical precision. The use of the combined Λ and $\bar{\Lambda}$ MC sample is hence justified.

4.8 Background

The decay angle expectation value for background is interpolated into the signal region assuming its linear dependence on mass (cf. Eqn. 4.21). To test this assumption, the expectation value for background events in the MC samples are plotted in Figure 4.35 for the minimum bias MC (left) and the di-jet MC (right).

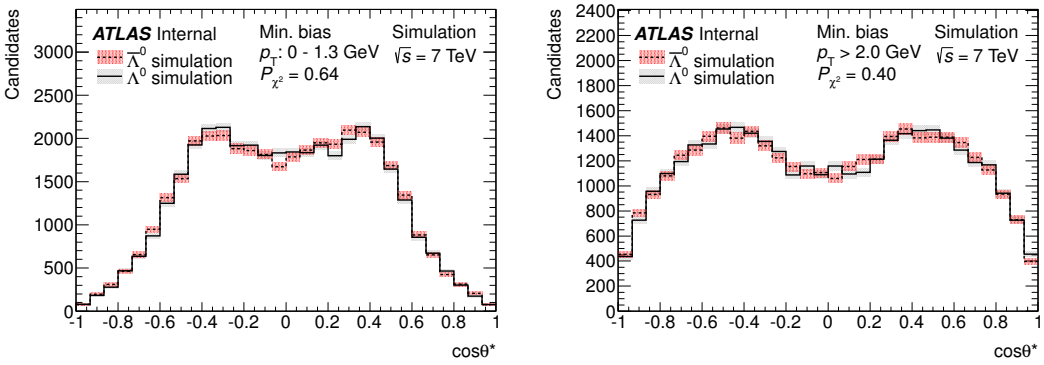

Figure 4.34: Comparison of the Λ and $\bar{\Lambda}$ decay angle distributions in the MC sample, for low-p_{T} (left) and high-p_{T} (right) candidates.

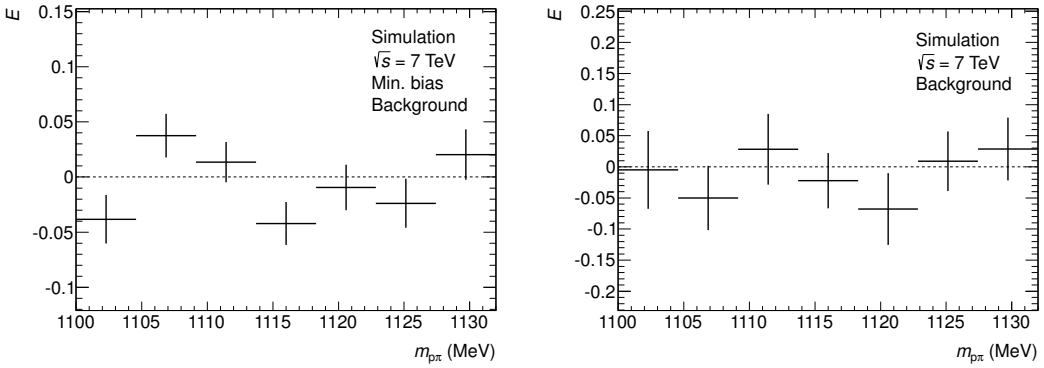

Figure 4.35: Decay angle expectation value as a function of mass for the minimum bias MC background (left) and the di-jet MC background (right).

The plots illustrate that the assumption of the linear dependence is justified. Furthermore, the background component in the central mass bin (where the sensitivity to the value of the polarization is greatest) is quite small (as seen in Figure 4.20) making the expectation value fit quite insensitive to the choice of the background parametrization.

4.9 Polarization Extraction

4.9.1 Decay Angle Expectation Value Fit

The decay angle expectation values for MC samples with known polarization, E_0^{MC} and E_1^{MC}, are calculated. These values are used in the fit function (4.21) where they serve as a correction for detector efficiency and resolution effects. The values

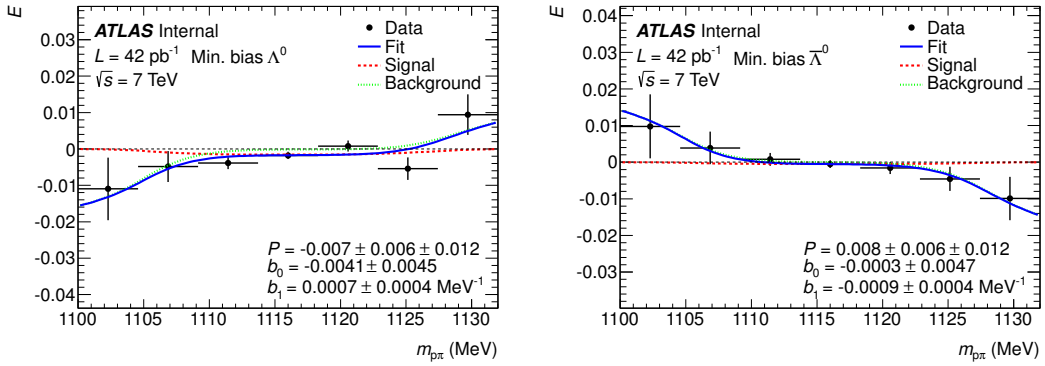

Figure 4.36: The decay angle expectation value fit for the Λ (left) and $\bar{\Lambda}$(right) minimum bias data. The data points are fitted with the function (4.21).

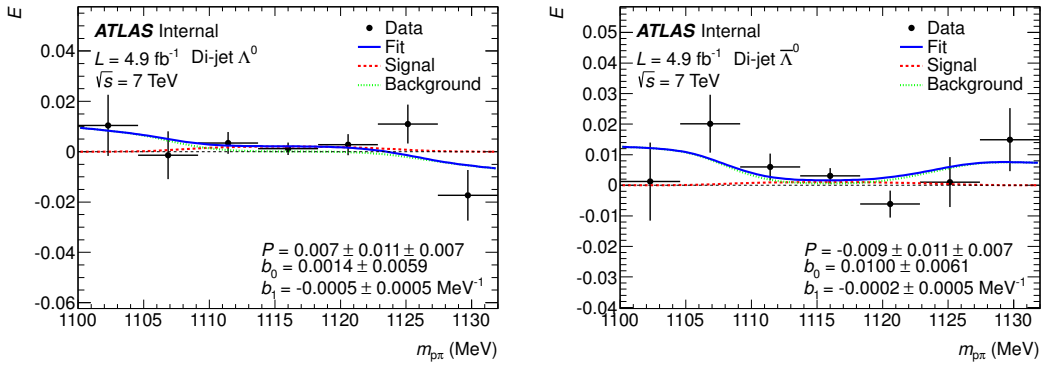

Figure 4.37: The decay angle expectation value fit for the Λ (left) and $\bar{\Lambda}$(right) di-jet data. The data points are fitted with the function (4.21).

E_0^{MC} and $_1^{\mathrm{MC}}$ are calculated for the whole Λ and $\bar{\Lambda}$ sample and separately in bins of the Λ transverse momentum, p_{T}, and Feynman-x variable, x_{F}, for the minimum bias MC; and in bins of the transverse momentum w.r.t. the jet axis, k_{T}, and the jet Λ momentum fraction, z, in case of the di-jet MC sample. The value of the MC expectation values as well as the definition of the bin ranges are shown in Table 4.3 for the minimum bias and in Table 4.4 for di-jet MC samples.

In data, the decay angle expectation value is calculated in 7 bins of Λ invariant mass. The plot is then fitted with the function (4.21) and the value of polarization is extracted. The expectation value plots together with the fitted function are shown in Figure 4.36 for the minimum bias and Figure 4.37 for the di-jet data. To gauge the quality of the fit, the MC samples are weighted using the extracted polarization values and the decay angle distributions are compared to data, as shown in Figures 4.38 and 4.39. Only events in the signal mass range,

Table 4.3: The decay angle expectation values in the minimum bias MC sample. E_0^{MC} and E_1^{MC} are the expectation values calculated using the MC sample weighted to polarization, $P = 0$ and $P = 1$, respectively. The expectation values for the whole sample and for samples binned in p_{T} and x_{F} are listed. The listed uncertainties are statistical only.

Sample	**Exp. values for Λ**		**Exp. values for $\bar{\Lambda}$**	
	$\boldsymbol{E_0^{\mathrm{MC}}}$	$\boldsymbol{E_1^{\mathrm{MC}}}$	$\boldsymbol{E_0^{\mathrm{MC}}}$	$\boldsymbol{E_1^{\mathrm{MC}}}$
Whole sample	-0.001 ± 0.001	0.143 ± 0.001	0.001 ± 0.001	-0.143 ± 0.001
$\boldsymbol{p_{\mathrm{T}}}$ **bins (GeV)**	$\boldsymbol{E_0^{\mathrm{MC}}}$	$\boldsymbol{E_1^{\mathrm{MC}}}$	$\boldsymbol{E_0^{\mathrm{MC}}}$	$\boldsymbol{E_1^{\mathrm{MC}}}$
$p_{\mathrm{T}} < 1.3$	0.002 ± 0.002	0.111 ± 0.002	-0.002 ± 0.002	-0.111 ± 0.002
$1.3 < p_{\mathrm{T}} < 2.03$	-0.004 ± 0.002	0.138 ± 0.002	0.004 ± 0.002	-0.138 ± 0.002
$2.03 < p_{\mathrm{T}}$	-0.000 ± 0.002	0.181 ± 0.002	0.000 ± 0.002	-0.181 ± 0.002
$\boldsymbol{x_{\mathrm{F}}}$ **bins ($\boldsymbol{10^{-4}}$)**	$\boldsymbol{E_0^{\mathrm{MC}}}$	$\boldsymbol{E_1^{\mathrm{MC}}}$	$\boldsymbol{E_0^{\mathrm{MC}}}$	$\boldsymbol{E_1^{\mathrm{MC}}}$
$x_{\mathrm{F}} < 5$	-0.001 ± 0.002	0.135 ± 0.002	0.001 ± 0.002	-0.135 ± 0.002
$5 < x_{\mathrm{F}} < 10.5$	0.000 ± 0.002	0.144 ± 0.002	-0.000 ± 0.002	-0.144 ± 0.002
$10.5 < x_{\mathrm{F}}$	-0.001 ± 0.002	0.152 ± 0.002	0.001 ± 0.002	-0.152 ± 0.002

$1109.7 < m_{p\pi} < 1121.7$ MeV, are used to make the decay angle plots. A background contribution for the MC plots is interpolated from the data invariant mass sidebands, $m_{p\pi} < 1105.7$ MeV and $m_{p\pi} > 1125.7$ MeV. A modified Pearson's χ^2-test (see Appendix 5) is used to compare data and MC histograms, a goodness of the agreement parametrized using the χ^2 probability value. The figures show a good agreement between the data and MC plots.

The polarization is also extracted from samples binned in p_{T} and x_{F} for the minimum bias data sample and in k_{T} and z for the di-jet samples. A definition of the bin ranges is shown in Figures 4.3 and 4.4. The fits for the binned samples are shown in Appendix 5 and the results are listed in Section 4.9.4.

4.9.2 Systematic Uncertainty Estimation

Systematic uncertainties are estimated by modifying various aspects of the analysis and observing how they affect the extracted value of polarization. The estimated values are summarized in Table 4.5 for both the minimum bias and di-jet analyses. It is observed, that the dominant contribution to the systematic uncertainty comes from the limited MC statistics which is typically several times larger than

Table 4.4: The decay angle expectation values in the di-jet MC sample. E_0^{MC} and E_1^{MC} are the expectation values calculated using the MC sample weighted to polarization, $P = 0$ and $P = 1$, respectively. The expectation values for the whole sample and for samples binned in k_{T} and z are listed. The listed uncertainties are statistical only.

Sample	**Exp. values for Λ**		**Exp. values for $\bar{\Lambda}$**	
	$\boldsymbol{E_0^{\mathrm{MC}}}$	$\boldsymbol{E_1^{\mathrm{MC}}}$	$\boldsymbol{E_0^{\mathrm{MC}}}$	$\boldsymbol{E_1^{\mathrm{MC}}}$
Whole sample	0.001 ± 0.001	0.205 ± 0.001	-0.001 ± 0.001	-0.205 ± 0.001
$\boldsymbol{k_{\mathrm{T}}}$ **bins (GeV)**	$\boldsymbol{E_0^{\mathrm{MC}}}$	$\boldsymbol{E_1^{\mathrm{MC}}}$	$\boldsymbol{E_0^{\mathrm{MC}}}$	$\boldsymbol{E_1^{\mathrm{MC}}}$
$k_{\mathrm{T}} < 0.07$	0.001 ± 0.001	0.199 ± 0.001	-0.001 ± 0.001	-0.199 ± 0.001
$0.7 < k_{\mathrm{T}} < 1.5$	-0.001 ± 0.001	0.207 ± 0.001	0.001 ± 0.001	-0.207 ± 0.001
$1.5 < k_{\mathrm{T}}$	0.001 ± 0.001	0.209 ± 0.001	-0.001 ± 0.001	-0.209 ± 0.001
z bins	$\boldsymbol{E_0^{\mathrm{MC}}}$	$\boldsymbol{E_1^{\mathrm{MC}}}$	$\boldsymbol{E_0^{\mathrm{MC}}}$	$\boldsymbol{E_1^{\mathrm{MC}}}$
$z < 0.026$	-0.001 ± 0.001	0.213 ± 0.001	0.001 ± 0.001	-0.213 ± 0.001
$0.026 < z < 0.1$	0.001 ± 0.001	0.207 ± 0.001	-0.001 ± 0.001	-0.207 ± 0.001
$0.1 < z$	-0.001 ± 0.001	0.174 ± 0.001	0.001 ± 0.001	-0.174 ± 0.001

any other estimated uncertainty. Therefore, in some cases, an over-conservative approach can be used to estimate a systematic uncertainty if it turns out to be small compared to the dominant contribution. The listed systematic uncertainties are assumed uncorrelated and are added in quadrature to obtain a total systematic uncertainty.

Details on the individual uncertainties estimation follow.

MC Statistics

Limited MC statistics projects into a precision with which the MC moments E_0^{MC} and E_1^{MC} are determined. In case of the di-jet sample the method of the MC re-sampling is used to greatly reduce uncertainty due to statistical fluctuations in MC, however, the result still depends on the original MC sample statistics since the kinematic distributions of Λ and jets are not re-sampled. To estimate what effect the limited MC statistics has on the polarization measurement, both the minimum bias and di-jet MC samples are divided into 4 statistically independent sub-samples. A measurement is then performed with each individual sub-sample and difference to the baseline result is calculated. The uncertainty is estimated as a standard deviation of the obtained differences scaled down by a factor of $\sqrt{4}$, to

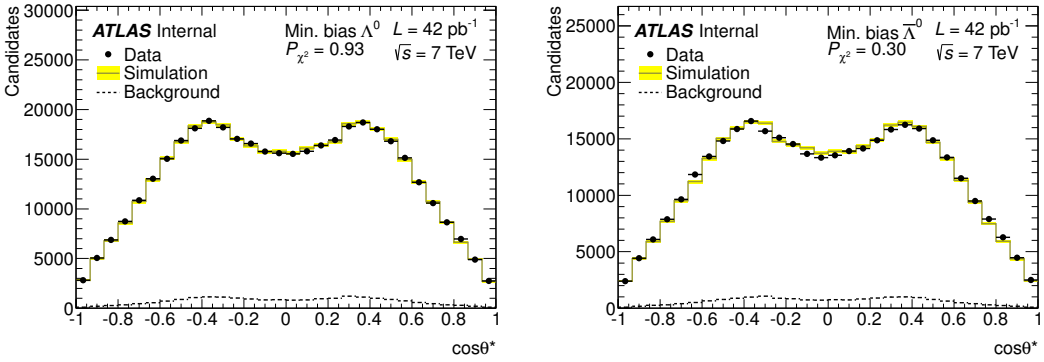

Figure 4.38: Comparison of the decay angle distributions for Λ (left) and $\bar{\Lambda}$ (right) in the minimum bias data and MC samples. The MC events are re-weighted using the extracted value of polarization, $P = -0.007$ for Λ and , $P = 0.008$ for $\bar{\Lambda}$. The background contribution for the MC plots is interpolated from the data invariant mass sidebands.

account for the fact that each sub-sample has 4-times smaller number of events than the original one.

Histogram Binning

The decay time expectation value is calculated in 7 bins of the invariant mass. A dependence of the result on the choice of the binning is tested by using alternatively 5 and 9 bins. An uncertainty is taken as a quadratic sum of the obtained differences w.r.t. the baseline result.

Background

Figure 4.35 shows that the dependence of the expectation value on the invariant mass for the background MC candidates can be treated as linear, however, background expectation value independent of the invariant mass also seems like a viable model. It is used as an alternative background model to probe dependence of the result on the background parametrization. Another source of the background systematic uncertainty originates in the uncertainty of the signal fraction, f_{sig}, extracted from the mass fit. Table 4.2 show statistical uncertainties of f_{sig} determined from the fit, $\sigma^{\text{stat}}_{f_{\text{sig}}} = 0.003$ for the minimum bias and $\sigma^{\text{stat}}_{f_{\text{sig}}} = 0.005$ for the di-jet data. Furthermore, a systematic uncertainty of the signal fraction is estimated as a difference between the signal fraction extracted from the fit and the true signal fraction determined using the MC truth information: $\sigma^{\text{syst}}_{f_{\text{sig}}} = 0.064$ for

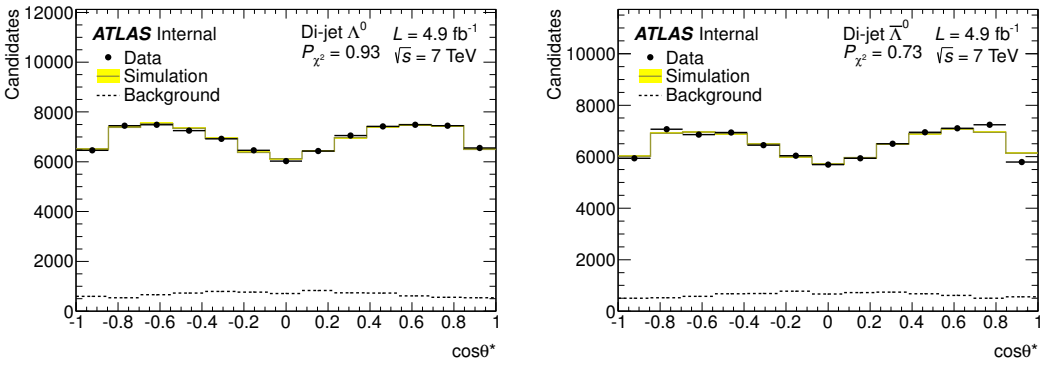

Figure 4.39: Comparison of the decay angle distributions for Λ (left) and $\bar{\Lambda}$ (right) in the di-jet data and MC samples. The MC events are re-weighted using the extracted value of polarization, $P = 0.007$ for Λ and , $P = -0.009$ for $\bar{\Lambda}$. The background contribution for the MC plots is interpolated from the data invariant mass sidebands.

the minimum bias and $\sigma^{\text{syst}}_{f_{\text{sig}}} = 0.014$ for the di-jet sample. Applying these variations to the signal fraction in the fitted function (4.21), new values of polarization are extracted and the quadratic sum of the differences to the baseline result is taken as an estimate of the systematic uncertainty due to background.

Track p_{T} Scale

An uncertainty on the track momentum scale can be estimated using the fits to the Λ invariant mass (see Table 4.2). The difference between the fitted Λ mass in data and MC is 0.02 MeV for the minimum bias and 0.18 MeV for the di-jet samples. This difference can be used to estimate uncertainty of the track p_{T} scale. The Λ mass shift is not directly proportional to the track p_{T} scale uncertainty, since the mass of the proton is not negligible compared to the mass of Λ. The MC simulation was used to estimate the track p_{T} shift corresponding to the Λ mass shift of 0.18 MeV, $\Delta p^{\text{trk}}_{\text{T}}/p^{\text{trk}}_{\text{T}} = 0.9995$. Scaling track momenta by this amount does not yield any significant change in the extracted value of the polarization.

Track p_{T} Resolution

The value of mass resolution obtained from the invariant mass fit (see Table 4.2) can be used to estimate uncertainty due to mis-modeling of the track resolution in MC. The difference between the data and MC mass resolution is $\Delta\sigma_m = 0.53$ MeV for the minimum bias and $\Delta\sigma_m = 0.03$ MeV for the di-jet samples. The MC tracks momenta were smeared to account for the difference between the mass resolution in

Table 4.5: Summary of systematic uncertainties. Symbol "–" is used when the uncertainty is not applicable for a given sample.

Systematic uncertainty	**Min. bias**		**Di-jet**	
	$\boldsymbol{\Lambda}$	$\bar{\boldsymbol{\Lambda}}$	$\boldsymbol{\Lambda}$	$\bar{\boldsymbol{\Lambda}}$
MC statistics	0.012	0.012	0.005	0.005
Binning	0.001	0.001	0.001	0.001
Background	0.002	0.001	0.001	0.002
Track p_{T} scale	0.000	0.000	0.000	0.000
Track p_{T} resolution	0.000	0.000	0.000	0.000
Jet p_{T} scale	—	—	0.000	0.000
Jet direction	—	—	0.000	0.001
MC re-sampling	—	—	0.002	0.002
Trigger	—	—	0.003	0.003
Kinematic weighting	0.002	0.002	0.001	0.001
Pileup contamination	—	—	0.000	0.000
Fit non-linearity	0.000	0.000	0.000	0.000
Uncertainty of α	0.000	0.000	0.000	0.000
Total	0.012	0.012	0.007	0.007

data and MC, this momentum smearing, however, does not produce any significant change in the extracted value of the polarization.

Jet p_{T} Scale

An uncertainty on the jet p_{T} scale was obtained using the standard ATLAS tool (JetUncertaintyProvider). The uncertainty is provided as a function of the jet p_{T}, η, the number of collision vertices, and the distance to the closest jet. The jet momenta are varied by a given jet scale uncertainty and the measurement is repeated, taking a quadratic sum of the result differences as a final polarization uncertainty. This systematic uncertainty is only applicable to the di-jet analysis.

Jet Direction

Using the MC sample, mean values of the jet direction shift, $\Delta\eta_{\mathrm{j}} = \eta_{\mathrm{j}}^{true} - \eta_{\mathrm{j}}$ and $\Delta\phi_{\mathrm{j}} = \phi_{\mathrm{j}}^{true} - \phi_{\mathrm{j}}$, are measured to be -0.0002 and 0.0006, respectively. To allow

for the mis-modeling of the jet reconstruction in MC, the jet direction is varied by first $\Delta\eta_{\mathrm{j}}$, then by $\Delta\phi_{\mathrm{j}}$; and the polarization measurement is performed using these modified samples. Mis-modeling of the jet direction resolution is probed by smearing jet momenta by 0.014 in η and 0.014 in ϕ, which are the values corresponding to the resolutions observed in the MC sample. The systematic uncertainty on polarization is again estimated as a quadratic sum of the observed differences to the baseline result. While assuming 100% uncertainty on jet direction reconstruction and its resolution might be a bit too pessimistic, it can be justified since the final polarization uncertainty from this effect is very small compared to the dominant effect of the MC statistics. This systematic uncertainty is only applicable to the di-jet analysis.

MC Re-sampling

The precision of the re-sampled MC decay angle expectation values $E_{0,1}^{\mathrm{MC}}$ is given by the precision of the efficiency and resolution map, which is binned in Λ p_{T}, η, $\cos\theta_{\mathrm{L}}^{*}$, and ϕ_{L}^{*}. The size of the bins is chosen so that a reasonable (few hundreds) number of candidates from the single Λ sample falls into each bin. By enlarging the bin size, a precision of the efficiency value in each bin is increased, but the efficiency is integrated over a larger area. By decreasing the bin size, one looses the precision of the efficiency value. To estimate the effect that the choice of the map binning has on the final result, 4 alternative maps are created with different bin sized, both smaller and larger bins are used. The MC decay angle moments are then calculated with the MC re-sampled using these maps. A quadratic sum of differences to the baseline result is used as a final systematic uncertainty. This systematic uncertainty is only applicable to the di-jet analysis.

Trigger

Traditionally, jet triggers are used only in the p_{T} range, where their efficiency flattens out (so called plateau of the the efficiency curve). However, in this analysis the entire p_{T} range, including the region where trigger is not yet fully efficient (so called turn-on region), is used. Although triggers are modeled in the simulation, it is not guaranteed that the turn-on regions are modeled well, especially at level-1 of the trigger chain. In the turn-on region, the trigger can not only bias p_{T} but also jet's η or the size of the jet. To gauge what effect the use of the full range of

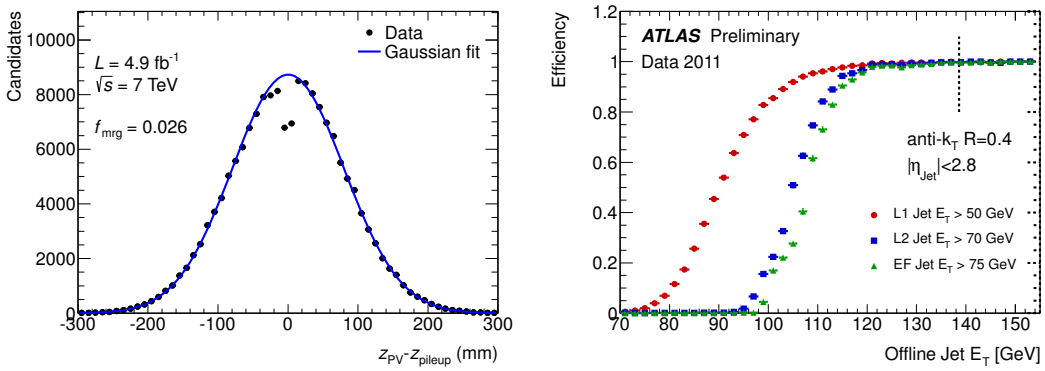

Figure 4.40: Determination of the fraction of of the merged pileup vertices fraction, f_{mrg} (left). z_{PV} and z_{pileup} are coordinates of the vertex and pileup vertex, respectively. The data are fitted with a Gaussian function in range $|\Delta z| > 30$ mm. The efficiency for anti-k_{T} jets with $R = 0.4$ to satisfy Level-1 (L1), Level-2 (L2), and the Event Filter (EF) inclusive jet trigger for a single L1→L2→EF trigger chain (right).

the trigger acceptance has, the trigger selection is disabled in MC, and the sample is re-weighted in jet p_{T} to match the data. This means that the p_{T} trigger bias is reproduced, but all other possible trigger biases are not. Using this alternative MC sample, the polarization is extracted again and a difference to the baseline result is taken as a systematic uncertainty. This systematic uncertainty is only applicable to the di-jet analysis, since the minimum bias analysis use a single trigger which is found to be nearly 100% efficient.

Kinematic Weighting

Figures 4.23 and 4.25 show that the worst agreement between data and weighted MC is in distributions of jet pseudo-rapidity, η_{j_1}, and Λ rapidity, y. The MC sample is re-weighted including jet and Λ rapidities into the list of weighted variables to test the result's sensitivity to residual discrepancies between data and MC. A difference of the new results to the baseline result is taken as a systematic uncertainty.

Pileup Contamination

The minimum bias analysis does not distinguish between Λ coming from the primary vertex or pile-up vertices. However, in case of the di-jet analysis, pile-up can become a source of systematic uncertainty if Λ and di-jet object originate in different collision vertices and are therefore uncorrelated. The primary vertex jet

track fraction cut, f_{PV}, and the Λ impact parameter significance cut, a_0/σ_{a_0}, are used to reject these cases. However, if the pileup vertex is too close to the primary vertex, the two vertices may merge and the removal cuts will become inefficient. The effect of the vertex merging can be seen in the distribution of difference in z-coordinate of the two vertices, $\Delta z = z_{\mathrm{PV}} - z_{\mathrm{pileup}}$, as shown in Figure 4.40, left. The distribution is fitted with a Gaussian function using only bins in the range $|\Delta z| > 30$ mm. Events where the pileup vertex is merged with the PV can be seen as a drop in the data distribution w.r.t. the fitted function close to $\Delta z = 0$. From the difference in the respective areas, it is estimated that 2.6% of the events have merged pileup and primary vertices. A conservative estimate of systematic uncertainty is made assuming that every event with the merged vertices contains fake, and therefore unpolarized, signal (note that in reality this fraction will be much smaller since not every pileup collision creates a reconstructible jet or Λ). A modified fit function with 2.6% of unpolarized signal modeling the pileup contamination is used to extract polarization. A difference of the extracted polarization to the baseline result is used and an estimate of the systematic uncertainty.

Fit Non-linearity

When deriving the fit function (4.21) it was assumed that the total efficiency, ε_{T}, does not depend on polarization. This is, however, only an approximation and may not be valid, if for instance the differential efficiency, $\varepsilon(\cos\theta^*_{\mathrm{true}})$, is not symmetric. In fully general case the $1/\varepsilon_{\mathrm{T}}$ factors in formula (4.18) must be replaced by $1/\varepsilon_{\mathrm{T}}(P)$, where $\varepsilon_{\mathrm{T}}(P)$ is a linear function of P. In MC it was verified that the dependence of the total efficiency on polarization is small, and it can therefore be approximated by the first two terms of the Taylor expansion:

$$\begin{aligned}
\frac{1}{\varepsilon_{\mathrm{T}}(P)} &= \frac{1}{\varepsilon^0_{\mathrm{T}} + (\varepsilon^1_{\mathrm{T}} - \varepsilon^0_{\mathrm{T}})P} \approx \frac{1}{\varepsilon^0_{\mathrm{T}}}\left(1 - \frac{\varepsilon^1_{\mathrm{T}} - \varepsilon^0_{\mathrm{T}}}{\varepsilon^0_{\mathrm{T}}}P\right), \text{or} \\
\frac{1}{\varepsilon_{\mathrm{T}}(P)} &= \frac{1}{\varepsilon^1_{\mathrm{T}} + (\varepsilon^0_{\mathrm{T}} - \varepsilon^1_{\mathrm{T}})(1-P)} \approx \frac{1}{\varepsilon^1_{\mathrm{T}}}\left[1 - \frac{\varepsilon^0_{\mathrm{T}} - \varepsilon^1_{\mathrm{T}}}{\varepsilon^1_{\mathrm{T}}}(1-P)\right],
\end{aligned}$$

where $\varepsilon^0_{\mathrm{T}}$ is the total efficiency for polarization $P = 0$ and $\varepsilon^1_{\mathrm{T}}$ for polarization $P = 1$. With this new normalization, the definition of factors C_0 and C_1 in

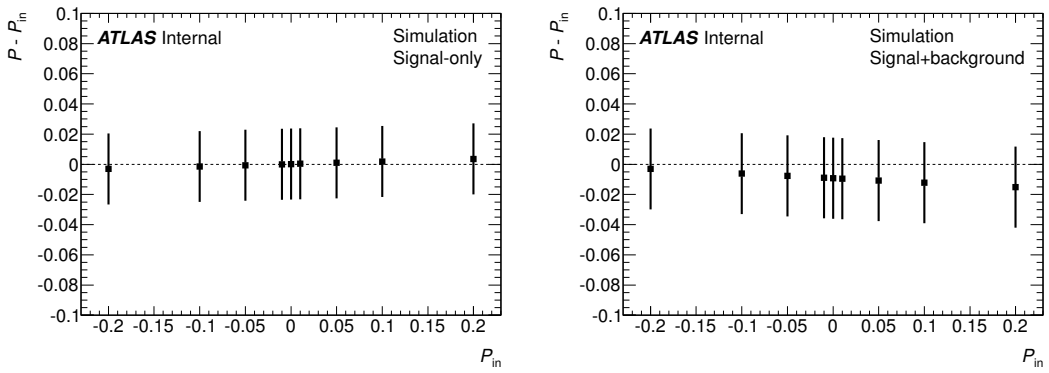

Figure 4.41: MC closure test. The plots show difference between the MC input polarization, P_{in}, and the value, P, extracted using the decay angle expectation value fit. The left plot shows the closure for signal-only MC sample, the right plots is made using the sample containing both signal and background events.

formula (4.18) will change:

$$\begin{aligned} C_0(P) &\approx E_0\left(1-\frac{\varepsilon_{\text{T}}^1-\varepsilon_{\text{T}}^0}{\varepsilon_{\text{T}}^0}P\right), \\ C_1(P) &\approx E_1\left[1-\frac{\varepsilon_{\text{T}}^0-\varepsilon_{\text{T}}^1}{\varepsilon_{\text{T}}^1}(1-P)\right]-E_0\left(1-\frac{\varepsilon_{\text{T}}^1-\varepsilon_{\text{T}}^0}{\varepsilon_{\text{T}}^0}P\right). \end{aligned}$$

Using this new definition of the C_0 and C_1 factors in the fit function, however, does not significantly change the extracted value of polarization.

Uncertainty of the α Parameter

The Λ decay asymmetry parameter, α, has been measured with precision $\sigma_\alpha = 0.013$ [15]. Since this value is used in the definition of the fit function (4.21), this uncertainty will affect the extracted value of the polarization. However, it has been found negligible compared to other uncertainties.

4.9.3 Cross-checks

MC Closure Test

The di-jet MC sample is used to test the polarization extraction technique. The sample is divided into two halves: the first half is used to calculate the MC moments E_0^{MC} and E_1^{MC}, the second half is used as a test sample. The test sample is weighted to polarizations ranging from $P_{\text{in}} = -0.2$ to 0.2. Polarization is than

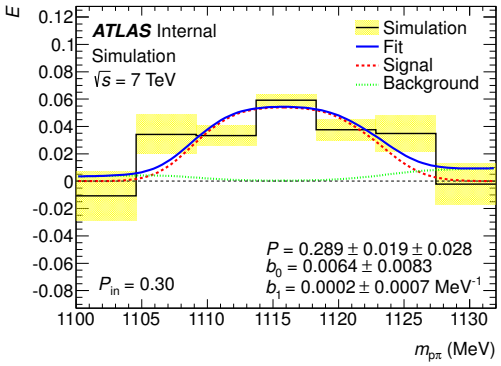

Figure 4.42: An example of the decay angle expectation value fit for MC sample weighted to $P_{\text{in}} = 0.3$.

Table 4.6: Division between the plateau and turnon trigger regions for different trigger items.

Trigger	j10	j15	j20	j30	j40	j55
$\boldsymbol{p_{\text{T,j1}}}$ **(GeV)**	29.9	39.8	46.5	53.1	73.0	106.2
Trigger	j75	j100	j135	j180	j240	
$\boldsymbol{p_{\text{T,j1}}}$ **(GeV)**	139.4	172.6	205.8	265.6	331.9	

extracted using the decay angle expectation value fit. Differences between input and extracted values of polarization are shown in Figure 4.41 for pure MC signal and the sample containing both signal and background events. The plots show good closure within the estimated precision. An example of the expectation value fit for the MC sample weighted to polarization $P_{\text{in}} = 0.3$ is shown in Figure 4.42.

Trigger Plateau and Turn-on Regions

The systematic uncertainty caused by the trigger selection of di-jet sample was estimated using the MC simulation, as described in the previous section. Additional cross-check is done using data, splitting the data sample into two: the first containing events triggered in the plateau region while the second containing events triggered in the turn-on region of the lowest threshold trigger firing in the given event. The discriminating cuts are listed in Table 4.6. Figure 4.40, right, shows an example of an efficiency curve for the j75 trigger and the chosen division between the plateau and turn-on regions. The thresholds are chosen so that exactly half of the events fall into each region.

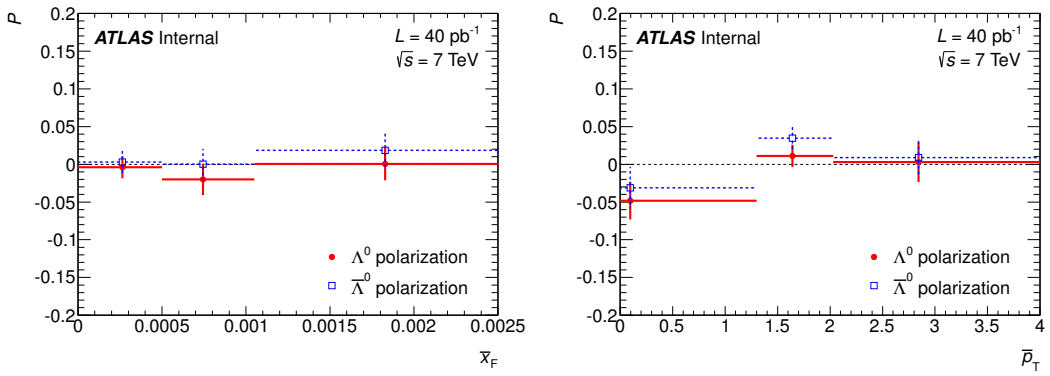

Figure 4.43: Λ polarization in the beam-Λ reference frame (minimum bias data) as a function of the Feynman-x variable, x_{F} (left), and the transverse momentum, p_{T} (right). Displayed error bars are statistical and systematic uncertainties combined.

Polarization measured in each sub-sample is:

$$\begin{aligned} P_{\mathrm{p}} &= -0.001 \pm 0.015(\mathrm{stat}) \qquad \text{in the plateau trigger region and} \\ P_{\mathrm{t}} &= 0.009 \pm 0.016(\mathrm{stat}) \qquad \text{in the turnon trigger region.} \end{aligned}$$

These values are consistent with each other and with the baseline results within their statistical precision, which means that there is no additional significant systematic effect due to the trigger selection that would make this difference larger.

Pythia vs Herwig MC

To verify that the Pythia and Herwig di-jet MC samples are consistent, the polarization is measured using Pythia and Herwig samples independently. Although the estimated precision of these measurements is smaller (esp. for the Herwig sample, which has small number of events) both measurements are consistent with the baseline results and one another within their estimated uncertainty:

$$\begin{aligned} P_{\mathrm{Py}} &= 0.011 \pm 0.011(\mathrm{stat}) \pm 0.009(\mathrm{syst}) \quad \text{with the Pythia MC sample and} \\ P_{\mathrm{Hw}} &= -0.009 \pm 0.011(\mathrm{stat}) \pm 0.020(\mathrm{syst}) \quad \text{with the Herwig MC sample.} \end{aligned}$$

Table 4.7: Polarization in the beam-Λ reference frame measured for the whole sample and in bins of x_{F} and p_{T}. $\bar{x}_{\mathrm{F}}^{\mathrm{true}}$ and $\bar{p}_{\mathrm{T}}^{\mathrm{true}}$ are average values of the true Feynman-x variable and the true Λ transverse momentum, respectively. The table lists both statistical and systematic uncertainties.

Sample		**Polarization in the Λ-beam reference frame**	
		$\boldsymbol{\Lambda}$	$\boldsymbol{\bar{\Lambda}}$
Whole sample		$-0.007 \pm 0.006 \pm 0.012$	$0.008 \pm 0.006 \pm 0.012$
$\boldsymbol{x_{\mathrm{F}}}$ **bins** $\boldsymbol{(10^{-4})}$	$\boldsymbol{\bar{x}_{\mathrm{F}}^{\mathrm{true}}}$	$\boldsymbol{\Lambda}$	$\boldsymbol{\bar{\Lambda}}$
$x_{\mathrm{F}} < 5$	2.63	$-0.004 \pm 0.009 \pm 0.011$	$0.003 \pm 0.010 \pm 0.012$
$5 < x_{\mathrm{F}} < 10.5$	7.50	$-0.020 \pm 0.010 \pm 0.018$	$0.000 \pm 0.011 \pm 0.017$
$10.5 < x_{\mathrm{F}}$	18.8	$0.001 \pm 0.011 \pm 0.019$	$0.018 \pm 0.012 \pm 0.019$
$\boldsymbol{p_{\mathrm{T}}}$ **bins (GeV)**	$\boldsymbol{\bar{p}_{\mathrm{T}}^{\mathrm{true}}}$	$\boldsymbol{\Lambda}$	$\boldsymbol{\bar{\Lambda}}$
$p_{\mathrm{T}} < 1.3$	0.980	$-0.048 \pm 0.012 \pm 0.022$	$-0.031 \pm 0.013 \pm 0.024$
$1.3 < p_{\mathrm{T}} < 2.03$	1.641	$0.011 \pm 0.010 \pm 0.011$	$0.035 \pm 0.011 \pm 0.011$
$2.03 < p_{\mathrm{T}}$	2.837	$0.003 \pm 0.009 \pm 0.025$	$0.009 \pm 0.010 \pm 0.023$

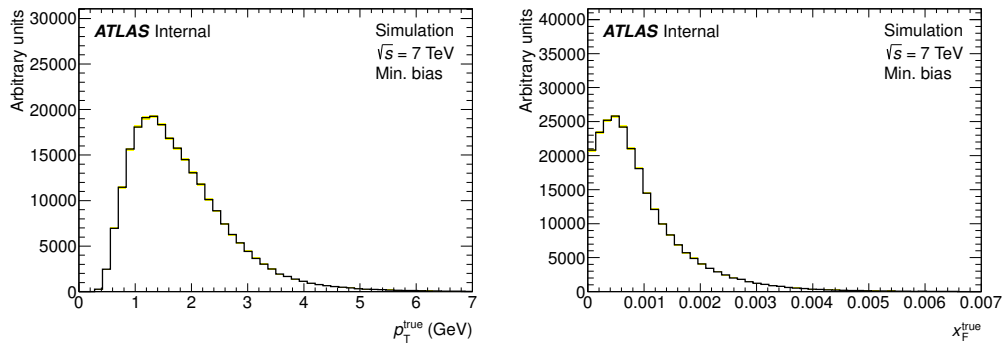

Figure 4.44: Distributions of the true Λ transverse momentum, $p_{\mathrm{T}}^{\mathrm{true}}$ (left), and the true Feynman-x variable, $x_{\mathrm{F}}^{\mathrm{true}}$ (right), in the minimum bias sample.

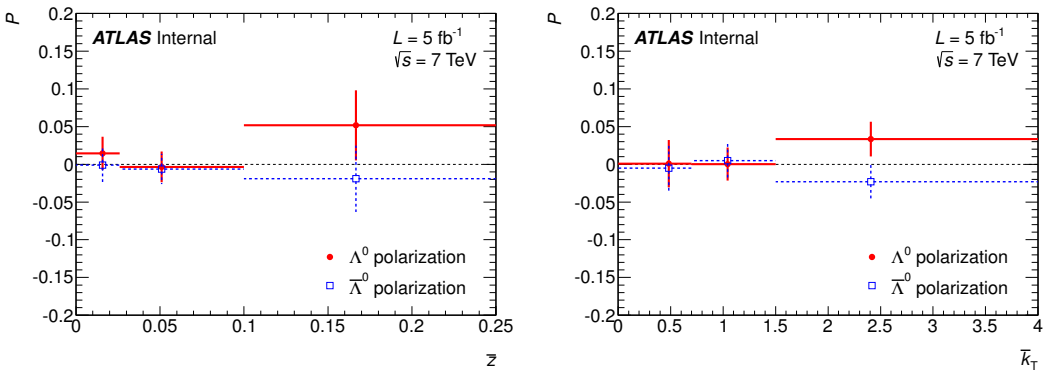

Figure 4.45: Λ polarization in the di-jet reference frame as a function of the jet Λ momentum fraction, z (left), and the transverse momentum relative to the jet axis, k_{T} (right). Displayed error bars are statistical and systematic uncertainties combined.

4.9.4 Results

Using the 2010 minimum bias sample, polarization in the beam-Λ reference frame is measured to be

$$\begin{aligned} P_{\Lambda} &= -0.007 \pm 0.006(\mathrm{stat}) \pm 0.012(\mathrm{syst}) \text{ and} \\ P_{\bar{\Lambda}} &= 0.008 \pm 0.006(\mathrm{stat}) \pm 0.012(\mathrm{syst}). \end{aligned}$$

Polarization in the beam-Λ reference frame is also measured in bins of Λ transverse momentum, p_{T}, and the Feynman-x variable, x_{F}. The results are shown in Figure 4.43 and are listed in Table 4.7. Distributions of the true kinematic variables $p_{\mathrm{T}}^{\mathrm{true}}$ and $x_{\mathrm{F}}^{\mathrm{true}}$ for the minimum bias sample are shown in Figure 4.44. Corresponding distributions for the binned samples are shown in Appendix 5, Figures B.9 and B.10. No significantly large polarization in the beam-Λ reference frame is observed.

Using the di-jet sample, polarization in the di-jet reference frame is measured to be

$$\begin{aligned} P_{\Lambda} &= 0.007 \pm 0.011(\mathrm{stat}) \pm 0.007(\mathrm{syst}) \text{ and} \\ P_{\bar{\Lambda}} &= -0.009 \pm 0.011(\mathrm{stat}) \pm 0.007(\mathrm{syst}). \end{aligned}$$

To probe the dependence on the event kinematics, polarization is also measured in bins of the Λ transverse momentum relative to the jet axis, k_{T}, and the jet Λ momentum fraction, z. The results are shown in Figure 4.45 and are listed in

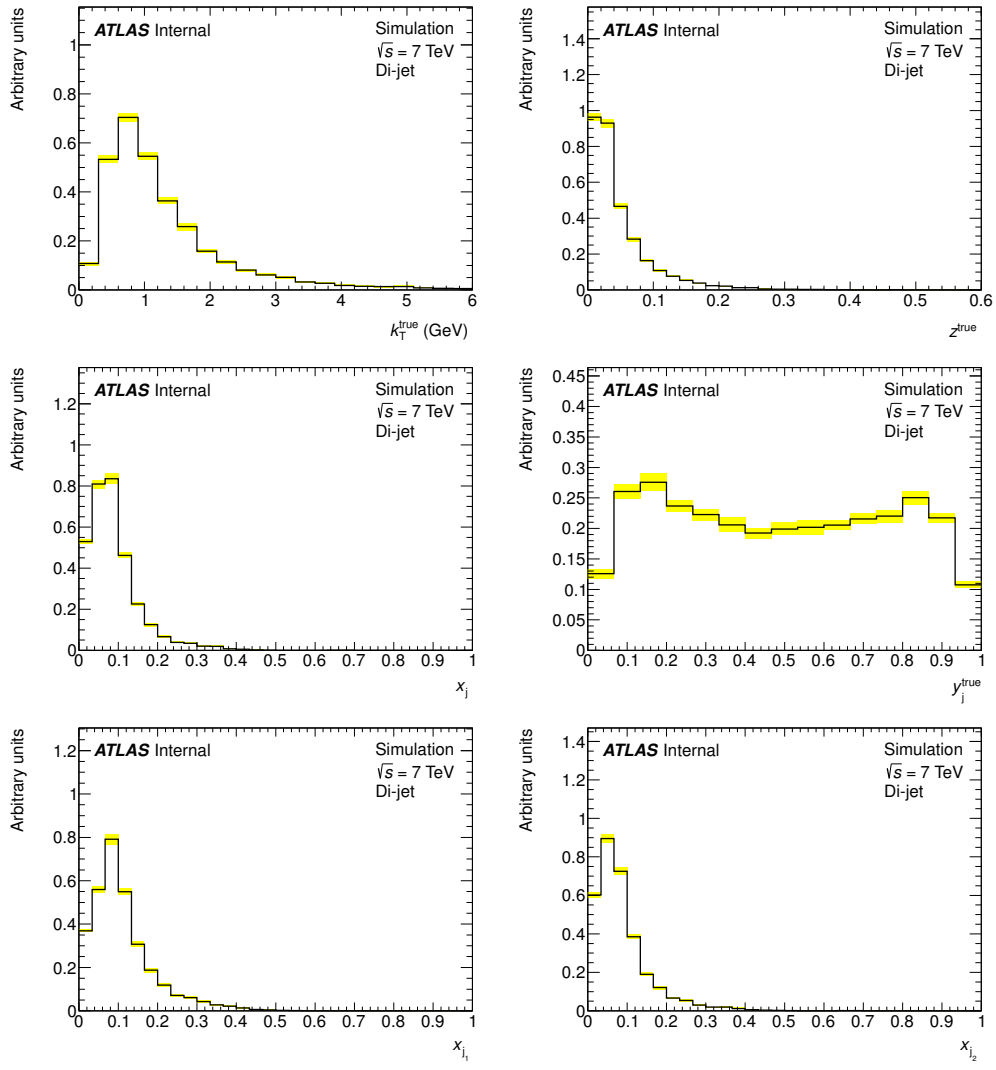

Figure 4.46: Distributions of the true Λ transverse momentum relative to the jet axis, $k_{\mathrm{T}}^{\mathrm{true}}$ (top left), the true jet Λ momentum fraction, z^{true} (top right), the true jet momentum fraction, $x_{\mathrm{j}}^{\mathrm{true}}$ (middle left), for the jet containing Λ, the true di-jet variable, $y_{\mathrm{j}}^{\mathrm{true}}$ (middle right), and the true jet momentum fraction, $x_{\mathrm{j1}}^{\mathrm{true}}$ (bottom left) and $x_{\mathrm{j2}}^{\mathrm{true}}$ (bottom right), for the leading and sub-leading jets, respectively.

Table 4.8: Polarization in the di-jet reference frame measured for the whole sample and in bins of z and k_{T}. $\bar{z}^{\mathrm{true}}$ and $\bar{k}_{\mathrm{T}}^{\mathrm{true}}$ are average values of the true jet Λ momentum fraction and the true Λ transverse momentum relative to the jet axis, respectively. The table lists both statistical and systematic uncertainties.

Sample		**Polarization in the di-jet reference frame**	
		$\boldsymbol{\Lambda}$	$\bar{\boldsymbol{\Lambda}}$
Whole sample		$0.007 \pm 0.011 \pm 0.007$	$-0.008 \pm 0.011 \pm 0.007$
$\boldsymbol{z}$ **bins**	$\bar{\boldsymbol{z}}^{\mathbf{true}}$	$\boldsymbol{\Lambda}$	$\bar{\boldsymbol{\Lambda}}$
$z < 0.026$	0.0159	$0.014 \pm 0.016 \pm 0.015$	$-0.001 \pm 0.017 \pm 0.016$
$0.026 < z < 0.1$	0.0503	$-0.003 \pm 0.017 \pm 0.011$	$-0.006 \pm 0.017 \pm 0.011$
$0.1 < z$	0.150	$0.052 \pm 0.039 \pm 0.026$	$-0.019 \pm 0.040 \pm 0.019$
$\boldsymbol{k_{\mathrm{T}}}$ **bins (GeV)**	$\bar{\boldsymbol{k}}_{\mathbf{T}}^{\mathbf{true}}$	$\boldsymbol{\Lambda}$	$\bar{\boldsymbol{\Lambda}}$
$k_{\mathrm{T}} < 0.07$	0.041	$0.001 \pm 0.022 \pm 0.022$	$-0.005 \pm 0.023 \pm 0.023$
$0.7 < k_{\mathrm{T}} < 1.5$	0.047	$0.000 \pm 0.016 \pm 0.015$	$0.005 \pm 0.016 \pm 0.016$
$1.5 < k_{\mathrm{T}}$	0.057	$0.033 \pm 0.021 \pm 0.010$	$-0.023 \pm 0.021 \pm 0.009$

Table 4.8. Distributions of the true kinematic variables $k_{\mathrm{T}}^{\mathrm{true}}$ and z^{true} for the minimum bias sample are shown in Figure 4.46, together with the distributions of the true jet momentum fraction, $x_{\mathrm{j}}^{\mathrm{true}}$, for the jet containing Λ, the true di-jet variable, $y_{\mathrm{j}}^{\mathrm{true}}$, and the true jet momentum fraction, $x_{\mathrm{j1}}^{\mathrm{true}}$ (bottom left) and $x_{\mathrm{j2}}^{\mathrm{true}}$ (bottom right), for the leading and sub-leading jets. The variable x_{j} is defined as

$$x_{\mathrm{j}} = \frac{2|\vec{k}_{\mathrm{j}}|}{\sqrt{s}},$$

where $\vec{k}_{\mathrm{j}}$ is the jet momentum and $\sqrt{s}$ is the total energy of the colliding beams. Corresponding distributions for the binned samples are shown in Appendix 5, Figures B.11–B.16. The plots show distributions of variables calculated at the true particle level. No significantly large polarization in the di-jet reference frame is observed.

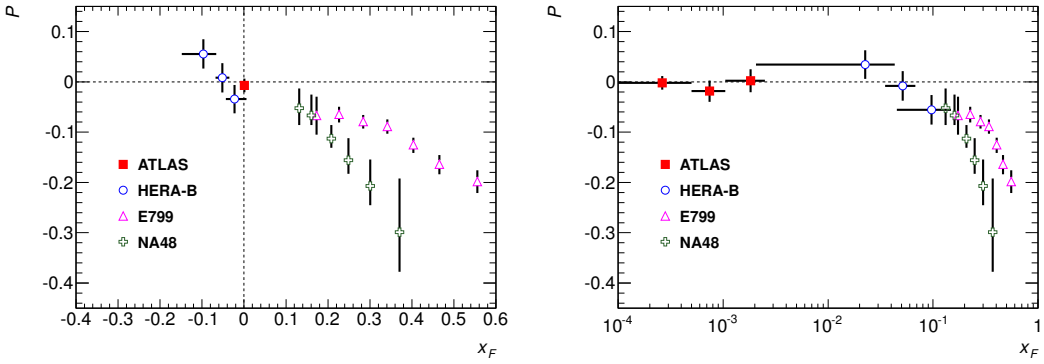

Figure 4.47: The ATLAS values of Λ polarization in the beam-Λ reference frame in context of the other measurements. HERA-B data are taken from Ref [42], E799 data from Ref [40], and NA48 data from Ref [41]. The ATLAS values show statistical and systematic uncertainties added in quadrature. The HERA-B experiment uses different reference frame than the other experiments. In the right plot the HERA-B data points have been transposed to the reference frame used by ATLAS. E799 and NA48 data points show a different slope since they cover a different p_{T} range.

4.10 Conclusions of the Λ Polarization Measurements

Results of the first measurement of Λ polarization using a 7 TeV collider have been reported here. This chapter encompasses two analyses: a measurement of Λ polarization in the beam-Λ reference frame, which is a direct extension of the previous fixed-target experimental approach, and a new measurement of Λ polarization in the di-jet frame, following a strategy proposed by Boer et al. in Ref [54]. In the analysis presented in this thesis, it has been demonstrated that the Λ hyperon can be clearly identified through its decay into $p\pi$, both in minimum bias events and also in the high track density environment of a jet. This is a first attempt to measure polarization of Λ produced inside a jet.

Previous experimental data suggest that polarization in the beam-Λ reference frame decreases with the value of the Feynman-x variable, $x_{\mathrm{F}} = p_z/p_{\mathrm{beam}}$. The x_{F} reach of the ATLAS experiment is very limited due to its rapidity acceptance: only Λ hyperons with x_{F} up to about 0.005 can be reconstructed. Therefore, large polarization could only be observed if some new production mechanism came into play at collision energy of 7 TeV. However, no significantly large polarization has been observed in ATLAS, as shown in the summary plot in Figure 4.43 and Table 4.7. Figure 4.47 shows the ATLAS results in a context of other selected

experiments, HERA-B [42], E799 [40], and NA48 [41]. The ATLAS result is consistent with expectations in the absence of the onset of new physics.

Λ polarization in the di-jet frame is not constrained by the x_{F} acceptance of the detector, since the relevant analyzing direction is defined as a cross-product of the Λ momentum and an axis of the jet containing Λ, in the di-jet rest frame, and is therefore decoupled from x_{F}. There are no experimental measurements prior to this one that would constrain the value of polarization in this frame, although an extrapolation of the previous (fixed target) data has been performed using the framework of the polarizing fragmentation functions and is shown in Ref [54] and Figure 4.7 in this document. This prediction, however, suffers from a large uncertainty. Furthermore, data used to extract the polarizing fragmentation functions used for this prediction are at much lower energy than the LHC and are therefore dominated by the valence quark interactions, whereas at the LHC the gluon contribution is dominant. The Λ and $\bar{\Lambda}$ polarization has been measured in bins of the jet Λ momentum fraction, z, and the relative transverse momentum, k_{T}, and the results are shown in Figure 4.45 and Table 4.8. In the analyzed Λ phase-space all the polarization values are consistent with zero within 2-σ range, which is in an agreement with the above mentioned prediction. This suggests that the large gluon component at the LHC does not contribute to the polarizing fragmentation functions at low values of z.

It is hoped that, with increased statistics accumulated in future years of the LHC running, researchers will be able to use this technique to explore the spin properties of the fragmentation process in a way never before possible and extend the phase-space coverage of the measurement toward larger values of z, where significant values of the polarization could be observed. The z reach of the experiment is naturally constrained by the detector p_{T} acceptance, which is only able to reconstruct Λ candidates up to about 200 GeV (with reconstruction efficiency at these energies being very low). Therefore, it is preferable to analyze events with as low jet p_{T} as possible, since inside high p_{T} jets only low-z Λ candidates can be reconstructed. As the p_{T} threshold of the jet triggers will likely increase in the future years of the ATLAS operation to cope with the larger instantaneous luminosity of the LHC, it is likely that the number of low-p_{T} jets will form a much smaller fraction of the future datasets than it was in 2011. However, low-p_{T} jets should still be present in multi-jet events, where high p_{T} jet is accompanied by one or more low-p_{T} ones, which can contain Λ hyperons.

The mystery of the large polarization observed in inclusive hyperon production is one that has gone unexplained for many decades. The use of the Boer and Sivers techniques may open a new window that allows the identification and exploration of the processes that could produce large polarizations even in the TeV energy domain.

Chapter 5

Summary and Outlook

This thesis summarizes results of two measurements using the Λ and Λ_b baryons: the Λ_b lifetime and mass measurement (Chapter 3), and the measurement of Λ polarization in minimum bias and di-jet events (Chapter 4). Each measurement is described in a separate chapter with its own detailed conclusion section, i.e. Section 3.7 for the Λ_b and 4.10 for the Λ measurements.

The Λ_b lifetime is predictable within a framework of the heavy quark expansion (HQE) calculations, which is widely and successfully used in b-physics. In past decade, the Λ_b lifetime has received some special attention due to a discrepancy between the theoretical prediction and experimental results. The measurement presented here improves on the precision of the previous measurements and helps resolving this discrepancy. The analysis uses a signal sample of about 2200 Λ_b and $\bar{\Lambda}_b$ decays and it employs a simultaneous mass and decay time maximum likelihood fit to extract the lifetime and mass. They are measured to be

$$\begin{aligned} \tau_{\Lambda_b} &= 1.449 \pm 0.036(\text{stat}) \pm 0.017(\text{syst}) \text{ ps, and} \\ m_{\Lambda_b} &= 5619.7 \pm 0.7(\text{stat}) \pm 1.1(\text{syst}) \text{ MeV.} \end{aligned}$$

A value of the Λ_b and B_d^0 lifetime ratio is measured, too, with the value of

$$R = \tau_{\Lambda_b}/\tau_{B_d} = 0.960 \pm 0.025(\text{stat}) \pm 0.016(\text{syst}),$$

and it has been compared to the previous results and theoretical predictions in Figure 3.26. The ATLAS result suggests that the role of the spectator quarks in the Λ_b decay is less significant than it would seem from the latest HQE calculations

(which include the NLO spectator quark contribution and predict value of 0.86 ± 0.05) and is in a better agreement with the previous LO calculations, predicting a value around 0.95. Given the complicated history of the Λ_b lifetime measurements (outlined in Section 3.1.1), one has to wonder whether the most recent value of the theoretical prediction is not just a consequence of theorists' struggle to achieve agreement with the old LEP and Tevatron measurements, which measured the value of about 0.8. On the other hand, one should keep in mind that the current experimental value is compatible with both predictions within a 2-σ error margin.

The first measurement of the transverse polarization of Λ hyperons produced in minimum bias and di-jet events at the center-of-mass energy of 7 TeV was reported in this thesis, too. Large hyperon polarization observed at low-energy fixed target experiments has been puzzling physicists for decades, since their results are incompatible with perturbative QCD calculations. This suggests that some unknown mechanism, which cannot be described by pQCD, is responsible for the hyperon polarization. The measurements describe in this thesis opens up a new avenue for study of the hyperon polarization, since the measurement of polarization of the Λ hyperon produced within a jet becomes possible for the first time. This measurement probes non-perturbative QCD processes, fragmentation and hadronization, as possible sources of the hyperon polarization. The analysis uses minimum bias and di-jet events, collected in years 2010 and 2011. The polarization was measured for all events in the acceptance region of the ATLAS detector. In addition, measurements in kinematic bins of the Λ transverse momentum, p_{T}, and the Feynman-x variable, x_{F}, were performed for the minimum bias data. For di-jet data, polarization was measured in bins of Λ transverse momentum relative to the jet axis, k_{T}, and the jet Λ momentum fraction, z. In the minimum bias sample polarization is measured to be $-0.007 \pm 0.006(\mathrm{stat}) \pm 0.012(\mathrm{syst})$ for Λ and $0.008 \pm 0.006(\mathrm{stat}) \pm 0.012(\mathrm{syst})$ for $\bar{\Lambda}$. In the di-jet sample polarization is $0.007 \pm 0.011(\mathrm{stat}) \pm 0.007(\mathrm{syst})$ for Λ and $-0.009 \pm 0.011(\mathrm{stat}) \pm 0.007(\mathrm{syst})$ for $\bar{\Lambda}$. Binned results are shown in Figures 4.43 and 4.45. The observed results agree with the extrapolation of the low-energy data (see Figure 4.47), which suggest that polarization becomes small as x_{F} approaches zero.

The measurements reported in this thesis (esp. the Λ polarization measurement) represent the first steps toward further studies involving spin and QCD. Using the method of moments, similar to the one used in the Λ analysis, the polarization and decay asymmetry of Λ_b can be measured. This measurement,

although more challenging than the Λ one due to the complicated final state, has been shown feasible (Ref [6]) and is currently under way. Physics interest in this measurement is twofold: firstly, the value of the Λ_b decay asymmetry, α_b, is predictable by calculations exploiting the factorization theorem in perturbative QCD [64] or withing the framework of the Heavy Quark Effective Theory [65, 66], and offers therefore an excellent testing ground for these predictions. Secondly, measurement of the Λ_b polarization in the similar kinematic range used for the Λ measurement will probe the effect that presence of the heavy b quark has on the baryon polarization. This analysis is challenging due to lack of statistics and may require more data to achieve desired precision. The LHCb experiment has already reported its findings in Ref [67], even though for a different rapidity range than ATLAS.

Although Λ polarization in both the beam-Λ and di-jet reference frames was measured consistent with zero, there can still be some interesting spin-orbital effects accessible to the ATLAS experiment, if one looks into correlations between the Λ spin and other observables in the event. One such avenue is a study of the correlation between the Λ spin and other particles in a jet containing Λ, proposed by Sivers in Ref [59]. These studies should probe if the $s\bar{s}$ are produced in an orbitally excited state. Similarly, analysis of the Λ-$\bar{\Lambda}$ spin correlation may provide additional insights into the production process of $s\bar{s}$ pairs (see Ref [68]), since various production models predict different spin correlation scenarios.

Both the Λ helicity amplitudes measurement and the Λ-$\bar{\Lambda}$ correlation analysis are currently pursued by the University of Michigan group, with a contribution of the author of this thesis.

Appendix A

Measurement of the Λ_b Lifetime and Mass

A.1 Single-muon Trigger Efficiencies

The trigger selection efficiency as a function of the muon d_0 measured using the tag-and-probe method in both data and MC in 5 bins of muon p_{T} is shown in Figures A.1 for muons in barrel and A.2 for muons in endcap.

A.2 Λ_b Lifetime and Mass Fit Correlations

An estimate of the simultaneous Λ_b lifetime and mass fit correlation matrix is shown in Table A.1.

Table A.1: Λ_b fit full correlation matrix

	m_{Λ_b}	τ_{Λ_b}	b	$\tau_{\mathrm{bkg},1}$	$\tau_{\mathrm{bkg},2}$	$\tau_{\mathrm{bkg},3}$	f_{sig}	f_1	f_2	f_3	S_m	S_τ
m_{Λ_b}	1.000	0.002	-0.056	0.003	-0.007	0.001	0.013	0.003	-0.004	0.001	0.026	0.000
τ_{Λ_b}	0.002	1.000	0.011	0.175	0.010	0.003	0.149	0.048	0.020	0.005	0.040	0.000
b	-0.056	0.011	1.000	0.004	0.003	-0.000	0.030	0.012	-0.003	-0.000	0.010	0.000
$\tau_{\mathrm{bkg},1}$	0.003	0.175	0.004	1.000	0.289	0.022	0.030	0.026	-0.585	-0.019	0.004	0.000
$\tau_{\mathrm{bkg},2}$	-0.007	0.010	0.003	0.289	1.000	-0.062	0.009	0.557	-0.184	0.056	-0.003	0.000
$\tau_{\mathrm{bkg},3}$	0.001	0.003	-0.000	0.022	-0.062	1.000	0.002	-0.143	-0.151	0.644	-0.001	0.000
f_{sig}	0.013	0.149	0.030	0.030	0.009	0.002	1.000	0.182	-0.051	0.001	0.366	0.000
f_1	0.003	0.048	0.012	0.026	0.557	-0.143	0.182	1.000	0.339	-0.109	0.138	0.000
f_2	-0.004	0.020	-0.003	-0.585	-0.184	-0.151	-0.051	0.339	1.000	-0.080	-0.067	0.000
f_3	0.001	0.005	-0.000	-0.019	0.056	0.644	0.001	-0.109	-0.080	1.000	-0.002	0.000
S_m	0.026	0.040	0.010	0.004	-0.003	-0.001	0.366	0.138	-0.067	-0.002	1.000	0.000
S_τ	0.000	0.000	0.000	0.000	0.000	0.000	0.000	0.000	0.000	0.000	0.000	0.000

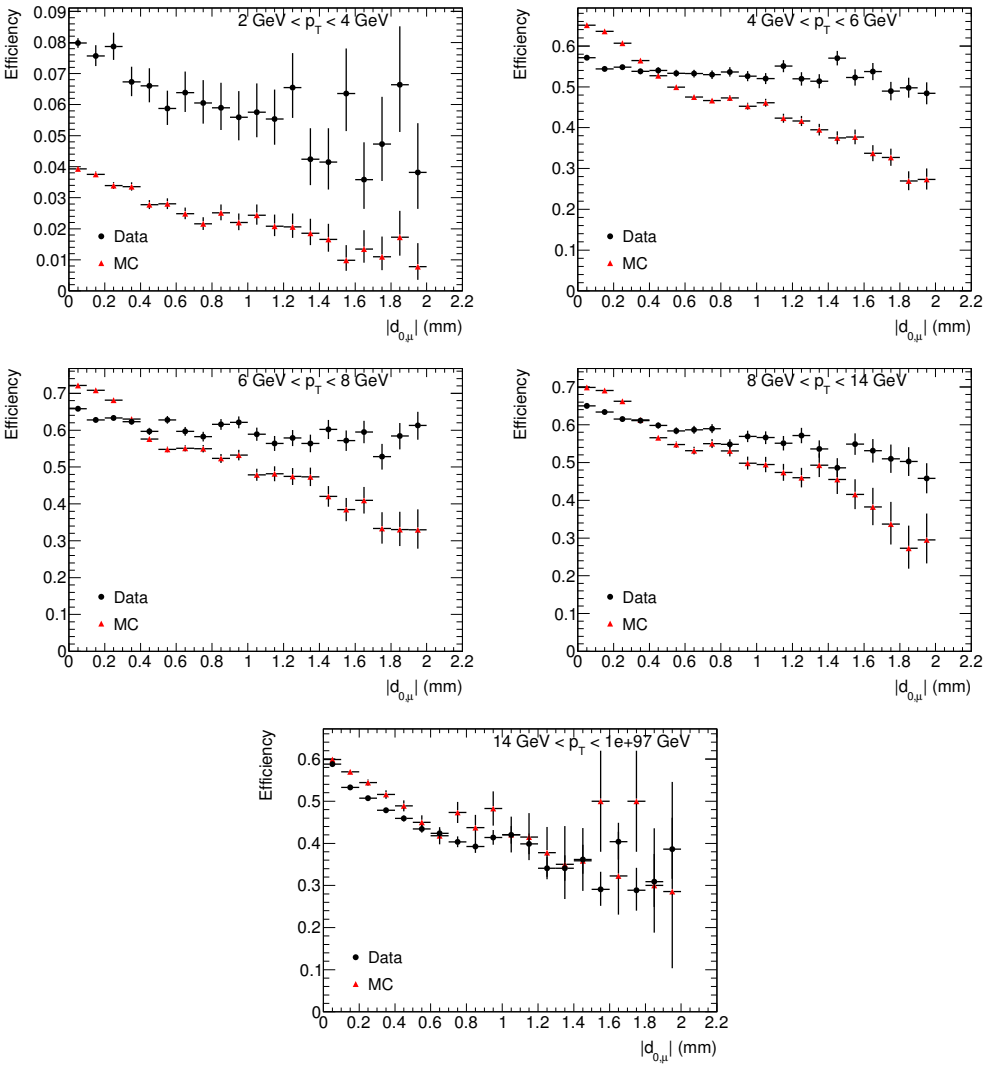

Figure A.1: Trigger selection efficiency as a function of the muon transverse impact parameter, d_0, in barrel.

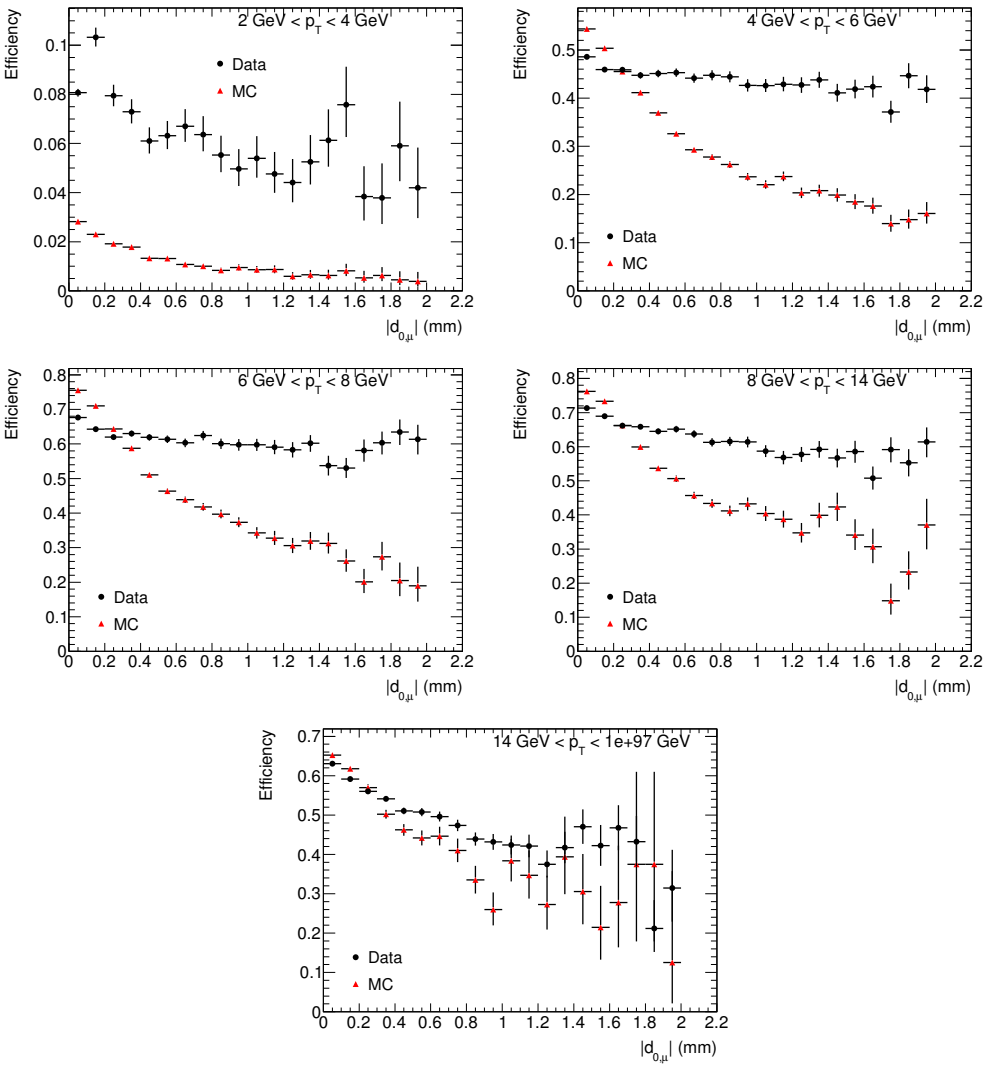

Figure A.2: Trigger selection efficiency as a function of the muon transverse impact parameter, d_0, in endcap.

Appendix B

Measurement of Λ Polarization

B.1 Modified Pearson's χ^2-test

Data and MC histograms are compared using a modified version of the Pearson's χ^2-test designed to compare unweighted (data) and wighted (MC) histograms [69]. It operates under assumption that two compared histograms have the same number of bins, r, and represent the same distribution. In other words, this means that there is a set of probabilities, p_i, of an event to belong to the i-th bin of either histograms such that $\sum_{i=1}^{r} p_i = 1$. Observed number of entries in unweighted (data) histogram, n_i, will follow a Poisson distribution:

$$w(n_i|p_i) = \frac{1}{n_i!}(Np_i)^{n_i}\, e^{-Np_i}, \tag{B.1}$$

where N is total number of entries in the histogram, $N = \sum_{i=1}^{r} n_i$. On the other hand, a weight in the i-th bin of the weighted histogram (MC), w_i, can be approximated by the Gaussian distribution:

$$w(w_i|p_i) = \frac{1}{\sqrt{2\pi\sigma_i^2}}\, e^{-\frac{(Wp_i - w_i)^2}{2\sigma_i^2}}, \tag{B.2}$$

where $W = \sum_{i=1}^{r} w_i$ is the sum of weights in all the bins and σ_i^2 is the variance of the weight w_i. This variance is inherently unknown, but it can be approximated by its estimate, s_i^2, which is the sum of squares of weights of events in the i-th bin. The maximum likelihood estimator of the probability in the i-th bin, $\hat{p}_i$, under assumption that both the histograms represent the same distribution, can be then

found by maximizing the log-likelihood function:

$$\begin{aligned}\log L(p_i) &= \log w(n_i|p_i) + \log w(w_i|p_i) \\ &= n_i \log Np_i - Np_i - \log n_i! - \frac{(Wp_i - w_i)^2}{2s_i^2} - \log\sqrt{2\pi s_i^2}, \end{aligned} \quad \text{(B.3)}$$

which is maximized when

$$p_i = \hat{p}_i \equiv \frac{Ww_i - Ns_i^2 + \sqrt{(Ww_i - Ns_i^2)^2 + 4W^2 s_i^2 n_i}}{2W^2}. \quad \text{(B.4)}$$

Having the best estimates $\hat{p}_i$ one can use the test statistic

$$\chi^2 = \sum_{i=1}^{r} \left[\frac{(n_i - N\hat{p}_i)^2}{N\hat{p}_i} + \frac{(w_i - W\hat{p}_i)^2}{s_i^2} \right] \quad \text{(B.5)}$$

as a measure of likeness of the two histograms. It follows approximately χ^2_{r-1} distribution if some conditions are satisfied. According to Ref. [69] there should be more than 25 entries in each bin of the histograms, which is satisfied in this analysis.

B.2 Results of the Polarization Extraction in Kinematic Bins

B.2.1 Polarization in the Beam-Λ Reference Frame

Figures B.1 and B.2 show the results of the fits extracting polarization in the beam-Λ reference frame in bins of Λ transverse momentum, p_{T}. Figures B.3 and B.4 show the results in bins of the Feynman variable, x_{F}.

B.2.2 Polarization in the Di-jet Reference Frame

Figures B.5 and B.6 show the results of the fits extracting polarization in the di-jet reference frame in bins of Λ transverse momentum relative to the jet axis, k_{T}. Figures B.7 and B.8 show the results in bins of the jet Λ momentum fraction z.

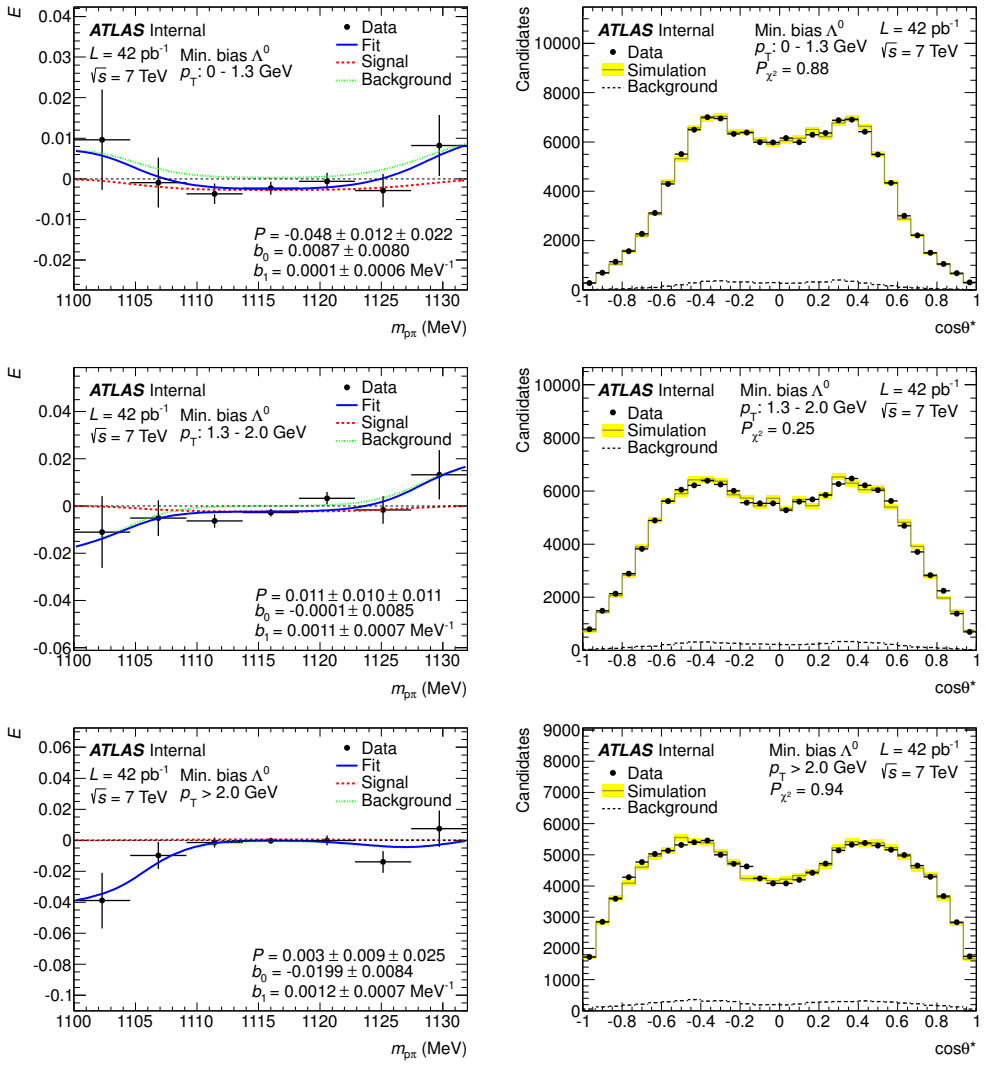

Figure B.1: Results of the fits of Λ polarization in the beam-Λ reference frame in bins of p_{T}. Plots in the left column show the decay angle expectation value fits, plots in the right column show the agreement between the decay angle distribution in data and MC weighted to the extracted polarization. The used p_{T} bin ranges are indicated in the plots.

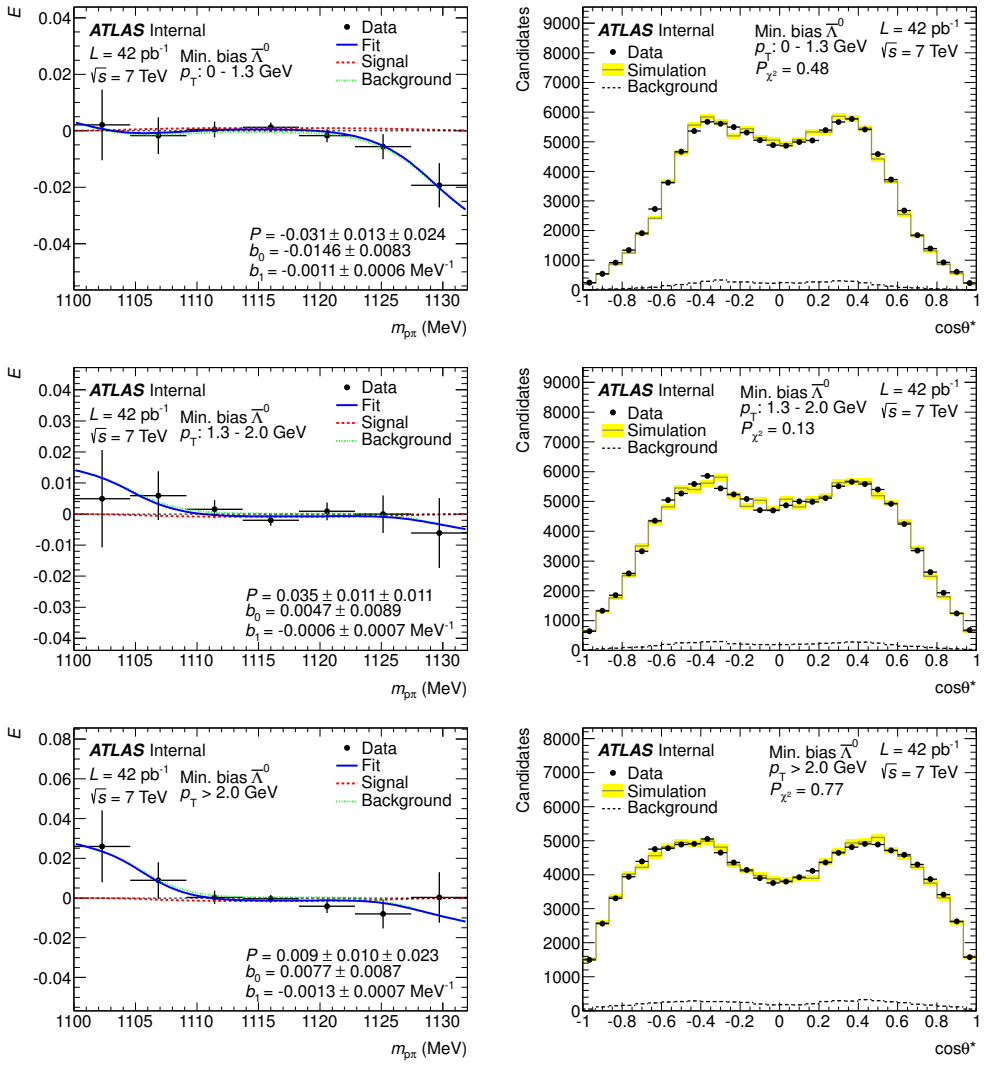

Figure B.2: Results of the fits of $\bar{\Lambda}$ polarization in the beam-Λ reference frame in bins of p_{T}. Plots in the left column show the decay angle expectation value fits, plots in the right column show the agreement between the decay angle distribution in data and MC weighted to the extracted polarization. The used p_{T} bin ranges are indicated in the plots.

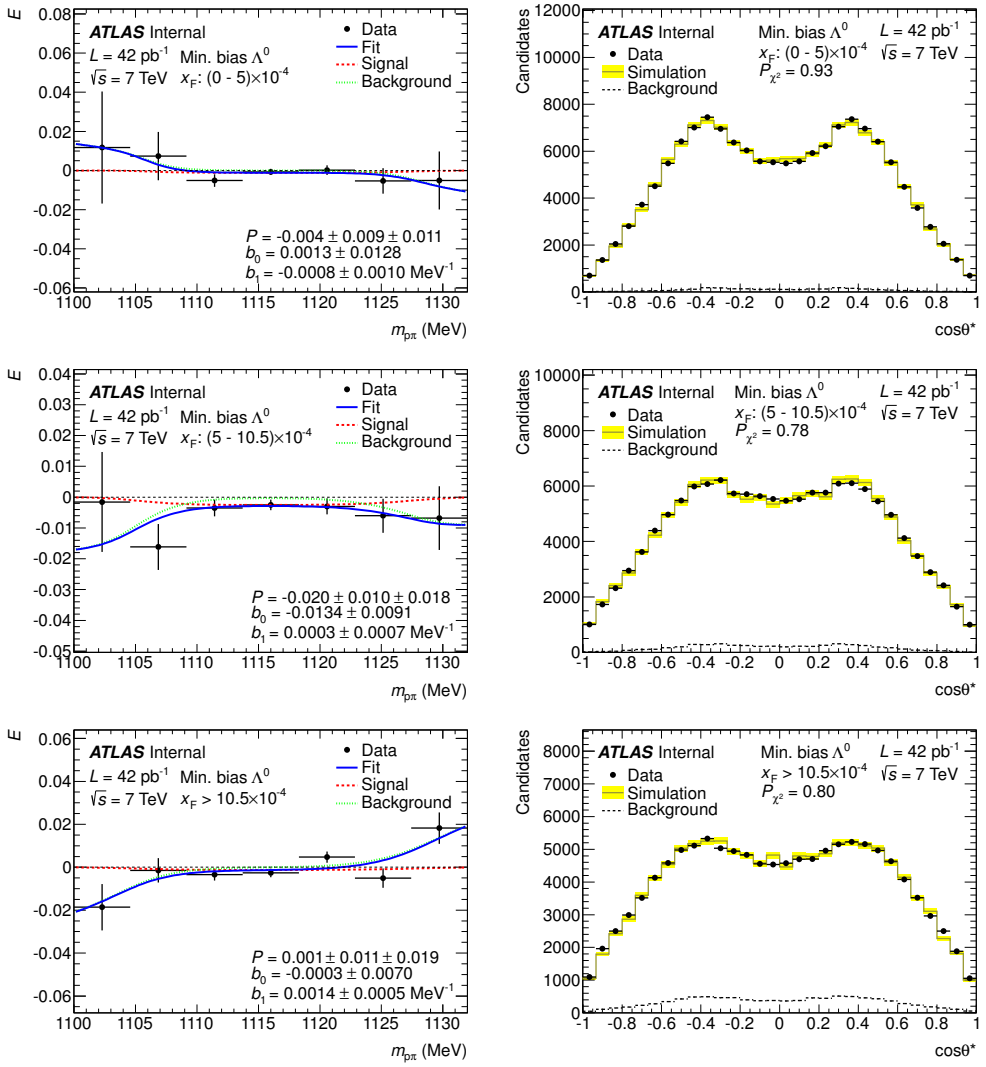

Figure B.3: Results of the fits of Λ polarization in the beam-Λ reference frame in bins of x_{F}. Plots in the left column show the decay angle expectation value fits, plots in the right column show the agreement between the decay angle distribution in data and MC weighted to the extracted polarization. The used x_{F} bin ranges are indicated in the plots.

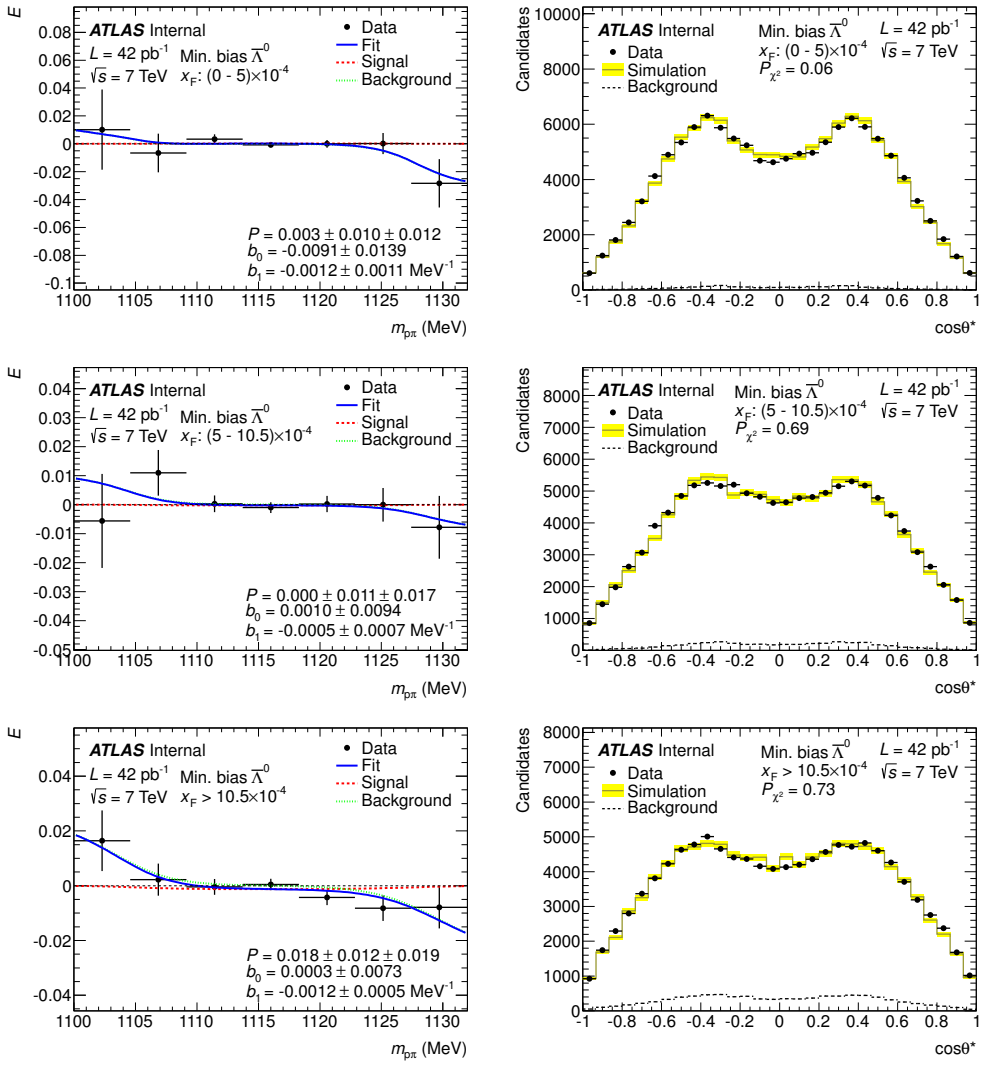

Figure B.4: Results of the fits of $\bar{\Lambda}$ polarization in the beam-Λ reference frame in bins of x_{F}. Plots in the left column show the decay angle expectation value fits, plots in the right column show the agreement between the decay angle distribution in data and MC weighted to the extracted polarization. The used x_{F} bin ranges are indicated in the plots.

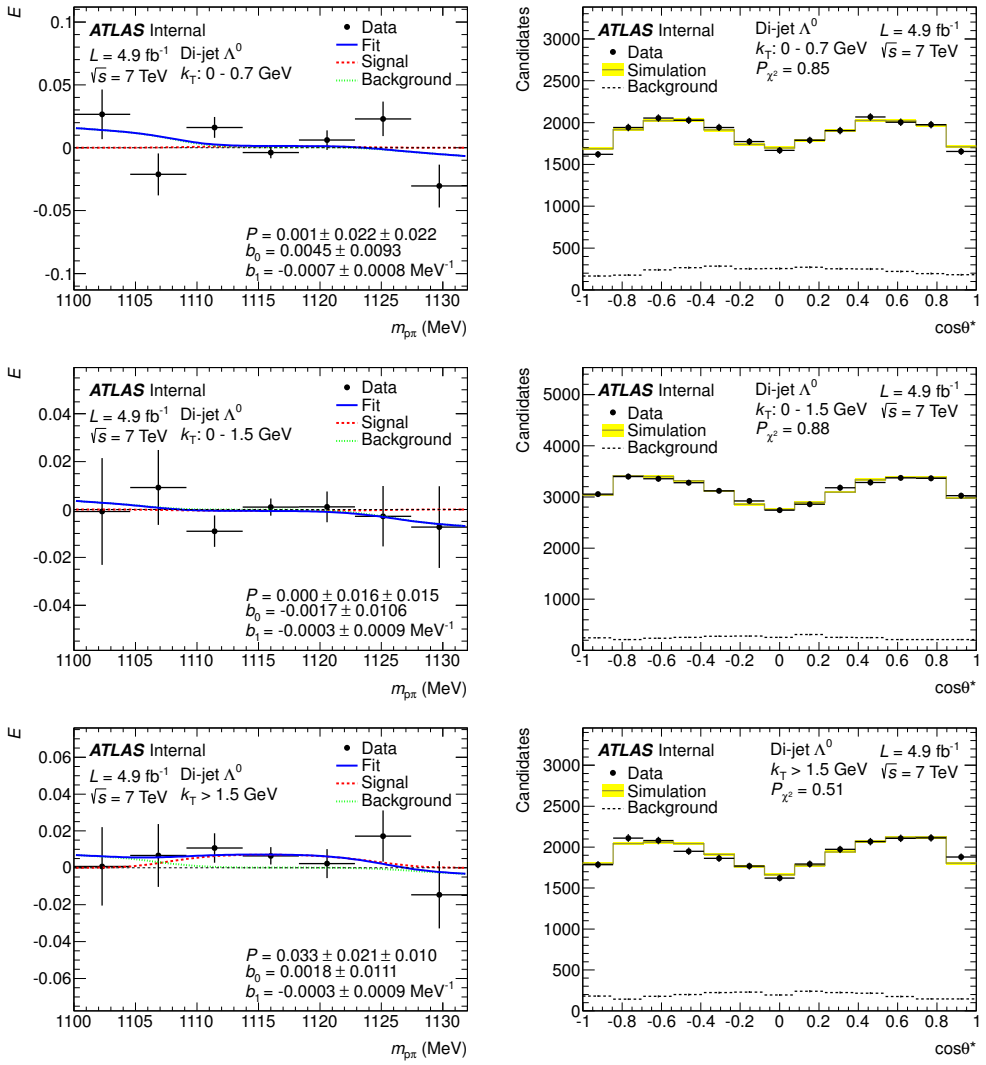

Figure B.5: Results of the fits of Λ polarization in the di-jet reference frame in bins of k_{T}. Plots in the left column show the decay angle expectation value fits, plots in the right column show the agreement between the decay angle distribution in data and MC weighted to the extracted polarization. The used k_{T} bin ranges are indicated in the plots.

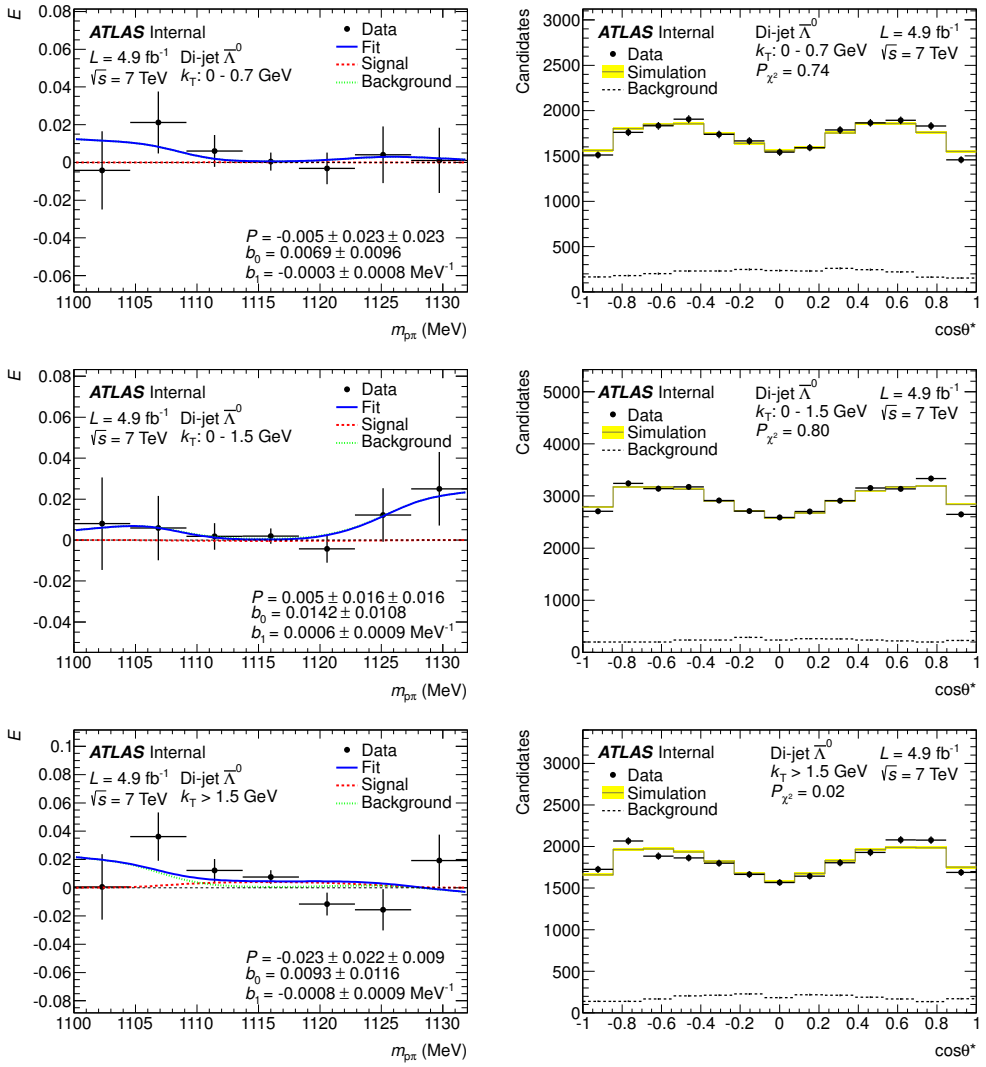

Figure B.6: Results of the fits of $\bar{\Lambda}$ polarization in the di-jet reference frame in bins of k_{T}. Plots in the left column show the decay angle expectation value fits, plots in the right column show the agreement between the decay angle distribution in data and MC weighted to the extracted polarization. The used k_{T} bin ranges are indicated in the plots.

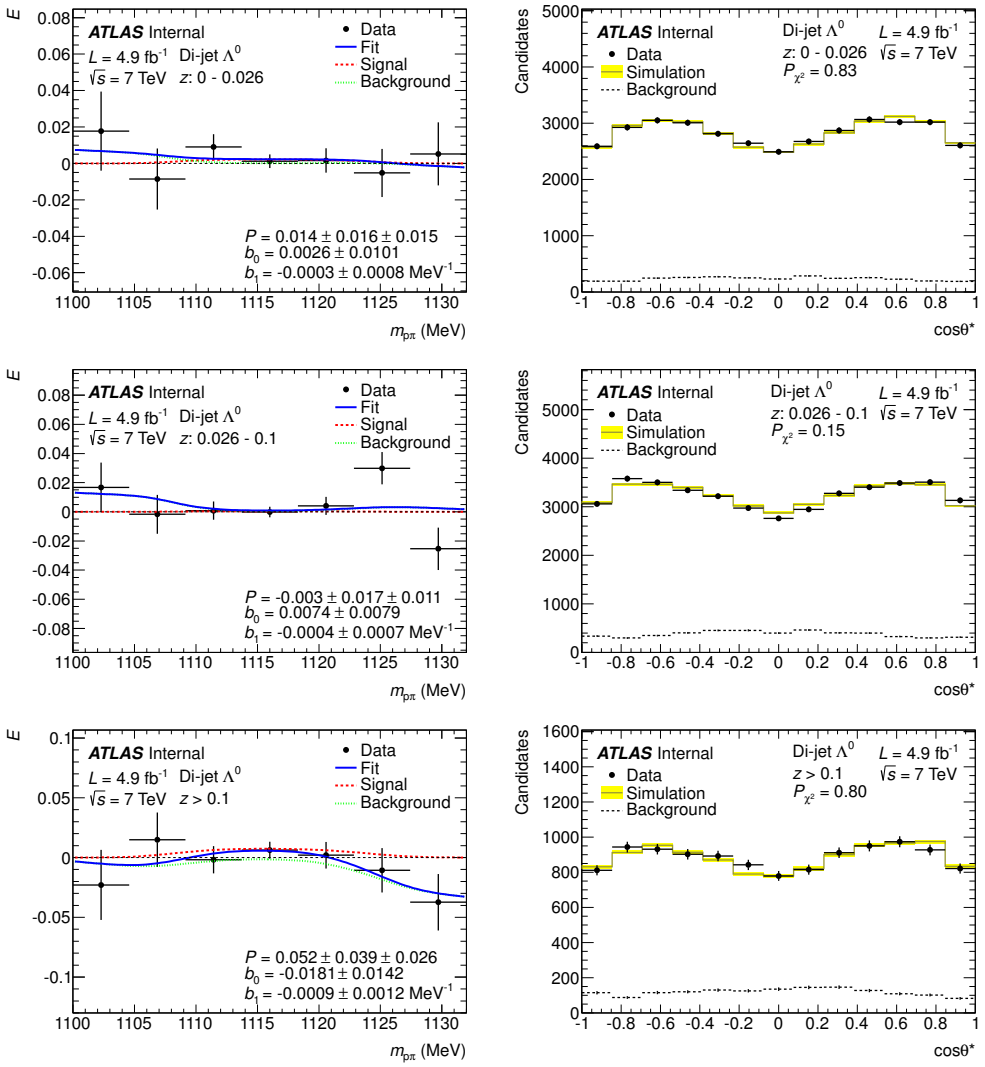

Figure B.7: Results of the fits of Λ polarization in the di-jet reference frame in bins of z. Plots in the left column show the decay angle expectation value fits, plots in the right column show the agreement between the decay angle distribution in data and MC weighted to the extracted polarization. The used z bin ranges are indicated in the plots.

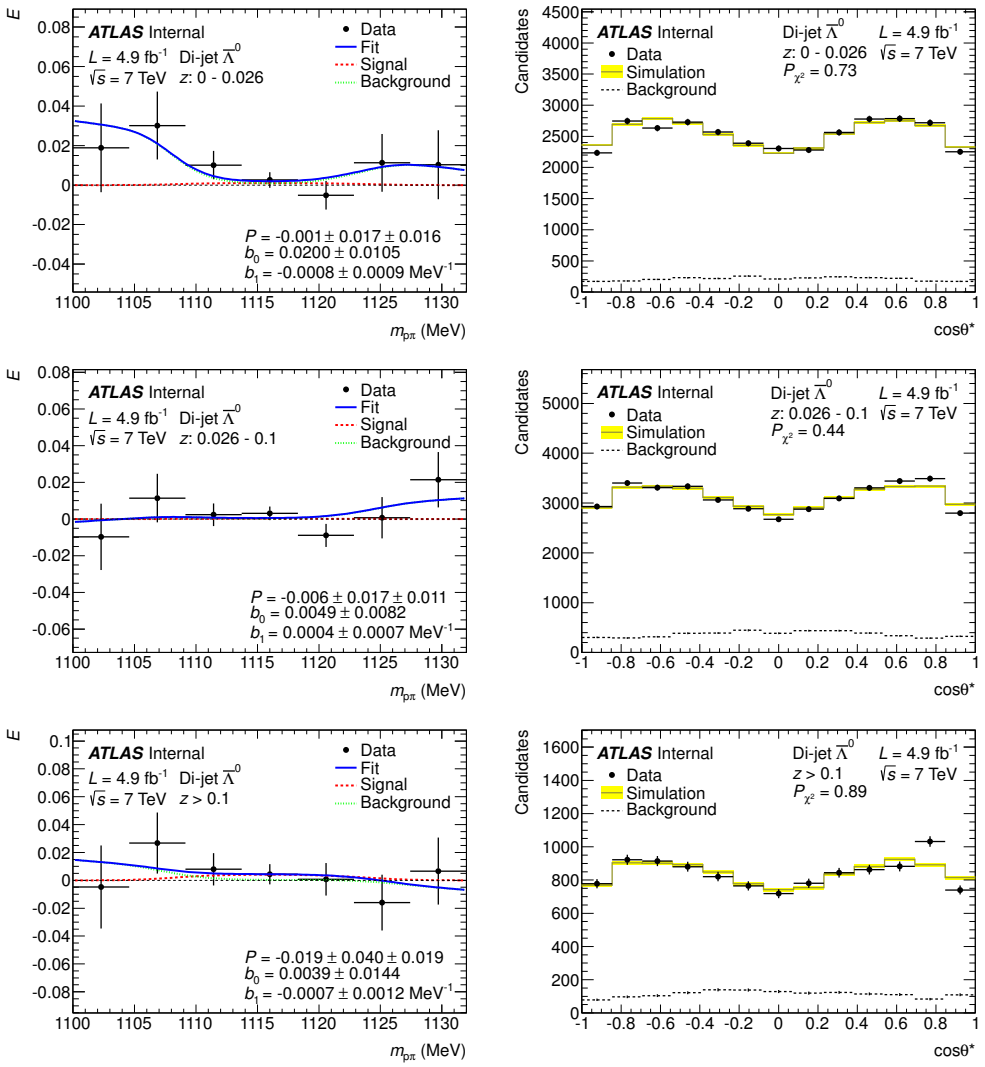

Figure B.8: Results of the fits of $\bar{\Lambda}$ polarization in the di-jet reference frame in bins of z. Plots in the left column show the decay angle expectation value fits, plots in the right column show the agreement between the decay angle distribution in data and MC weighted to the extracted polarization. The used z bin ranges are indicated in the plots.

B.3 Λ Kinematic Distributions

B.3.1 Kinematic Distributions of Minimum Bias Data

Figures B.9 and B.10 show distributions of the true Λ transverse momentum, $p_{\mathrm{T}}^{\mathrm{true}}$, and the true Feynman variable, $x_{\mathrm{F}}^{\mathrm{true}}$, for the minimum bias sample binned in p_{T} and x_{F}, respectively.

B.3.2 Kinematic Distributions of Di-jet Data

Figures B.11 and B.12 show distributions of the true Λ transverse momentum relative to the jet axis, $k_{\mathrm{T}}^{\mathrm{true}}$, and the true jet Λ momentum fraction, z^{true}, for the di-jet sample binned in p_{T} and x_{F}, respectively. Figures B.13 and B.14 show distributions of the true jet momentum fraction, $x_{\mathrm{j}}^{\mathrm{true}}$, for the jet containing Λ, and the true di-jet variable, $y_{\mathrm{j}}^{\mathrm{true}}$. Finally, Figures B.15 and B.16 show distributions of the true jet momentum fraction, $x_{\mathrm{j_1}}^{\mathrm{true}}$ and $x_{\mathrm{j_2}}^{\mathrm{true}}$, for the leading and sub-leading jets, respectively. The variable x_{j} is defined as

$$x_{\mathrm{j}} = \frac{2|\vec{k}_{\mathrm{j}}|}{\sqrt{s}},$$

where $\vec{k}_{\mathrm{j}}$ is the jet momentum and $\sqrt{s}$ is the total energy of the colliding beams.

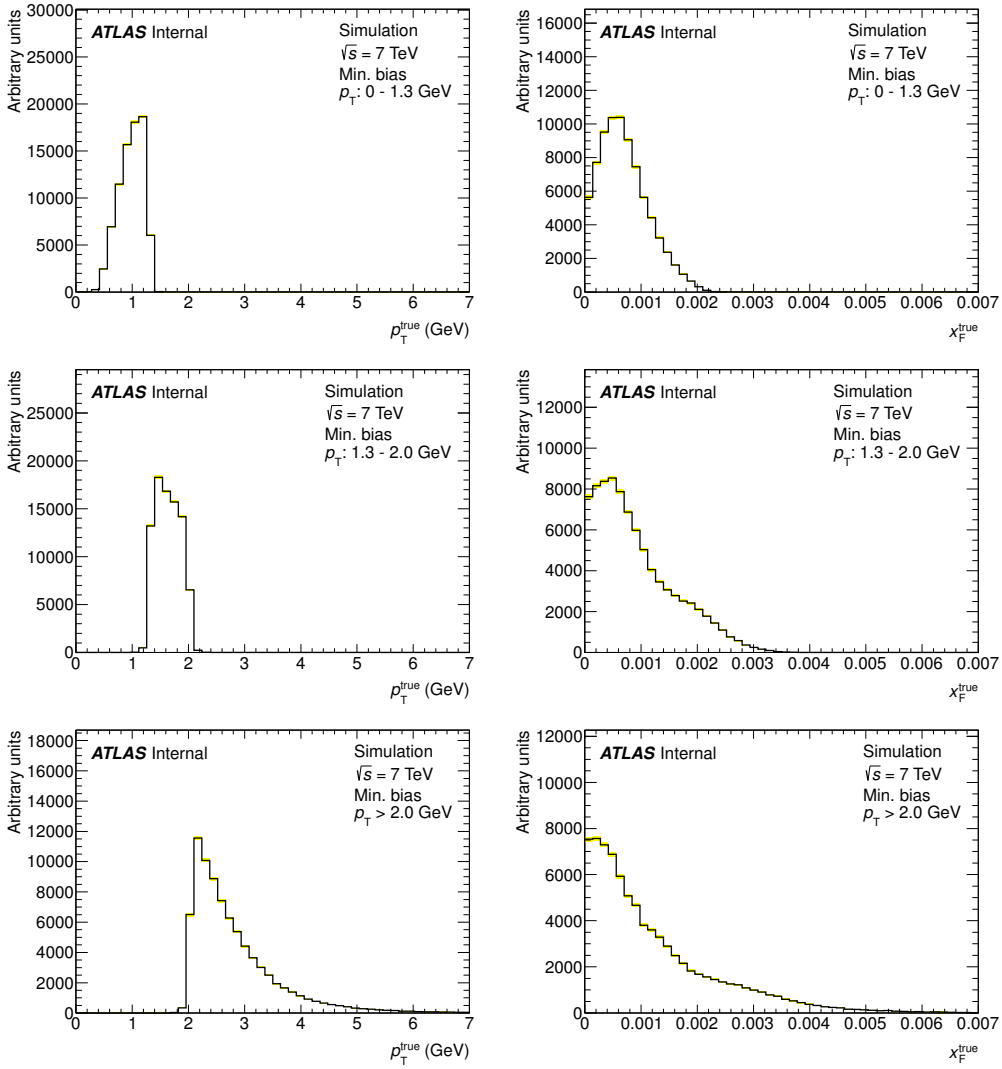

Figure B.9: Distributions of the true Λ transverse momentum, $p_{\mathrm{T}}^{\mathrm{true}}$ (left), and the true Feynman variable, $x_{\mathrm{F}}^{\mathrm{true}}$ (right), in bins of p_{T}. The used p_{T} bin ranges are indicated in the plots.

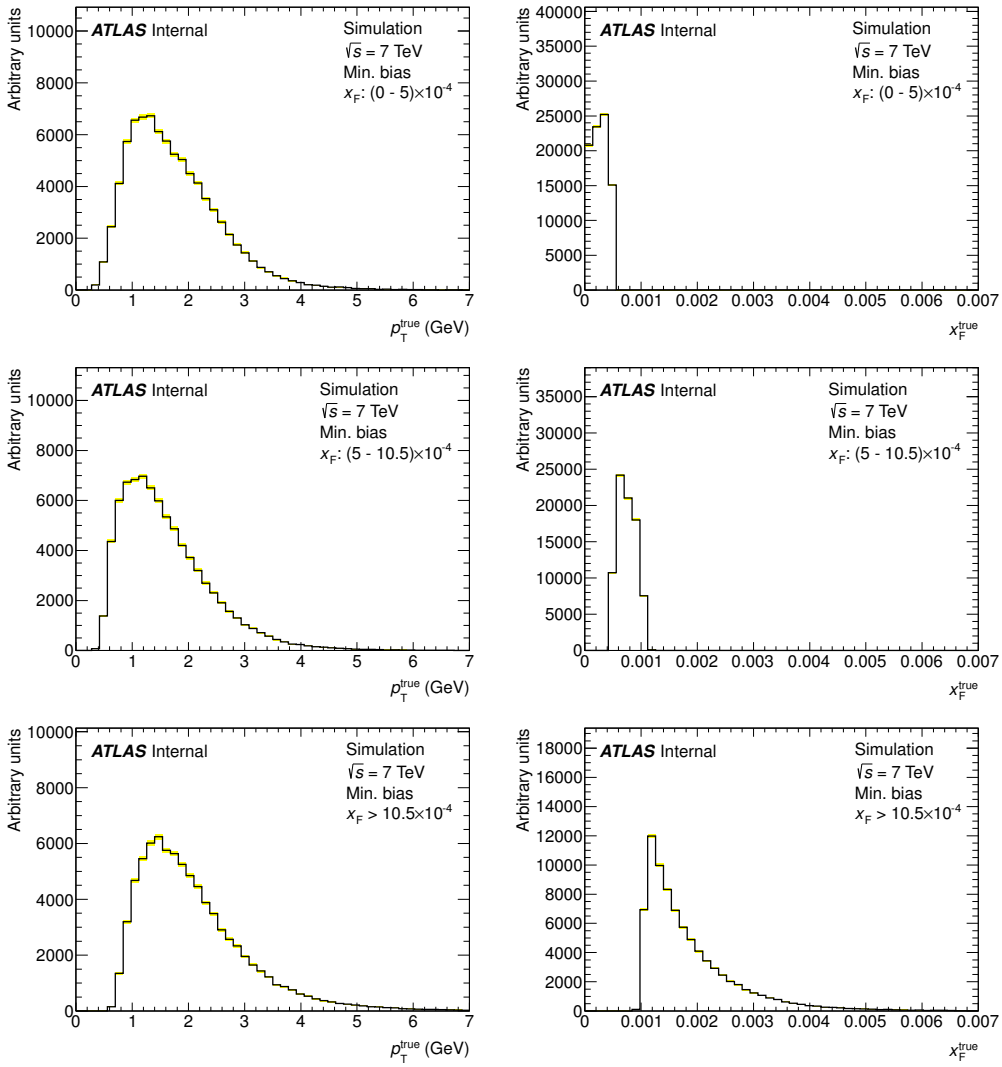

Figure B.10: Distributions of the true Λ transverse momentum, $p_{\mathrm{T}}^{\mathrm{true}}$ (left), and the true Feynman variable, $x_{\mathrm{F}}^{\mathrm{true}}$ (right), in bins of x_{F}. The used x_{F} bin ranges are indicated in the plots.

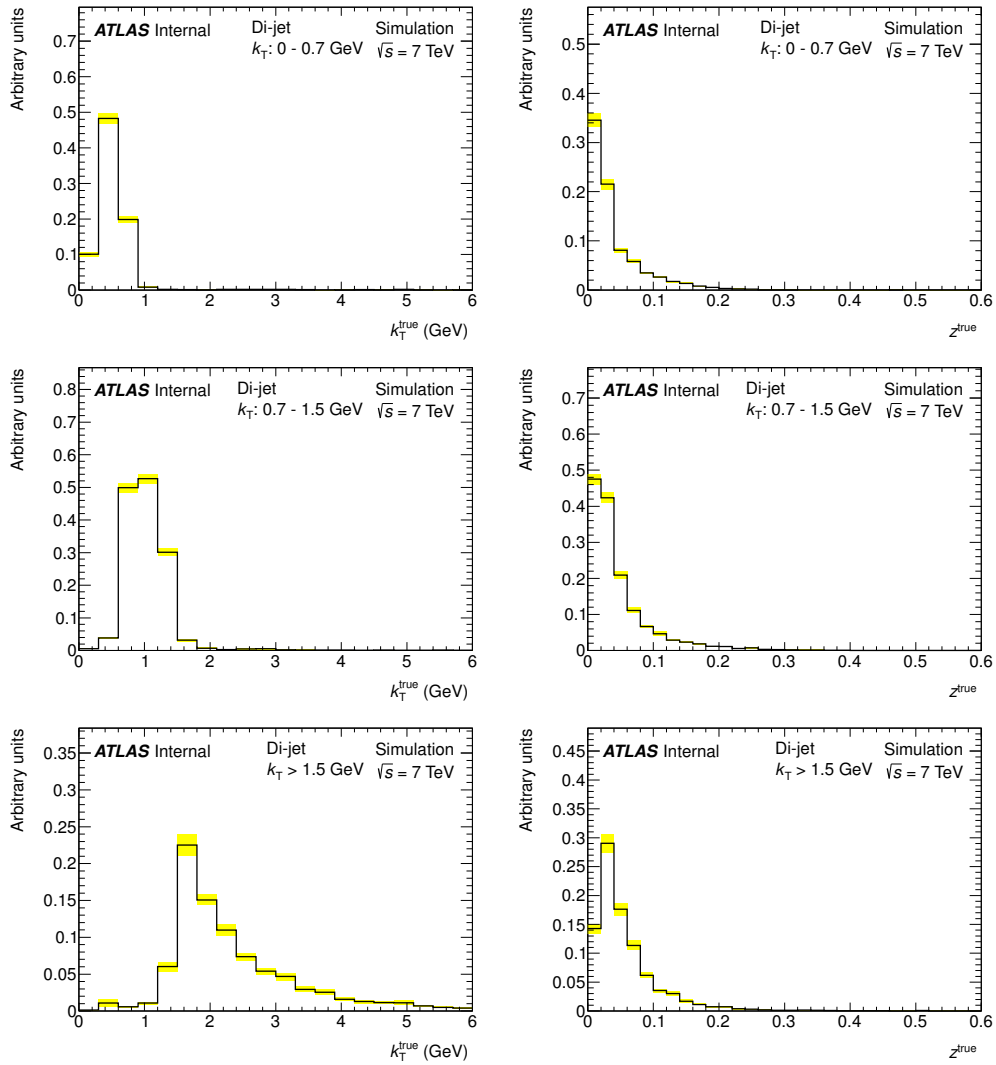

Figure B.11: Distributions of the true Λ transverse momentum relative to the jet axis, $k_{\mathrm{T}}^{\mathrm{true}}$ (left), and the true jet Λ momentum fraction, z^{true} (right), in bins of k_{T}. The used k_{T} bin ranges are indicated in the plots.

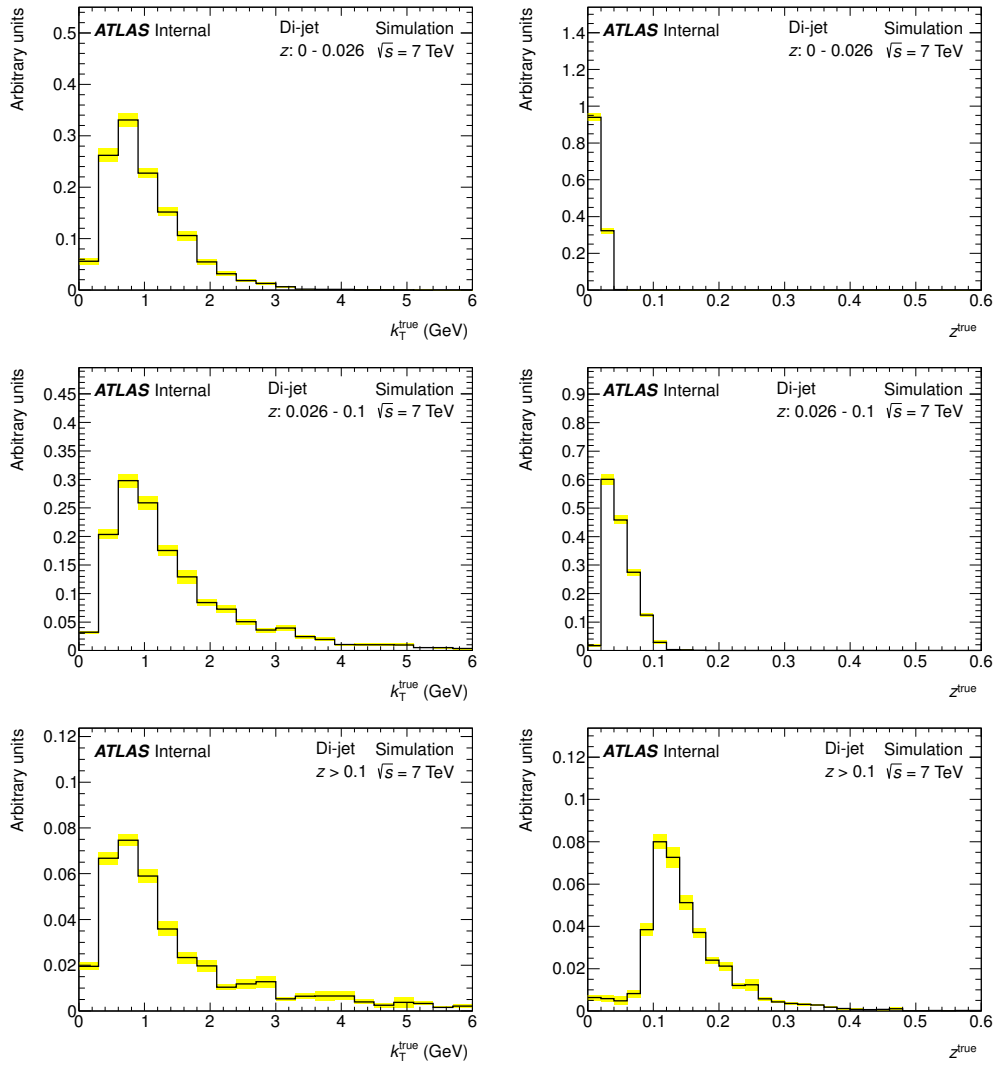

Figure B.12: Distributions of the true Λ transverse momentum relative to the jet axis, $k_{\mathrm{T}}^{\mathrm{true}}$ (left), and the true jet Λ momentum fraction, z^{true} (right), in bins of z. The used z bin ranges are indicated in the plots.

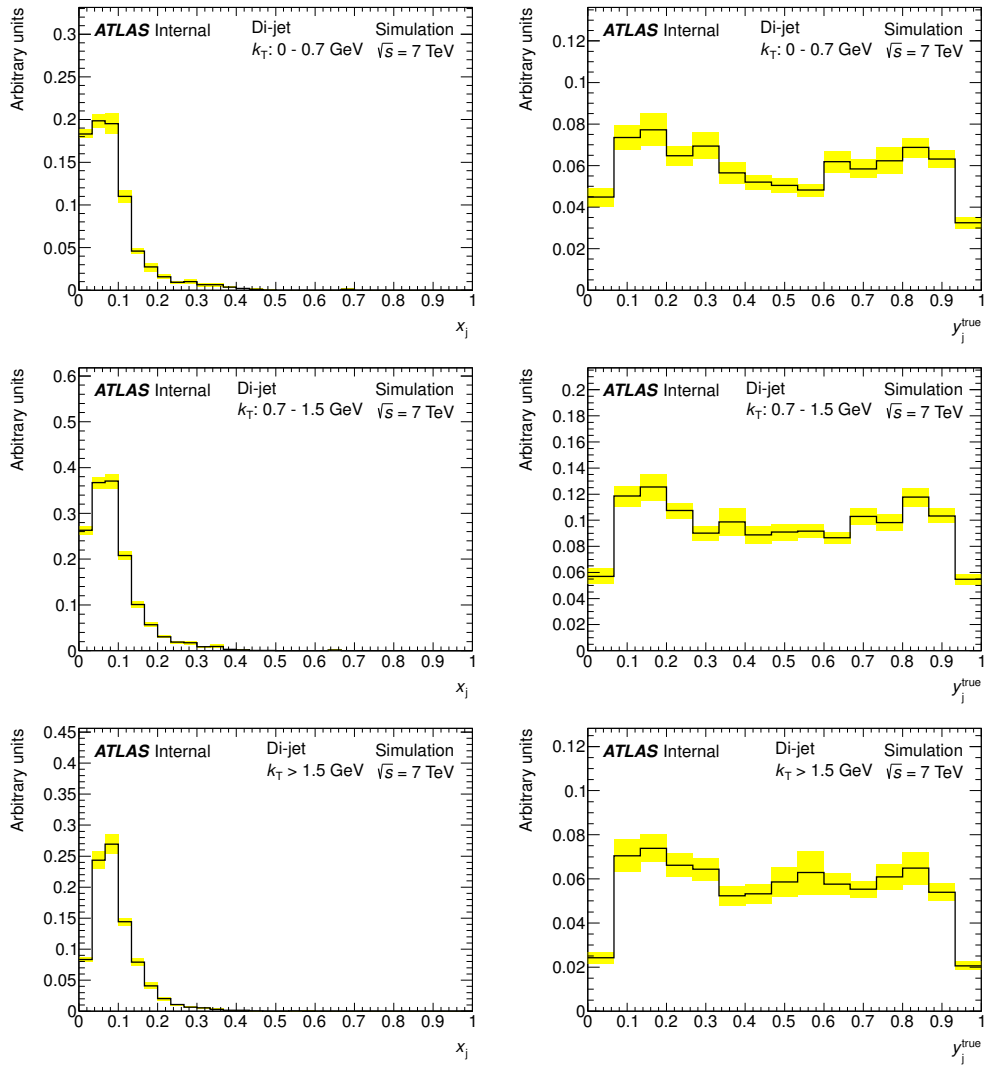

Figure B.13: Distributions of the true jet momentum fraction, $x_{\mathrm{j}}^{\mathrm{true}}$ (left), for the jet containing Λ, and the true di-jet variable, $y_{\mathrm{j}}^{\mathrm{true}}$ (right), in bins of k_{T}. The used k_{T} bin ranges are indicated in the plots. The variable x_{j} is defined as $x_{\mathrm{j}} = 2|\vec{k}_{\mathrm{j}}|/\sqrt{s}$, where $\sqrt{s}$ is the total energy of the colliding beams.

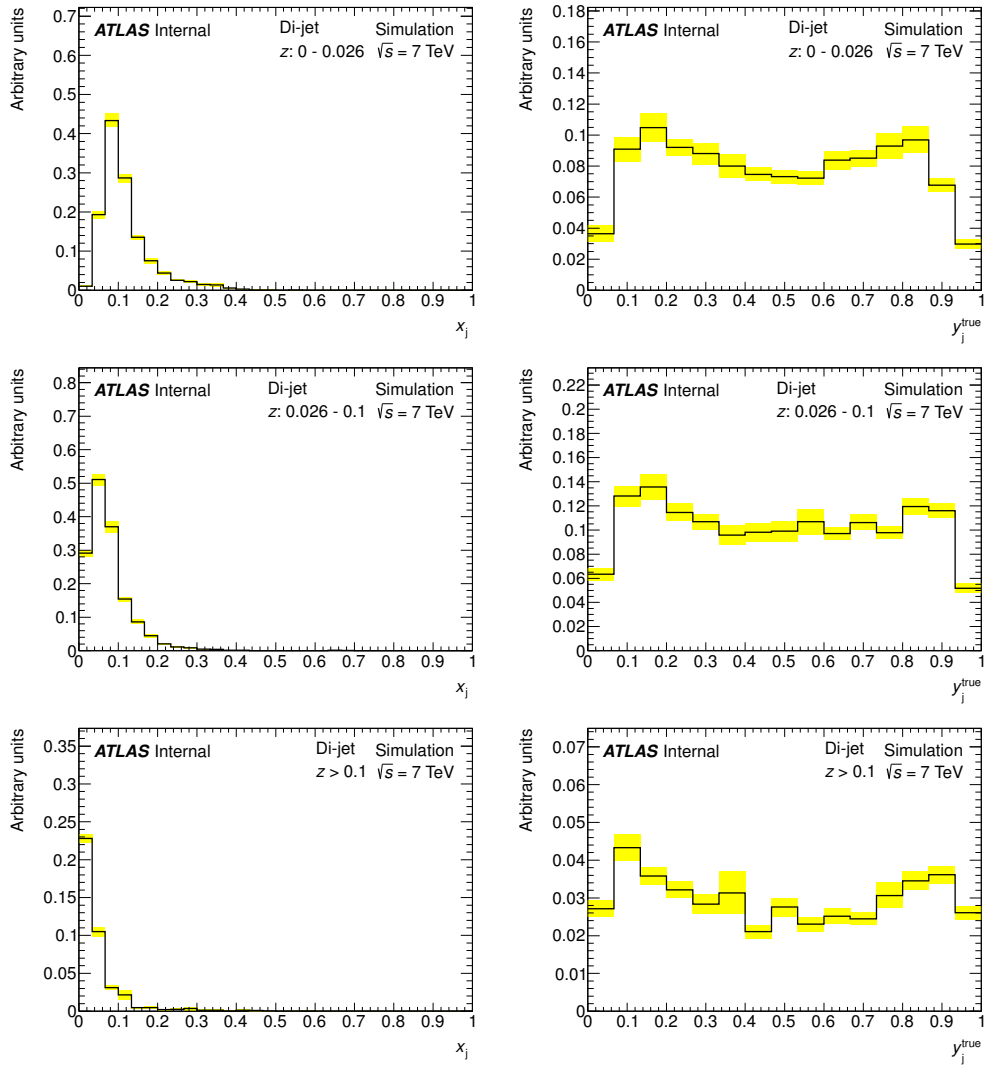

Figure B.14: Distributions of the true jet momentum fraction, $x_{\mathrm{j}}^{\mathrm{true}}$ (left), for the jet containing Λ, and the true di-jet variable, $y_{\mathrm{j}}^{\mathrm{true}}$ (right), in bins of z. The used z bin ranges are indicated in the plots. The variable x_{j} is defined as $x_{\mathrm{j}} = 2|\vec{k}_{\mathrm{j}}|/\sqrt{s}$, where $\sqrt{s}$ is the total energy of the colliding beams.

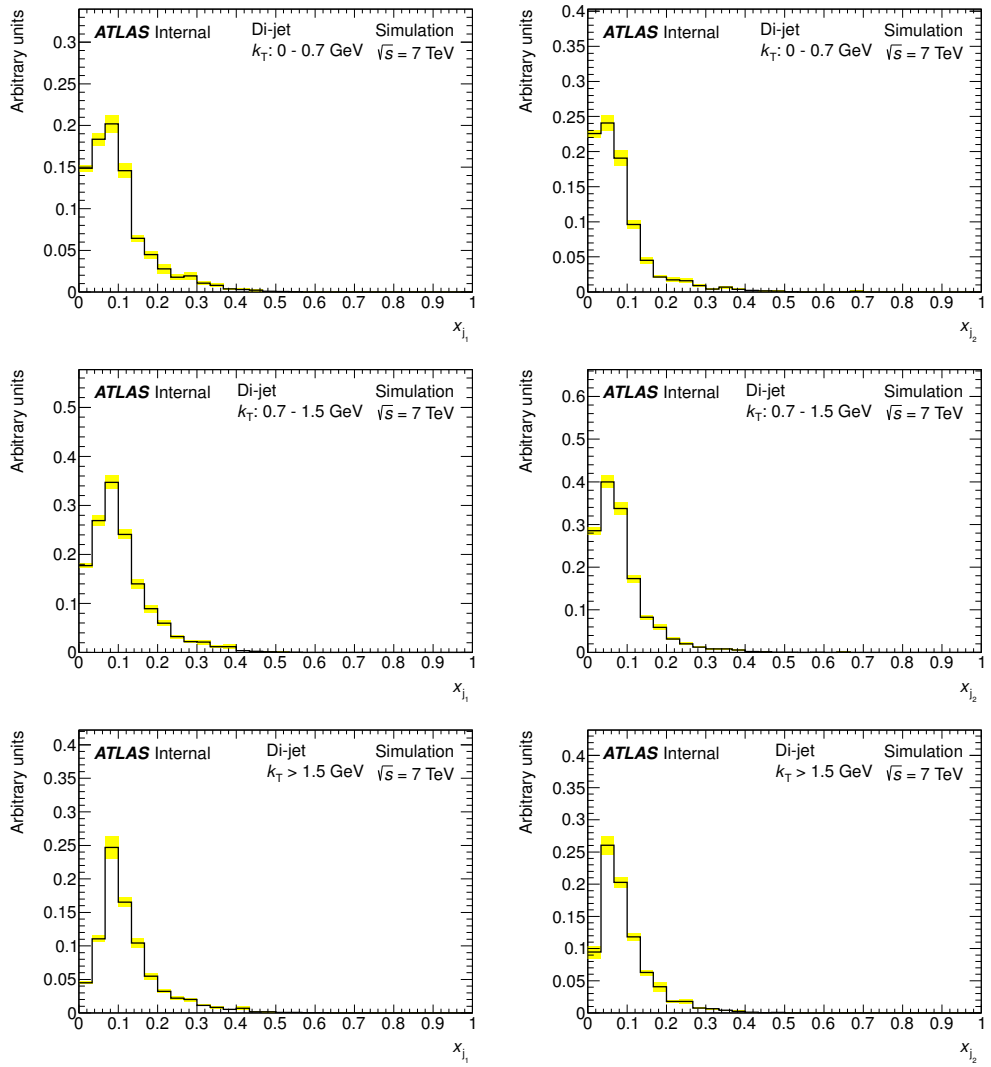

Figure B.15: Distributions of the true jet momentum fraction, $x_{\mathrm{j1}}^{\mathrm{true}}$ (left) and $x_{\mathrm{j2}}^{\mathrm{true}}$ (right), for the leading and sub-leading jets, respectively, in bins of k_{T}. The used k_{T} bin ranges are indicated in the plots. The variable $x_{\mathrm{j}i}$ is defined as $x_{\mathrm{j}_i} = 2|\vec{k}_{\mathrm{j}_i}|/\sqrt{s}$, where $\sqrt{s}$ is the total energy of the colliding beams.

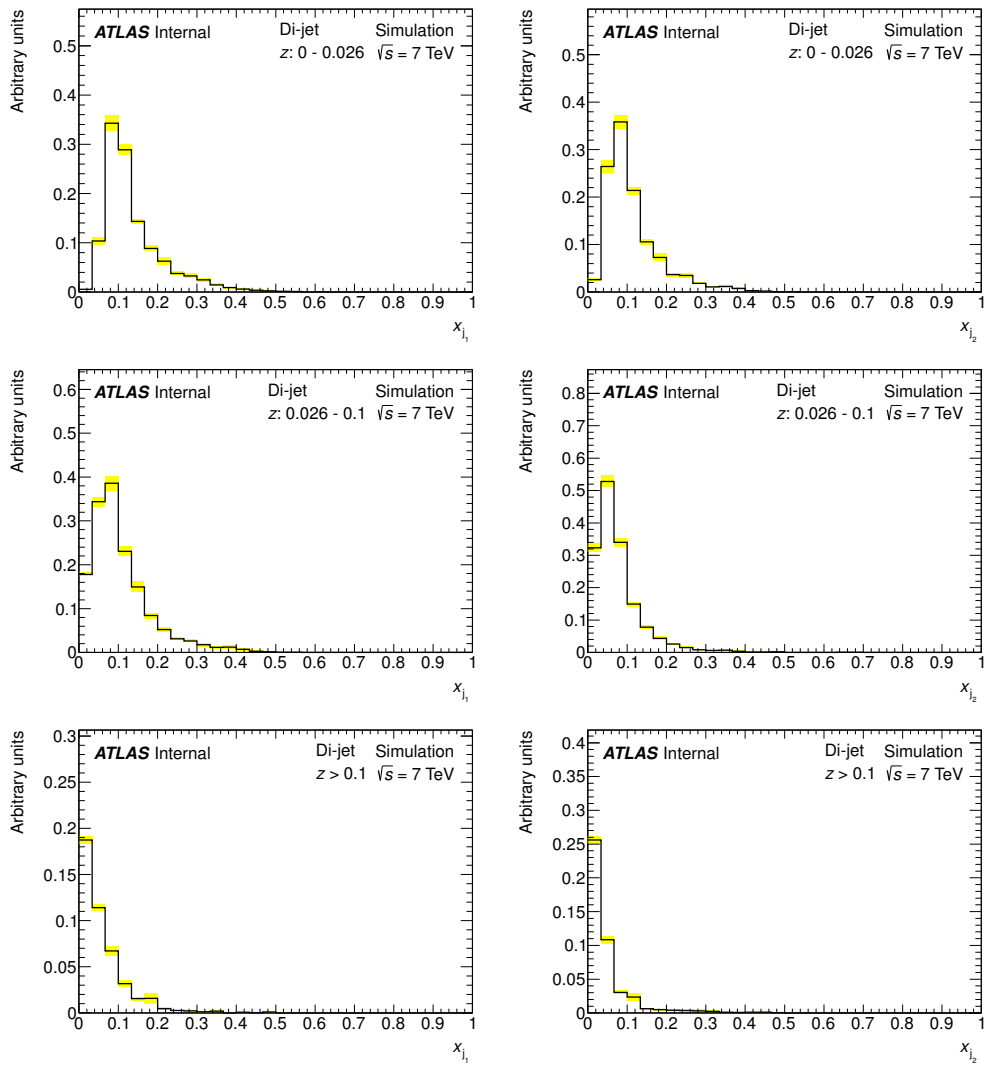

Figure B.16: Distributions of the true jet momentum fraction, $x_{\mathrm{j1}}^{\mathrm{true}}$ (left) and $x_{\mathrm{j2}}^{\mathrm{true}}$ (right), for the leading and sub-leading jets, respectively, in bins of z. The used z bin ranges are indicated in the plots. The variable $x_{\mathrm{j}i}$ is defined as $x_{\mathrm{j}_i} = 2|\vec{k}_{\mathrm{j}_i}|/\sqrt{s}$, where $\sqrt{s}$ is the total energy of the colliding beams.

References

[1] ATLAS Collaboration, *Observation of the decay $B_d^0 \to J/\psi(\mu^+\mu^-)K_S^0(\pi^+\pi^-)$ with the ATLAS experiment at the LHC*, ATLAS-CONF-2011-105. http://cdsweb.cern.ch/record/1369830.

[2] ATLAS Collaboration, *Observation of the decay $\Lambda_b^0 \to J/\psi(\mu^+\mu^-)\Lambda^0(p^+\pi^-)$ with the ATLAS experiment at the LHC*, ATLAS-CONF-2011-124, 2011. http://cdsweb.cern.ch/record/1378514.

[3] The ATLAS Collaboration, *Measurement of the Λ_b^0 lifetime and mass in the ATLAS experiment*, Phys. Rev. D **87** (2013) 032002. http://link.aps.org/doi/10.1103/PhysRevD.87.032002.

[4] D. Scheirich, H. A. Neal, and J. Zhu, *Measurement of Λ^0 polarization in ATLAS*, ATL-COM-PHYS-2011-1672 (internal). http://cds.cern.ch/record/1405443.

[5] ATLAS Collaboration, *Performance of the ATLAS Trigger System in 2010*, Eur. Phys. J. **C72** (2012) 1849.

[6] ATLAS Collaboration, *Expected performance of the ATLAS experiment : detector, trigger and physics*, CERN-OPEN-2008-020. http://cdsweb.cern.ch/record/1125884.

[7] ATLAS Collaboration, *ATLAS Detector and Physics Performance, Technical Design Report, Volumes I and II*, CERN/LHCC 99-14 and CERN/LHCC 99-15, 1999.

[8] ATLAS Collaboration, *Observation of a new particle in the search for the Standard Model Higgs boson with the ATLAS detector at the LHC*, Phys. Lett. B **716** (2012) no. 1, 1.

[9] ATLAS Collaboration, *ATLAS Inner Detector, Technical Design Report, Volumes I and II*, CERN/LHCC/97-16 and CERN/LHCC/97-17, 1997.

[10] ATLAS Collaboration, *ATLAS Calorimeter Performance, Technical Design Report*, CERN/LHCC/96-40, 1997.

[11] ATLAS Collaboration, *The ATLAS Experiment at the CERN Large Hadron Collider*, JINST **3** (2008) S08003.

[12] ATLAS Collaboration, *ATLAS Muon Spectrometer, Technical Design Report*, CERN/LHCC 97-22, 1997.

[13] ATLAS Collaboration, *ATLAS Level-1 Trigger, Technical Design Report*, ATLAS TDR-12, 1998.

[14] ATLAS Collaboration, *ATLAS High-Level Trigger Data Acquisition and Controls, Technical Design Report*, CERN/LHCC 2003-022, 2003.

[15] Particle Data Group Collaboration, J. Beringer et al. Phys. Rev. D **86** (2012) 010001.

[16] LHCb Collaboration, *Measurement of b-hadron masses*, Phys. Lett. B **708** (2012) 241 – 248.

[17] CDF Collaboration, T. Aaltonen et al., *Measurement of the* Λ_b^0 *Lifetime in* $\Lambda_b^0 \to \Lambda_c^+\pi^-$ *Decays in* $p\bar{p}$ *Collisions at* $\sqrt{s} = 1.96\ TeV$, Phys. Rev. Lett. **104** (2010) 102002.

[18] CDF Collaboration, T. Aaltonen et al., *Measurement of b hadron lifetimes in exclusive decays containing a J/psi in p-pbar collisions at sqrt(s)=1.96TeV*, Phys. Rev. Lett. **106** (2011) 121804.

[19] D0 Collaboration, V. M. Abazov et al., *Measurement of the* Λ_b^0 *lifetime in the exclusive decay* $\Lambda_b^0 \to J/\psi\Lambda^0$ *in* $p\bar{p}$ *collisions at* $\sqrt{s} = 1.96\ TeV$, Phys. Rev. D **85** (2012) 112003.

[20] N. Uraltsev Phys. Lett. B **376** (1996) 303.

[21] I. Bigi, M. Shifman, and N. Uraltsev Ann. Rev. of Nucl. Part. Science **47** (1997) 591.

[22] D. Pirjol and N. Uraltsev Phys. Rev. D **59** (1999) 034012.

[23] M. B. Voloshin Phys. Rev. D **61** (2000) 074026.

[24] F. Gabbiani, A. I. Onishchenko, and A. A. Petrov, *Spectator effects and lifetimes of heavy hadrons*, Phys. Rev. **D70** (2004) 094031.

[25] CDF Collaboration, *B-physics at CDF*, Fermilab-Conf-04/081-E, 2004. `arXiv:arXiv:hep-ex/0406021`.

[26] D0 Collaboration Phys. Rev. Lett. **99** (2007) 142001.

[27] T. Sjostrand, S. Mrenna, and P. Z. Skands, *PYTHIA 6.4 Physics and Manual*, JHEP **05** (2006) 026.

[28] ATLAS Collaboration, *ATLAS tunes of PYTHIA 6 and Pythia 8 for MC11*, ATL-PHYS-PUB-2011-009, 2011. `http://cds.cern.ch/record/1363300`.

[29] ATLAS Collaboration, *Alignment Performance of the ATLAS Inner Detector Tracking System in 7 TeV proton-proton collisions at the LHC*, ATLAS-CONF-2010-067, 2010. `http://cdsweb.cern.ch/record/1281342`.

[30] ATLAS Collaboration, *Alignment of the ATLAS Inner Detector Tracking System with 2010 LHC proton-proton collisions at sqrts = 7 TeV*, ATLAS-CONF-2011-012, 2011. `http://cdsweb.cern.ch/record/1334582`.

[31] A. Barton, I. Bozovic-Jelisavcic, J. Catmore, W. Dearnaley, A. Dewhurst, C. Heller, T. Jakoubek, R. Jones, T. Jovin, J. Kirk, L. Oakes, P. Reznicek, J. Schieck, and M. Smizanska, *Internal documentation for "Time dependent angular analysis of $B_{0s} \to J/\psi\phi$ decay and extraction of $\Delta\Gamma$ and the CP violating weak phase φ in ATLAS"*, ATL-COM-PHYS-2012-155 (internal), 2012. `http://cdsweb.cern.ch/record/1423324`.

[32] ATLAS Collaboration, *A study of the material in the ATLAS inner detector using secondary hadronic interactions*, JINST **7** (2012) P01013.

[33] J. J. Sakurai, *Modern Quantum Mechanics*. Addison Wesley; Rev Sub edition, 1993.

[34] M. Jacob and G. Wick Ann. Phys. **7** (1959) 404.

[35] W. G. Dharmaratna and G. R. Goldstein, *Single quark polarization in quantum chromodynamics subprocesses*, Phys.Rev. **D53** (1996) 1073–1086.

[36] Bunce et al., *Lambda0 hyperon polarization in inclusive production by 300-GeV protons on Beryllium*, Phys. Rev. Lett. **36** (1976) 1113–1116.

[37] Heller et al., *Polarization of Lambdas and Anti-Lambdas produced by 400-GeV protons*, Phys. Rev. Lett. **41** (1978) 607.

[38] Heller et al., *Polarization of Xi0 and Lambda hyperons produced by 400-GeV protons*, Phys. Rev. Lett. **51** (1983) 2025–2028.

[39] B. S. Yuldashev, *Neutral strange particle production in p Ne-20 and p N interactions at 300-GeV/c*, Phys. Rev **D43** (1991) 2792–2802.

[40] E799 Collaboration, E. J. Ramberg et al., *Polarization of Lambda and anti-Lambda by 800-GeV protons*, Phys. Lett. **B338** (1994) 403–408.

[41] NA48 Collaboration, V. Fanti et al., , Eur. Phys. J. **C6** (1999) 265.

[42] HERA-B Collaboration, Abt et al., *Polarization of Lambda and anti-Lambda in 920-GeV fixed-target proton-nucleus collisions*, Phys. Lett. **B638** (2006) 415–421.

[43] *Proceedings of 9th International Symposium on High Energy Spin Physics.* Springer-Verlag, Bonn, Germany, 1990. K. Heller, p97.

[44] E. B. Klinkby, $\Lambda/\bar{\Lambda}$ *polarization studies in proton nucleus collisions at 920 GeV proton beam energy.* PhD thesis, University of Copenhagen, 2004.

[45] H. A. Neal and E. De La Cruz Burelo, *Hyperon Polarization in a Quark-Quark Scattering Model*, `arXiv:arXiv:hep-ph/0602079`.

[46] T. A. Degrand and H. I. Miettinen, *Quark dynamics of polarization in inclusive hadron production*, Phys. Rev. **D23** (1981) 1227.

[47] T. A. Degrand and H. I. Miettinen, *Models of polarization asymmetry in inclusive hadron production*, Phys. Rev. **D24** (1981) 2419.

[48] T. Fujita and T. Matsuyama, *Comment on the DeGrand-Miettinen model for the polarization of lambda in proton-proton collisions*, Phys. Rev. D **38** (1988) 401–402.

[49] H. A. Neal and H. B. Nielsen Phys. Lett. **B51** (1974) 79.

[50] H. A. Neal, J. B. Kuah, and H. B. Nielsen Phys. Lett. **B439** (1998) 407.

[51] B. Andersson, G. Gustafson, and G. Ingelman, *A Semiclassical Model for the Polarization of Inclusively Produced Lambda 0 Particles at High-Energies*, Phys.Lett. **B85** (1979) 417.

[52] D. W. Sivers, *Single-spin production asymmetries from the hard scattering of pointlike constituents*, Phys. Rev. D **41** (1990) 83–90.

[53] D. W. Sivers, *Hard-scattering scaling laws for single-spin production asymmetries*, Phys. Rev. D **43** (1991) 261–263.

[54] D. Boer et al., *Spin asymmetries in jet-hyperon production at LHC*, Phys. Lett. **B659** (2007) 127–136, `arXiv:arXiv:0709.1087v2 [hep-ph]`.

[55] D. W. Sivers, *The Fractured Boer-Mulders Effect in the Production of Polarized Baryons*, Phys. Rev. D **81** (2010) 034029.

[56] J. Felix, *On Theoretical Studies of Lambda0 Polarization*, Mod. Phys. Lett A **14** (1999) 827–842.

[57] J. Soffer, *Is the Riddle of the Hyperon Polarization Solved?*, arXiv:hep-ph/9911373 (1999) .

[58] D. Boer, *Transverse Lambda polarization at high energy colliders*, PoS **DIS2010** (2010) 215, `arXiv:1007.3145 [hep-ph]`.

[59] D. Sivers, *Quantum number density asymmetries within QCD jets correlated with Λ^0 polarization*, Phys. Rev. D **85** (2012) 014024.

[60] M. Bahr, S. Gieseke, M. A. Gigg, D. Grellscheid, K. Hamilton, O. Latunde-Dada, S. Platzer, P. Richardson, M. H. Seymour, A. Sherstnev, and B. R. Webber, *Herwig++ physics and manual*, The European Physical Journal C **58** (2008) no. 4, 639–707. `http://dx.doi.org/10.1140/epjc/s10052-008-0798-9`.

[61] S. Agostinelli et al., *Geant4: A simulation toolkit*, Nucl. Instrum. Meth. A **506 no.3** (2003) 250 – 303.

[62] ATLAS Collaboration, *Jet energy scale and its systematic uncertainty in proton-proton collisions at sqrt(s)=7 TeV with ATLAS 2011 data*, ATLAS-COM-CONF-2012-171 (internal), 2012. http://cds.cern.ch/record/1475233.

[63] ATLAS Collaboration, *Recommendations for jet cleaning for data 2011*, tWiki (internal), 2011. http://twiki.cern.ch/twiki/bin/viewauth/AtlasProtected/HowToCleanJets2011.

[64] C.-H. Chou, H.-H. Shih, and H.-N. Li Phys.Rev. **D65** (2002) 074030, arXiv:arXiv:hep-ph/0112145.

[65] O. Leitner, Z. Ajaltouni, and E. Conte Nucl.Phys. **A755** (2005) 435, arXiv:arXiv:hep-ph/0412131.

[66] Z. Ajaltouni, E. Conte, and O. Leitner Phys.Lett. **B614** (2005) 165, arXiv:arXiv:hep-ph/0412116.

[67] LHCb Collaboration, *Measurements of the Lambda_b0 -¿ J/psi Lambda decay amplitudes and the Lambda_b0 polarisation in pp collisions at sqrt(s) = 7 TeV*, Lhcb-paper-2012-057. arXiv:arXiv:hep-ex/1302.5578.

[68] Ellis, J. and Hwang, D. S., *Spin Correlations of Lambda anti-Lambda Pairs as a Probe of Quark-Antiquark Pair Production*, Cern-ph-th/2011-212. arXiv:arXiv:hep-ph/1108.5319.

[69] N. Gagunashvili, *Pearson's Test Modifications for Comparison of Unweighted and Weighted Histograms and Two Weighted Histograms*, PoS(ACAT) **060** (2007) .